

**Calibration-free Wavelength Modulation Spectroscopy  
with Elimination of Residual Amplitude Modulation**

**Arup Lal Chakraborty**

Centre for Microsystems and Photonics  
Department of Electronic and Electrical Engineering  
University of Strathclyde  
204 Royal College Building  
Glasgow

A thesis submitted to the Department of Electronic and Electrical  
Engineering at the University of Strathclyde for the degree of Doctor of  
Philosophy

**May 2010**

# **Declaration of Authenticity**

This thesis is the result of the author's original research. It has been composed by the author and has not been previously submitted for examination which has led to the award of a degree.

Signed: .....

Date: .....

# **Declaration of Author's rights**

The copyright of this thesis belongs to the author under the terms of the United Kingdom Copyright Acts as qualified by University of Strathclyde Regulation 3.50. Due acknowledgement must always be made of the use of any material contained in, or derived from, this thesis.

Signed: .....

Date: .....

## Acknowledgement

This thesis is the culmination of the hard work put in by many people at various times over the last few years. I do not have the gift of words to even begin to express my gratitude to all of you. It is perhaps best to start in a chronological way which should also help to weave a short tale of how I landed up in Glasgow.

Walter and Brian, I owe both of you a debt of gratitude that cannot ever be repaid. You have taught me more than you know. I hardly dreamt that our meeting at Photonics 2006 in Hyderabad would lead to my landing up in this fascinating country.

Walter, thanks for being a critical but a very patient and helpful supervisor. My wife and I are extremely grateful for all your help in getting us settled in (including tips on how to operate the oven!). Your amazing equanimity even when things were getting desperate is something that I need to learn. It is not often that people have touched my life and left such a lasting impression. Whatever little I have done here is my only way of saying “Thank you” to you for the way you have changed my life.

Thank you Brian for giving me the opportunity to test my teaching skills, although I must admit I was jealous of you because while you were enjoying the Indian sun I was braving the winter rain in Glasgow! Thank you for giving me the confidence to get in at the deep end right at the beginning. Taking up that challenge was very rewarding, and I learnt more about myself than I would have if you had not gently persuaded me.

George, I have learnt a lot from the short chats with you about some of the intricacies of our work. I deeply admire the simple way in which you are able to explain things. There is an old Sanskrit adage – true learning brings humility. You epitomize this philosophy.

I am extremely grateful to you Sadie for all your help with arranging the first flat. Thanks a lot for viewing the two flats, sending me the pictures and finally sorting out all the paper work. I cannot think of any one else who would have done that. I record my thanks for Carole too, for helping me during that transition period. You and Sadie formed two pillars of the group. Thanks to Rachel (who has stepped in only recently) for helping me by making arrangements for the necessary memos for submission.

Thanks to Kevin for his patience during those early days when I could never remember whether we were using the 1650nm laser or the 1648 nm one!

Many thanks to you Ian for the excellent LabVIEW programs and for making those small changes that I asked for from time to time.

Keith, it has been an absolute pleasure to work with you. I wish was half as meticulous as you are whether in the lab or in keeping all relevant data sorted and properly filed. I am sure you will have a great PhD. Thanks for improving my abysmal Microsoft skills!

Mick is deeply disappointed in me for not giving LaTeX a shot. My apologies to you, Mick. I have really enjoyed our infrequent but very weighty conversations (although mainly at those five-course conference dinners!). Please don't reveal all you have come to know about how I process my data!

What can I say about you David that has not already been said! I maintain that guys like Mick and you should never be allowed to go on leave at the same time because the office becomes really dull. Don't forget my two and a half quid - that's less than half the national hourly rate!

Jamie, the many stimulating discussions with you about cricket and the occasional chat about our collective efforts in gas sensing, have been very enjoyable. I hope you will help to convince Mick that I was definitely not hung over at the Hofbrauhaus!

I am grateful to my parents for providing an academic atmosphere at home and for my early grounding in scientific thinking.

The two people who have been my greatest source of support and sustenance through this roller-coaster ride are my wife, Manobina and our daughter, Angana, who is now a wee Scottish lass! I could not have done this without my wife's sacrifices and constant encouragement when things looked bleak. Thank you for all that you have done for me including the packed lunches that regularly distracted David! When this is all finally over we must catch up on a lot that we have missed especially during the last six months. To my daughter, who is our greatest blessing, all I can say is that someday when you are doing a PhD and have a daughter yourself, you will realize what wonders a child can do to relieve the stress and frustration of this period. I love you and am proud of you and I deeply admire the way you have accepted and adjusted to your "grumpy" father.

## Abstract

Tunable diode laser spectroscopy (TDLS) is a versatile and powerful technique that is widely used for the measurement of gas concentration and pressure for industrial process control applications. TDLS is used in conjunction with wavelength modulation (TDLS-WMS) to make quantitative measurements on near-infrared as well as mid-infrared absorption lines of gases. Traditional WMS based on the detection of 1<sup>st</sup> harmonic ( $1f$  WMS) and 2<sup>nd</sup> harmonic ( $2f$  WMS) signals requires signal calibration for the extraction of gas parameters. This is because the acquired electrical signals are not related in a straightforward way to the gas parameters since these signals are affected by several system parameters that are subject to variation or drift such as the laser intensity, optical throughput of the system and detector gain. Systematic errors due to calibration drift require periodic re-calibration which is inconvenient for stand-alone instruments and continuous operation in harsh conditions. Recently two calibration-free  $1f$  WMS techniques namely the RAM method and the Phasor Decomposition method (PDM), have been developed by researchers at the University of Strathclyde. These techniques represent significant advances in this field because the absolute gas absorption line shape is recovered directly from which it is possible to extract gas parameters by using simple least-squares curve fitting routines. However the fidelity of signal recovery in both techniques is limited by a high concentration-independent residual amplitude modulation (RAM) signal that arises due to the intensity modulation of the laser. The detection electronics are easily saturated by the RAM when the lock-in amplifier gain is increased to detect low-level concentration-dependent signals that are superimposed on the RAM.

The work presented in this thesis presents a fiber-optic RAM nulling technique to eliminate the  $1f$  RAM component and thereby alleviate the problem of detector saturation. The technique involves splitting the modulated output of a DFB laser and introducing a relative phase shift of  $\pi$  between the *intensity modulation* on the two components. This is achieved by passing one component through a delay fiber of appropriately chosen length. The other component is passed through a gas cell. The

intensities of the two anti-phase components are carefully balanced and then recombined so that the intensity modulation is cancelled in the absence of gas or in spectral regions where there is no absorption. The concentration-dependent gas signal therefore appears on a zero background and the gain of the detection system can then be increased to amplify and extract low level gas signals. The proposed technique is validated through calibration-free measurements carried out on various concentrations of methane using the two techniques mentioned earlier. The generic nature of the RAM nulling strategy is also demonstrated by extending the technique to eliminate the  $2f$  RAM component that is significant for some lasers. This is relevant to calibration-free  $2f$  WMS that has recently been demonstrated by other researchers.

The initial results obtained with the two  $1f$  calibration-free techniques with RAM nulling incorporated in them have been promising. It should be possible to optimize the system further to realize a sensitive, calibration-free, automated sensor system for quantitative measurement of gas parameters for industrial process control.

# Contents

<b>1. Introduction</b>	<b>15</b>
1.1. Applications of gas sensing	15
1.2. Conventional techniques of gas sensing	18
1.3. Optical techniques of gas sensing	19
1.3.1. Basics of gas sensing using Tunable Diode Laser Spectroscopy	20
1.3.2. Need for calibration in Tunable Diode Laser Spectroscopy	22
1.4. Conclusion	24
1.5. References	27
<b>2. Review of Tunable Diode Laser Spectroscopy</b>	<b>30</b>
2.1. Introduction	30
2.2. Classification of TDLS techniques	33
2.2.1. Direct detection	33
2.2.2. Modulation spectroscopy	36
2.3. Classification of Modulation spectroscopy	38
2.3.1. Frequency Modulation Spectroscopy (FMS)	38
2.3.2. Wavelength Modulation Spectroscopy (WMS)	40
2.4. Mathematical description of WMS	44
2.4.1. Calibration-free $1f$ WMS using the RAM method	47
2.4.2. Calibration-free $1f$ WMS using the Phasor Decomposition method	50
2.4.3. Correction factors for high modulation indices	53
2.5. Limitation of calibration-free $1f$ WMS techniques – Residual Amplitude Modulation	55
2.6. Thesis Objectives	58
2.7. Overview of thesis	59
2.8. References	61

<b>3. Analytical Methodologies – Fundamentals of Molecular Spectroscopy</b>	<b>69</b>
3.1. Introduction	69
3.2. Origin of spectral absorption lines	70
3.3. Vibrational Energy levels	72
3.3.1. Simple Harmonic Oscillation of a diatomic molecule	74
3.3.2. The Anharmonic Oscillator	76
3.4. Rotational Energy levels	78
3.5. Vibration-Rotation Spectra	79
3.6. Influence of rotation on the spectra of polyatomic molecules	81
3.6.1. Vibrations of polyatomic molecules	82
3.6.2. Influence of rotation on the spectrum	84
3.7. Width of Spectral Lines	87
3.7.1. Natural line width	87
3.7.2. Doppler broadening	89
3.7.3. Collision broadening	90
3.7.4. The Voigt profile	91
3.8. Intensity of Spectral Lines	91
3.8.1. Transition probability	91
3.8.2. Population of states	92
3.8.3. The Beer-Lambert law	92
3.9. Extracting Concentration and Pressure from Spectral Lines	93
3.9.1. Concentration and Derivative signals	93
3.9.2. Pressure and Derivative signals	96
3.10. Modelling spectral lines	99
3.11. Conclusion	101
3.12. References	103
<b>4. RAM nulling – Principles and Experimental Methods</b>	<b>104</b>
4.1. Introduction	104
4.2. Principles of operation of RAM nulling	107

4.3. Basic analytical treatment of RAM nulling	118
4.4. Description of experimental conditions and setup	121
4.4.1. Choice of absorption line	121
4.4.2. Signal source and Drive Electronics	123
4.4.3. Design of the gas cell	124
4.4.4. Wavelength-referencing of time-indexed signals	125
4.4.5. Setting up the lock-in amplifier for signal measurement	128
4.4.6. Setting the modulation index	129
4.5. Conclusion	130
4.6. References	132
<b>5. Calibration-free 1f WMS with RAM nulling – Validation of technique</b>	<b>135</b>
5.1. Introduction	135
5.2. Preliminary demonstration of RAM nulling	136
5.2.1. Elimination of the 1f background RAM	137
5.2.2. Normalization of signals	138
5.2.3. Practical method for signal normalization	140
5.3. Experimental results using the RAM technique with nulling	145
5.3.1. RAM method with background nulling for 10.13% CH <sub>4</sub>	145
5.3.2. Comparison with RAM method without nulling	148
5.3.3. RAM method with background nulling for 1.02% CH <sub>4</sub>	149
5.3.4. Comparison with RAM method without nulling	152
5.4. Experimental results using the Phasor Decomposition method with RAM nulling	153
5.4.1. Analytical description of PDM with RAM nulling	153
5.4.2. PDM with RAM nulling for 10.13% CH <sub>4</sub>	157
5.4.3. PDM with RAM nulling for 1.02% CH <sub>4</sub>	161
5.4.4. Discussion of results	164
5.5. Comparison of signals for low concentration with and without RAM nulling	164

5.6. Conclusion	167
5.7. References	169
<b>6. Mathematical model RAM nulling</b>	<b>170</b>
6.1. Introduction – unexpected nature of RAM nulled signals	170
6.2. Modelling of the RAM-nulled output	173
6.2.1. Configuration 1: DFB connected to IP <sub>2</sub> of coupler <sub>1</sub> ; output taken from OP <sub>1</sub> of coupler <sub>2</sub>	174
6.2.2. Configuration 2: DFB connected to IP <sub>2</sub> of coupler <sub>1</sub> ; output taken from OP <sub>2</sub> of coupler <sub>2</sub>	177
6.2.3. Configuration 1: DFB connected to IP <sub>1</sub> of coupler <sub>1</sub> ; output taken from OP <sub>1</sub> of coupler <sub>2</sub>	179
6.3. Simulation of RAM nulled output	180
6.4. Results of simulation and experiments	187
6.4.1. Comparison of simulation and experiments for the three configurations	187
6.4.2. Implications of mathematical model of RAM nulling for practical applications	190
6.5. FIR filtering to eliminate etalon fringes	192
6.6. Conclusion	199
6.7. References	201
<b>7. Extension of RAM nulling to 2f WMS</b>	<b>203</b>
7.1. Introduction	203
7.2. Origin of 2f Residual Amplitude Modulation	210
7.3. Elimination of the 2f background RAM	217
7.3.1. Experimental arrangement for 2f RAM nulling	217
7.3.2. Experimental demonstration of 2f RAM nulling	218
7.4. Application of Phasor Decomposition to 2f WMS with 2f RAM nulling	226
7.5. Calibration-free 2f WMS with 2f RAM nulling	230
7.6. Estimating linear and nonlinear IM	233

7.7. Conclusion	239
7.8. References	240
<b>8. Conclusion and Future Research</b>	<b>243</b>
8.1. Conclusions	243
8.2. Future Work	248
8.2.1. Variation of the RAM and 1 <sup>st</sup> derivative signals with modulation frequency	249
8.2.2. Scope for RAM nulling at high modulation frequencies	252
8.2.3. Implementation of RAM nulling at mid-infrared wavelengths	253
8.2.4. Correction factors for accurate recovery of line shapes for high modulation indices	254
8.2.5. WMS with the gas cell placed outside the RAM nulling setup	254
8.3. Conclusion	256
8.4. References	257
Appendix A : MATLAB program for PDM with RAM-nulling	260
Appendix B : MATLAB program for PDM with RAM-nulling	265

## RESEARCH PUBLICATIONS

### Journal papers

1. Keith Ruxton, Arup Lal Chakraborty, Walter Johnstone, Michael Lengden, George Stewart and Kevin Duffin, “Tunable diode laser spectroscopy with wavelength modulation – elimination of residual amplitude modulation in a phasor decomposition approach”, submitted to Sensors and Actuators B
2. Arup Lal Chakraborty, Keith Ruxton, and Walter Johnstone, “Recovery of the second harmonic signal in isolation from the effects of the linear and nonlinear intensity modulation for widely-tunable and quantitative wavelength modulation spectroscopy applications”, submitted.
3. Arup Lal Chakraborty, Keith Ruxton and Walter Johnstone, “Influence of the wavelength-dependence of fiber couplers on the background signal in wavelength modulation spectroscopy with RAM-nulling”, **Optics Express**, Vol. 18, Issue 1, pp. 267-280 (2010). doi:10.1364/OE.18.000267.
4. I. Armstrong, W. Johnstone, K. Duffin, M. Lengden, A. L. Chakraborty, K. Ruxton “Detection of CH<sub>4</sub> in the Mid-IR using Difference Frequency Generation with Tunable Diode Laser Spectroscopy”, **IEEE Journal of Lightwave Technology**, Vol. 28, Iss. 10, pp 1435-1442 (2010). doi:10.1109/JLT.2010.2042789.
5. Arup Lal Chakraborty, Keith Ruxton, Walter Johnstone, Michael Lengden and Kevin Duffin, “Elimination of residual amplitude modulation in tunable diode laser wavelength modulation spectroscopy using an optical fiber delay line”, **Optics Express**, Vol. 17, Issue 12, pp. 9602-9607 (2009). doi:10.1364/OE.17.009602.

## Conference papers

1. Keith Ruxton, Arup Lal Chakraborty, Andrew J. McGettrick, Kevin Duffin, Walter Johnstone and George Stewart, “Recent advance in tunable diode laser spectroscopy with background RAM Nulling for industrial applications”, 20<sup>th</sup> International Conference on **Optical Fibre Sensors (OFS-20)**, 5-9 October 2009, Edinburgh, UK Proc. SPIE, Vol. 7503, 750313 (2009); doi: 10.1117/12.833000.
2. Arup Lal Chakraborty, Keith Ruxton and Walter Johnstone, “Tunable diode laser spectroscopy with RAM nulling – current status and future possibilities”, International Conference on the **Field Laser Applications in Industry and Research (FLAIR)**, 6-11 September 2009, Grainau, Germany.
3. Keith Ruxton, Arup Lal Chakraborty, Andrew J. McGettrick, Kevin Duffin, Walter Johnstone and George Stewart, “Diode laser spectroscopy using a calibration-free phasor decomposition approach with RAM nulling”, 7<sup>th</sup> International Conference on **Tunable Diode Laser Spectroscopy (TDLS-2009)**, 13-17 July 2009, Zermatt, Switzerland.
4. I. Armstrong, A. Chakraborty, K. Ruxton, and W. Johnstone, “An investigation of TDLS modulation schemes as applied to the Mid-IR spectral region by difference frequency generation in PPLN”, 7<sup>th</sup> International Conference on **Tunable Diode Laser Spectroscopy (TDLS-2009)**, 13-17 July 2009, Zermatt, Switzerland.
5. Arup Lal Chakraborty, Keith Ruxton, Walter Johnstone, Michael Lengden and Kevin Duffin, “Elimination of residual amplitude modulation in TDLS-WMS”, **Conference on Lasers and Electro-Optics/ European Quantum Electronics Conference (CLEO Europe/EQEC-2009)**, Conference Digest (Optical Society of America), paper CH-P10, 14-19 June 2009, Munich, Germany

# *Chapter 1*

---

## *Introduction*

---

### **1.1 Applications of gas sensing**

Non-intrusive techniques of monitoring industrial processes have increasingly gained importance in the modern technology-driven world. Remote and automated quantitative measurements of various critical parameters are vitally important to maximize the efficiency of many physical and chemical processes. In some systems such measurements required to determine the concentration, composition, temperature and pressure, are based on the detection of specific gases that are present in the environment being monitored. These gases may either be produced directly by the process or they may already be part of the process environment. Detection and concentration

## Chapter 1: Introduction

measurements of trace amounts of a particular species are important if the chemistry of the process is expected to change and that species is an unambiguous signature of a particular chemical reaction within a larger and more complex process. In other situations, the physical conditions of a given process need to be ascertained and monitored to understand the process better and control it in some cases. Physical conditions of interest can include temperature, pressure and flow of a gas. In some situations a particular gas is known to exist within a process and the condition of the process is reflected indirectly but accurately by the effects it produces on the gas. In such situations information about the process can be extracted by making quantitative measurements on that particular gas. The physical and chemical condition of a process can therefore be studied and controlled by first detecting emitted gases and then making quantitative measurements on them. In some systems accurate measurements of these parameters facilitate control over the process and optimization of the efficiency.

Examples of a few diverse fields in which useful information may be gained from the detection of gases and measurement of gas parameters are as follows -

**a. Industry** – The gas and petrochemical industry is one of the largest sectors that needs robust and dependable gas measurement systems. Real-time monitoring of advanced propulsion and combustion processes [1-4] in internal combustion engines (ICEs) is a very important field of research for the automotive sector. The ability to accurately measure the temperature, pressure and flow of a gas is crucial to better understanding of many processes that lead to greater optimization. Solid oxide fuel cell (SOFC) technology is one such example. The importance of such diagnostics is obvious since the efficiency of such processes translates directly to superior quality of engines, higher economic gains, and more environment-friendly technology.

**b. Healthcare** – Clinical breath analysis has not received the level of attention that traditional pathological diagnostic techniques have. This picture is slowly but surely changing. All metabolic processes in a living body emit characteristic gases such as carbon dioxide, ammonia, hydrogen cyanide, nitrogen dioxide [5] and carbon monoxide [6]. The concentration of such gases varies with the conditions of specific organs.

## Chapter 1: Introduction

Abnormal physiological conditions can therefore be detected with highly sensitive and precise spectroscopic techniques long before full blown symptoms are detectable by conventional means. The focus in such applications is on high-sensitivity detection of trace amounts of gases. *In situ* evaluation of surgical cuts is also an active field of investigation.

**c. Homeland security** – The importance and relevance of civilian and military security concerns can not be stressed enough in today's scenario of unconventional and unscrupulous warfare. Detection of explosives [7], with extremely high-sensitivity is a particularly challenging field for remote, non-intrusive detection methods. Explosives such as TNT emit ammonia vapour that can be used as its signature. Clandestine nuclear enrichment programmes may be uncovered by detecting  $\text{UF}_6$ ,  $^{14}\text{C}$  and tritium that are signs of fissile nuclear materials.

**d. Environment monitoring** – The on-going debate on climate change and ways to mitigate its adverse effects makes it imperative to review and improve the understanding of various industrial processes that contribute to the build up of greenhouse gases. The focus is often on detecting those gases that are precursors to more hazardous chemicals. A common example is the detection of sulphur dioxide that is responsible for the formation of sulphuric acid. Monitoring of ozone [8], for instance, is important both because the gas plays a beneficial role in the upper atmosphere and also because its presence even in the low parts-per-billion (ppb) level in the lower atmosphere is harmful to animal and plant life because of its toxicity.

**e. Scientific research** – High-resolution spectroscopy is an invaluable tool in basic science. Fundamental understanding of the chemistry and biology of life is greatly enhanced by highly sophisticated techniques for studying trace amounts of gas molecules. Man's ambitious exploration of space for signs of extra-terrestrial life is critically dependent on the analysis of gases that form many of the planets of the solar system.

## 1.2 Conventional techniques for gas sensing

Traditional techniques for gas detection and measurement make use of chemical reactions and infrared light for the identification of gases. Such techniques include electrochemical gas sensors, gas chromatography (GC), pellistors and non-dispersive infrared (NDIR) sensors among others [9-11]. The major drawbacks of these techniques in general are slow speed of response, limited sensitivity and poor selectivity due to cross-sensitivity to different species. For electro-chemical sensors in particular, a major problem is their susceptibility to corrosion due to catalytic poisoning in harsh environments and therefore the need for periodic maintenance and ultimately replacement. Conventional methods such as gas chromatography are very slow to analyze a sample and are only suited to laboratory tests. Different detectors are often required for different species of target gases and of these some (flame ionization detector, FID) are destructive. This precludes their use in non-destructive evaluation/testing (NDE/NDT). The bulky size of some conventional instruments severely limits the range of applications in which they can be used directly. For instance it is impossible to use a GC in an aircraft engine for in-flight tests. Very limited quantitative measurements can be carried out with these systems. To improve sensitivity a GC is often used in conjunction with a mass spectrometer (MS), the combination being known as a GC-MS. However, this only makes the system more bulky, expensive and less suited to field measurements.

Another distinct and very important problem that deserves special mention is the need for calibration of these instruments that makes engineering such systems for real-world situations very difficult. It is acknowledged in all branches of engineering that any instrument that requires calibration is susceptible to errors due to calibration-drift that in turn requires periodic recalibration to be carried out. This will be explained in greater detail in Sec. 1.3.2.

Many modern process control applications require portable instrumentation for highly sensitive, calibration-free, real-time measurement with minimum requirement of maintenance. Conventional methods of detecting gases clearly do not meet the demands

## **Chapter 1: Introduction**

of such applications and therefore alternative technology must be explored. The work reported in this thesis represents advancements in the field of an alternative optical diagnostic technique, namely Tunable Diode Laser Spectroscopy (TDLS), that is capable of meeting the demands of modern gas sensing applications.

### **1.3 Optical techniques for gas sensing**

Optical diagnostic techniques have been widely used for gas detection and monitoring applications primarily because these are non-destructive and non-intrusive: the essential requirement is that there has to be interaction between a light beam and a target gas over a given path length. Other important factors that make optical gas sensing attractive are the sensitivity to a wide range of gas species, inherently safe operation, extremely high sensitivity, low start-up and running cost, and the ease with which compact systems can be built. The principle involves directing a beam of light at the target volume and using a photo-detector to measure the transmitted intensity of the light as a function of the emitted wavelength. This is essentially a spectroscopic measurement of the molecular absorption lines of gases that are either already present or are produced by the process itself. Many gases are able to absorb certain characteristic wavelengths of light depending on their molecular configuration. This makes it possible to uniquely identify those gases by interrogating them with the wavelength of light that they are known to absorb. Different gases often have non-overlapping absorption lines. By judicious choice of interrogating wavelengths, it is possible to simultaneously detect and make measurements on multiple gas species. While the spectral absorption is used to distinguish different gases, their relative concentrations are determined by monitoring the amount of light energy absorbed at each wavelength. Strong absorption of a particular wavelength therefore indicates the presence of a significant amount of a particular gas. It is therefore possible to identify and quantify several gases using this method of multiplexing several distinct wavelengths and measuring the absorption for each wavelength.

## **Chapter 1: Introduction**

Although any broadband light source in conjunction with wavelength discriminating device such as diffraction grating can, in principle, be used for this purpose, lasers are most widely used. This is primarily because lasers have very narrow line widths in comparison to the width of a typical absorption line, high spectral brightness, high directionality, high power and wide wavelength tuning range. These properties enable the detection of multiple molecular species with high resolution, high species selectivity and high detection sensitivity over long detection path lengths. This technique has been known by the generic name Laser Absorption Spectroscopy (LAS). For compact, field-deployable industrial systems semiconductor diode lasers are widely used and this specific technology that has come to be known as Tunable Diode Laser Spectroscopy (TDLS) [12-16], and has gained significant popularity in several areas. All of the applications briefly discussed earlier are served very reliably by TDLS in one form or another.

### ***1.3.1 Basics of Gas sensing using Tunable Diode Laser Spectroscopy***

The basic mechanism of a TDLS system is to tune the emission wavelength of a diode laser across a molecular absorption line of a target gas and measure the absorption of the light as a function of the wavelength. The technique is based on the measurement of the incident and the transmitted light intensities and calculating the relative reduction in intensity. This basic method is known as direct detection. Highly sensitive, spectrally-resolved measurements performed with this method are very useful in not only uniquely identifying several gases [4-6] but also in making quantitative measurements to extract concentration, pressure and temperature of the gas [3, 17-20]. This is achieved by recovering the gas absorption line from the spectrally-resolved measurement of the transmitted light. The gas absorption line shape and line strength are strongly dependent on the parameters mentioned above, which allows these parameters to be extracted by applying multi-component least squares fits to the absorption line that has been recovered with high accuracy.

## Chapter 1: Introduction

TDLS is often used with an additional modulation impressed on its injection current. When the laser's injection current is modulated there is a wavelength modulation (WM) as well as a synchronous intensity modulation (IM) of the laser output. This innovation, known as modulation spectroscopy [1-4, 17, 18] leads to much higher sensitivity than direct detection. For most gas sensing applications the frequency of modulation is on the order of a few tens to a few hundreds of kHz. This regime which is the focus of attention in this thesis is known as Wavelength Modulation Spectroscopy (WMS). While the applied modulation is most often a single-frequency sinusoid the detection is performed at various harmonics of that frequency. It turns out, that the  $n^{\text{th}}$  harmonic signal component bears the characteristic signature of the  $n^{\text{th}}$  derivative of the absorption line shape, although the relationship is not simply the respective derivatives. The WMS literature is replete with reports of gas detection using 1<sup>st</sup> harmonic ( $1f$ ) and 2<sup>nd</sup> harmonic ( $2f$ ) detection. Higher harmonics are rarely used.

To be specific, in  $1f$  detection the recovered signal resembles the 1<sup>st</sup> derivative of the absorption line shape. The concentration of the target gas is proportional to the signal amplitude and the slope of the curve through line centre. For  $2f$  detection the recovered signal resembles the 2<sup>nd</sup> derivative of the absorption line. The only parameter relevant for the extraction of concentration in this case is the peak height of the signal at line centre. Pressure measurements are related to the separation of the maximum and the minimum of a 1<sup>st</sup> derivative signal in  $1f$  WMS, while in  $2f$  WMS the pressure is related to the two zero crossings of the signal. This is illustrated in Fig. 1.1 in which representative traces for a sample of gas of constant concentration at two pressure values are depicted. In Fig. 1.1a the relative transmission corresponding to a representative absorption line is shown for two pressure values. The corresponding 1<sup>st</sup> derivative and 2<sup>nd</sup> derivative signals are shown in the two lower plots. It is seen that at the line centre where there is maximum absorption, the corresponding value of the relative transmission is minimum, the 1<sup>st</sup> derivative is zero and the 2<sup>nd</sup> derivative signal attains the maximum value. These are characteristic features of such signals.

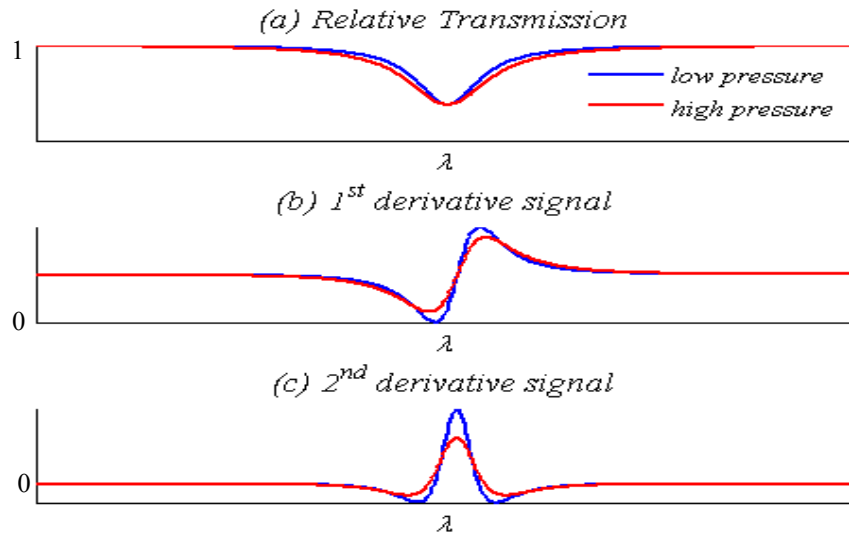


*Fig. 1.1: A gas absorption line and the typical 1f and 2f signals obtained in WMS for two representative values of pressure*

It is seen that for constant concentration the effect of increasing the pressure is to cause a broadening of the absorption line shape. The corresponding 1<sup>st</sup> derivative and 2<sup>nd</sup> derivative signals reduce in height and the zero crossings are moved further away from the line centre. It is also noted that the 1<sup>st</sup> derivative signal has an appreciable non-zero offset but the 2<sup>nd</sup> derivative signal appears on a zero level. These are characteristic of the respective signals and depend on the level of modulation and the type of laser used. The effect of the non-zero background signal is part of the central theme of this thesis and this issue will be discussed in greater detail in chapter 2.

### ***1.3.2 Need for Calibration in Tunable Diode Laser Spectroscopy***

It is important to bear in mind that TDLS is often used in harsh environments. Although the technique is extremely versatile, a particular issue of concern for process control applications is the need for signal calibration. This is to say that the 1<sup>st</sup> and 2<sup>nd</sup> derivative signals are not directly and simply related to the absorption line shape. Therefore the 1f and 2f detection the experimental signal measured for an unknown quantity of gas must be calibrated against the signal from a control sample of the same

## Chapter 1: Introduction

gas maintained under accurately known conditions. In industrial applications the pressure of the gas often varies significantly and may be unknown. This in turn means that the absorption line width is also variable. In TDLS-WMS applications the magnitude of the recovered signal is strongly dependent on the line width as explained in chapter 3. The amplitude of the 1<sup>st</sup> derivative signal in  $1f$  WMS varies as  $1/\gamma^2$  where  $\gamma$  is the half-width-half-maximum value of the line width. The amplitude of the 2<sup>nd</sup> derivative signal in  $2f$  WMS varies as  $1/\gamma^3$ . It is therefore clear that environmental conditions strongly affect the recovered signal.

In TDLS-WMS an important systematic factor in determining the form and amplitude of the recovered signals is the so-called modulation index,  $m$ . The  $m$ -value is defined as the ratio of the amplitude of the WM ( $\delta\nu$ ) to  $\gamma$ , mathematically expressed as  $m = \delta\nu/\gamma$ . The  $m$ -value features prominently as a system scaling factor in the expressions for the harmonic/derivative signals as shown later in chapter 3. Therefore even if the WM amplitude of the laser is held constant by constant amplitude of the modulation current the  $m$ -value can vary as a result of the variation of the line width caused by pressure variations.

In addition to the variation of the pressure that must also be measured there are other spurious systematic effects that vary unpredictably with time. These include the possible variation in laser power and other laser parameters, the variable optical throughput of the system due to poor and variable coupling possibly due to mechanical vibrations, and the contamination of windows and optical surfaces by the environment. The cumulative effect of these factors is that the recovered electrical signal level is liable to vary significantly due to reasons other than the variation of the properties of the gas. Therefore the measurement needs to be calibrated against a signal from a control sample of gas maintained under accurately-known conditions of temperature and pressure. Although this may be acceptable in laboratory environments, it is clearly an impractical and undesirable requirement in the field.

## Chapter 1: Introduction

These were the problem that the gas sensing community had learnt to live with until it was very recently demonstrated [17-20], that calibration-free recovery of absolute gas absorption line shapes is possible with  $1f$  detection. This opens up new possibilities in industrial process control because the direct recovery of absorption lines simplifies data processing significantly. However, the problem of a high gas concentration-independent background signal in the recovery of the  $1f$  signal persists. The background signal is an artefact of the modulation of the laser and arises specifically due to the IM of the laser. The high background signal tends to severely limit detection sensitivity particularly in  $1f$  WMS. Therefore in order to make  $1f$  calibration-free WMS competitive with other traditional WMS methods it is imperative to devise a method to eliminate the background signal.

The need to remove the background signal in  $1f$  calibration-free WMS is the main motivation of carrying out this research. The brief discussion presented here serves to provide a backdrop against which the theoretical and experimental work contained in this thesis has been carried out.

## 1.4 Conclusion

This chapter aims to gently introduce the field of non-intrusive and non-destructive gas sensing with glimpses of the wide spectrum of applications that are important in the modern world. In many of the applications it is not enough to merely detect trace amounts of gases. It is necessary to be able to make quantitative measurements on them in order to extract useful information about the environment that produces the gases. Conventional gas sensing techniques are briefly discussed and their shortcomings are pointed out. It is clear from the sheer diversity of applications that conventional sensing techniques are not adequate. In this context the advent of tunable diode laser spectroscopy (TDLS) is a major technological development. A very basic qualitative discussion of the technique has been presented with more details to be introduced in chapter 2. The practical issue of calibration of recovered signals in industrial

## Chapter 1: Introduction

applications has also been highlighted since the work presented in this thesis is oriented towards industrial applications.

The separate but equally important problem of a high background signal in WMS that contains no information about the gas itself has also been touched upon. It has been briefly explained that this background signal arises due to the IM of the laser that accompanies the WM. The background signal is the main factor that limits the sensitivity of WMS particularly if signal recovery is performed at the modulation frequency (that is 1<sup>st</sup> harmonic or  $1f$  detection is performed). The main motivation of this thesis is the development of a technique to remove this background signal and thereby make 1<sup>st</sup> harmonic WMS a viable technique in quantitative gas measurement.

Chapter 2 provides a detailed review of the TDLS technology. Current technological trends are briefly outlined, including the growing interest in newer varieties of laser sources and novel fiber optic technology as substitutes for conventional measurement systems. Next, the two categories of signal recovery, namely Direct detection and Modulation spectroscopy are discussed along with their relative merits and demerits. The two operational regimes of Modulation spectroscopy, namely frequency modulation spectroscopy (FMS) and wavelength modulation spectroscopy (WMS) are discussed next, with greater focus on WMS. A mathematical description of WMS introduces the various terminologies to the reader and also illustrates the various signal components that are encountered later.

The two calibration-free 1<sup>st</sup> harmonic WMS signal recovery techniques are reviewed next. This is necessary because this forms the starting point of the thesis. Much of the subsequent work involves applying these two techniques in conjunction with the main technique to eliminate the high background signal that is the subject of this thesis. Finally, the presence of a high background signal that limits the sensitivity of these techniques is explained in greater detail both qualitatively as well as mathematically. At this point the stage is set for the introduction and detailed discussion of the actual technique that has been termed RAM nulling.

## **Chapter 1: Introduction**

Detailed objectives of the thesis are presented at the end of chapter 2 only after a comprehensive review of TDLS is carried out that brings the reader up to date with the terminology, nature of signals and the latest developments as far as  $1f$  and  $2f$  calibration-free signal recovery algorithms are concerned. Since this thesis deals with the removal of a very specific problem that has long plagued TDLS-WMS, it is necessary to first lay out this background so that the context in which this work is carried out becomes easier to appreciate.

## 1.5 References

1. T. Fernholz, H. Teichert, V. Ebert, "Digital phase-sensitive detection for in situ diode laser spectroscopy under rapidly changing transmission conditions", *Appl. Phys. B* **75**, 229-236 (2002).
2. I. Linnerud, P. Kaspersen, T. Jaeger, "Gas monitoring in the process industry using diode laser spectroscopy," *Appl. Phys. B* **67**, 297-305 (1998).
3. T. Aizawa, T. Kamimoto, T. Tamaru, "Measurements of OH radical concentration in combustion environments by wavelength-modulation spectroscopy with a 1.55 $\mu$ m distributed-feedback diode laser," *Appl. Opt.* **38** (9), 1733-1741 (1999).
4. M. E. Webber, R. Claps, F. V. Englich, F. K. Tittel, J. B. Jeffries, R. K. Hanson, "Measurements of NH<sub>3</sub> and CO<sub>2</sub> with distributed-feedback diode lasers near 2.0  $\mu$ m in bioreactor vent gases," *Appl. Opt.* **40** (24), 4395-4403 (2001).
5. L. Menzel, A. A. Kosterev, R. F. Curl, F. K. Tittel, C. Gmachl, F. Capasso, D. L. Sivco, J. N. Baillargeon, A. L. Hutchinson, A. Y. Cho, W. Urban, "Spectroscopic detection of biological NO with a quantum cascade laser," *Appl. Phys. B* **72**, 859-863 (2001).
6. Y. Morimoto, W. Durante, D. G. Lancaster, J. Klattenhoff, F. K. Tittel, "Real-time measurements of endogenous CO production from vascular cells using an ultra-sensitive laser sensor," *Am. J. Physiol. Heart. Circ. Physiol.* **280**: H483-H488 (2001).
7. H. Liu, Y. Chen, G. J. Bastiaans, X. -C. Zhang, "Detection and identification of explosive RDX by THz diffuse reflection spectroscopy," *Opt. Exp.* **14** (1), 415-423 (2006).
8. D. Bortoli, A. M. Silva, M. J. Costa, A. F. Domingues, G. Giovanelli, "Monitoring of atmospheric ozone and nitrogen dioxide over the south of Portugal by ground-based and satellite observations," *Opt. Express* **17**, 12944-12959 (2009)

## Chapter 1: Introduction

9. S. P. Griff, "Structure determination of carbonates and diglycol carbonates by gas chromatography-mass spectrometry," *Appl. Spectrosc.* **37** (4), 354-357 (1983).
10. S. L. Smith, S. E. Garlock, G. E. Adams, "Industrial applications of a capillary gas chromatography/Fourier transform infrared system," *Appl. Spectrosc.* **37** (2), 192-196 (1983).
11. P. R. Griffiths, D. A. Heaps, P. R. Brejna, "The gas chromatography/infrared interface – past, present and future," *Appl. Spectrosc.* **62**(10), 259A-270A (2008).
12. E. D. Hinkley, "High resolution infrared spectroscopy with a tunable diode laser," *Appl. Phys. Lett.* **16** (9), 351-354 (1970).
13. E. D. Hinkley, P. J. Kelly, "Detection of air pollutants with tunable diode lasers," *Science* **171** (3972), 635-639 (1971).
14. J. Reid, J. Shewchun, B. K. Garside, E. A. Ballik, "High sensitivity pollution detection employing tunable diode lasers," *Appl. Opt.* **17**(2), 300-307 (1978).
15. J. Reid, B. K. Garside, J. Shewchun, M. El-Sherbiny, E. A. Ballik, "High sensitivity point monitoring of atmospheric gases employing tunable diode lasers," *Appl. Opt.* **17** (11), 1806-1810 (1978).
16. J. Reid, M. El-Sherbiny, B. K. Garside, E. A. Ballik, "Sensitivity limits of a tunable diode laser spectrometer, with application to the detection of NO<sub>2</sub> at the 100-ppt level," *Appl. Opt.* **19** (19), 3349-3354 (1980).
17. K. Duffin, A. J. McGettrick, W. Johnstone, G. Stewart, D. G. Moodie, "Tunable diode laser spectroscopy with wavelength modulation: a calibration-free approach to the recovery of absolute gas absorption line shapes," *J. Lightwave Technol.* **25**, 3114-3125 (2007).
18. A. J. McGettrick, K. Duffin, W. Johnstone, G. Stewart, D. G. Moodie, "Tunable diode laser spectroscopy with wavelength modulation: a phasor decomposition method for calibration-free measurements of gas concentration and pressure," *J. Lightwave Technol.* **26**, 432-440 (2008).

## Chapter 1: Introduction

19. W. Johnstone, A. J. McGettrick, K. Duffin, A. Cheung, G. Stewart, "Tunable diode laser spectroscopy for industrial process applications: system characterization in conventional and new approaches," *IEEE Sensors J.* **8** (7), 1079-1088 (2008).
20. A. J. McGettrick, W. Johnstone, R. Cunningham, J. D. Black, "Tunable diode laser spectroscopy with wavelength modulation: calibration-free measurements of gas compositions at elevated temperatures and varying pressure," *IEEE J. Lightwav. Technol.*, **27** (15), 3150-3161 (2009).

# *Chapter 2*

---

## *Review of Tunable Diode Laser Spectroscopy*

---

### **2.1 Introduction**

This chapter presents a more detailed discussion of tunable diode laser spectroscopy (TDLS) but is by no means exhaustive. The development of this field is discussed in a chronological way to some extent although it was understandably not possible to include every development. As a result of this approach the discussion moves back and forth between near-infrared and mid-infrared TDLS.

TDLS is a well-established technique for trace gas detection [1-6], and quantitative analysis of various gas parameters that are of significant importance in industrial, chemical, medical, security and environmental applications. Since the late 1960s this

## Chapter 2: Review of Tunable Diode Laser Spectroscopy

field has enjoyed the continued attention of the scientific world and many highly significant advances have been witnessed. The key technological advances have been the development of new, rugged, high-power light sources in a wide range of wavelengths and highly sensitive optical detectors. These basic ingredients have been ably supported by the astonishing increase in the speed and precision of electronics that form the backbone of data acquisition and signal processing hardware. The rapid rise of optical fiber technology produced unprecedented levels of miniaturization, stability and ruggedness, leading to the realization of low-cost, compact and portable instruments. A fourth factor that has contributed immensely to the development of this technology and its subsequent application to diverse areas is the improved theoretical understanding of the underlying principles. Recently, it has been possible to push this technology to its limit because these physical principles have been better understood and, crucially, more accurately and completely described mathematically.

Sensitive detection of various gases [3, 5, 8-11], and accurate measurement of various parameters of a target gas such as pressure, concentration and temperature [10, 12-22] is widely performed using TDLS with high sensitivity and accuracy. The basic technique involves tuning the centre wavelength of a diode laser source with high spectral brightness across one or several strong vibration-rotational absorption lines of a gas while monitoring the wavelength-dependent relative transmission of the system. The vibration-rotational absorption lines of various gases are well documented in spectroscopic databases such as HITRAN [23]. For molecules with discrete absorption features it is often possible to recover a single, well-isolated and sufficiently strong absorption line in order to extract relevant gas parameters. Early systems were based on mid infrared lead salt diode lasers that required liquid helium or liquid nitrogen cooling of the laser head [1]. Although the mid-infrared region allows the strong fundamental gas absorption lines to be probed, the need for liquid nitrogen cooling was a considerable hurdle that prevented TDLS from gaining the kind of widespread popularity in field applications that it enjoys today. However the advent of the telecommunications age brought about a sea-change in this field. The development of spectrally bright, high-power, frequency-agile, low-cost near-infrared distributed

## Chapter 2: Review of Tunable Diode Laser Spectroscopy

feedback (DFB) laser diodes with Peltier cooling has led to the development of robust field-deployable systems [10]. This provided the much-needed impetus for TDLS to step out of the laboratory environment and in to the real world. The availability of high-sensitivity near-infrared (NIR) photo-detectors that operate at room temperatures and various fiber-optic components have also greatly facilitated this rapid growth. The developments in the optical communications industry has made it possible to miniaturize previously bulky equipment, and realize remote and distributed sensing using optical fibers.

Single and multiple gas species detection has been traditionally performed in the mid-infrared (MIR) using widely tunable parametric difference frequency generation (DFG) systems [24-26]. However the bulky nature of such systems and the total cost involved are prohibitive in many cases. The invention of quantum cascade lasers (QCLs) [27] and the demonstration of room temperature, high power and narrow line width operation [28], was a major development that fuelled rapid growth of mid-infrared spectroscopic applications [29-32]. The introduction of near-IR vertical cavity surface emitting lasers (VCSELs) [33] was the next major development that took place. The low drive currents (few mA) and therefore the reduced power consumption of VCSELs are attractive features for battery-powered hand-held instruments. Operation of such lasers well above room temperature [34, 35], and at high powers [36], has been demonstrated which is important for industrial applications under harsh conditions. In addition widely-tunable spectroscopic detection of multiple gas lines has been demonstrated using such lasers [37-39].

The use of hollow core optical fibers [40], for gas sensing is another interesting development that can potentially lead to even greater levels of system integration. The long effective path lengths offered by such fibers [41, 42], and the high degree of overlap between the gas and the laser beam makes it an attractive alternative to conventional gas cells. In such systems the light source and detector can be directly coupled to the hollow core fiber, and the gas to be detected permeates to the core. Solid-core fibers have also been used for evanescent wave detection of chemicals [43]. Mid-

## **Chapter 2: Review of Tunable Diode Laser Spectroscopy**

infrared optical fiber technology is yet to attain the level of maturity that its near infrared counterpart has enjoyed for a long time now. Although mid-infrared fibers exist, they are expensive and have too much loss (0.1dB/m at best) [44, 45], to prove useful in practical systems. One hopes that this technology improves as the material science issues are better understood and associated problems are solved.

The present scenario suggests that TDLS is a very active and fast-evolving field of research. It will continue to see major technical innovations as better light sources and detectors become available, and as other contributing technologies mature.

## **2.2 Classification of TDLS techniques**

The TDLS detection technique is classified into two regimes, namely, Direct detection and Modulation spectroscopy, according to the signal modulation and detection method used.

### ***2.2.1 Direct detection***

The technique essentially involves tuning the wavelength of a spectrally narrow probe laser across a strong, well-isolated absorption feature of a target gas and monitoring the transmitted intensity as a function of the wavelength. In accordance with the Beer-Lambert law the relative transmission is a function of the product of the absorbance of the gas and the path length over which the laser light interacts with the gas sample.

A distributed feedback (DFB) diode laser's centre wavelength can be tuned very conveniently and precisely by varying the injection current or the temperature. Temperature tuning allows a wider spectral region to be scanned and is often preferred for widely tunable direct detection of multiple species. Current tuning covers a much smaller range. Although both approaches are used, current tuning is by far the more popular method. The DFB is initially temperature-tuned close to a target vibration-rotational line and a slow (few Hz) ramp is applied to the injection current to repetitively scan the DFB laser's wavelength across the absorption line. The transmitted intensity with the target gas present is normalized by the "no gas" signal in controlled laboratory

## Chapter 2: Review of Tunable Diode Laser Spectroscopy

conditions but in a practical system a baseline fit to the intensity trend must be used. The total spectral absorbance is obtained by using the Beer-Lambert law given by,

$$I_t(\lambda) = I_0(\lambda)e^{-A(\lambda)l} = I_0(\lambda)e^{-\alpha(\lambda)Cl} \quad (2.1)$$

where,

$I_t(\lambda)$  is the intensity of the transmitted radiation,

$I_0(\lambda)$  is the intensity of incident radiation,

$A(\lambda) = \alpha(\lambda)C = S(T)\phi(\lambda - \lambda_0)$ , is the absorbance of the medium,

$\alpha(\lambda)$  is the absorption cross-section,

$C$  is the concentration (number density) of the absorbing species,

$S(T)$  is the line strength of the molecule at a temperature  $T$ ,

$\phi(\lambda - \lambda_0)$  is the line shape function for the particular absorption line, and

$\lambda_0$  is the centre frequency of the transition

The dependence of the spectral absorbance  $A(\lambda)$  on the gas concentration ( $C$ ), temperature ( $T$ ) through the line strength  $S(T)$ , and pressure ( $P$ ) through  $\phi(\lambda - \lambda_0)$  makes it possible to extract information regarding these quantities from absorption profiles accurately recovered by low noise direct detection.

A typical experimental arrangement used in direct detection is shown in Fig. 2.1 below.

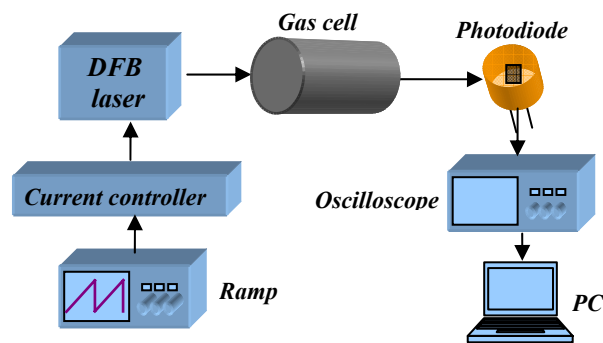


*Fig. 2.1: Typical experimental arrangement for TDLS with Direct detection*

## Chapter 2: Review of Tunable Diode Laser Spectroscopy

A semi-conductor DFB laser is tuned across a gas absorption line by applying a ramp (saw tooth) voltage to the current controller. The transmitted intensity at the output of the gas cell is detected by a photodiode and displayed on an oscilloscope and the digitized data is transferred to a computer for further processing. Figure 2.2 shows a representative photodiode output signal (solid) and a baseline fit (dotted) on the left, and the corresponding normalized relative transmission on the right. The concentration of the gas is proportional to the depth of the relative transmission profile while the pressure is proportional to the full-width-at-half-maximum (FWHM).

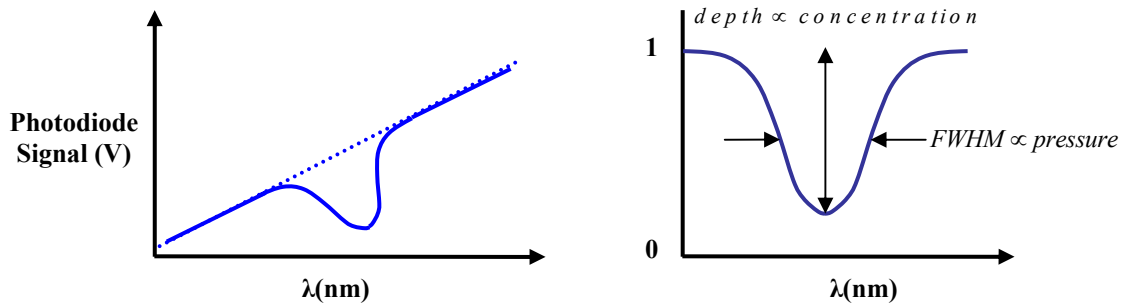


*Fig. 2.2: Raw photodiode signal and relative spectral transmission profile obtained by normalizing the raw signal by a baseline fit*

The relative transmission profile is compared with a theoretical model simulated by considering a Lorentzian, Gaussian or Voigt line shape  $\phi(\lambda - \lambda_0)$ , depending on the range of operating pressures, and line strengths  $S(T)$ , taken from standard data bases such as HITRAN. The attractive feature of this method is the simplicity of implementation and signal interpretation since the absolute absorption profile is directly recovered by simply normalizing the recovered absorption profile by a baseline fit to the non-absorbing spectral wings. However, the disadvantage of this method is the poor signal-to-noise ratio (SNR), because for low gas concentration it is difficult to detect and quantize small changes in transmitted intensity that are superimposed on a high background signal. The low frequency laser noise, the  $1/f$  noise, the detector noise and digitization noise therefore often limit its use in near infrared detection of gases of low concentration. This is not to say that direct detection is an obsolete technology. On the

## Chapter 2: Review of Tunable Diode Laser Spectroscopy

contrary, it is widely used in many mid-infrared systems based on difference frequency generation (DFG) systems [46], and mid-infrared QCLs [47] essentially because of the straightforward way in which information can be extracted from the recovered signal. Very high sensitivity is achievable even with direct detection in the mid-infrared because the fundamental absorption lines of gases are significantly stronger than the near-infrared overtones. It is often the first method to be tried in near infrared systems for industrial process control where the concentration levels are reasonably high owing to the ease of signal interpretation [48]. However, for a large number of high-sensitivity near infrared applications, variants of this basic approach have been implemented that involve modulation of the laser source. Such modulation spectroscopy is now a standard detection technique for near infrared spectroscopic measurement. The direct detection method will therefore not be discussed further.

### ***2.2.2 Modulation spectroscopy***

The main limitation of direct detection arises from the need to detect a very small change in transmitted intensity that is superimposed on the large background signal due to the laser intensity itself. The signal-to-noise ratio (SNR) is further degraded by the presence of low frequency noise that includes  $1/f$  noise and the laser noise. To increase the detection sensitivity, various modulation formats have been used, of which a particular variant termed wavelength modulation spectroscopy (WMS) [2, 4-8], has been very popular because it is relatively straightforward to implement and affords greater sensitivity than direct detection. Modulation spectroscopy has become the method of choice for such experiments.

In a generic modulation spectroscopy experiment, the centre emission wavelength of a tunable laser source is slowly scanned across an absorption line as in direct detection, and simultaneously the instantaneous laser wavelength is modulated by a high frequency modulation signal. The interaction of this wavelength modulated laser output with the target gas produces signals at various harmonics of the modulating signal. The amplitude of each of the harmonic signals is uniquely related to the absorption line shape. For low

## Chapter 2: Review of Tunable Diode Laser Spectroscopy

amplitudes of the modulation signal, the amplitude envelope of the  $n^{\text{th}}$  harmonic signal resembles the  $n^{\text{th}}$  derivative of the absorption line shape. Typically, phase sensitive, harmonic detection is used to recover the amplitude envelope of a particular harmonic and the absorption-dependent amplitude of that envelope is measured to infer gas parameters. This method is inherently narrow-band as far as signal recovery is concerned and therefore has superior SNR than direct detection.

A very convenient way to achieve the double modulation of the laser output is to use a semiconductor diode laser and modulate its injection current by two modulation signals of appropriate frequencies. A low frequency saw tooth (or triangular) voltage ramp is used to slowly tune the laser's centre frequency across an absorption line and a high-frequency sinusoidal voltage is used to modulate the instantaneous wavelength. The injection current modulation capability of such lasers is a very useful feature for compact, low-power and portable instruments. These features make current modulation an attractive alternative to external phase modulation although it is important to note that current modulation does give rise to significant levels of intensity modulation (IM) of the laser that is synchronous with the wavelength modulation (WM). This issue is particularly relevant to the work presented in this thesis and will be discussed in greater detail shortly.

The general theory of modulation spectroscopy developed much earlier in the 1960s paved the way for subsequent advances made in this field. One of the earliest investigations of the broadening of Lorentzian lines under modulation was carried out by Hugo Wahlquist [49], and within a span of a few years phase sensitive detection of such signals was also investigated by Russell and Torchia [50]. Modulation broadening of nuclear magnetic resonance (NMR) and electron spin resonance (ESR) line shapes were analysed by Wilson [51], for Gaussian and Lorentzian line shapes. Using a Fourier analysis, the signal amplitude and line shapes were calculated for the first three harmonics of the absorption line as a function of the modulation amplitude. Shortly after this Arndt developed analytical expressions for modulation-broadened Lorentzian line shapes [52]. The expressions for the first two harmonic signals proved to be very useful

## Chapter 2: Review of Tunable Diode Laser Spectroscopy

for subsequent researchers. Experimental validation [6], of these theoretical developments that were relevant to TDLS followed much later however.

Modulation spectroscopy is further classified into two regimes depending on the choice of the modulation frequency,  $f_m$ , and modulation amplitude. The two classes are Frequency Modulation Spectroscopy (FMS) and Wavelength Modulation Spectroscopy (WMS). The two methods are different manifestations of the same underlying concept and are briefly described in the following sections.

### 2.3 Classification of Modulation spectroscopy

Modulation spectroscopy is broadly classified as frequency modulation spectroscopy (FMS) and wavelength modulation spectroscopy (WMS). The underlying principle of both techniques is essentially the same. They differ mainly in their operating regimes, mathematical formalism and applications. The two techniques are discussed next with the major emphasis being placed on WMS since this is the technique that is used in the rest of the thesis.

#### 2.3.1 Frequency Modulation spectroscopy (FMS)

FMS was pioneered by Bjorklund [53], in 1980 with external phase modulation of a single axial mode dye laser to probe the absorption lines of iodine and sodium vapour. In this technique, the modulation frequency  $f_m$  is comparable to the full-width-half-maximum (FWHM) of the absorption line being probed and is typically on the order of a few GHz. For a given laser modulated at a frequency  $f_m$ , a current modulation of amplitude  $\Delta i$  produces a frequency deviation about the instantaneous centre frequency. The amplitude of the frequency modulation,  $\Delta\nu$ , is determined by the frequency tuning parameter,  $\delta\nu/\delta i$ , for that laser and  $f_m$ . The frequency modulation (FM) index is given as  $\beta = \Delta\nu/f_m$ . In general, the laser's FM spectrum under modulation consists of the carrier field and a set of equally spaced sidebands with the spacing being equal to  $f_m$ . The number of sidebands is determined by the FM index. The electric field amplitudes

## Chapter 2: Review of Tunable Diode Laser Spectroscopy

of the sidebands are given by the values of Bessel functions and therefore rapidly reduce in amplitude as  $\beta$ , and therefore the number of sidebands, increases. Physically this is equivalent to a redistribution of the total energy of the unmodulated light across the entire sideband structure. For typical FMS applications, however,  $f_m$  is on the order of a few GHz and  $\beta$ , is typically much less than unity. Mathematically the spectrum can then be said to consist of only the dominant carrier field with a pair of equally spaced and anti-symmetric sidebands. The target sample is probed with this pure FM spectrum and, from the differential response of the sample to the two sidebands the absorption and dispersion of the sample can be measured. FMS is a very sensitive and versatile technique and is widely used. However, the need for fast modulators and detectors leads to higher equipment costs.

Subsequent to Bjorklund's seminal paper on cw FMS, a pulsed version of the method for fast absorption measurements was reported [54]. These experiments used externally-modulated lasers that produced pure FM. Soon after these initial studies Lenth implemented the same technique using an injection-current modulated semiconductor diode laser [55, 56]. Sensitive detection of NO<sub>2</sub> was also demonstrated [8], with such a modulated laser. The FM and the IM that occur simultaneously were considered along with the phase difference,  $\psi$  [57, 58], that is characteristic of such lasers. The treatment took the view that modulation of the injection current directly modulated the electric field amplitude of the laser output. It has been suggested later by Zhu and Cassidy [59], that a more accurate point of view would be to consider the output intensity rather than the electric field to be directly modulated by the modulation of the injection current. Although these points of view are equivalent, it turns out that the different mathematical formalism predicts different results for harmonic signal components when there is no absorbing medium. The verification of this prediction [59] makes the latter description more accurate. The FMS technique will not be discussed further since the work presented in this thesis is in the regime of WMS.

### 2.3.2 Wavelength Modulation spectroscopy (WMS)

The WMS technique was developed and refined in parallel with the developments in FMS. The basic mechanism in WMS is the same, but owing to the very different modulation conditions, the final situation is very different and a different mathematical description needs to be adopted. Here  $f_m$  is much smaller than the FWHM of the absorption line being probed, and is typically on the order of a few tens to a few hundreds of kilohertz. Since the corresponding FM index,  $\beta$ , is extremely large in this case, the field spectrum consists of a very large number of densely spaced sidebands equally spaced in frequency around the carrier. An electric field description in this case is impractical since the response of an extremely large number of sidebands must be added. For WMS therefore, an intensity based description is used, in which the modulation of the net intensity is considered instead of the intensity resulting from each of the modulated sidebands. Information about absorption by a sample can be extracted but information related to dispersion is lost.

Figure 2.3 shows the basic setup used in a generic WMS experiment.

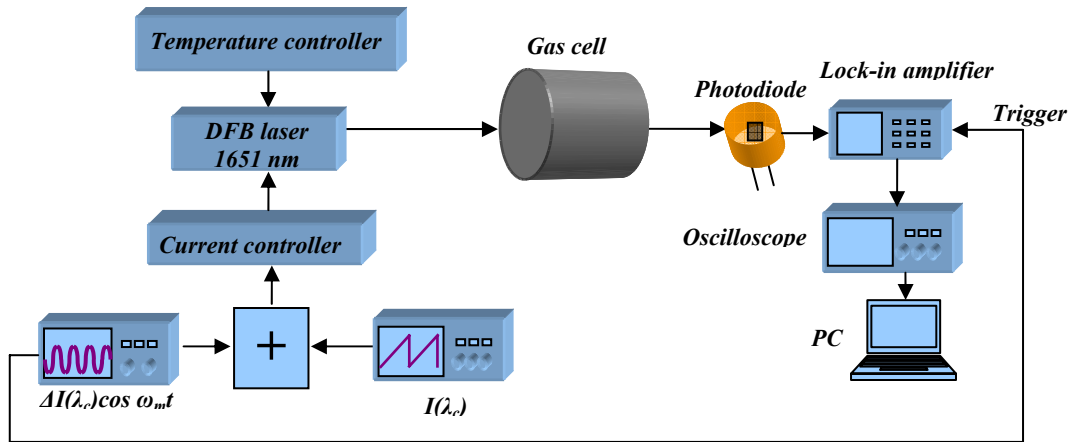


Fig. 2.3: Illustration of wavelength modulation spectroscopy

As in the case of direct detection a current-modulated laser source is used as the spectrally-narrow probe. A double modulation in the form of a slow ramp voltage (few tens of Hz) and a faster sinusoidal modulation voltage (few tens to a few hundreds of

## Chapter 2: Review of Tunable Diode Laser Spectroscopy

kHz) is applied simultaneously to the laser's current controller. The application of the ramp results in a slow periodic sweeping of the central wavelength of the laser across the target absorption line. The sinusoidal modulation of the current leads to a simultaneous but much faster modulation of the instantaneous value of the laser's wavelength about the slowly-varying local value set by the ramp. The modulation of the injection current produces the desired WM as well as a synchronous IM of the laser with a phase difference,  $\psi$  [57, 58], between them. The value of  $\psi$  is a function of  $f_m$  and is specific to a particular laser diode. The IM is predominantly linear although a smaller nonlinear component at  $2f_m$  also exists for high modulation indices but will be neglected at this stage. When the interaction of the doubly-modulated (IM and WM) laser output with the gas in the cell is monitored as a function of the mean laser wavelength, it is observed that signal components at various harmonics of the modulation frequency are produced. The output is detected by the photo-detector as usual and a lock-in amplifier (LIA) is used to select and recover the amplitude envelope of a particular harmonic.

In WMS the modulation index,  $m = \frac{\delta\nu}{\gamma}$ , is used to specify the operational conditions. Here  $\delta\nu$  denotes, as before, the amplitude of frequency deviation about the mean laser frequency (wavelength), and  $\gamma$  is the half width at half maximum of the absorption line being probed. Both these values are commonly expressed in frequency units (Hz). WMS experiments are widely characterized by the value of  $m$  used. The term *Derivative Spectroscopy* is often used to describe the scenario for experiments with low  $m$  because the recovered envelope of the  $n^{\text{th}}$  harmonic signal resembles the  $n^{\text{th}}$  derivative of the line shape to a reasonable approximation. However, since low  $m$ -values lead to low SNR this situation is of little relevance to practical environments where low-noise measurements need to be made in harsh conditions. In such situations high  $m$ -values need to be used, but the harmonic signals are no longer simple derivatives of the absorption lines.

The complications with WMS arise from the fact that a DFB laser's current-intensity relation and current-wavelength relation are nonlinear to varying degrees. Therefore a purely sinusoidal current modulation at  $f_m$ , does not translate to a purely sinusoidal IM.

## Chapter 2: Review of Tunable Diode Laser Spectroscopy

The nonlinear current-intensity relation gives rise to progressively smaller levels of IM at increasingly higher harmonics of  $f_m$ . In an analogous way, the WM too is a nonlinear process. The effect of the WM of the DFB can be visualized to be equivalent to a spectral modulation of the absorption profile around a local value of the wavelength. This periodic modulation of the spectral absorption allows a mathematical description in terms of Fourier series expansion of the spectrally-modulated transmission. The interaction of the doubly modulated laser output intensity with a spectrally modulated value of transmission therefore gives rise to signals at various harmonics of  $f_m$ . Typically though, phase sensitive detection of only one harmonic component of the output signal is carried out to extract quantitative information about the gas. The  $n^{\text{th}}$  harmonic signal is dominated by the  $n^{\text{th}}$  Fourier component of the modulated absorption line along with an associated asymmetry mainly due to the linear IM. For  $n^{\text{th}}$  harmonic detection, it is essentially the existence of the synchronous IM that causes projections of higher and lower derivatives of the line shape to distort the  $n^{\text{th}}$  harmonic signal [65]. To be specific, if 1<sup>st</sup> harmonic detection is performed, the main signal resembles the 1<sup>st</sup> derivative of the line shape. However signal components that correspond to the absorption line shape itself (0<sup>th</sup> derivative) and the 2<sup>nd</sup> derivative affect the form of the main 1<sup>st</sup> derivative signal. The distorting effect of the  $(n+1)^{\text{th}}$  and  $(n-1)^{\text{th}}$  derivatives is predominant for most lasers since these derivatives couple to the  $n^{\text{th}}$  harmonic through the predominantly linear IM. However, lasers with greater nonlinearity in their characteristics produces significant levels of nonlinear IM particularly for high  $m$ -values. The nonlinear IM can couple higher order derivatives of the absorption line on to the  $n^{\text{th}}$  derivative signals corresponding to  $n^{\text{th}}$  harmonic detection. For most applications, however, it is sufficient to consider only the linear IM. The extent of such cross-coupling and the degree of distortion is specific to a particular laser, and operating conditions significantly influence these effects. This demands careful consideration of these aspects of the system and often requires judicious choice of operating conditions. A mathematical description of these interactions is provided later in this chapter as well as in chapter 7.

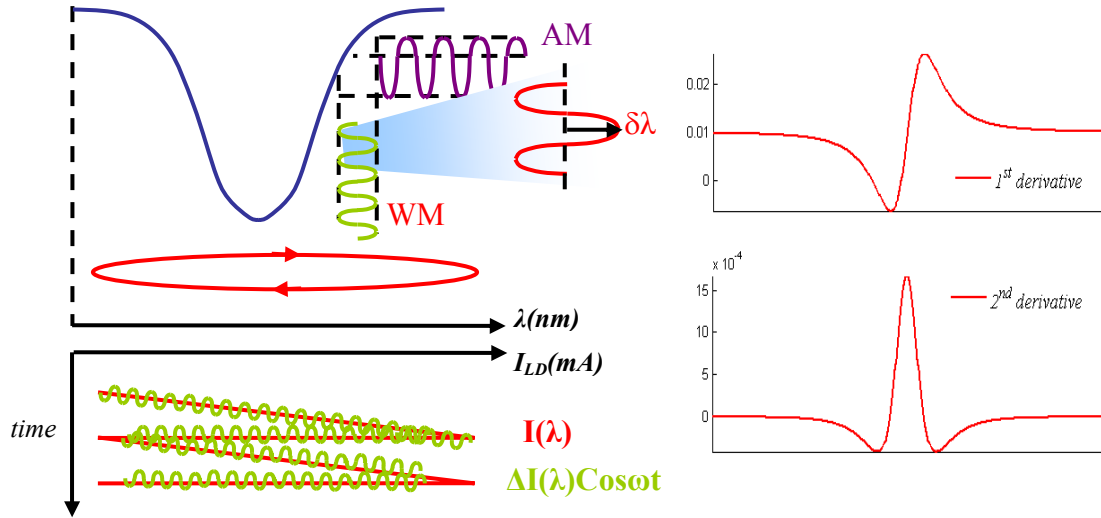


Fig.2.4: Illustration of wavelength modulation spectroscopy and typical representative 1<sup>st</sup> harmonic and 2<sup>nd</sup> harmonic signals

Figure 2.4 shows a simplified simulated representation of the process of wavelength modulation in a typical WMS experiment. The sinusoidal WM at a local value of the slowly-varied wavelength produces a modulation of the transmission that is in general not perfectly sinusoidal. This in turn produces various Fourier components of the line shape. The 1<sup>st</sup> and 2<sup>nd</sup> harmonic signals of an absorption profile obtained in a typical WMS experiment are also shown alongside. The concentration of the gas is related to the depth of the absorption line shape, or equivalently to the peak-to-peak height of the 1<sup>st</sup> derivative signal, and to the peak height of the 2<sup>nd</sup> derivative signal. The gas pressure can be extracted from the FWHM of the absorption line shape, or equivalently from the spacing of the maximum and the minimum of the 1<sup>st</sup> derivative signal, or from the zero-crossings of the 2<sup>nd</sup> derivative signal.

The 1<sup>st</sup> derivative signal is seen to have a baseline that offsets it from zero but the 2<sup>nd</sup> harmonic signal has zero offset under typical conditions. The background signal in the 1<sup>st</sup> derivative signal is a direct consequence of the IM of the laser. The origin of this background and the problems it causes in signal recovery will be discussed in detail later. The absence of a baseline in the 2<sup>nd</sup> harmonic signal has made it an attractive candidate for trace gas detection as well as quantitative WMS applications. For the sake

## Chapter 2: Review of Tunable Diode Laser Spectroscopy

of simplicity the harmonic signals have been shown to be symmetric. This is strictly the case if there is no synchronous IM present. The presence of laser IM complicates matter because it tends to distort the symmetry of the signals [65] as will be seen in experimental results presented later in the thesis.

A major drawback of the technique of harmonic detection is the complexity of signal interpretation since the absolute absorption line shape cannot be recovered in a straightforward way. More important, both these techniques require calibration of the recovered signal levels to measurements performed with a known composition of gas maintained under known conditions. This is because the raw electrical signals cannot be directly related to the corresponding harmonic/derivative signal since there are many additional variable factors that affect the signal. These variable factors include laser intensity, optical throughput of the system, photo-detector gain and lock-in amplifier gain. The need for calibration is an impractical requirement in many industrial applications. In recent times, considerable research has been focused on this aspect of sensor design. This has led to the demonstration of two  $1f$  calibration-free WMS techniques, namely the RAM method [21], and the Phasor Decomposition method (PD) [22], for gas composition measurement demonstrated by previous research within this group at the University of Strathclyde. Calibration-free  $2f$  WMS has also been demonstrated by researchers [20]. These techniques will be discussed in greater detail in the course of this thesis.

## 2.4 Mathematical description of WMS

To appreciate the intricacies of WMS it is necessary to consider a mathematical description of the process. In the early mathematical descriptions of WMS, the spectral point of view was considered [60-63], and the detected intensity was represented in terms of the modulated electric field and Bessel functions. This was a natural extension of the FMS formalism, and although not inaccurate, it is distinctly non-intuitive and the resulting expressions are very cumbersome and not directly applicable in practice. Reid and Labrie had considered the intensity-based viewpoint in their detailed experimental

## Chapter 2: Review of Tunable Diode Laser Spectroscopy

work [6], to establish much of the preceding theoretical work, but assumed the laser intensity to be constant over the scan range of the laser. Additionally and perhaps more crucially, their treatment did not account for the synchronous IM of the laser and was therefore incomplete. These two factors were accounted for in a later mathematical treatment in terms of a Fourier series representation developed by Phillippe and Hanson [12]. This paper explicitly considered the linear IM as well as the phase shift between the IM and the WM. The expressions derived for the signal at the first two harmonics of  $f_m$  were obtained in terms of the first three Fourier coefficients and give a much clearer picture of the process. This representation has since been widely adopted and subsequently extended by others in the same group to include the effect of nonlinear IM as well [18, 20]. A much more complicated Fourier representation was also developed by Kluczynski and Axner [64], which considered a nonlinear IM term as well. A much clearer description of the combined effect of the laser WM and linear IM was presented by Schilt and Thevanaz [65], based on Arndt's model for pure FM for a Lorentzian line, with the effect of IM factored in. The distorting effect of the IM on the various harmonic signals was brought out very clearly in this paper.

An alternative description based on the Taylor series has also been used. Such a description is easier to relate to because the various derivatives of the absorption line shape appear explicitly. One of the first instances of the use of the alternative Taylor series treatment [66] correctly incorporates an intensity term and a linear IM term, both of which vary over the scan range of the laser. A much more recent Taylor series description [21], presents a more detailed investigation of WMS along with a highly practical method of performing calibration-free measurements on gases. The Fourier description is rigorous but certainly less intuitive and therefore daunting to the uninitiated. For the sake of clarity the Taylor series description is presented in the section that follows immediately after this one. The more involved Fourier description is reserved for a later chapter.

A brief review of the various signal components for  $1f$  WMS experiment helps to explain the origin of the various terms and thereby elicit the main problem that this

## Chapter 2: Review of Tunable Diode Laser Spectroscopy

this thesis aims to address. For the present discussion the slowly-varying mean laser wavelength set by the current ramp is denoted by  $\lambda_c$ . The mean laser intensity  $I(\lambda_c)$  is assumed to be linearly modulated with the amplitude of modulation given by  $\Delta I(\lambda_c)$ , at a modulation frequency  $\omega$ , with a phase shift  $\psi$  between the linear IM and WM.

The transmitted intensity according to the Beer-Lambert law is given by,

$$I_{out} = [I(\lambda_c) + \Delta I(\lambda_c) \cos \omega t] e^{-\alpha(\lambda_c).C.l} \quad (2.2)$$

The exponential term may be expanded in a Taylor series and for low modulation indices the expansion may be limited to the 1<sup>st</sup> order. The expression for the output intensity may then be expressed as,

$$I_{out} \approx [I(\lambda_c) + \Delta I(\lambda_c) \cos \omega t] \left[ 1 - \alpha(\lambda_c).C.l - \frac{d\alpha(\lambda)}{d\lambda} \Big|_{\lambda_c} .C.l.\delta\lambda.\cos(\omega t - \psi) \right] \quad (2.3)$$

The expression for the 1<sup>st</sup> harmonic signal is given by,

$$I_{1f} \approx \Delta I(\lambda_c) \cos \omega t - \Delta I(\lambda_c) \alpha(\lambda_c).C.l \cos \omega t - I(\lambda_c) \frac{d\alpha(\lambda)}{d\lambda} \Big|_{\lambda_c} .C.l.\delta\lambda.\cos(\omega t - \psi) \quad (2.4)$$

As can be seen from the expression, information regarding the gas is embedded in the form of the absorption line shape itself, along with its first derivative. More accurately, the dominant terms are a linear IM-induced concentration-independent term and a concentration-dependent term that follows the absorption line shape, and the conventional intensity-dependent 1<sup>st</sup> derivative term. These latter two concentration-dependent terms are accompanied by the term  $\Delta I(\lambda_c) \cos \omega t$  due to the direct IM of the laser that gives rise to a high concentration-independent background 1<sup>f</sup> residual amplitude modulation (RAM) term. It is important to note that there is a phase difference between the 1<sup>st</sup> derivative term and the other IM-induced terms. This phase difference is dependent on  $f_m$  and is specific to the particular laser used and therefore needs to be determined.

## Chapter 2: Review of Tunable Diode Laser Spectroscopy

Early  $1f$  WMS research traditionally focused on the  $1^{\text{st}}$  derivative signal alone, with the  $1f$  RAM being regarded as a totally undesirable artifact that saturated the detection electronics. These conventional measurements based on the  $1^{\text{st}}$  derivative signal (and also the  $2^{\text{nd}}$  derivative) require calibration of the experimental data to signals from a control sample of gas maintained under known conditions. This is the main drawback of such traditional methods. It has only recently been recognized [21, 22] that by exploiting the phase-sensitive detection capability of a lock-in amplifier, the IM-induced term,  $\Delta I(\lambda_1)\{1 - \alpha(\lambda).C.l\}$  can be isolated and the absolute absorption line shape recovered directly. Background normalization of the extracted signal yields the absorption profile from which concentration and pressure may be inferred. This method is discussed in more detail in the next section.

### ***2.4.1 Calibration-free $1f$ WMS using the RAM method***

In traditional  $1f$  WMS for gas sensing, the  $1^{\text{st}}$  derivative-like signal component is recovered and quantitative information about the gas pressure (P) and concentration (C) are extracted by least squares fitting of the simulated theoretical model by varying P and C to match the experimental signal. The RAM signal component due to the direct laser IM was traditionally considered an unwanted side effect since it presents considerable difficulties in signal recovery and curve fitting process. An alternative technique, known as the RAM technique, has recently been proposed [21], which exploits the RAM components and the phase difference  $\psi$  between the IM and the WM to recover the absolute line shape from a standard WMS experiment. This is achieved by fully aligning one of the lock-in amplifier axes with the  $1^{\text{st}}$  derivative signal component in Eq. 2.4, but measuring the signal recovered on the orthogonal axis. Due to the non-zero value of  $\psi$  the orthogonal channel recovers a projection of the first two RAM terms but is totally isolated from the  $1^{\text{st}}$  derivative term since it is aligned along the orthogonal axis.

To be specific, the phase of the lock-in amplifier's reference signal is adjusted to completely align channel Y with the  $1^{\text{st}}$  derivative signal. This is equivalent to multiplying the whole expression by  $\cos(\omega t - \psi)$  and considering only the resulting dc

## Chapter 2: Review of Tunable Diode Laser Spectroscopy

terms. This is essentially how the process of phase-sensitive harmonic detection works. The signal on channel Y is then given by,

$$I_{1fChY} = \Delta I(\lambda_c) \{1 - \alpha(\lambda_c).C.l\} \cos \psi - I(\lambda_c) \left. \frac{d\alpha(\lambda)}{d\lambda} \right|_{\lambda_c} .C.l.\delta\lambda \quad (2.5)$$

It is seen that while the entire 1<sup>st</sup> derivative signal is recovered on channel Y, there is also a  $\psi$ -dependent projection of the IM-induced term. The signal on the orthogonal channel X is similarly obtained by multiplying the right hand side of Eq. 2.4 by  $\sin(\omega t - \psi)$  and considering dc terms again. The signal on channel X is then given by,

$$I_{1fChX} = \Delta I(\lambda_c) \{1 - \alpha(\lambda_c).C.l\} \sin \psi \quad (2.6)$$

Channel X therefore recovers only a  $\psi$ -dependent projection of the IM-induced term  $\Delta I(\lambda_c)[1 - \alpha(\lambda_c).C.l]$  with no distortion due to the 1<sup>st</sup> derivative signal. By normalizing this signal by the linear IM,  $\Delta I(\lambda_c)$  which is essentially the background RAM reduced by the same factors  $\sin \psi$ , the relative transmission profile can be extracted. In practical situations, the background signal can be obtained by fitting a baseline to the non-absorbing spectral wings of the measured absorption signal. The concentration and pressure can then be extracted by applying a least-square fit of an appropriate line shape function (Lorentzian, Gaussian or Voigt) with concentration and pressure as the free parameters. Note that a separate measurement is not required to get a normalization signal. This technique is calibration-free because the absorption profile is recovered directly and no comparison to a signal from a gas sample under known conditions is required. Note that this method is directly applicable for modulation indices up to about 0.2. For higher  $m$ -values additional correction factors need to be incorporated in to the recovery algorithm to account for higher order terms in the Taylor series expansion that have been neglected so far. This will be discussed shortly.

## Chapter 2: Review of Tunable Diode Laser Spectroscopy

Figure 2.5 and Fig. 2.6 help to elucidate how the RAM method works.

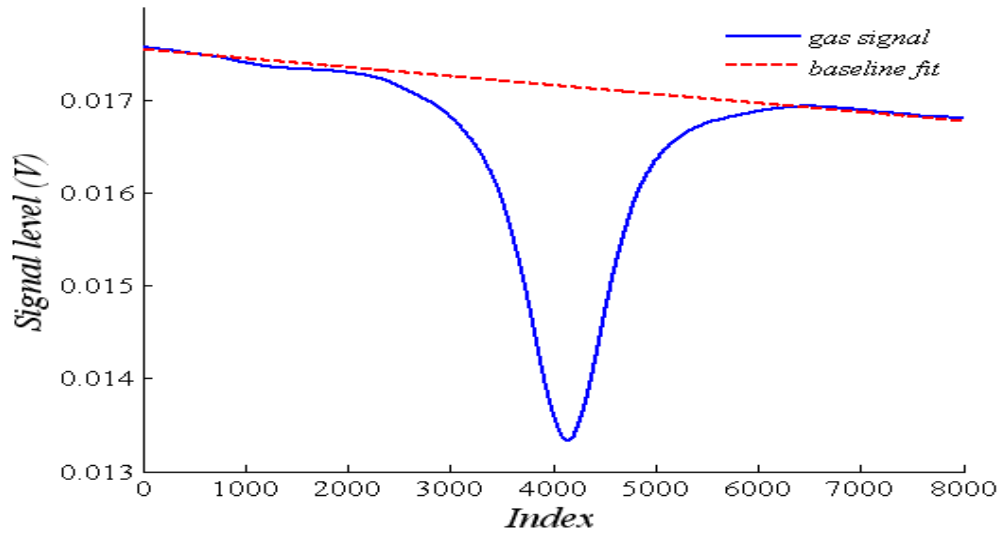


*Fig. 2.5: Gas absorption signal and baseline for 10.13% methane in nitrogen balance at a pressure of 1.028 bar and temperature of 20.1°C, and a modulation index of 0.2.*

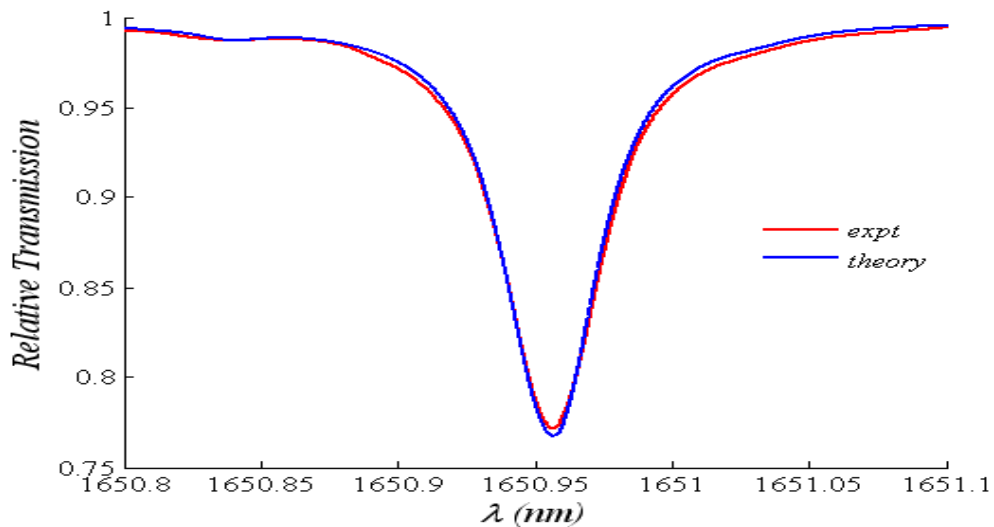


*Fig. 2.6: Recovery of relative transmission profile for 10.13% methane in nitrogen balance at a pressure of 1.028 bar and temperature of 20.1°C, and a modulation index of 0.2*

In Fig. 2.5 the time-indexed signal  $I_{1fChX}$  recovered by the lock-in amplifier (LIA) is shown in blue while a baseline fit to the non-absorbing spectral wings is shown in red. In

## Chapter 2: Review of Tunable Diode Laser Spectroscopy

a laboratory demonstration the baseline may be obtained by purging the cell of gas and thereby taking an actual “no-gas” measurement although in a real-life situation baseline fitting will have to be made. This practical issue will be discussed towards the end of this chapter and at other relevant junctures in the thesis. The relative transmission profile is extracted by point-by-point normalization of the gas signal by this baseline and subsequent wavelength-referencing of the time-indexed value as explained later. The experimental result for  $m$  value of 0.2 is shown in Fig. 2.6 along with the theoretical trace simulated using the HITRAN spectroscopic database [23]. Clearly the absorption profile is recovered with good accuracy.

### 2.4.2 Calibration-free 1f WMS using the Phasor Decomposition method

The RAM method has the drawback of recovering a projection of the full IM-induced signal. An alternate method of signal recovery is to completely align the channel Y of the lock-in amplifier with the IM-induced term  $\Delta I(\lambda_c)[1 - \alpha(\lambda_c).C.I]$ . A  $\psi$ -dependent projection of the 1<sup>st</sup> derivative signal is also detected simultaneously. This is equivalent to multiplying the whole expression by  $\cos \omega t$  in this case and considering only the resulting dc terms. The signal on channel Y is given by,

$$I_{1fChY} = \Delta I(\lambda_c) \{1 - \alpha(\lambda_c).C.I\} - I(\lambda_c) \left. \frac{d\alpha(\lambda)}{d\lambda} \right|_{\lambda_c} .C.I.\delta\lambda \cos \psi \quad (2.7)$$

Note that unlike in the RAM method, here the full IM-induced component is recovered on channel Y along with a distorting projection of the 1<sup>st</sup> derivative signal. The signal on the orthogonal channel X is similarly obtained by multiplying the right hand side of Eq. 2.5 by  $\sin \omega t$  and considering dc terms again. The signal on channel X is given by,

$$I_{1fChX} = -I(\lambda_c) \left. \frac{d\alpha(\lambda)}{d\lambda} \right|_{\lambda_c} .C.I.\delta\lambda \sin \psi \quad (2.8)$$

## Chapter 2: Review of Tunable Diode Laser Spectroscopy

It is seen that channel X recovers only a  $\psi$ -dependent projection of the 1<sup>st</sup> derivative signal with no distortion due to the IM-induced term  $\Delta I(\lambda)[1 - \alpha(\lambda).C.I]$ . Now, the full IM-induced term can be extracted from Eq. 2.7 and Eq. 2.8 and knowledge of  $\psi$  by,

$$I_{RAM} = I_{1fChY} - \frac{I_{1fChX}}{\tan \psi} = \Delta I(\lambda_c) \{1 - \alpha(\lambda_c).C.I\} \quad (2.9)$$

The normalization process is identical to the previous RAM approach. The various signal components are depicted in Fig. 2.7 for a typical measurement. A low  $m$ -value of 0.2 was chosen in this case as well. The blue trace represents the projection of the 1<sup>st</sup> derivative signal recovered on channel X and the red trace represents the complementary projection of this signal along with the embedded IM-induced term,  $\Delta I(\lambda_c)[1 - \alpha(\lambda_c).C.I]$ . The high RAM background is clearly evident on the red trace. The green trace represents the baseline to the IM-induced term which is used as the normalization signal for the absorption-dependent term extracted using Eq. 2.9.

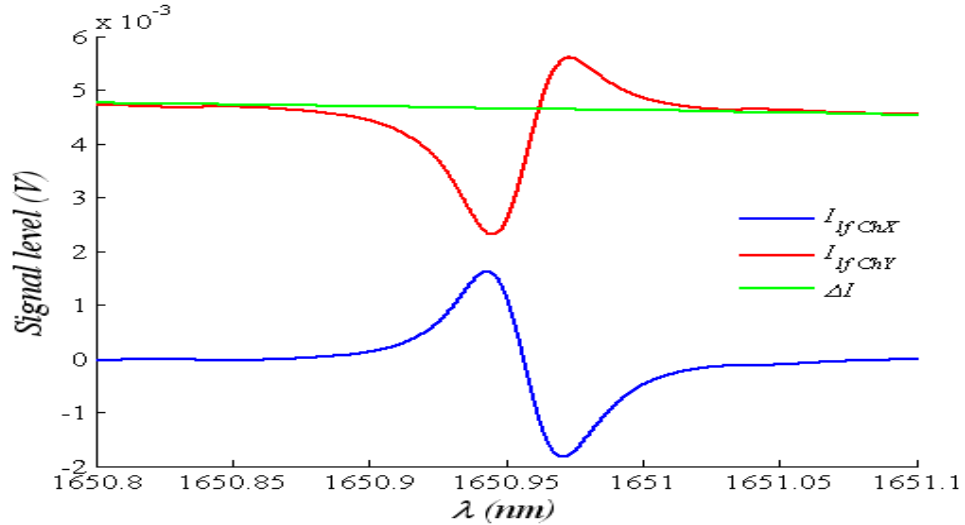


**Fig. 2.7:** Signal components used in PDM on 10.13% methane in nitrogen balance at a pressure of 1.056 bar and temperature of 19.7°C, at a modulation index of 0.2.

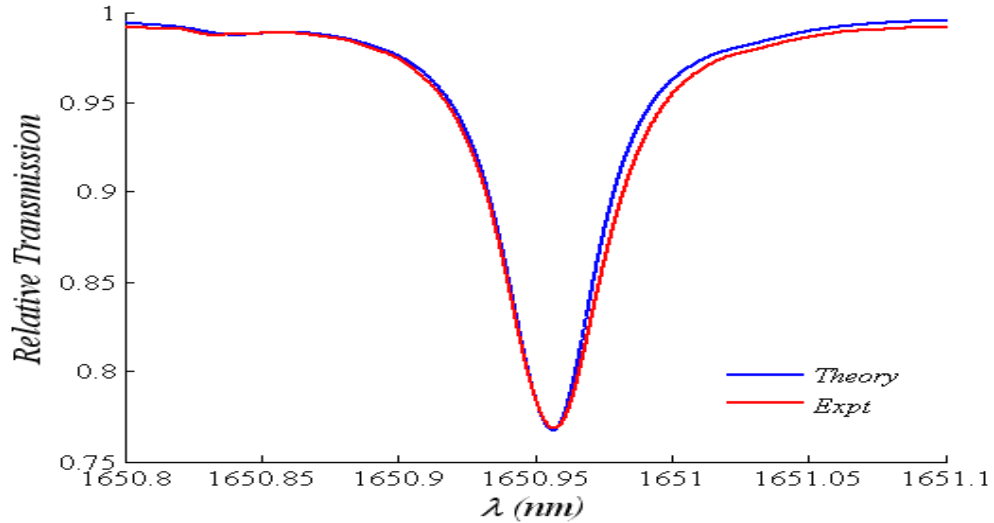


**Fig. 2.8:** Relative transmission profile for 10.13% methane in nitrogen balance at a pressure of 1.056 bar and temperature of 19.7°C, and a modulation index of 0.2

The relative transmission profile is shown in Fig. 2.8, where the experimental trace in red is compared with the theoretical trace simulated based on the HITRAN spectroscopic database.

The main advantage of the PDM over the RAM technique is that the full RAM signal is projected on to channel Y and then extracted by Eq. 2.9. In the RAM method the signal recovered by the lock-in amplifier is the full RAM signal scaled by  $\sin \psi$ . For lasers with a low value of  $\psi$ , this projection will also be correspondingly smaller and the SNR of the RAM method will be degraded. The PDM on the other hand recovers two signals that are both strong and therefore easier to digitize and subsequent processing to extract the RAM component is easier. Another advantage of this method is that for an isolated and symmetric spectral feature, the value of  $\psi$  can be very easily calculated [22] from the two measured signals given by Eq. 2.7 and Eq. 2.8. This is a very convenient feature for *in situ* periodic self-characterization of field-deployable stand-alone systems.

These results serve to convey the essence of the two new calibration-free 1f WMS signal recovery techniques established by previous researchers in this group. For further details of these two techniques and for gas composition measurements at high

## Chapter 2: Review of Tunable Diode Laser Spectroscopy

temperatures and for varying pressures, the interested reader is referred to several recently published papers [21, 22, 67, 68].

### 2.4.3 Correction factors for high modulation indices

For optimum signal to noise ratio in WMS measurements it is necessary to use modulation indices greater than 0.2. However for high modulation indices, limiting the Taylor series expansion to only the first order leads to significant errors, since higher order terms of significant value are not included. If a second order expansion of the Taylor series is used the expression for intensity may be expressed as,

$$I_{out} \approx [I(\lambda_c) + \Delta I(\lambda_c) \cos \omega t] \left[ 1 - \alpha(\lambda_c) \cdot C.I. - \frac{d\alpha(\lambda)}{d\lambda} \Big|_{\lambda_c} \cdot C.I. \delta\lambda \cdot \cos(\omega t - \psi) - \frac{1}{2!} \frac{d^2\alpha(\lambda)}{d\lambda^2} \Big|_{\lambda_c} \cdot C.I. (\delta\lambda)^2 \cos^2(\omega t - \psi) \right] \quad (2.10)$$

The expression for the 1<sup>st</sup> harmonic signal is given by,

$$I_{1f} = \left[ \Delta I(\lambda_c) \{1 - \alpha(\lambda_c) \cdot C.I.\} - \frac{1}{4} \Delta I(\lambda_c) \frac{d^2\alpha(\lambda)}{d\lambda^2} \Big|_{\lambda_c} \cdot C.I. (\delta\lambda)^2 \right] \cos \omega t - \left[ I(\lambda_c) \frac{d\alpha(\lambda)}{d\lambda} \Big|_{\lambda_c} \cdot C.I. \delta\lambda \right] \cos(\omega t - \psi) - \left[ \frac{1}{8} \Delta I(\lambda_c) \frac{d^2\alpha(\lambda)}{d\lambda^2} \Big|_{\lambda_c} \cdot C.I. (\delta\lambda)^2 \right] \cos(\omega t - 2\psi) \quad (2.11)$$

It is seen that there are the two extra 2<sup>nd</sup> derivative terms in the expression for the 1<sup>st</sup> harmonic signal. These two 2<sup>nd</sup> derivative terms are given by,

## Chapter 2: Review of Tunable Diode Laser Spectroscopy

$$-\frac{1}{4}\Delta I(\lambda_c)\left.\frac{d^2\alpha(\lambda)}{d\lambda^2}\right|_{\lambda_c}.C.I.(\delta\lambda)^2\cos\omega t \quad (2.12)$$

and,

$$-\frac{1}{8}\Delta I(\lambda_c)\left.\frac{d^2\alpha(\lambda)}{d\lambda^2}\right|_{\lambda_c}.C.I.(\delta\lambda)^2\cos(\omega t - 2\psi) \quad (2.13)$$

Both these terms have their peak values at line-centre and if they are of appreciable value they can significantly affect the line-centre value of the RAM signal. When large values of current modulation are used to attain high modulation indices, the corresponding value of the IM,  $\Delta I(\lambda_c)$  is also large and the effect of these terms can become significant. This leads to errors in the values of concentration extracted from the absorption line shape recovered using the RAM technique or the PDM. To address this problem a suitable correction strategy was devised by previous research within the group [22, 69] that allows higher values of the modulation index to be used. It was shown that for this 2<sup>nd</sup> order approximation of the Taylor series, a 2<sup>nd</sup> order correction factor needs to be used, and is given by,

$$2^{nd} \text{ order correction} = \frac{1}{4}\Delta I(\lambda_c)m^2 B\alpha(\lambda_c)Cl \cos\theta \quad (2.14)$$

where,  $B = \frac{3\Delta^2 - 1}{(1 + \Delta^2)^2}$  and  $\Delta = \frac{\nu_c - \nu_0}{\gamma}$ .

In a similar way if a 4<sup>th</sup> order expansion of the Taylor series is considered the corresponding 4<sup>th</sup> order correction factor is given by,

$$4^{th} \text{ order correction} = \frac{1}{8}\Delta I(\lambda_c)m^4 D\alpha(\lambda_c)Cl \cos\theta \quad (2.15)$$

where,  $D = \frac{1 - 10\Delta^2 + 5\Delta^4}{(1 + \Delta^2)^4}$ .

## Chapter 2: Review of Tunable Diode Laser Spectroscopy

It was determined experimentally that these correction factors were able to account for the effects of the IM for  $m$ -values up to 0.7. Although the correction factors are used in the processing of results in chapter 5, the theory of the strategy is not described in greater detail in this thesis. The interested reader is referred to Ref [69] for a detailed discussion of the topic. At present concurrent research is also going on within the group with the aim of devising a more general correction factor strategy that will permit arbitrarily high modulation indices to be used.

### **2.5 Limitation of calibration-free $1f$ WMS techniques – Residual Amplitude Modulation (RAM)**

Although the two techniques discussed in the preceding section allow calibration-free recovery of the absolute gas absorption line shape, there is one aspect that limits the sensitivity that can be achieved. In the absence of gas the concentration-independent direct IM term survives and gives rise to what is known as the RAM term. The RAM forms the large background signal component on which the absorption signal is superimposed. This is shown in Fig. 2.9 in which the IM-induced signals as given by Eq. 2.6 for methane concentrations of 10%, 1% and 0.1% are shown. The LIA is easily overloaded when one attempts to increase its sensitivity to measure small concentration-dependent changes. The respective lock-in sensitivities have been maximized without causing overloading. The concentration-dependent absorption signals are seen to reduce drastically with the concentration. For low concentrations, the off-peak background signal saturates the input stages of the LIA thereby limiting the full dynamic range of the instrument. Digitization of signals for post-processing becomes prone to quantization noise of the analog-digital conversion. Therefore it is clear that the  $1f$  RAM sets an operational limit on the detection sensitivity achievable with the RAM technique or the PDM.

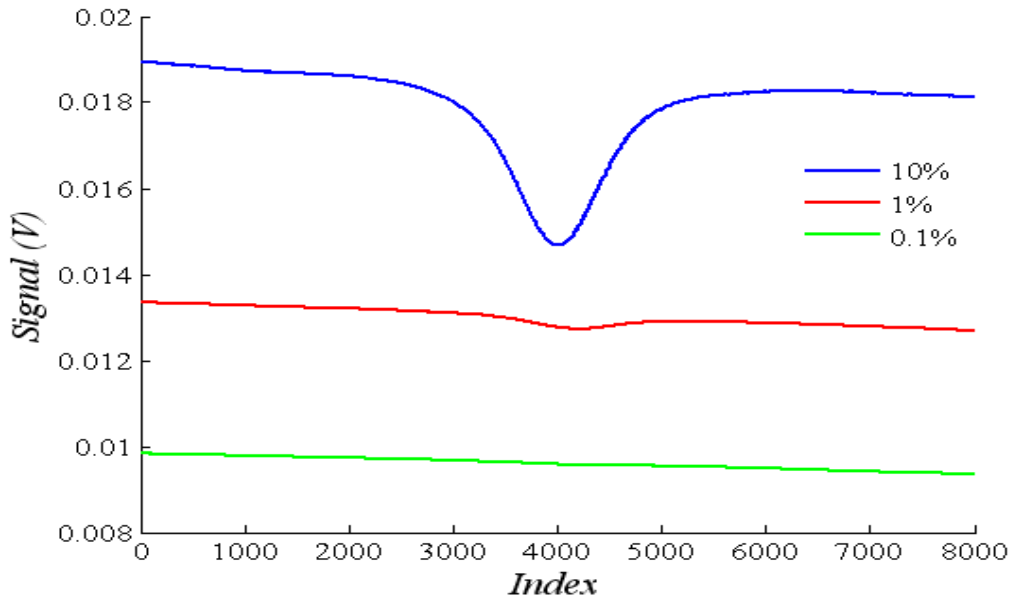


*Fig. 2.9: Comparison of signals for 10%, 1% and 0.1% methane showing drastic decrease in the absorption-dependent signal as the concentration decreases*

Most of the work reported in the literature is based on 2<sup>nd</sup> harmonic detection to circumvent the problem, where the background signal is nearly zero. This allows the signal for low concentrations to be amplified to a greater extent than is possible in 1 $f$  WMS. However a background signal for 2 $f$  WMS has also been reported in the literature [19, 64], although the problem is not nearly as severe as it is in 1 $f$  WMS. Although detection at higher harmonics alleviates the problem of signal overload, the penalty one has to pay is increased complexity of signal interpretation since most 2 $f$  WMS measurements require calibration to a sample of gas maintained under known conditions. The need for calibration is a distinctly non-trivial problem in automated stand-alone systems and is best avoided if possible. For applications such as industrial process control, a simple method of line shape recovery is desirable, and it is in this context, that the two 1 $f$  calibration-free techniques are important. However, since these two methods are limited by the 1 $f$  background RAM, a method to eliminate the limiting 1 $f$  background RAM is highly relevant. Successful implementation of this technique is expected to be a significant improvement in this field.

## Chapter 2: Review of Tunable Diode Laser Spectroscopy

A second drawback of both these techniques is the need to obtain a baseline fit to the offline regions of a gas line for signal normalization. This aspect is often not appreciated when working in a laboratory situation. The need to obtain a baseline region requires the laser to be scanned over a wide range across a well isolated absorption line so that regions sufficiently far away from the absorption peak and on either side of it are recovered. This may prove to be inconvenient for absorption lines broadened under high pressure due to the limited tuning range of DFB lasers. Even when the tuning range is not a restriction, identification of offline points and therefore efficient baseline fitting may be difficult in spectrally congested regions due to the presence of other interfering gas lines. Moreover, the baseline fit requires a certain degree of optimization by direct user-intervention. This may be impractical in automated systems for real-time monitoring that do not afford the benefit of such optimization. Since the emphasis in these techniques is on the accurate recovery of gas absorption lines, the dependence on baseline fitting is undesirable.

To address these issues, a new fiber-optic approach to eliminate the 1/f background RAM is introduced in Chapter 4 along with a detailed explanation of the various design aspects that must be considered for the technique to be useful. Preliminary results are presented to demonstrate the method. The method is fully validated by applying it to the RAM method and the Phasor Decomposition Method (PDM) explained earlier for a range of modulation indices and three values of concentration. The crucial requirement of a suitable normalization signal is also considered and fulfilled, that finally leads to a convincing demonstration of a sensitive, robust and practical system for calibration-free WMS.

## 2.6 Thesis objectives

The objectives of this thesis are as follows –

1. Demonstrate a new fiber-optic technique, termed RAM nulling, to eliminate the gas concentration-independent background RAM signal that arises due to direct intensity modulation of the laser. The background RAM signal tends to saturate the detection electronics and thereby limits the sensitivity of TDLS-WMS particularly with 1<sup>st</sup> harmonic detection. It is therefore expected that higher detection sensitivity will be achieved if this technique is successfully implemented.
2. Devise an appropriate and operationally convenient signal normalization strategy for the proposed method. As a consequence of the background elimination the gas absorption signal appears on a zero level. The absence of suitable, readily-available, non-zero, off-line regions therefore makes it important to develop a new normalization strategy.
3. Demonstrate calibration-free recovery of absolute gas absorption lines using the two previously-demonstrated calibration-free  $1f$  WMS techniques namely, the RAM technique and Phasor Decomposition Method (PDM) with RAM nulling incorporated in both techniques.
4. Extend the RAM nulling technique to 2<sup>nd</sup> harmonic WMS to eliminate the  $2f$  background signal. Successful realization of this is expected to be directly applicable to recently-proposed, calibration-free, quantitative  $2f$  WMS techniques for concentration and temperature measurement, in which the background needs to be separately measured and subtracted. Trace gas detection using newly-developed laser sources that have shown significant  $2f$  background RAM are also expected to benefit.

## 2.7 Overview of thesis

The subsequent chapters of this thesis are arranged as follows:

Chapter 3 introduces the basics of those elements of molecular spectroscopy that are used in the course of this work. This includes the origin of absorption spectra, their shapes, strengths and widths, and their dependence on various gas parameters. The method of extracting useful information such as concentration and pressure are also discussed. This chapter is by no means an exhaustive discussion of molecular spectroscopy in general.

Chapter 4 discusses the basics of the technique used to alleviate the problem of high background in WMS. This technique, termed RAM nulling, is explained using a succinct mathematical formalism. The experimental arrangement is discussed in detail and the equipment used in the experiments is also described. The issue of optical interference noise and the method to minimize it is also discussed.

Chapter 5 presents a more detailed study of the performance of the RAM nulling technique for different concentrations of gas. The RAM nulling technique is incorporated in to the Phasor Decomposition method and results are presented to demonstrate the success. An unexpected aspect of the signals encountered in RAM nulling are shown by these results. A more detailed analysis of the mechanism of RAM nulling is carried out, and a comparison of simulated and experimental results is made that resolves the apparent conflict.

Chapter 5 examines the RAM nulling process theoretically. A mathematical model is developed that investigates the wavelength dependence of various signal components as well as physical components of the system. The resultant slope on RAM nulled signals for three different experimental configurations is discussed and the best configuration for cancellation of the slope is also pointed out. The implications of this investigation for laser structures that have significantly nonlinear power-current characteristics are also discussed.

## **Chapter 2: Review of Tunable Diode Laser Spectroscopy**

Chapter 7 describes the extension of RAM nulling to 2<sup>nd</sup> harmonic signals. A review of the recent developments in quantitative  $2f$  WMS is presented that explains the relevance of  $2f$  RAM nulling. Experimental results are presented that demonstrate the robust  $2f$  background nulling using the same experimental setup. Finally an alternative form of calibration-free  $2f$  WMS technique is outlined that incorporates RAM nulling and normalization by the  $2f$  RAM. This should be useful for quantitative  $2f$  WMS currently being widely used in industrial control applications.

Chapter 8 summarizes the entire thesis and provides suggestions for future scope for work in calibration-free gas sensing applications. Important concurrent work is also briefly discussed that should help in making this technique highly competitive in comparison to other existing techniques.

## 2.8 References

1. E. D. Hinkley, "High resolution infrared spectroscopy with a tunable diode laser," *Appl. Phys. Lett.* **16** (9), 351-354 (1970).
2. E. D. Hinkley, P. J. Kelly, "Detection of air pollutants with tunable diode lasers," *Science* **171** (3972), 635-639 (1971).
3. J. Reid, J. Shewchun, B. K. Garside, E. A. Ballik, "High sensitivity pollution detection employing tunable diode lasers," *Appl. Opt.* **17**(2), 300-307 (1978).
4. J. Reid, B. K. Garside, J. Shewchun, M. El-Sherbiny, E. A. Ballik, "High sensitivity point monitoring of atmospheric gases employing tunable diode lasers," *Appl. Opt.* **17** (11), 1806-1810 (1978).
5. J. Reid, M. El-Sherbiny, B. K. Garside, E. A. Ballik, "Sensitivity limits of a tunable diode laser spectrometer, with application to the detection of NO<sub>2</sub> at the 100-ppt level," *Appl. Opt.* **19** (19), 3349-3354 (1980).
6. J. Reid, D. Labrie, "Second-harmonic detection with tunable diode lasers – comparison of experiment and theory," *Appl. Phys. B* **26**, 203-210 (1981).
7. D. T. Cassidy, J. Reid, "Atmospheric pressure monitoring of trace gases using tunable diode lasers," *Appl. Opt.* **21** (7), 1185-1190 (1982).
8. W. Lenth, M. Gerhertz, "Sensitive detection of NO<sub>2</sub> using high frequency heterodyne spectroscopy with a GaAlAs diode laser," *Appl. Phys. Lett.* **47** (12), 1263-1265 (1985).
9. D. T. Cassidy, L. J. Bonnell, "Trace gas detection with short-external-cavity InGaAsP diode laser transmitter modules operating at 1.58 $\mu$ m," *Appl. Opt.* **27** (13), 2688-2693 (1988).
10. A. Lucchesini, I. Longo, C. Gabbanini, S. Gozzini, L. Moi, "Diode laser spectroscopy of methane overtone transitions," *Appl. Opt.* **32** (27), 5211-5216 (1993).

## Chapter 2: Review of Tunable Diode Laser Spectroscopy

11. M. Gabrysch, C. Corsi, F. S. Pavone, M. Inguscio, "Simultaneous detection of CO and CO<sub>2</sub> using a semiconductor DFB diode laser at 1.578 $\mu$ m," Appl. Phys. B **65**, 75-79 (1997).
12. L. C. Philippe, R. K. Hanson, "Laser diode wavelength modulation spectroscopy for simultaneous measurement of temperature, pressure and velocity in shock-heated oxygen flows," Appl. Opt. **32** (30), 6090-6103 (1993).
13. M. F. Miller, W. J. Kessler, M. G. Allen, "Diode laser-based air mass flux sensor for subsonic aeropropulsion inlets," Appl. Opt. **35** (24), 4905-4912 (1996).
14. I. Linnerud, P. Kaspersen, T. Jaeger, "Gas monitoring in the process industry using diode laser spectroscopy," Appl. Phys. B **67**, 297-305 (1998).
15. T. Aizawa, T. Kamimoto, T. Tamaru, "Measurements of OH radical concentration in combustion environments by wavelength-modulation spectroscopy with a 1.55 $\mu$ m distributed-feedback diode laser," Appl. Opt. **38** (9), 1733-1741 (1999).
16. M. E. Webber, R. Claps, F. V. Englich, F. K. Tittel, J. B. Jeffries, R. K. Hanson, "Measurements of NH<sub>3</sub> and CO<sub>2</sub> with distributed-feedback diode lasers near 2.0  $\mu$ m in bioreactor vent gases," Appl. Opt. **40** (24), 4395-4403 (2001).
17. T. Aizawa, "Diode-laser wavelength-modulation absorption spectroscopy for quantitative in situ measurements of temperature and OH radical concentration in combustion gases," Appl. Opt. **40** (27), 4894-4903 (2001).
18. J. T. C. Liu, J. B. Jeffries, R. K. Hanson, "Wavelength modulation absorption spectroscopy with  $2f$  detection using multiplexed diode lasers for rapid temperature measurements in gaseous flows," Appl. Phys. B **78**, 503-511 (2004).
19. J. T. C. Liu, J. B. Jeffries, R. K. Hanson, "Large-modulation-depth  $2f$  spectroscopy with diode lasers for rapid temperature and species measurements in gases with blended and broadened spectra," Appl. Opt. **43** (35), 6500-6509 (2004).

## Chapter 2: Review of Tunable Diode Laser Spectroscopy

20. H. Li, G.B Reiker, X. Liu, J. B. Jeffries, R. K. Hanson, "Extension of wavelength modulation spectroscopy to large modulation depth for diode laser absorption measurements in high-pressure gases," *Appl. Opt.* **45** (5), 1052-1061 (2006).
21. K. Duffin, A. J. McGettrick, W. Johnstone, G. Stewart, D. G. Moodie, "Tunable diode laser spectroscopy with wavelength modulation: a calibration-free approach to the recovery of absolute gas absorption line shapes," *J. Lightwav. Technol.* **25**, 3114-3125 (2007).
22. A. J. McGettrick, K. Duffin, W. Johnstone, G. Stewart, D. G. Moodie, "Tunable diode laser spectroscopy with wavelength modulation: a phasor decomposition method for calibration-free measurements of gas concentration and pressure," *J. Lightwav. Technol.* **26**, 432-440 (2008).
23. L.S. Rothman et al., "The HITRAN 2004 molecular spectroscopic database," *J. Quant. Spectrosc. Radiat. Transfer*, Vol. 96, pp 139-204, 2005
24. K. P. Petrov, R. F. Curl, F. K. Tittel, "Compact laser difference-frequency spectrometer for multi-component trace gas detection," *Appl. Phys. B*, **66**, 531-538 (1998).
25. D. G. Lancaster, R. Weidner, D. Richter, F. K. Tittel, J. Limpert, "Compact CH<sub>4</sub> sensor based on difference-frequency mixing of diode lasers in quasi-phase-matched LiNbO<sub>3</sub>," *Opt. Commun.* **175**, 461-468 (2000).
26. D. Ritchie, A. Fried, B. P. Wert, J. G. Walegda, F. K. Tittel, "Development of a tunable mid-IR frequency laser source for highly sensitive airborne trace gas detection," *Appl. Phys. B*, **75**, 281-288 (2002).
27. J. Faist, F. Capasso, D. L. Sivco, C. Sirtori, A. L. Hutchinson, A. Y. Cho, "Quantum Cascade Laser," *Science*, **264**, 553-556 (1994).
28. J. Faist, C. Gmachl, F. Capasso, C. Sirtori, D. L. Sivco, J. N. Baillargeon, A. Y. Cho, "Distributed feedback quantum cascade laser," *Appl. Phys. Lett.* **70** (20), 2670-2672 (1997).

## Chapter 2: Review of Tunable Diode Laser Spectroscopy

29. K. Namjou, S. Cai, E. A. Whittaker, J. Faist, C. Gmachl, F. Capasso, D. L. Sivco, A. Y. Cho, "Sensitive absorption spectroscopy with a room temperature distributed feedback quantum cascade laser," *Opt. Lett.* **23** (3), 219-221 (1998).
30. A. A. Kosterev, R. F. Curl, F. K. Tittel, C. Gmachl, F. Capasso, D. L. Sivco, J. N. Baillargeon, A. L. Hutchinson, A. Y. Cho, "Methane concentration and isotope composition measurements with a mid-infrared quantum cascade laser," *Opt. Lett.* **24** (23), 1762-1764 (1999).
31. A. A. Kosterev, F. K. Tittel, C. Gmachl, F. Capasso, D. L. Sivco, J. N. Baillargeon, A. L. Hutchinson, A. Y. Cho, "Trace gas detection in ambient air with a thermoelectrically cooled, pulsed quantum-cascade distributed feedback laser," *Appl. Opt.* **39** (23), 1762-1764 (1999).
32. L. Menzel, A. A. Kosterev, R. F. Curl, F. K. Tittel, C. Gmachl, F. Capasso, D. L. Sivco, J. N. Baillargeon, A. L. Hutchinson, A. Y. Cho, W. Urban, "Spectroscopic detection of biological NO with a quantum-cascade distributed feedback laser," *Appl. Phys. B*, **72**, 859-863 (2001).
33. Kenichi Iga, "Surface-emitting laser—its birth and generation of new optoelectronics field", *IEEE Journal of Selected Topics in Quantum Electronics* **6** (6), 1201–1215 (2000).
34. C. Lauer, M. Orstieffer, R. Shau, J. Roskopf, G. Bohm, E. Ronneberg, F. Kohleer, M. C. Amann "80°C continuous-wave operation of 2.01 $\mu$ m wavelength InGaAlAs-InP vertical-cavity surface-emitting lasers," *IEEE Photon. Tech. Lett.* **16**, 2209-2211 (2004).
35. J. M. Ostermann, F. Rinaldi, P. Debernardi, R. Michalzik, "VCSELs with enhanced single-mode power and stabilized polarization for oxygen sensing," *IEEE Photon. Tech. Lett.* **17**, 2256-2258 (2005).
36. A. Haglund; J.S. Gustavsson; J. Vukusic; P. Modh; A. Larsson," Single fundamental-mode output power exceeding 6 mW from VCSELs with a shallow surface relief," *IEEE Photon. Tech. Lett.* **17**, 2256-2258 (2005).

## Chapter 2: Review of Tunable Diode Laser Spectroscopy

37. Hans P. Zappe, Martin Hess, Michael Moser, Rainer Hövel, Karlheinz Gulden, Hans-Peter Gauggel, and Fabrice Monti di Sopra, "Narrow-Linewidth Vertical-Cavity Surface-Emitting Lasers for Oxygen Detection," *Appl. Opt.***39**, 2475-2479 (2000)
38. M. Lackner, M. Schwarzott, F. Winter, B. Kogel, S. Jatta, H. Halbritter, P. Meissner, "CO and CO<sub>2</sub> spectroscopy using a 60 nm broadband tunable MEMS-VCSEL at ~1.55µm", *Opt. Lett.*, **31** (21), 3170-3172, (2006).
39. A. Hangauer, J. Chen, R. Strzoda, M. Orstiefer, M. -C. Amann, "Wavelength modulation spectroscopy with a widely tunable InP-based 2.3 µm vertical-cavity surface-emitting laser", *Opt. Lett.*, **33**, 1566-1568, (2008)
40. Kornaszewski, L W; Gayraud, N; Stone, J M; MacPherson, W N; George, A K; Knight, J C; Hand, D P; Reid, D T, "Mid-infrared methane detection in a photonic bandgap fiber using a broadband optical parametric oscillator," *Opt. Exp.* **15** (18), 11219-11224 (2007).
41. A. M. Cubillas, M. Silva-Lopez, J. M. Lazaro, O. M. Conde, M. N. Petrovich, and J. M. Lopez-Higuera, "Methane detection at 1670-nm band using a hollow-core photonic bandgap fiber and a multiline algorithm," *Opt. Exp.* **15**, 17570-17576 (2007).
42. Cubillas, A.M.; Lazaro, J.M.; Silva-Lopez, M.; Conde, O.M.; Petrovich, M.N.; Lopez-Higuera, J.M., "Methane sensing at 1300 nm band with hollow-core photonic bandgap fibre as gas cell," *Electronics Letters*, Vol. 44, Iss. 6, 403 - 404 (2008).
43. T. G. Euser, J. S. Y. Chen, M. Scharrer, P. St. J. Russell, N. J. Farrer, P. J. Sadler, "Quantitative broadband chemical sensing in air-suspended solid-core fibers," *J. Appl. Phys.*, Vol. 103, Iss. 10, pg. 103108 (2008).
44. <http://www.ceramoptec.com/>
45. <http://www.iguide-irphotonics.com/>

## Chapter 2: Review of Tunable Diode Laser Spectroscopy

46. L. Ciaffoni, R. Grilli, G. Hancock, A. J. Orr-Ewing, R. Peverall, G. A. D. Ritchie, “3.5  $\mu\text{m}$  high resolution gas sensing employing a  $\text{LiNbO}_3$  QPM-DFG waveguide module,” *Appl. Phys. B* **94**, 517-525 (2009).
47. A. Kosterev, G. Wysocki, Y. Bakhirkin, S. So, R. Lewicki, M. Fraser, F. Tittel, R. F. Curl, “Application of quantum cascade lasers to trace gas analysis,” *Appl. Phys. B* **90**, 165-176 (2008).
48. G. B. Reiker, J. B. Jeffries, R. K. Hanson, “Measurements of high-pressure  $\text{CO}_2$  absorption near 2.0  $\mu\text{m}$  and implications on tunable diode laser sensor design,” *Appl. Phys. B* **94**, 51-63 (2009).
49. H. Wahlquist, “Modulation broadening of unsaturated Lorentzian lines,” *J. Chem. Phys.* **35** (5) 1708-1710 (1961).
50. A. M. Russell, D. A. Torchia, “Harmonic analysis in systems using phase sensitive detection,” *Rev. Sci. Instr.* **33** (4) 442-444 (1962).
51. G. V. H. Wilson, “Modulation broadening of NMR and ESR line shapes,” *J. Appl. Phys.* **34** (4) 442-444 (1962).
52. R. Arndt, “Analytical line shapes for Lorentzian signals broadened by modulation,” *J. Appl. Phys.* **36** (8), 2522-2524 (1965).
53. G. C. Bjorklund, “Frequency-modulation spectroscopy: a new method for measuring weak absorptions and dispersions,” *Opt. Lett.* **5** (1), 15-17 (1980).
54. W. Lenth, C. Ortiz, G. C. Bjorklund, “Pulsed frequency-modulation spectroscopy as a means for fast absorption measurements,” *Opt. Lett.* **6** (7), 351-353 (1981).
55. W. Lenth, “Optical heterodyne spectroscopy with frequency- and amplitude-modulated semiconductor lasers,” *Opt. Lett.* **8** (11), 575-577 (1983).
56. W. Lenth, “High-frequency heterodyne spectroscopy with current-modulated diode lasers,” *IEEE J. Quant. Elec.* **29** (9), 1045-1050 (1984).
57. S. Kobayashi, Y. Yamamoto, M. Ito, T. Kimura, “Direct frequency modulation in  $\text{AlGaAs}$  semiconductor lasers,” *IEEE J. Quant. Elec.* **18** (4), 582-595 (1982).

## Chapter 2: Review of Tunable Diode Laser Spectroscopy

58. G. Jacobsen, H. Olesen, F. Birkedahl, "Current/frequency modulation characteristics for directly optical frequency-modulated lasers at 830nm and 1.3 $\mu$ m," *Electron. Lett.* **18** (20), 874-876 (1982).
59. X. Zhu, D. T. Cassidy, "Modulation spectroscopy with a semiconductor diode laser by injection-current modulation," *J. Opt. Soc. Am. B* **14**, 1945-1950 (1997).
60. J. Silver, "Frequency-modulation spectroscopy for trace species detection: theory and comparison among experimental results," *Appl. Opt.* **31** (6), 707-717 (1992).
61. D. S. Bomse, A. C. Stanton, J. Silver, "Frequency modulation and wavelength modulation spectroscopy: comparison of experimental methods using a lead-salt diode laser," *Appl. Opt.* **31** (6), 718-731 (1992).
62. J. M. Supplee, E. A. Whittaker, W. Lenth, "Theoretical description of frequency modulation and wavelength modulation spectroscopy," *Appl. Opt.* **33** (27), 6294-6302 (1992).
63. R. Großkloß, P. Kersten, W. Demtroder, "Sensitive amplitude- and phase-modulated absorption-spectroscopy with a continuously tunable diode laser," *Appl. Phys. B* **58**, 137-142 (1994)
64. P. Kluczynski, O. Axner, "Theoretical description based on Fourier analysis of wavelength-modulation spectroscopy in terms of analytical and background signals," *Appl. Opt.* **38**, 5803-5815 (1999).
65. S. Schilt, L. Thevenaz, P. Robert, "Wavelength modulation spectroscopy: combined frequency and intensity laser modulation," *Appl. Opt.* **42**, 6728-6738 (2003).
66. A. Lucchesini, M. De Rosa, D. Pelliccia, A. Ciucci, C. Gabanini, S. Gozzini, "Diode laser spectroscopy of overtone bands of acetylene," *Appl. Phys. B* **63**, 277-283 (1996).
67. W. Johnstone, A. J. McGettrick, K. Duffin, A. Cheung, G. Stewart, "Tunable diode laser spectroscopy for industrial process applications: system characterization in conventional and new approaches," *IEEE Sensors J.* **8** (7), 1079-1088 (2008).

## Chapter 2: Review of Tunable Diode Laser Spectroscopy

68. A. J. McGettrick, W. Johnstone, R. Cunningham, J. D. Black, "Tunable diode laser spectroscopy with wavelength modulation: calibration-free measurements of gas compositions at elevated temperatures and varying pressure," *IEEE J. Lightwav. Technol.*, **27** (15), 3150-3161 (2009).
69. A. J. McGettrick, "Wavelength modulation spectroscopy with tunable diode lasers: A calibration-free approach to the recovery of absolute gas absorption line shapes," Ph.D. Thesis, Dept. of EEE, Univ. Strathclyde, Glasgow, Scotland, 2007.

# *Chapter 3*

---

## *Analytical Methodologies – Fundamentals of Molecular Spectroscopy*

---

### **3.1 Introduction**

This chapter presents a discussion of those theoretical aspects of basic molecular spectroscopy that are relevant to the experimental work presented in this thesis. The chapter begins with a discussion of the origin of gas absorption spectra and moves on to the topic of vibrational and rotational energy levels of a diatomic molecule that is assumed to execute simple harmonic oscillations. The effects of anharmonicity are introduced next. The different modes of vibration of polyatomic molecules are then discussed since this is relevant to methane that is used as the experimental gas in this

### Chapter 3: Analytical Methodologies – Fundamentals of Molecular Spectroscopy

thesis. The width of absorption lines and the various broadening mechanisms that influence the width are then briefly discussed. This is followed by a discussion of the factors that determine the intensity of spectral lines. The practical aspect of extracting information about the concentration and pressure of a gas from a single recovered absorption line is explained. This helps to bring out more clearly the relation between gas parameters and the various parameters of the harmonic/derivative signals such as peak height. Signal slope through line-centre and separation of zero crossings. The chapter ends with an explanation of the method used to simulate the gas absorption lines using the HITRAN spectroscopic database. The theoretical discussion serves only to give the reader a fundamental background of molecular spectroscopy and is in no way comprehensive. For a more detailed reviews of the topics highlighted in this chapter the reader is directed towards standard texts on molecular spectroscopy [1-3].

## 3.2 Origin of spectral absorption lines

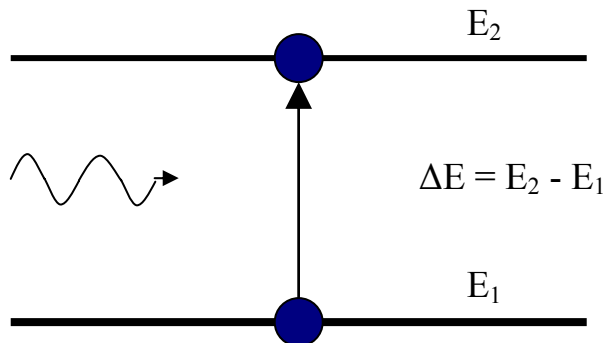
The absorption or emission of electromagnetic radiation by a molecule is a result of a change in its internal energy. The most familiar energy transition mechanism is the excitation of electrons between allowed energy levels in an atom. However molecules can also store energy in vibrations and rotations. Like the electronic transitions, vibrational and rotational transitions occur between discrete, allowed levels. The allowed energy levels and the selection rules that permit or forbid transitions between them are given by rigorous quantum-mechanical calculations that are beyond the scope of this thesis and will therefore be assumed throughout this chapter.

Figure 3.1 shows a representative energy transition induced by the absorption of electromagnetic energy. The quantum of electromagnetic energy required to make the jump from one energy level to another is given by,

$$\Delta E = h\nu = \frac{hc}{\lambda} \quad (3.1)$$

### Chapter 3: Analytical Methodologies – Fundamentals of Molecular Spectroscopy

Where,  $h$  is Planck's constant ( $6.63 \times 10^{-34}$  Js) and  $\nu$  and  $\lambda$  are the frequency and wavelength of the electromagnetic radiation respectively.



*Figure 3.1: Absorption of electromagnetic radiation*

The absorption of electromagnetic energy by an atom or molecule is a very selective process determined by the molecular arrangement and is a function of the frequency/wavelength of the electromagnetic radiation. Therefore, if a single frequency source, such as a DFB laser operating at frequency  $\nu$  as defined by Eq. 3.1, is directed through a gas consisting of this molecule only specific frequencies will be absorbed and the molecule will make the transition from the level  $E_1$  to  $E_2$ . If the laser's frequency is scanned over a wide range it will be observed that the transmitted intensity decreases over a very narrow range of frequencies as shown in Fig. 3.2. This represents one of several possible absorption lines of the atom or molecule as the case may be.

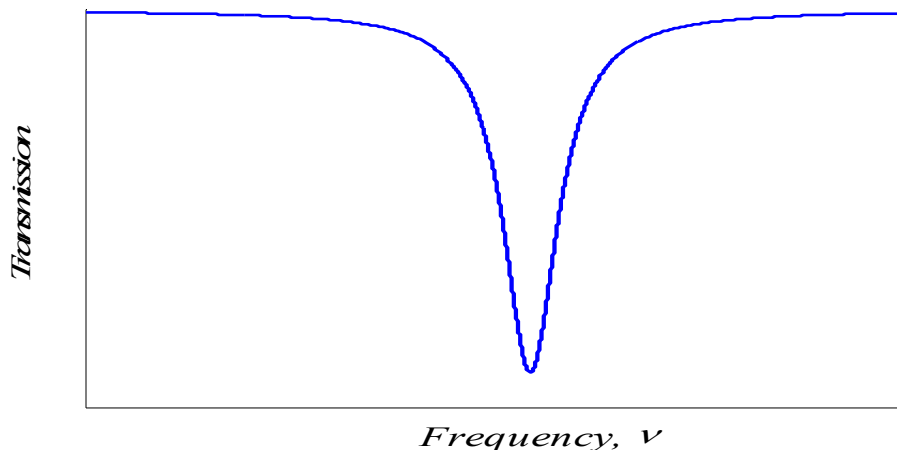


*Figure 3.2: Absorption of laser intensity at as function of laser frequency  $\nu$*

### Chapter 3: Analytical Methodologies – Fundamentals of Molecular Spectroscopy

This type of a measurement is known as a spectroscopic measurement. Since molecules have specific structures, it is possible to identify the whole molecule or even specific molecular bonds within it by such spectroscopic measurement of the absorption/transmission spectrum.

There are general regions in the electromagnetic spectrum into which molecular energy transitions can be categorized. At radio wavelengths (from approximately 1m upwards) the energy change arises from the reversal of spin of nucleus or of the electrons surrounding the nucleus. In the microwave region (approximately  $10^{-3}$  to 1m) energy is stored in the form of molecular rotations. Rotation of a molecule gives rise to a periodic change in the dipole moment. The interaction of an electromagnetic field with this changing dipole moment gives rise to the absorption or emission of energy. The region of greatest interest is the infra-red (IR) region where energy is stored in the form of molecular vibrations. Again, it is the interaction of the resultant changing dipole moment with electromagnetic radiation which leads to observable spectra. The infra-red wavelengths extend from  $10^{-6}$  to  $10^{-4}$  m. Transitions at shorter wavelengths also occur and these include visible, ultra-violet, X-rays and  $\gamma$ -rays involve transitions that require much higher energy.

## 3.3 Vibrational Energy Levels

When two atoms combine to form a molecule, they do so because the net energy of the molecule is lower than the system of separate non-interacting atoms. Although the energy of the system is minimized this does not mean that the molecule is at rest. Molecular energy states are produced as a result of two distinct mechanisms. The molecule can rotate as a whole about an axis of rotation, and the atoms that form a molecule are also able to vibrate about their mean positions. These two degrees of freedom give rise to rotational and vibrational spectra.

The following observations apply to the various kinds of vibrational and rotational motions that a molecule can undergo:

### Chapter 3: Analytical Methodologies – Fundamentals of Molecular Spectroscopy

1. Rotational states are separated by quite small energy intervals ( $10^{-3}$  eV is typical). The spectra that arise from transitions between these states are therefore in the microwave region of the electromagnetic spectrum with wavelengths of 0.1mm to 1cm.
2. Vibrational states have larger separation (1eV) and vibrational spectra are in the infrared region with wavelengths of  $1\mu\text{m}$  to 0.1mm. This region referred to as the near infrared (NIR), mid-infrared (MIR) and far-infrared (far IR) is most relevant to gas sensing applications.
3. Molecular electronic states have the highest energy with the typical spectra in the visible and ultra-violet region of the spectrum with the typical separation of the outer electrons of several eV.

When suitably excited, the molecule may be considered to vibrate at a certain frequency like an elastic spring. Figure 3.3 shows the stretching and contraction of a polar molecule. The vibration of the molecule gives rise to an oscillating dipole moment. A dipole moment exists because there is a charge separation between the two atoms; the larger atom in this case has a slightly negative charge and the smaller atom has a slightly positive charge. The dipole moment is at a maximum when the bond is maximally stretched and is at a minimum when the bond is in the equilibrium position.

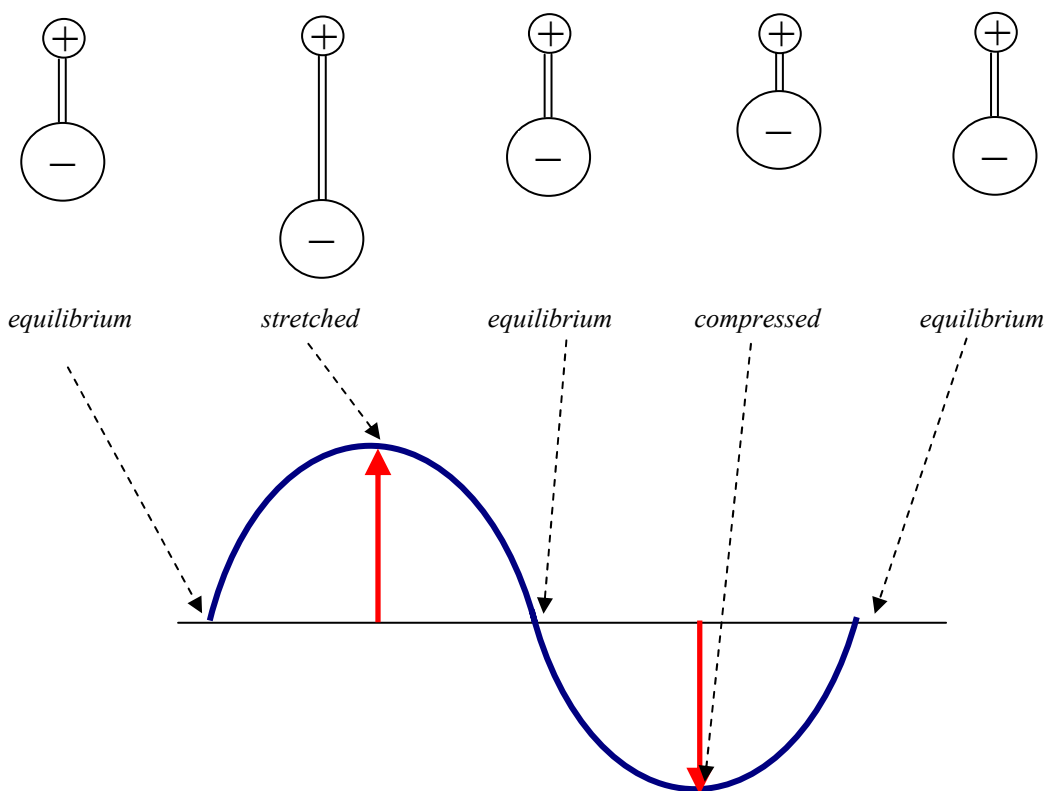


*Figure 3.3: (a) stretching and compression of the diatomic molecule HCl (b) Resulting change in dipole moment*

### 3.3.1 Simple Harmonic Oscillation of a diatomic molecule

A molecule may have different modes of vibration. For the present discussion diatomic molecules are considered although the main ideas of the discussion are valid for more complex molecules as well. The simplest vibrating diatomic molecule can be considered to be a simple harmonic oscillator consisting of the two atoms connected by an elastic spring. The two atoms oscillate relative to each other in accordance with Hooke's law. This is to say that the amplitude of oscillation is sufficiently small so that the restoring force is proportional to the inter-nuclear distance  $r$ , between the molecules. The equation describing the energy/bond length relationship is thus given by:

$$E = \frac{1}{2}k(r - r_{eq})^2 \quad (3.2)$$

### Chapter 3: Analytical Methodologies – Fundamentals of Molecular Spectroscopy

When  $k$  is the force constant of the spring,  $r$  is the bond length and  $r_{eq}$  is the bond length at which the bond is in equilibrium.

Under this approximation the potential energy of the system is a parabolic function of the inter-nuclear distance. This is depicted by the representative Fig. 3.4. The frequency of oscillation of such an oscillator is given by the well-known relation,

$$\nu_0 = \frac{1}{2\pi} \sqrt{\frac{k}{m'}} \quad (3.3)$$

Where  $\nu_0$  is the oscillation frequency and  $m'$  is the reduced mass of the system given by

$$m' = \frac{m_1 m_2}{m_1 + m_2}.$$

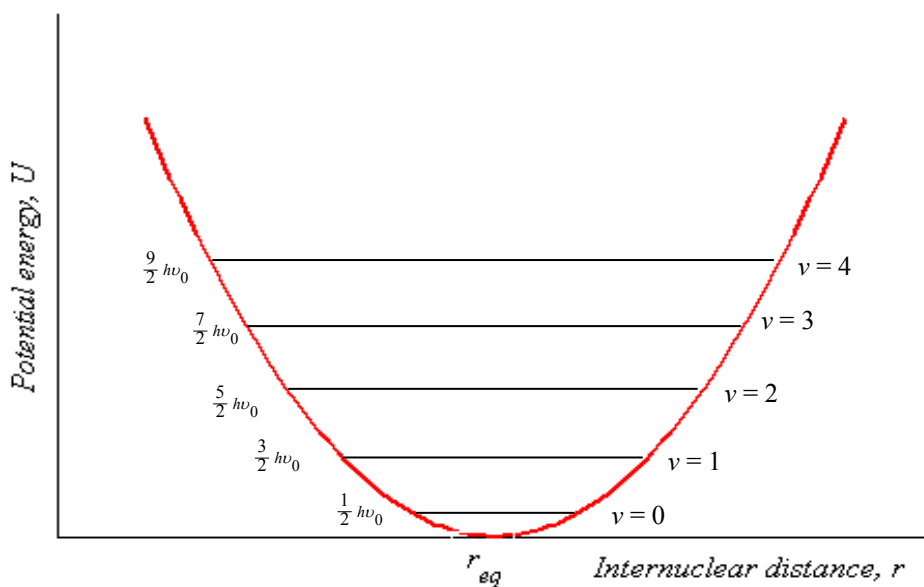


Figure 3.4: Variation of potential energy of a simple harmonic oscillator

When the harmonic oscillator problem is solved quantum mechanically [3] the energy of the oscillator turns out to be restricted to the values,

$$E_v = (v + \frac{1}{2})h\nu_0 \quad (3.4)$$

### Chapter 3: Analytical Methodologies – Fundamentals of Molecular Spectroscopy

where  $\nu$  is the vibrational quantum number, with the quantized values of  $\nu$  given by  $\nu = 0, 1, 2, 3, \dots$ . Consequently the vibrational energy levels are also quantized.

It is important to note that the lowest vibrational state ( $\nu = 0$ ) has a zero-point energy of  $\frac{1}{2}h\nu_0$  and not the classical value of zero. This is a consequence of Heisenberg's Uncertainty principle according to which the product of the momentum uncertainty and the position uncertainty must be greater than or equal to the reduced Planck's constant. Mathematically this is written as  $\Delta p \cdot \Delta x \geq \frac{h}{2\pi}$ . Therefore if the molecule is at rest its position uncertainty is zero which implies that the momentum must be infinitely uncertain which contradicts the earlier assumption that the molecule is at rest. The vibrational energy levels of a harmonic oscillator are therefore seen to be quantized and equally spaced. However the spacing does not remain constant for higher vibrational states because for vibrations of larger amplitudes the parabolic approximation becomes less and less valid.

The possible transitions that the molecule can make between the different vibrational levels is given by the Selection rule that states that only those transitions are permitted for which,

$$\Delta\nu = \pm 1 \quad (3.5)$$

It should be borne in mind that the spectra corresponding to vibrational energy changes will be observable only if the vibration produces a net dipole moment of the molecule. Therefore homonuclear molecules will not have observable spectra.

#### 3.3.2 The Anharmonic Oscillator

The behaviour of real molecules deviates from that of the simple harmonic oscillator model because real molecular bonds do not obey Hooke's law. For large extensions and compressions of the bond (greater than 10 percent of the bond length) the vibration is no longer perfectly harmonic and the expression for the potential energy is much more complicated. Figure 3.5 shows the typical energy distribution of a diatomic molecule

### Chapter 3: Analytical Methodologies – Fundamentals of Molecular Spectroscopy

experiencing anharmonic oscillation. It should be noted that large extensions of the bond results in the bond being broken and the molecule dissociating. It is also clear that the energy spacing is no longer equal and reduces as the energy increases. The potential energy curve of a diatomic molecule is given by the purely empirical Morse function and is given by,

$$E = D_{eq} [1 - \exp\{-a(r - r_{eq})\}]^2 \quad (3.6)$$

Where,  $a$  is a constant for a molecule and  $D_{eq}$  is the dissociation energy.

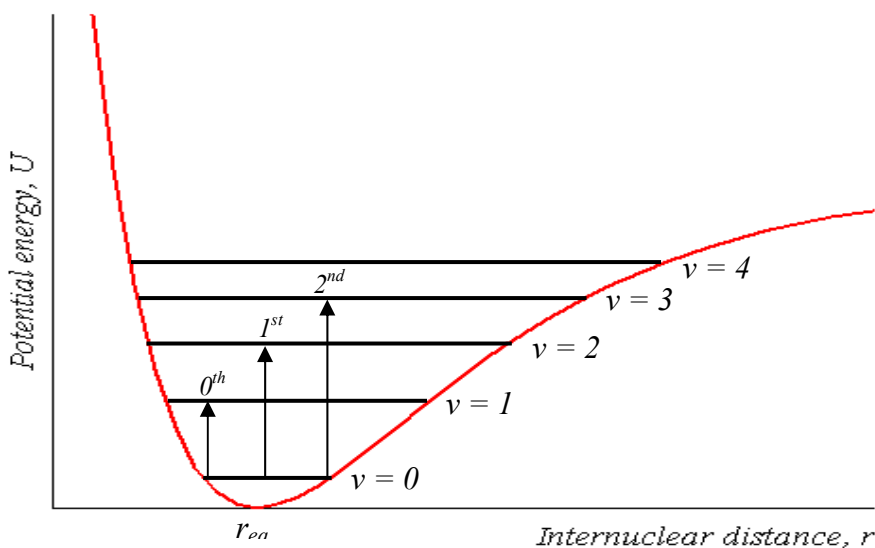


Figure 3.5: Realistic distribution of energies for a diatomic molecule

When this expression is used to solve the Schrodinger equation the allowed quantized energy levels are given by,

$$E = \left\{ 1 - \chi_e \left( \nu + \frac{1}{2} \right) \right\} \left( \nu + \frac{1}{2} \right) h\omega_e \quad (3.7)$$

Where  $\omega_e$  is the new oscillation frequency given by  $\omega_e = \omega[1 - \chi_e(\nu + \frac{1}{2})]$  and  $\chi_e$  is the anharmonicity constant. It should be noted that the anharmonic oscillator behaves like

### Chapter 3: Analytical Methodologies – Fundamentals of Molecular Spectroscopy

the harmonic oscillator but has an oscillation frequency that decreases steadily with increasing  $\nu$ .

The Selection Rules are also modified by the presence of the anharmonicity. In this case the selection rules allow energy transitions for  $\Delta\nu$  greater than  $\pm 1$ . Specifically the selection rules for an anharmonic oscillator are given by,

$$\Delta\nu = \pm 1, \pm 2, \pm 3, \dots \quad (3.8)$$

Although the anharmonicity allows for larger jumps in comparison to the harmonic oscillator the probability of these jumps reduce rapidly and normally only the lines corresponding to  $\Delta\nu = \pm 1, \pm 2$  and  $\pm 3$  at the most have observable intensity. It is straightforward to show that in accordance to the Boltzmann distribution for a vibrational level spacing of  $10\text{cm}^{-1}$  and at room temperature (300K), the ratio of the population of the first excited state to that of the ground state given by,

$\frac{N_{\nu=1}}{N_{\nu=0}} = \exp\left(-\frac{\Delta E}{kT}\right)$  is only about 0.01. This means that for all practical purposes

transitions originating from the  $\nu = 1$  state may be ignored since the population of that level is negligible in comparison to that of the ground state. Therefore it is correct to a very good approximation, to consider the transitions,  $\nu = 0 \rightarrow \nu = 1$ ,  $\nu = 0 \rightarrow \nu = 2$  and  $\nu = 0 \rightarrow \nu = 3$ . These transitions correspond to the so-called *fundamental* absorption line, the *first overtone* and the *second overtone* respectively. The first overtone also has appreciable intensity but for most practical purposes the second overtone is much smaller than the other two. The three transitions are shown in Fig. 3.5.

## 3.4 Rotational Energy Levels

In addition to vibrations the diatomic molecule can undergo rotation as well. The rotation of such a two-body system produces angular momentum  $L$ , given by,

$$L = \frac{h}{2\pi} \sqrt{J(J+1)} \quad (3.9)$$

### Chapter 3: Analytical Methodologies – Fundamentals of Molecular Spectroscopy

Angular momentum is always quantized and the rotational quantum number,  $J$ , can take on the values  $J = 0, 1, 2, 3, \dots$ . The energy levels of the rotating molecule are given by,

$$E_J = \frac{h^2}{8\pi^2 I} J(J+1) \quad (3.10)$$

where,  $I$  is the moment of inertia of the two-body system. Rotational spectra arise from transition between rotational energy levels. Only those molecules that have a permanent electric dipole moment can absorb or emit electromagnetic energy and undergo such *radiative* transitions. Nonpolar molecules and symmetric polyatomic molecules do not exhibit pure rotational spectra. It should be noted however that such molecules can undergo nonradiative rotational transitions during collisions.

Even in molecules with permanent electric dipole moments, not all transitions between rotational energy levels involve radiation. The Selection Rule that must be obeyed for radiative transitions between rotational levels is,

$$\Delta J = \pm 1 \quad (3.11)$$

The frequencies of the rotational transitions are easily calculated to be,

$$\nu_{J \rightarrow J+1} = \frac{h}{4\pi^2 I} (J+1) \quad (3.12)$$

It is worth reiterating that the rotational energies (0.1eV) are much smaller than the vibrational energies (1eV).

## 3.5 Vibration-Rotation Spectra

Although the two types of motion of molecules have been considered separately so far, in reality a molecule undergoes simultaneous vibration and rotation that gives rise to more complicated spectra. Pure vibrational spectra are observed only in liquids where the interactions of the closely spaced molecules inhibit rotation. In gases or vapours

### Chapter 3: Analytical Methodologies – Fundamentals of Molecular Spectroscopy

however the freely moving molecules are always rotating since the excitation energies involved in rotations are very small. This is the case regardless of the vibrational state of the molecules. The spectra of such molecules show densely packed spectral lines that result from transitions from rotational states of one vibrational level to those of another vibrational level.

To a first approximation the rotation and vibration can be considered to take place independent of each other, since the energies of the two motions are very different. This is known as the Born-Oppenheimer approximation. In this regime the total energy of the molecule can be considered to be the sum of the energies due to the two motions. This is to say that,

$$E_{total} = E_{rot} + E_{vib} \quad (3.13)$$

If the effect of anharmonicity is ignored, the energy of the diatomic molecule may be written as,

$$E_{v,J} = (v + \frac{1}{2})h\nu_0 + J(J+1)\frac{h^2}{8\pi^2 I} \quad (3.14)$$

The vibration-rotation lines for transitions between the rotational levels of the ground vibrational states and those of the first excited vibrational state for a diatomic molecule are shown in Fig 3.6. For these transitions it is convention to denote transitions from  $J \rightarrow J-1$  as the P-branch, and the transitions from  $J \rightarrow J+1$  as the R-branch. The transition for which  $\Delta J = 0$  is forbidden by the Selection rule and therefore there are no lines corresponding to such transitions that would otherwise have formed the Q-branch.

The frequencies corresponding to the P-branch are given by,

$$P\text{-branch} \quad \nu_p = \nu_0 - J\frac{h}{4\pi^2 I} \quad (3.15)$$

and for the R-branch the frequencies are given by,

$$R\text{-branch} \quad \nu_p = \nu_0 + J \frac{h}{4\pi^2 I} \quad (3.16)$$

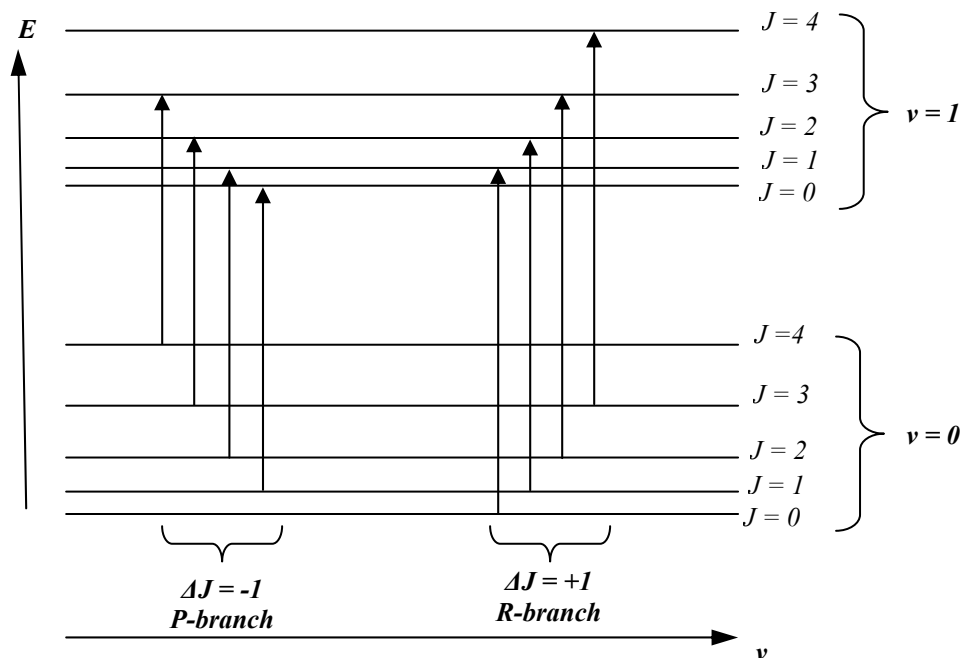


Figure 3.6: Vibration-rotation lines for a diatomic molecule

The Selection Rules for these motions is the combination of the rules for each of the two motions and are given by,

$$\Delta v = \pm 1, \pm 2, \pm 3 \dots \quad \text{and} \quad \Delta J = \pm 1 \quad (3.17)$$

### 3.6 Influence of rotation on the spectra of polyatomic molecules

So far the discussion assumes that vibrations and rotations are independent of each other and do not influence each other. This is justified to some extent because a molecule executes a very large number of vibrations in the time taken for one rotation. Therefore during one rotation the bond length and the moment of inertia change continuously. The process is much more complicated than this and the interested reader is referred to

### Chapter 3: Analytical Methodologies – Fundamentals of Molecular Spectroscopy

specialized texts [1] for a comprehensive discussion. A brief qualitative discussion is presented here for the sake of completeness. This discussion introduces the various modes of vibration of polyatomic molecules. This discussion is relevant because the methane gas that has been used in all experiments is a polyatomic molecule. Through this discussion the reason behind the appearance of the Q-branch in molecular spectra is also explained.

#### 3.6.1 Vibrations of Polyatomic Molecules

A polyatomic molecule with  $N$  atoms has  $3N-5$  fundamental vibrations if it is linear, and  $3N-6$  fundamental vibrations if it is non-linear. The  $N$ -atomic molecule obviously has  $N-1$  bonds, which means there can only be  $N-1$  stretching vibrations, leaving  $2N-4$  bending vibrations in linear molecules and  $2N-5$  bending vibrations in non-linear molecules. To illustrate, the fundamental modes of vibration it is useful to consider the example of the water ( $H_2O$ ) molecule which is a non-linear triatomic molecule. Figure 3.7 shows the three fundamental vibrations.

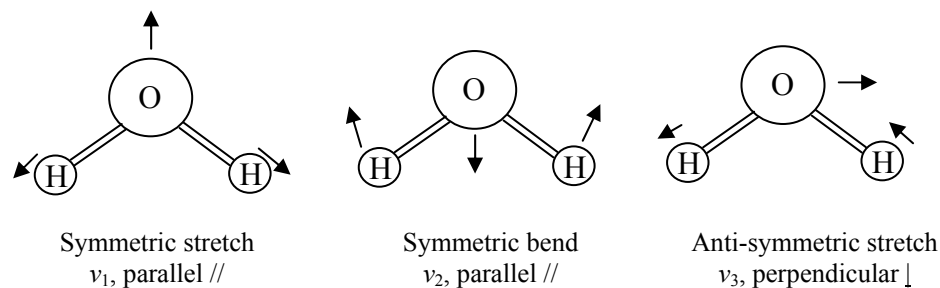


*Figure 3.7: The fundamental modes of vibration for the  $H_2O$  molecule*

For the vibration to be infrared active there must be a dipole change during the vibration. The dipole change can occur either parallel to the line of symmetry or perpendicular to it. This distinction is important in understanding the influence of rotation on the spectrum.

Methane ( $CH_4$ ) was chosen as the experimental gas for this research work because it is of great importance in various industries and occurs abundantly in nature. The fundamental vibrations of the  $CH_4$  molecule are shown in Fig. 3.8.  $CH_4$  is a non-linear,

### Chapter 3: Analytical Methodologies – Fundamentals of Molecular Spectroscopy

tetrahedral spherical-top molecule and thus was  $3(5) - 6 = 9$  vibrational modes, four of which are stretching vibrations and five are bending vibrations.

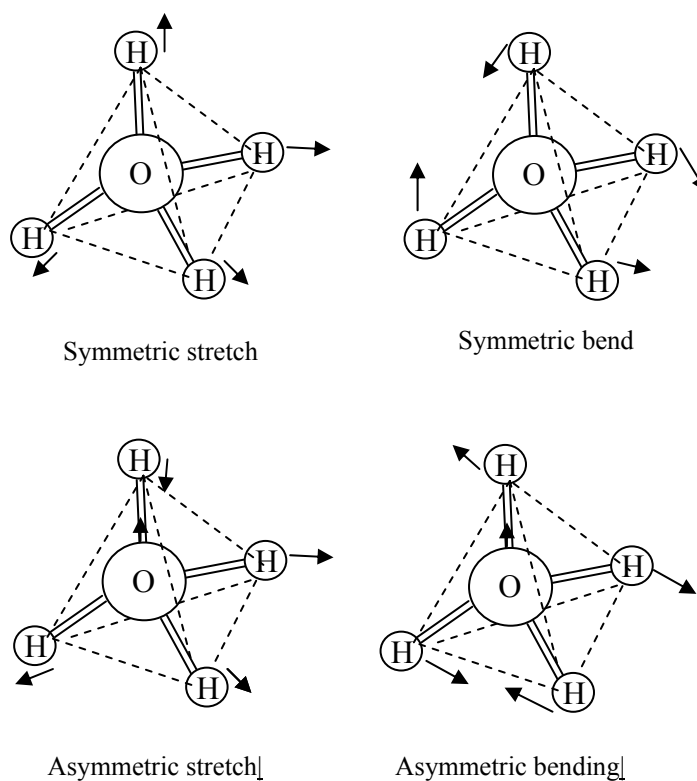


*Figure 3.8: Fundamental vibrations of CH<sub>4</sub> molecule*

CH<sub>4</sub> does not possess a permanent dipole moment, thus only the asymmetric vibrations ( $\nu_3$  and  $\nu_4$ ) are infra-red active.

### 3.6.2 Influence of rotation on the spectrum

The selection rules obtained previously stipulate that,

$$\Delta v = \pm 1, \pm 2, \pm 3 \dots \quad \Delta J = \pm 1 \quad \text{but } \Delta J \neq 0 \quad (3.18)$$

This resulted in a spectrum consisting of the P-branch and the R-branch only with approximately equally spaced lines about a central minimum that is designated as the band centre. It turns out that when the influence of the rotation on the vibration is also considered, the selection rules for the rotational transitions are modified according to the type of vibration (parallel or perpendicular) that the molecule undergoes. To be specific, for linear polyatomic molecules with parallel vibrations, there is no change in the selection rules. The only difference will be that the moment of inertia of the molecule will be larger and therefore the spacing of the lines in the P-branch and the R-branch will be smaller. For perpendicular vibrations, however, an important difference shows up. Considering simple harmonic motion of the molecule, the Selection rules are modified to,

$$\Delta v = \pm 1 \quad \Delta J = 0, \pm 1 \quad (3.19)$$

The Selection rules imply that, for the first time, a vibrational change can take place with *no simultaneous rotational transition*, since the  $\Delta J = 0$  transition is permitted in this case. Figure 3.9 below shows the same energy levels and transitions as in Fig 3.7 but with the addition of the  $\Delta J = 0$  transitions. These transitions form a central, densely-spaced spectral region known as the Q-branch.

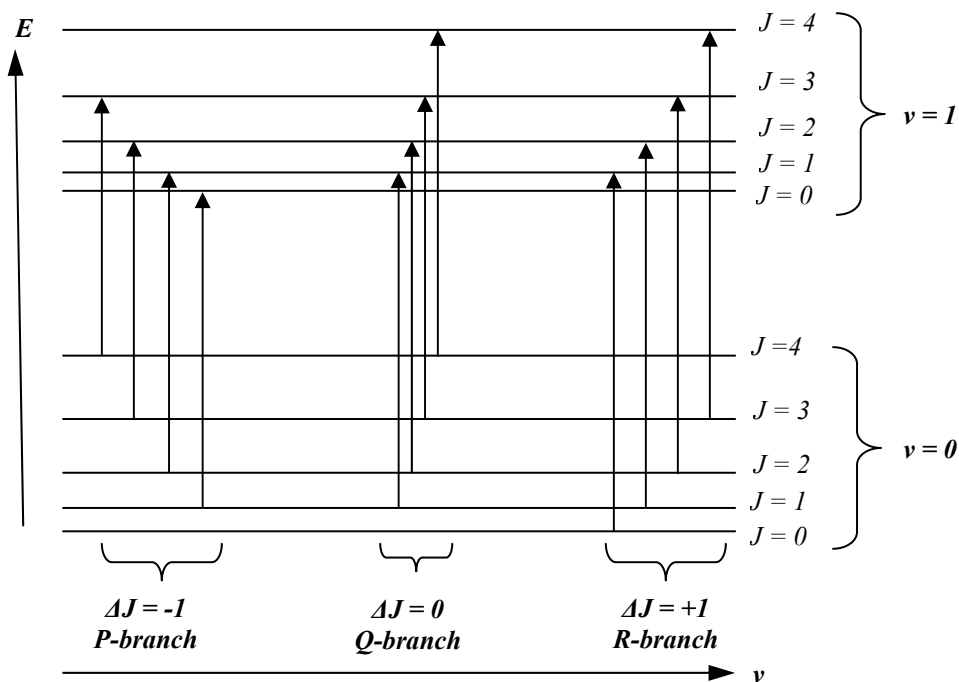
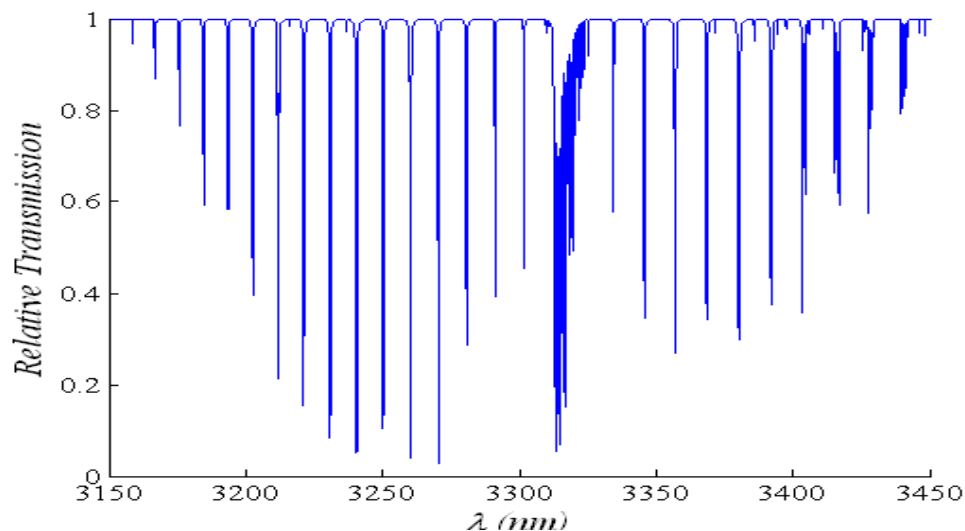


Figure 3.9: Vibration-rotation lines for a diatomic molecule showing the P-, Q-, and R-branches.

For a spherical-top molecule the following rotational transitions are allowed:  $\Delta J = 0, \pm 1$  and these give the energy level distribution shown in figure 3.9 below. Note here the labelling convention for the rotational energy transition bands;  $\Delta J = -1, 0, +1$ , denoted P, Q and R respectively.

As a specific example the vibration-rotational lines in the mid-infrared and near infrared region for methane are shown in Fig. 3.10 and Fig. 3.11. The P, Q and R branches for the fundamental, mid infra-red absorption band of methane, around  $3.3 \mu\text{m}$  ( $\sim 3030 \text{ cm}^{-1}$ ) and its accompanying near infrared, 1<sup>st</sup> overtone absorption band, around  $1650 \text{ nm}$  ( $\sim 6060 \text{ cm}^{-1}$ ) are shown. Note that the since the  $x$ -axis is in terms of wavelength instead of frequency, the positions of the P-branch and R-branch are the opposite of their positions in Fig. 3.9. The relative transmission was simulated using the HITRAN 2004 database for a cell length of  $5.9 \text{ cm}$  and for a 1% methane mixture in nitrogen at a pressure of  $1 \text{ atm}$  and temperature of  $22^\circ\text{C}$ .



*Figure 3.10: Simulated values of relative transmission for mid-infrared vibration-rotation lines for a sample of 1% methane at 22°C and 1 atm pressure for a cell length of 5.9 cm.*

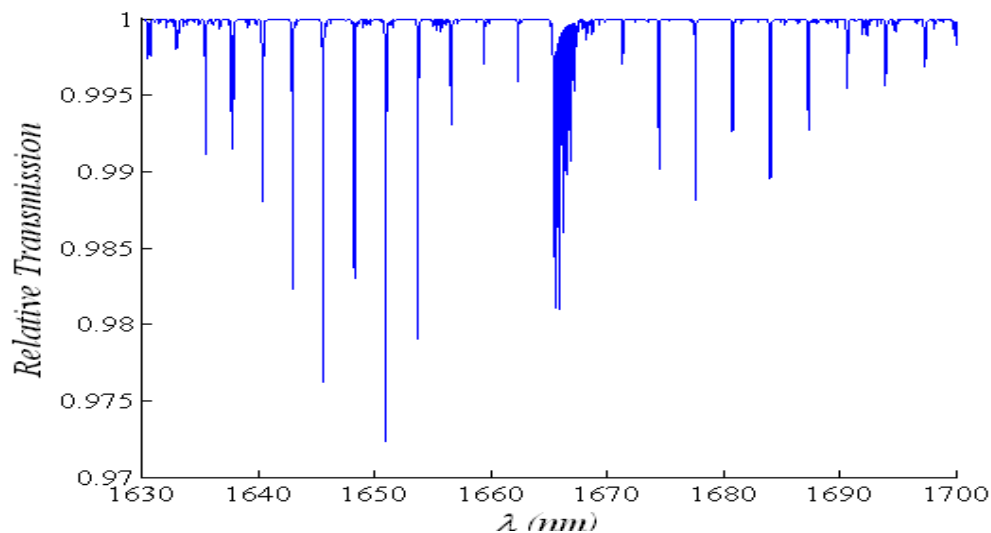


*Figure 3.11: Simulated values of relative transmission for near-infrared vibration-rotation lines for a sample of 1% methane at 22°C and 1 atm pressure for a cell length of 5.9 cm.*

It is important to compare the values of the relative transmission for the two cases. This clearly shows that the stronger fundamental mid-infrared transitions produce much larger relative changes in the transmission of the incident light. The detection sensitivity

is therefore higher if the fundamental transition of a molecule can be probed. This obviously requires an appropriate mid-infrared source and a detector.

## **3.7 Width of Spectral Lines**

Spectral lines in discrete absorption or emission spectra are not infinitely sharp but possess a finite width and shape dictated by the physical conditions of the molecule. For a molecule that makes a transition between an upper energy level  $E_i$  and a lower energy level  $E_k$  the absorbed or emitted intensity centred around the frequency  $\nu_0 = (E_i - E_k)/h$  is not strictly monochromatic. The function  $I(\nu)$  that denotes the spectral distribution of energy is known as the line profile. The line width  $\delta\nu = |\nu_2 - \nu_1|$  is defined as the difference between the two frequencies  $\nu_2$  and  $\nu_1$  at which the value of  $I(\nu)$  is down to half its maximum value. This parameter is also known as the full-width at half-maximum (FWHM) of the line or often simply the half-width. The half-width is denoted in terms of the angular frequency  $\omega$ , as  $\delta\omega = 2\pi\delta\nu$ , or in terms of the wavelength  $\lambda$  with  $\delta\lambda = |\lambda_2 - \lambda_1|$ . Using the relation  $\lambda = c/\nu$ , it follows that [2],

$$\delta\lambda = -\frac{c}{\nu^2} \delta\nu \quad (3.20)$$

Three main effects that contribute to the broadening of the width of spectral lines are, natural broadening, Doppler broadening and collision/pressure broadening. Each of these is briefly discussed in the next three subsections.

### ***3.7.1 Natural line width***

The natural line width is a consequence of the finite lifetime of the excited state due to spontaneous emission. An atom in an excited state can spontaneously emit its excitation energy as a photon. The classical viewpoint is to consider the emitted photons as wave trains that have the same frequency but are uncorrelated in phase. The addition of several such wave trains of different phases gives rise to a finite non-zero spectral width that is purely determined by the finite lifetime of the atom. The quantum-mechanical viewpoint explains this phenomenon in terms of the uncertainty of energy of the excited

### Chapter 3: Analytical Methodologies – Fundamentals of Molecular Spectroscopy

atom. According to the Uncertainty principle given by,  $\Delta E \Delta t \geq \frac{h}{2\pi}$ , the energy of the excited atom can be defined with high precision only for an infinitesimal duration. However the finite lifetimes of excited atom imply that there must be some uncertainty of energy levels. This uncertainty of energy means that the frequency of photons emitted during the transition must also have a corresponding uncertainty. This fundamental effect is responsible for the finite, non-zero width of spectral lines and since it affects all atoms in the same way this process is a homogeneous process.

If the excited atom or molecule is considered to be a damped harmonic oscillator, time-dependent oscillation can be mathematically written as,

$$x(t) = x_0 e^{-\frac{\gamma}{2}t} \cos \omega_0 t \quad (3.21)$$

where  $x(t)$  is the time-dependent position,  $x_0$  is the amplitude of oscillation,  $\omega_0$  is the angular frequency of oscillation and  $\gamma$  is the coefficient of damping. When the frequency-domain representation of the time-domain oscillation is obtained by Fourier transform the frequency distribution is given by a Lorentzian function given by,

$$L = \frac{\gamma/2\pi}{(\omega - \omega_0)^2 + (\gamma/2)^2} \quad (3.22)$$

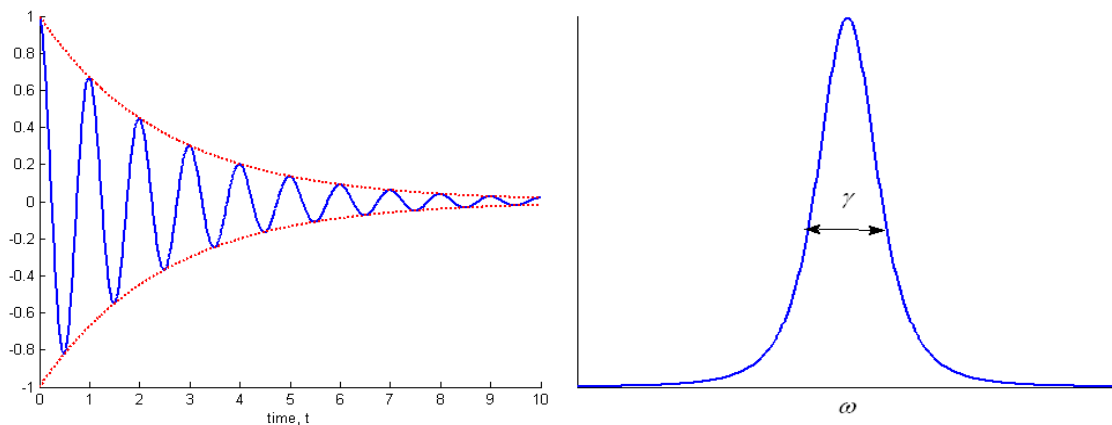


**Figure 3.12: Damped oscillation of a molecule and natural line width of spectral line**

### 3.7.2 Doppler Broadening

Doppler broadening is the broadening of spectral lines due to the Doppler effect caused by a distribution of velocities of the atoms or molecules particularly evident at low gas pressures. The Doppler effect is the apparent shift in the frequency of radiation that is emitted or absorbed by a body that is in motion. In terms of spectroscopy, the frequency of the radiation absorbed during a transition differs according to the direction and velocity of motion of the gas molecule, relative to the source of radiation. When the molecule is moving towards the source of radiation the source frequency appears higher (blue shifted). Consequently the frequency that is absorbed is lower than the frequency that would have been absorbed had the molecule been at rest. As the molecule moves away from the electromagnetic radiation, the frequency appears lower (red shifted), giving rise to absorption at a higher frequency. The amount of red or blue shift depends on the velocity of the molecules. Since the molecular motions are random both positive and negative frequency shifts are possible and a broad line shape can result.

At thermal equilibrium the molecules of a gas follow a Maxwellian velocity distribution. It can be shown that the intensity profile of a Doppler-broadened spectral line is given by [2],

$$I(\omega) = I_0 \exp \left[ - \left( \frac{c(\omega - \omega_0)}{\omega_0 v_p} \right)^2 \right] \quad (3.23)$$

Where  $v_p = (2kT/m)^{1/2}$  is the most probable velocity,  $T$  is the temperature,  $m$  is the mass of a molecule. This is a Gaussian profile with a FWHM given by,

$$\delta\omega_D = 2\sqrt{\ln 2} \frac{\omega_0 v_p}{c} = \frac{\omega_0}{c} \sqrt{8kT \ln 2 / m} \quad (3.24)$$

which is called the Doppler width. It is worth noting that the Doppler width is a function of the absolute temperature of the gas and provides a method to measure temperature from the recovered absorption line. The Doppler broadening effect is an inhomogeneous process since the molecules in a gas have different velocities and therefore undergo different Doppler shifts.

### 3.7.3 Collision Broadening

Collision broadening of a spectral line is a result of the constant and inevitable thermal motion of atoms and molecules in gaseous and liquid phases. A collision is defined as the mutual interaction of two collision partners at distances  $R \leq R_c$  and the radius  $R_c$  is known as the collision radius. Collisions between molecules lead to the rearrangement of energy levels  $E_i$  and  $E_k$  of the colliding molecules. This shift of energy levels depends on the electronic configuration of the two collision partners and on the intermolecular distance. The shifts in the energy levels are in general different for the two levels and may be positive or negative. The shift is positive if the interaction is repulsive, and negative if it is attractive. The type of collision in which there is no non-radiative transfer of internal energy of the collision partners is known as an elastic collision. It should be noted that the collisions take place in a very short but finite time given by  $\tau_c \approx R_c/v$  where  $v$  is the relative velocity.

If the molecule is considered to be a damped harmonic oscillator, an elastic collision does not change the amplitude of oscillation but disrupts the phase. Such collisions are therefore also referred to as phase-perturbing collisions. The perturbation of the phase manifests itself as another source of spectral broadening. This mechanism of broadening is also known as pressure broadening since it dominates at high pressure ( $\sim 1$  atm). This is intuitive since high pressure implies that the molecules are packed closer together and the probability of molecules colliding with each other is also greater. In general, molecular interactions are more likely to take place in liquids than in gases simply because the molecules are less free to move about. Therefore the effect of collisional broadening is less severe for gases and their spectra are much sharper than those of the corresponding liquid. Collisional broadening is a homogenous mechanism and the line shape of a collision-broadened spectral line is a Lorentzian profile.

### 3.7.4 The Voigt Profile

In spectroscopy the Voigt profile characterizes a spectral line profile that is broadened by two types of mechanism one of which on its own would produce a Lorentzian profile, while the other would produce a Gaussian line profile. Mathematically, this is equivalent to saying that the Voigt profile is a convolution of a Lorentzian profile and a Gaussian profile. It is generally accepted that at pressure greater than 200 mbar, collision broadening begins to dominate; therefore, a Lorentzian profile becomes increasingly more accurate with increasing pressure. However, this work was carried out at atmospheric pressures (~1bar) at which the absorption lines are best represented by a Voigt profile in the modelling algorithms (discussed in greater detail in Sec. 3.10). A Voigt profile is essentially a convolution of the Gaussian and Lorentzian profiles and has dampening coefficients in order to determine the influence each has on the overall profile.

## 3.8 Intensity of Spectral Lines

The intensity of a spectral line corresponding to a particular transition is determined by the probability of a molecule to undergo that particular transition and the populations of the energy levels involved. These are briefly discussed in the following sections.

### 3.8.1 Transition Probability

The transition probability represents the likelihood of a molecule making a transition from one energy level to another. This was touched on previously when discussing the selection rules for the rotational ( $\Delta J$ ) and vibrational ( $\Delta v$ ) energy transitions. The probabilistic interpretation of the selection rules is that some transitions are much more likely to take place than others. The spectral lines corresponding to the transitions that are more likely to take place are therefore expected to be much stronger than those transitions that are forbidden. For example, when discussing the methane molecule it was mentioned that the selection rule for the rotational energy transitions was  $\Delta J = 0, \pm$

### Chapter 3: Analytical Methodologies – Fundamentals of Molecular Spectroscopy

1; meaning transitions outside of this have zero intensity and consequently have no observable spectra.

#### 3.8.2 Population of States

The intensity of a spectral line corresponding to a transition from one level to another level is directly proportional to the populations of the respective levels. If there are two levels from which transitions to a third are equally probable, then obviously the most intense spectral line will arise from the level which initially has greater population. The populations of a set of energy levels are given by the statistical relation known as the Boltzmann distribution. The relation describing the ratio of the population of the upper energy state to the lower energy state is given by,

$$\frac{N_{upper}}{N_{lower}} = e^{\frac{-\Delta E}{kT}} \quad (3.25)$$

where  $\Delta E$  is the difference between energy states as before,  $k$  is the Boltzmann constant ( $1.38 \times 10^{-23} \text{ JK}^{-1}$ ) and  $T$  is the temperature in Kelvin.

#### 3.8.3 The Beer-Lambert law

The relationship between the incident intensity, the transmitted intensity, the concentration of the gas molecules and the path length is given by the Beer – Lambert law which is mathematically written as,

$$I_{out} = I_{in} e^{-\alpha Cl} \quad (3.26)$$

If the total absorbance of the sample is low, this expression can be approximated as,

$$I_{out} \approx I_{in} (1 - \alpha Cl) \quad (3.27)$$

In these expressions  $\alpha$  is the molar absorption coefficient of the absorbing medium (in this case the gas),  $C$  is the concentration of the gas and  $l$  is the length of the absorbing

path (in this case the micro – optic cell). This approximation is only accurate in the limit of  $\alpha Cl \ll 1$ . The concentration is normally expressed as a mole fraction or percentage, leaving the units of length and absorption coefficient to be the reciprocal of each other i.e. cm and  $\text{cm}^{-1}$  respectively.

## 3.9 Extracting Concentration and Pressure from Spectral Lines

In order to determine the concentration and pressure of a gas from the recovered absorption line transmission function or its corresponding derivatives, further analysis is required of the Beer–Lambert law given by Eq. 3.26.

### 3.9.1 Concentration and Derivative Signals

For gas monitoring at atmospheric pressure the gas absorption line, as a function of frequency, can be described by a Lorentzian profile [4], given by,

$$\alpha(\nu) = \frac{N_0 S}{\pi \gamma \left\{ \left( \frac{\nu - \nu_0}{\gamma} \right)^2 + 1 \right\}} = \frac{\alpha_0}{\Delta^2 + 1} \quad (3.28)$$

where  $N_0$  is the number of molecules at STP,  $S$  is the line strength ( $\text{cm. molecule}^{-1}$ ),  $\gamma$  is the half-width-half-maximum (HWHM) line width ( $\text{cm}^{-1}$ ) and  $\nu_0$  and  $\alpha_0$  are the frequency and absorption coefficient at line centre respectively, and  $\Delta = (\nu - \nu_0)/\gamma$ . Therefore, the recovered absolute gas transmission function is given by:

$$1 - \frac{I_{out}}{I_{in}} = \frac{N_0 S}{\pi \gamma (\Delta^2 + 1)} Cl = \frac{\alpha_0}{(\Delta^2 + 1)} Cl \quad (3.29)$$

This equation can be rearranged for  $C$ , and by setting  $\Delta = 0$ , the expression for the concentration at line centre is given by:

$$C = \frac{1 - \frac{I_{out}}{I_{in}}}{\alpha_0 l} \quad (3.30)$$

This simply means that the concentration at line centre is proportional to the depth of the relative transmission, as illustrated in Fig. 3.13 below.

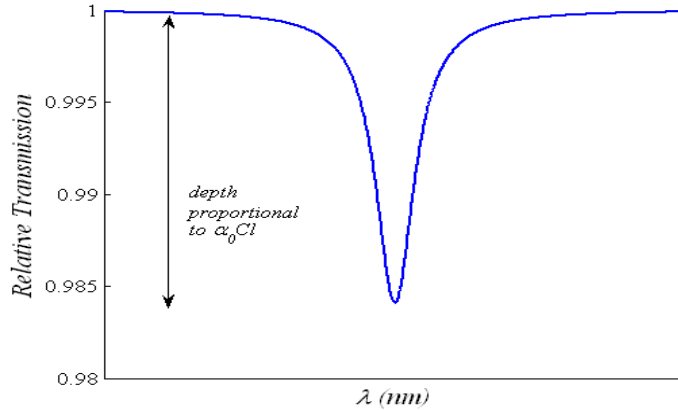


**Figure 3.13: Concentration from transmission function, scaled to path length and absorption coefficient**

In WMS/derivative measurements, the extraction of concentration is a little more complex. As mentioned in chapters 1 and 2, the amplitude of the 2<sup>nd</sup> derivative is proportional to the slope of the 1<sup>st</sup> derivative that in turn is proportional to the depth of the absolute transmission function at line centre. The simplest way to determine concentration in derivative spectroscopy is then to measure the amplitude of the 2<sup>nd</sup> derivative signal at line centre. Measured harmonic signals are proportional to the derivative signals in the limit of small modulation index ( $m = \delta\nu/\gamma \ll 1$ ), and the signals for the first two harmonics are given by Eq. 3.31 and Eq. 3.32.

$$I_{out \ 1f} = -I_{in} \frac{d\alpha(\nu)}{d\nu} C.l.\delta\nu = I_{in} C.l \frac{2N_0 S \Delta \delta\nu}{\pi\gamma^2 (\Delta^2 + 1)^2} = I_{in} C.l \frac{2\alpha_0 \Delta \delta\nu}{\gamma(\Delta^2 + 1)^2} \quad (3.31)$$

It can be seen then that the amplitude of the first harmonic has a dependency on  $\delta\nu/\gamma$ . This dependency becomes stronger with increasing order of harmonic and the second harmonic is then:

**Chapter 3: Analytical Methodologies – Fundamentals of Molecular Spectroscopy**

$$I_{out\ 2f} = -I_{in} C.l \frac{2N_0 S(3\Delta^2 - 1)(\delta\nu)^2}{\pi\gamma^3 (\Delta^2 + 1)^3} = -I_{in} C.l \frac{2\alpha_0(3\Delta^2 - 1)(\delta\nu)^2}{\gamma^2 (\Delta^2 + 1)^3} \quad (3.32)$$

At line centre  $\Delta = 0$  and the second harmonic signal then becomes:

$$I_{out\ 2f} = I_{in} C.l \frac{2\alpha_0(\delta\nu)^2}{\gamma^2} \quad (3.33)$$

Rearranging equation (3.33) the expression for the concentration is given by,

$$C = \frac{\gamma^2 I_{out\ 2f}}{2I_{in} l \alpha_0 (\delta\nu)^2} \quad (3.34)$$

Therefore, as expected, the concentration is proportional to the amplitude of the 2<sup>nd</sup> harmonic signal ( $I_{out\ 2f}$ ) at line centre, scaled by the input power, the absorption line width and the amplitude of the frequency (wavelength) modulation. The 1<sup>st</sup> and 2<sup>nd</sup> harmonic signals are shown, along with their relationship to concentration, in Fig. 3.14.

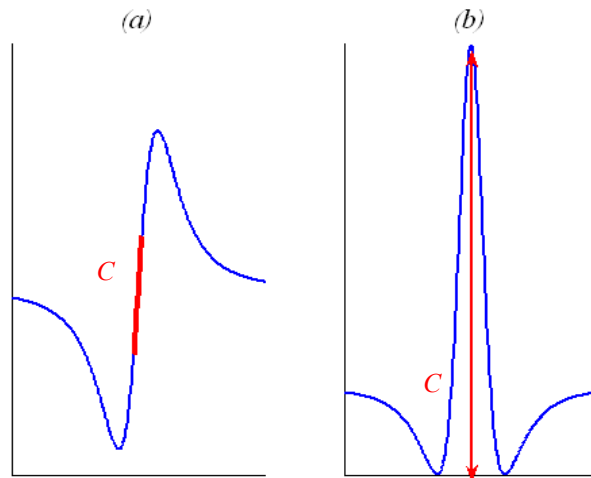


**Figure 3.14: Concentration from (a) 1<sup>st</sup> harmonic / derivative and (b) 2<sup>nd</sup> harmonic / derivative of transmission function, scaled to path length, absorption coefficient and input power**

### 3.9.2 Pressure and Derivative signals

If we consider pressures at which collision broadening dominates and concentrations at which the Beer-Lambert approximation holds, the relationship between pressure and line width for a pressure broadened Lorentzian profile (and consequently for directly measured line-shapes) is well known and is given by,

$$\gamma = \gamma_0 \left( \frac{P}{P_0} \right) \left( \frac{T}{T_0} \right)^{1/2} \quad (3.35)$$

where  $\gamma_0$  is the HWHM line width at pressure  $P_0 = 1$  atm temperature  $T_0 = 300$ K. The gas concentration,  $C$ , can be expressed as the number of gas molecules per unit volume ( $N$ ), relative to the number of gas molecules at STP per unit volume ( $N_0$ ):

$$C = \frac{N}{N_0} \quad (3.36)$$

Substituting equation (3.36) into (3.29) for direct measurements and considering only the amplitude of the transmission function at line centre gives:

$$1 - \frac{I_{out}}{I_{in}} = \frac{N_0 S l}{\pi \gamma} \quad (3.37)$$

Substituting equation (3.35) into (3.37) gives:

$$1 - \frac{I_{out}}{I_{in}} = \frac{N S l}{\pi \gamma_0 \left( \frac{P}{P_0} \right) \left( \frac{T}{T_0} \right)^{1/2}} \quad (3.38)$$

At a constant temperature equation (3.38) can be simplified to:

$$1 - \frac{I_{out}}{I_{in}} = \frac{N K l}{P} \quad (3.39)$$

### Chapter 3: Analytical Methodologies – Fundamentals of Molecular Spectroscopy

where  $K$  is a constant given by  $\frac{P_0 S}{\pi \gamma_0 \left( \frac{T}{T_0} \right)^{1/2}}$ . The ideal Gas Law is given by:

$$P = \frac{n N_A R T}{V} = N R T \quad (3.40)$$

Where  $P$  is the pressure (atm),  $n$  is the number of moles,  $R$  is the universal gas constant (82.0575 atm.cm<sup>3</sup> / mol<sup>-1</sup>K<sup>-1</sup>),  $T$  is the temperature (K),  $V$  is the volume (cm<sup>3</sup>),  $N_A$  is the Avogadro number, and  $N$  is number density (the number of gas molecules per unit volume), as before. Rearranging equation (3.40) for  $N$  and substituting into equation (3.39) gives:

$$1 - \frac{I_{out}}{I_{in}} = \frac{P K l}{P R T} = \frac{K l}{R T} \quad (3.41)$$

From the above analysis, the amplitude of the absolute absorption line transmission function appears to be independent of pressure/line width change for atmospheric pressure measurements. However, at lower pressures, where Doppler broadening is dominant, the transmission function amplitude shows a small dependence on the line width.

In TDLS / WMS measurements determining the line width is, again, a little more complex. Returning to equations (3.31) and (3.32) and the relationship between 1<sup>st</sup> and 2<sup>nd</sup> harmonics / derivatives, it is obvious that the peaks of the 1<sup>st</sup> harmonic / derivative are located at the points when the second harmonic / derivative is equal to zero. Therefore, removing the vertical scaling constants from equation (3.32) and setting to zero gives:

$$\frac{2(3\Delta^2 - 1)(\delta\nu)^2}{\gamma^3 (\Delta^2 + 1)^3} = 0 \quad (3.42)$$

### Chapter 3: Analytical Methodologies – Fundamentals of Molecular Spectroscopy

The solution to the equation is  $\Delta^2 = 1/3$ , which, when solved for  $\nu$ , gives two absolute frequency locations of  $\nu = \nu_0 \pm (\gamma/\sqrt{3})$  as illustrated in Fig. 3.15 below.

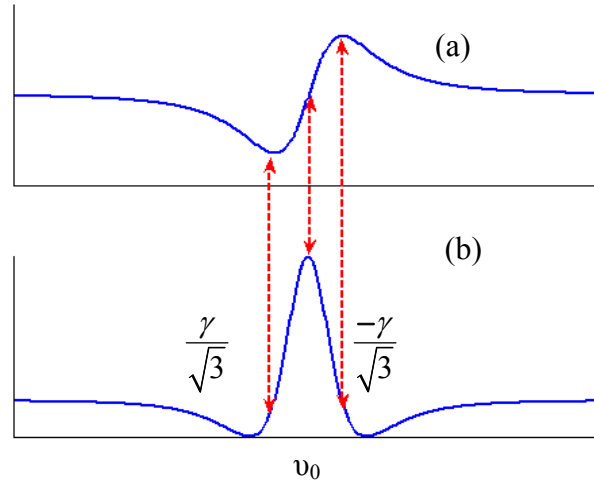


**Figure 3.15: Line width relationship between (a) 1<sup>st</sup> and (b) 2<sup>nd</sup> derivatives of transmission function**

Therefore, it is possible, in principle, to extract line width information from harmonic/derivative traces. From the above analysis several conclusions can be drawn:

1. For TDLS with direct detection gas concentration can be determined directly from the amplitude of the gas absorption line transmission function and, to a reasonable approximation, signal amplitude is independent of pressure/line width change at atmospheric pressures and above.
2. For TDLS-WMS detection the signal amplitude can no longer be regarded as independent of pressure/line width. The derivative signal amplitudes depend strongly on the system scaling factor  $\delta\nu/\gamma$ .
3. As well as measuring the concentration and pressure directly from the recovered signal amplitude and line width respectively, the parameters can be determined from curve fitting procedures, matching theoretical predictions to the recovered signals by varying P and C to obtain the best fit. The modelling of atmospheric gas absorption line transmission functions is explained in the next section.

### 3.10 Modelling Spectral Lines

The high-resolution transmission (HITRAN) molecular absorption database [5] is a compilation of spectroscopic parameters to enable the modelling of light transmission through atmospheric gases. The database stores, among others, the molecular energy transmission frequency,  $\nu$  ( $\text{cm}^{-1}$ ), the line intensity ( $\text{cm}^{-1}/(\text{molecule} \cdot \text{cm}^{-2})$ ), the air-broadening and self-broadening coefficients and the pressure shift. The information is for transitions at 296K. Obviously, in industrial applications the gas pressure and temperature varies from STP and the gas composition can vary from target gas / air mix; therefore, a program using the Agilent VEE runtime environment was developed by industrial collaborators Optosci Ltd (Glasgow, UK, [www.optosci.com](http://www.optosci.com)). The program uses a Voigt profile which is a convolution of the Gaussian (Doppler broadening) and Lorentzian (collision broadening) profiles. Traditionally the generation of a Voigt profile, by a process of numerical integration, was time consuming; however, recent progress in the development of very accurate approximation methods has allowed the VEE program to model atmospheric absorption profiles over a range of pressures. The process of convolution is mathematically represented by the following classic equation:

$$G(\nu) * L(\nu) = \int_{-\infty}^{+\infty} G(\nu')L(\nu - \nu')d\nu' \quad (3.43)$$

The Gaussian profile,  $G(\nu)$ , is given by:

$$G(\nu) = \frac{1}{\sigma\sqrt{2\pi}} \exp\left(\frac{-\nu^2}{2\sigma^2}\right) \quad (3.44)$$

where  $\sigma$  is the standard deviation.

Likewise, the Lorentzian profile,  $L(\nu)$ , is given by:

**Chapter 3: Analytical Methodologies – Fundamentals of Molecular Spectroscopy**

$$L(\nu) = \frac{\alpha_L}{1 + 4 \left( \frac{\nu}{\gamma_L} \right)^2} \quad (3.45)$$

where  $\alpha_L$  is the absorption coefficient as before and  $\gamma_L$  is the HWHM line width. The resulting Voigt profile is then given by:

$$I(\nu) = \frac{\gamma_L}{\gamma_G} \alpha_L \sqrt{\pi \ln(2)} V(X, Y) \quad (3.46)$$

Where  $\gamma_G$  is the HWHM line width of the Gaussian profile.  $V(X, Y)$  is given by,

$$V(X, Y) = \sum_{i=1}^4 \frac{C_i(Y - A_i) + D_i(X - B_i)}{(Y - A_i)^2 + (X - B_i)^2} \quad (3.47)$$

where  $A_i$  through  $D_i$  are a set of pre-defined constants given in Table 3.1.  $X$  and  $Y$  in Eq. 3.46 and Eq. 3.47 are given by,

$$X = 2 \frac{\sqrt{\ln(2)}}{\gamma_G} \nu \quad (3.48)$$

And

$$Y = \frac{\gamma_L \sqrt{\ln(2)}}{\gamma_G} \quad (3.49)$$

I	$A_i$	$B_i$	$C_i$	$D_i$
1	-1.2150	1.2359	-0.3085	0.0210
2	-1.3509	0.3786	0.5906	-1.1858
3	-1.2150	-1.2359	-0.3085	-0.0210
4	-1.3509	-0.3786	0.5906	1.1858

*Table 3.1: Parameters used in generating the Voigt profile*

### **Chapter 3: Analytical Methodologies – Fundamentals of Molecular Spectroscopy**

By using the Voigt profile and adhering to the Beer–Lambert law, the program developed by OptoSci Ltd. is capable of modelling gas absorption spectra for a wide range of concentration, pressure, temperatures and absorption path lengths. Fine adjustment of the broadening coefficients also permits the modelling of target gas absorption in host / balance gases other than air.

These theoretical predictions are compared to the measured absolute transmission functions, recovered either directly or through derivative methods. The curve fitting procedure requires only some fine adjustments over the pressure and concentration variables to provide the best match.

## **3.11 Conclusion**

A basic discussion of the relevant theoretical aspects of molecular spectroscopy has been presented in this chapter. The origin of spectra and the various types of motion of diatomic molecules including vibration and rotation are discussed. The vibration of the molecule is first treated as simple harmonic in nature in order to introduce the concepts of quantized vibrational energy levels, zero-point energy and selection rules. The more realistic case of anharmonic oscillations is discussed next. The modification of the selection rules follows as a natural extension. This explains the origin of overtone transitions, which is particularly relevant to this thesis since near infrared WMS involves overtone transitions. A discussion of rotational energy levels and the selection rules governing rotational transitions are discussed next, followed by the more complete picture of vibrational-rotational spectra. This enables the explanation of the spectral lines in the P-branch and R-branch. The modes of vibration of polyatomic molecules are briefly discussed next that briefly touches upon the methane molecule. The effect of rotation on the spectra of polyatomic molecules is finally discussed that helps to develop an appreciation of the existence of the Q-branch in molecular spectra. The discussion of these theoretical topics sets the stage for a comparison of fundamental mid-infrared spectral lines and near-infrared overtone spectral lines to be compared. The relative transmission through a 1% sample of methane under ambient conditions of temperature

### **Chapter 3: Analytical Methodologies – Fundamentals of Molecular Spectroscopy**

and pressure and for a 5.9cm interaction length are simulated for the near-infrared and mid-infrared spectral regions. The significantly large difference in the values helps to convey the message that the mid-infrared region offers much higher detection sensitivity. The reasons for the finite width of spectral lines are discussed next, that introduces concepts such as natural broadening, Doppler broadening, collision broadening and the Voigt profile that is widely used to model absorption lines. The two factors namely, transition probability and population of states, that affect the intensity of spectral lines are also discussed. The theoretical discussion ends with the discussion of the Beer-Lambert law.

The practical aspect of extraction of gas parameters from the derivatives of the absorption line is the last topic of discussion. The relationships between pressure, line width and concentration in direct absolute absorption line transmission profiles and their derivatives are described in detail. Finally a general description of the novel software designed by industrial collaborators OptoSci Ltd. to model the absorption of light through various atmospheric gas compositions is presented. It is reiterated that the objective of this chapter is only to give the reader a flavour of the correlation that exists between the underlying physics and the technological aspect of WMS for the extraction of gas parameters from a molecular absorption line and its derivatives. For more details of the theoretical aspects it is important to refer to the authoritative texts [1-3] in this field.

## 3.12 References

1. C. N. Banwell and E. M. McCash, “Fundamentals of Molecular Spectroscopy: Fourth Edition,” McGraw –Hill, 1994.
2. W. Demtroeder, “Laser Spectroscopy Vol 1 – Basic Principles,” Springer, 2008
3. A. Beiser, “Concepts in Modern Physics”, Tata-McGraw-Hill, New Delhi, 1997.
4. G. Stewart, C. Tandy, D. Moodie, M. A. Morante and F. Dong, “Design of a Fiber-optic Multi-Point Sensor for Gas Detection,” Sensors and Actuators B: Chemical, Vol. 51, pp 227-232, April 1998.
5. L.S. Rothman et al., “The HITRAN 2004 molecular spectroscopic database,” J. Quant. Spectrosc. Radiat. Transfer, Vol. 96, pp 139-204, 2005
6. A. B. McLean, C.E.J. Mitchell and D. M. Swanston, “Implementation of an Efficient Analytical Approximation to the Voigt Function for Photoemission Line shape Analysis,” Journal of electron Spectroscopy and related Phenomena, Vol. 69, No. 2, pp 125 – 132, September 1994

# *Chapter 4*

---

## *RAM nulling – Principles and Experimental Methods*

---

### **4.1 Introduction**

The  $1f$  RAM [1, 2], arising from direct IM of the laser, has long been a major limiting factor in TDLS with WMS particularly if  $1f$  detection is used. Recently, two  $1f$  calibration-free methods, namely the RAM method and the Phasor Decomposition Method (PDM), have been demonstrated [3, 4], for the direct recovery of absolute gas

#### Chapter 4: RAM nulling – Principles and Experimental Methods

absorption lines as described in chapter 2. It was pointed out that the main limitation of both these methods is the presence of the high concentration-independent  $1f$  background RAM signal that limits the use of these two techniques for low concentrations because signal amplification is limited by saturation of the detection electronics by the high background and there are significant sensitivity/resolution issues in the digital acquisition of signals. The objective of this work is to investigate a new fiber-optic technique to eliminate the  $1f$  RAM component due to the direct laser IM. Successful realization of this method would allow potentially higher sensitivity without having to detect at higher harmonics of the modulation frequency.

The origin of RAM in WMS and its distorting effects on various harmonic signals have been studied in great detail in several papers [5-7]. To circumvent the problem of high background signals,  $2f$  detection has been favoured, although, a background signal for  $2f$ -detection is known to exist [8], and is due to the nonlinear IM of the laser. The relatively low level of  $2f$  background RAM led most researchers to focus on  $2f$  WMS despite the acknowledged difficulty in signal interpretation. Attempts to eliminate the  $1f$  RAM have been few and far between. The earliest attempt at dealing with the limitation imposed by RAM is the only double-beam-single-detector configuration proposed by Gehrtz et al [9], for the FMS regime of operation. The strategy used was to split the laser output in two parts using a beam splitter, chop them synchronously, but  $180^\circ$  out of phase using a mechanical chopper or an acousto-optic modulator, balance the two signal strengths and finally coherently recombine them on a photo-detector. The path lengths traversed by the two beams were required to be equal, and were very short. In the absence of an absorbing species on one of the arms, the signal components at the chopping frequency cancel, and the output of a lock-in amplifier triggered by the chopping frequency is zero. The use of a mechanical chopper and the alignment requirements of this system are potential limitations for field-deployment in harsh industrial situations.

To address the problem more generally, electronic cancellation of RAM has also been performed. In two earlier double-beam two-tone-FMS (TTFMS) schemes [10, 11],

#### Chapter 4: RAM nulling – Principles and Experimental Methods

balanced homodyne detection was used. A different technique to cancel the background RAM in  $2f$  WMS and common-mode noise was reported by Zhu and Cassidy [12], in which an electronic subtractor circuit with two different photo-detectors was used. In the most recent attempt, the versatility of modern digital signal generator cards (NI DAQ cards) has been exploited to suppress the RAM. This is achieved by adding a digitally generated  $2f$  component to the laser modulation current with appropriately adjusted amplitude and phase so as to cancel any  $2f$  component of the laser current that will in turn suppress and  $2f$  IM [13]. A dual-modulation approach to cancel the RAM at  $2f$  has also been proposed for FMS applications. However the focus of the present discussion is the  $1f$  RAM and therefore a detailed discussion of the  $2f$  RAM will be reserved for a later chapter.

It appears that the  $1f$  RAM has been viewed as an artifact that must be suffered or at best avoided by  $2f$  detection. Consequently, no concerted effort has been made to eliminate the  $1f$  RAM at the *optical* level in TDLS-WMS and thereby make  $1f$  detection a viable option. This is possibly because  $2f$  WMS with its nearly zero background RAM was a ready and convenient alternative to  $1f$  WMS, and the extra processing to extract useful information was considered worth the effort. In this work a simple and robust fiber-optic technique to eliminate the concentration-independent RAM component at the *optical* level is presented. This potentially offers the possibility of  $1f$ , shot noise limited detection for calibration-free direct recovery of the absolute gas absorption lines.

This chapter introduces the RAM nulling technique with a detailed description of the experimental setup. The requirements on the modulation frequency and fiber length to ensure that the RAM background is eliminated are discussed next. The optical interference noise issues are then discussed and appropriate steps to minimize the noise are explained. It is shown that this source of noise is not the fundamental limiting factor in the performance of the system. The chapter ends with a brief mathematical description of the RAM nulling process. An expression for the relative transmission is derived that uses a normalization signal that can be extracted from the experimental arrangement directly.

## 4.2 Principles of operation of RAM nulling

Figure 4.1 below shows the experimental setup used for RAM nulling.

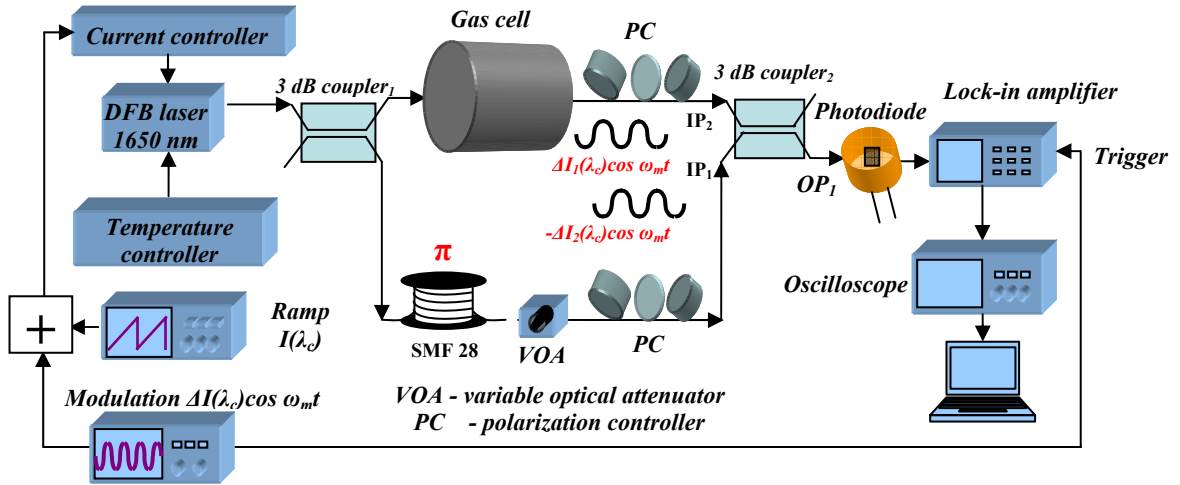


Fig. 4.1: Experimental setup for RAM nulling

The principle of operation of RAM nulling [20] is to split the intensity-modulated output of a DFB diode laser approximately equally using a fiber-optic 3-dB coupler, with the two outputs going to the gas cell and the SMF-28 fiber delay line respectively. The modulation frequency (delay) is so chosen as to introduce a relative phase shift of  $\pi$  between the two IM components on the two beams. The outputs of the gas cell, and the delay fiber, after attenuation by a fiber-optic variable optical attenuator (VOA) (model number Thorlabs VOA50-APC), pass through two fiber-optic polarization controllers (Thorlabs FPC562) to establish orthogonal polarization states for the two combining optical signals. This is necessary to minimize optical interference noise when the two signals are recombined through a second 3dB coupler. When the system is balanced in the absence of gas by adjustment of the VOA, the two sinusoidal IM components at  $f_m$  cancel. It was found necessary and sufficient to attenuate the output from the fiber delay arm only, because due to the appreciable loss through the gas cell, that signal component is weaker than the delayed signal by default. The resulting dc signal due to the addition of the two average intensity levels is rejected by the harmonic detection process, making

#### Chapter 4: RAM nulling – Principles and Experimental Methods

the output zero in the absence of absorption and thus eliminating the high background RAM signal. In the presence of gas the balanced condition is disturbed, and this imbalance is directly reflected at the output where a signal that is due to the concentration-dependent absorption of the gas is detected. The optical signals are detected by an InGaAs photodiode (OptoSci LNP-2) whose output is fed to a dual channel PerkinElmer 7280 DSP lock-in amplifier. The final output is observed on a Tektronix TDS 3014B 200MHz digital storage oscilloscope from which data is captured using a LabVIEW program over a GPIB interface.

To implement the  $1/f$  RAM technique explained in Sec 2.4.1, the LIA detection phase is adjusted to fully align one of the axes (channel Y in this case) with the classic WMS derivative signal. This implies that the signal recovered on the orthogonal channel X is a projection of the full RAM component that is recovered in complete isolation from the 1<sup>st</sup> derivative WMS signal.

The conditions that need to be met to ensure that the direct IM components cancel at the output of the second 3-dB coupler are –

- a) to ensure that the sinusoidal IM on the two input arms of the coupler are anti-phase
- b) to ensure that the relative amplitudes of these two signals are appropriately balanced so that they cancel at the coupler's output

The first condition requires that

$$\sin \omega_m t = -\sin(\omega_m t + \phi) \quad (4.1)$$

$$\Rightarrow \phi = \pi \quad (4.2)$$

Therefore, the required time delay through the fiber is

$$t_d = \frac{\pi}{\omega_m} \quad (4.3)$$

and the fiber length,  $L$ , required is given by,

$$L = \frac{c}{n} \frac{\pi}{\omega_m} = \frac{c}{2nf_m} \quad (4.4)$$

Where,  $c$  denotes the speed of light in free space,  $n$  denotes the effective index of the fiber and  $f_m$  is in Hz. For a fiber length of 1km and a typical value of 1.5 for  $n$ ,  $f_m$  is 100 kHz. In practice, a small adjustment of  $f_m$  is necessary to compensate for the small difference between assumed and actual values of both  $L$  and  $n$ . Simultaneous fulfilment of these two conditions results in a dc signal at  $OP_1$ , which in turn is rejected by the LIA, thereby giving zero output in the absence of gas.

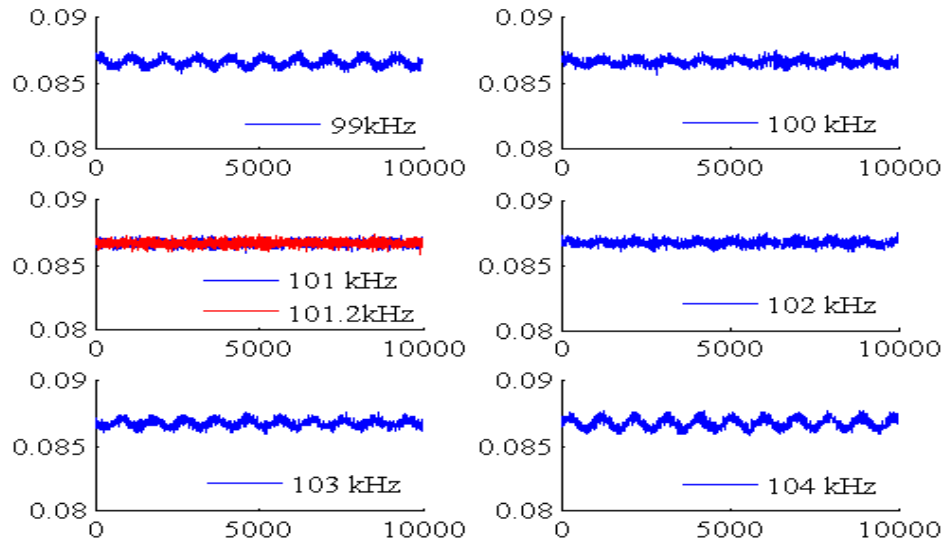


*Fig. 4.2: RAM nulled output displayed on the oscilloscope with only the modulation applied, as the modulation frequency is tuned past the ideal value (shown in red) required for perfect cancellation.*

Figure 4.2 shows the output of the photo-detector observed directly on the oscilloscope that illustrates the process of adjusting  $f_m$  to achieve RAM nulling. Both the signal arms are connected to the inputs of the coupler, the ramp is switched off and only the modulation is applied. The VOA has been adjusted to balance the amplitudes of the two IM components. The value of  $f_m$  is varied over a small range (99 kHz to 104 kHz) around the optimum RAM nulling frequency. It is observed that for the optimum value of 101.2 kHz the two IM components cancel almost perfectly. The net signal is therefore a dc level which is rejected by a LIA resulting in a zero output in the absence of gas. The

#### Chapter 4: RAM nulling – Principles and Experimental Methods

amplitude of sinusoidal IM increases as  $f_m$  is tuned further away from this value. The corresponding dc output of the lock-in amplifier would also increase proportionately. This demonstrates the background signal cancellation by destructive interference of two *electrical* signals.

The superposition of the two optical fields within the second coupler also gives rise to *optical* interference that appears as an additional noise component that can severely degrade the sensor performance unless it is controlled. If the RAM nulling technique is to work effectively appropriate mitigating steps must be taken to minimize the interference effects of such superposition. The optical interference can be minimized by ensuring that,

- a. the delay line length,  $L$ , is much longer than the coherence length,  $L_{coh}$ , of the laser source
- b. the polarization states of the two interfering electric fields are orthogonal

The first important consideration in this regard is the choice of  $f_m$  that in turn dictates the corresponding value of  $L$  (that varies inversely as  $f_m$ ). The fiber length should be much longer than the coherence length,  $L_{coh}$  of the laser so that no well-defined phase relationship exists between the light that traverses the gas cell and the light that propagates through the delay line.

The degree of coherence,  $g^1(\tau)$  of two optical fields having coherence time of  $\tau_c$ , that are superposed with a relative delay of  $\tau$  is given by [21],

$$g^{(1)}(\tau) = e^{-i\omega_0\tau - \frac{|\tau|}{\tau_c}} \quad (4.5)$$

for a Lorentzian (collision broadened) light source, and by,

$$g^{(1)}(\tau) = e^{-i\omega_0\tau - \frac{\pi}{2} \left( \frac{|\tau|}{\tau_c} \right)^2} \quad (4.6)$$

for a Gaussian (Doppler broadened) light source,

#### Chapter 4: RAM nulling – Principles and Experimental Methods

It is simple to show that,  $\frac{\tau}{\tau_c} = \frac{\Delta L}{L_{coh}}$  where  $\Delta L$  is the path length difference between the two arms (equal to  $L$  in this case) and so the real part of the two functions may be plotted as a function of the path difference between the two signal arms normalized by the coherence length of the laser. This is a more intuitive depiction of the process and is shown in Fig 4.3 for the DFB laser for which  $L_{coh}$  was determined to be  $\sim 43\text{m}$  for a line width of 7 MHz. Note that  $L_{coh}$  is much smaller than the chosen fiber length of 1 km.

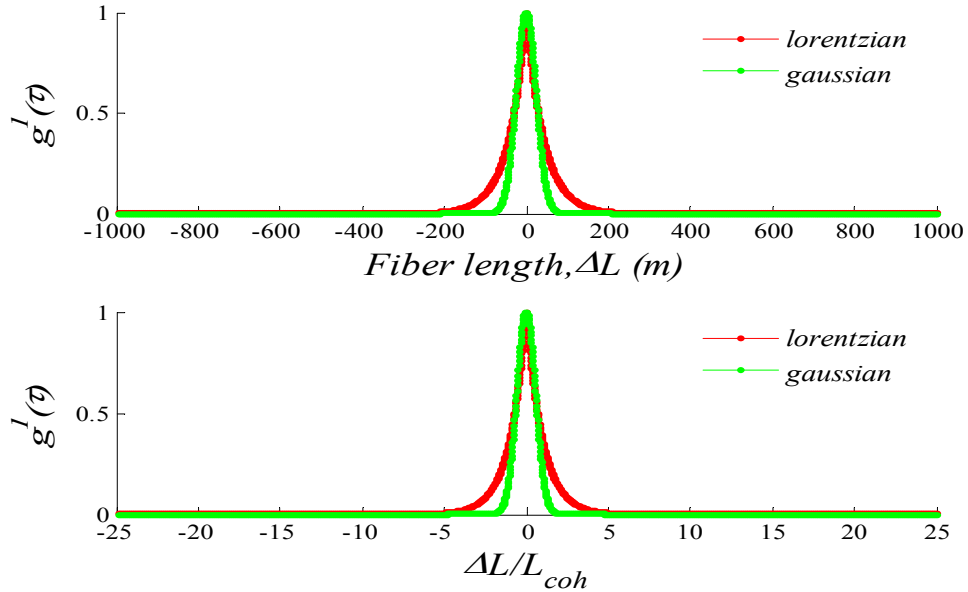


**Fig. 4.3: Rapid decay of the mutual coherence function  $g^1(\tau)$  as the ratio of path difference to laser coherence length increases. Therefore if the fiber length is large compared to the DFB laser's coherence length it should be possible to eliminate stable interference fringes at the output of the RAM nulling setup**

It is seen that for either case,  $g^1(\tau)$  reduces very rapidly as the ratio  $\frac{\Delta L}{L_{coh}}$  increases. Therefore, for path differences that are large in comparison to the coherence length of the laser, there will be no stable interference fringes, and the visibility of fringes will tend to zero. A comparison of the quality of fringes observed at  $OP_I$  for a path difference of 1km and 1m is shown in Fig. 4.4 that helps to clarify the situation.

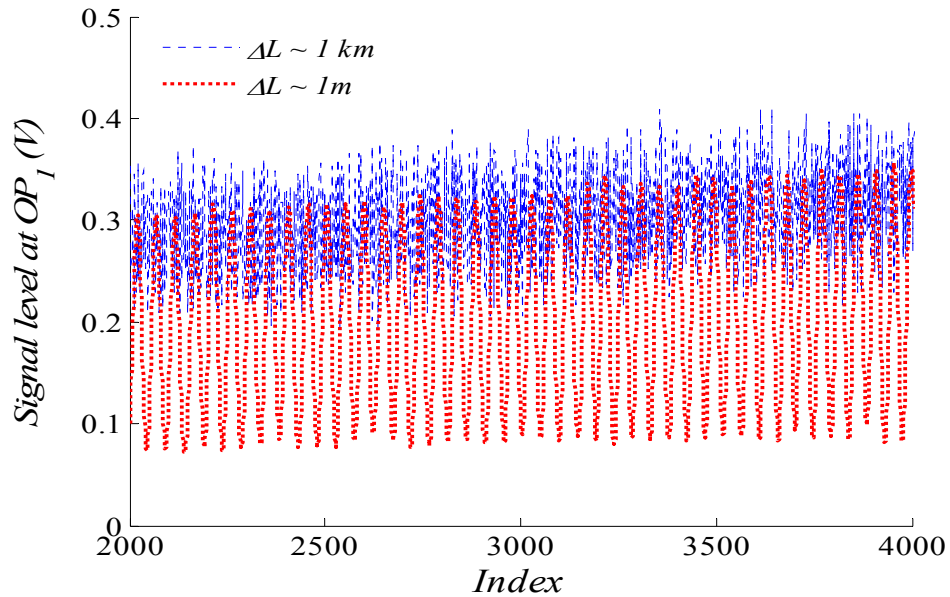


*Fig. 4.4: Comparison of interference effects for path length difference of 1km (blue) and 1m (red), using the same RAM nulling setup.*

The signal at  $OP_1$  was captured by the oscilloscope with only the ramp applied to the laser injection current and with no gas in the cell. The polarization controllers were removed from both arms so as not to inhibit the optical interference in any way. The fiber spool was replaced with an ordinary fiber-optic patch cord that served to introduce the path difference between the two arms. It is clearly seen that for a small path difference of about 1m, strong optical interference fringes are produced. For a path difference of 1km the stable fringes are no longer formed, but are replaced by what is essentially optical interference noise. This proves that optical interference fringes can indeed be eliminated if the path length difference between the two arms of the RAM nulling experimental setup is much larger than the coherence length of the laser source. The heights of the fringes increase because the laser power increases as the current is ramped up. The figure shows only a small range of the whole scan for the sake of clarity, and the increase in power over the scan range is therefore not sufficiently clear.

The variation of the optical interference noise across the full scan range of the laser current recorded directly by the oscilloscope is shown in Fig. 4.5. Two fiber-optic

#### Chapter 4: RAM nulling – Principles and Experimental Methods

polarization controllers (PC) were introduced on the two signal arms to control their individual polarization states before they are recombined, but the paddles were set at arbitrary positions.

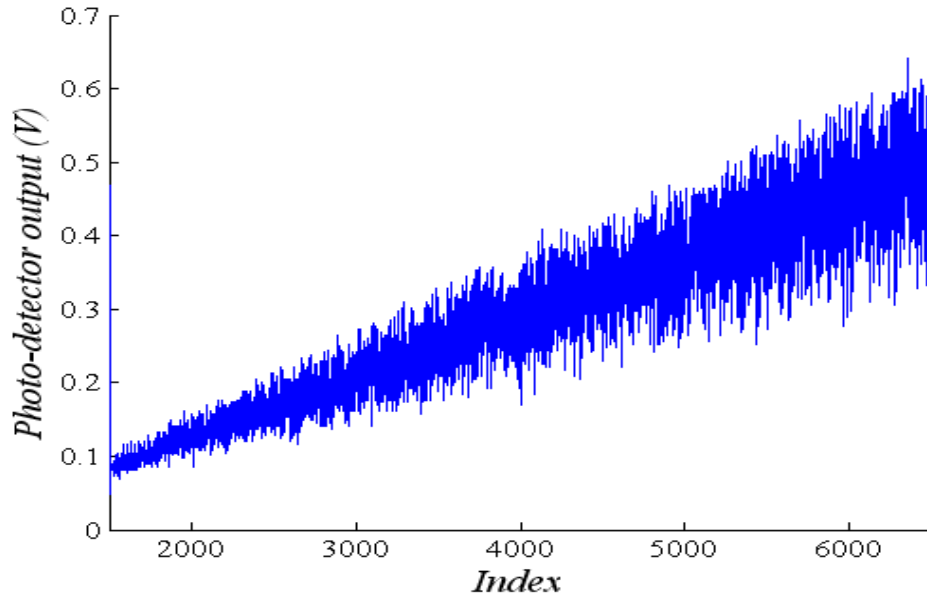


*Fig. 4.5: Photo-detector output at  $OP_1$  observed on the oscilloscope with only the ramp applied, showing the optical interference noise increasing as the laser intensity increases over the typical scan range of the laser current.*

As the laser current is ramped, its power also increases. The interference of the two signal components of increasing power produces interference noise that increases significantly over the scan range. This increasing optical interference noise severely limits detection sensitivity and must therefore be minimized to within the detector noise level for high signal-to-noise ratio.

In order to investigate the minimization of the optical interference noise, the experimental arrangement is frequency-tuned to the nulling point as explained earlier with the voltage ramp switched off. The two PCs are then carefully adjusted to establish orthogonal polarization states of the two optical components. This can be confirmed by observing the reduction of the dc noise output at the nulling point as the paddles are adjusted.

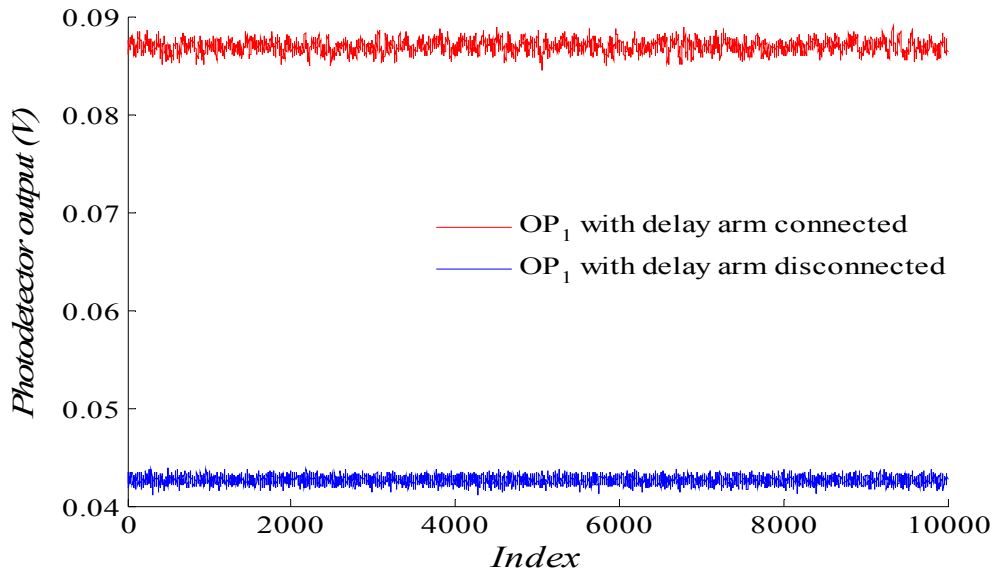


**Fig. 4.6: Photo-detector output with and without RAM nulling showing the effect of the polarization controllers on the net optical interference noise**

The effect of the PCs on the optical interference noise of the system is illustrated in Fig. 4.6. The lower blue trace is the output due to the signal from the gas cell only, with the delay line physically disconnected from the second coupler, the ramp and the modulation both switched off. The red trace represents the signal at  $OP_1$  with the delay fiber connected to the second coupler, the modulation applied and the relative intensities adjusted as accurately as possible in order to satisfy the RAM nulling condition. The x-axis (time base) corresponds to few tens of cycles of the 100 kHz modulation signal. When the delay line is connected to the coupler the average signal level is understandably doubled since the original laser output had been split in to two symmetrical parts that are now recombined. The careful adjustment of the VOA ensures that there is no net modulation of the output intensity. The optical noise in the signal does not increase greatly as a result of the superposition of the two signals. The interference noise has therefore been effectively suppressed by optimizing the two PCs.

An important experimental element that has contributed to the robust control over the optical interference noise is the modulation of the laser current. The effect of the laser current modulation on the optical interference noise deserves separate mention and is

#### Chapter 4: RAM nulling – Principles and Experimental Methods

shown in Fig. 4.7. The polarization controllers were optimized as in Fig. 4.6 to minimize the optical interference noise. The red trace in Fig. 4.7 shows the photo-detector output of the system with the sinusoidal modulation applied and is the same as the red trace in Fig. 4.6, while the blue trace is the output with the modulation switched off. The optical noise is seen to increase significantly when the modulation is switched off without changing anything else.

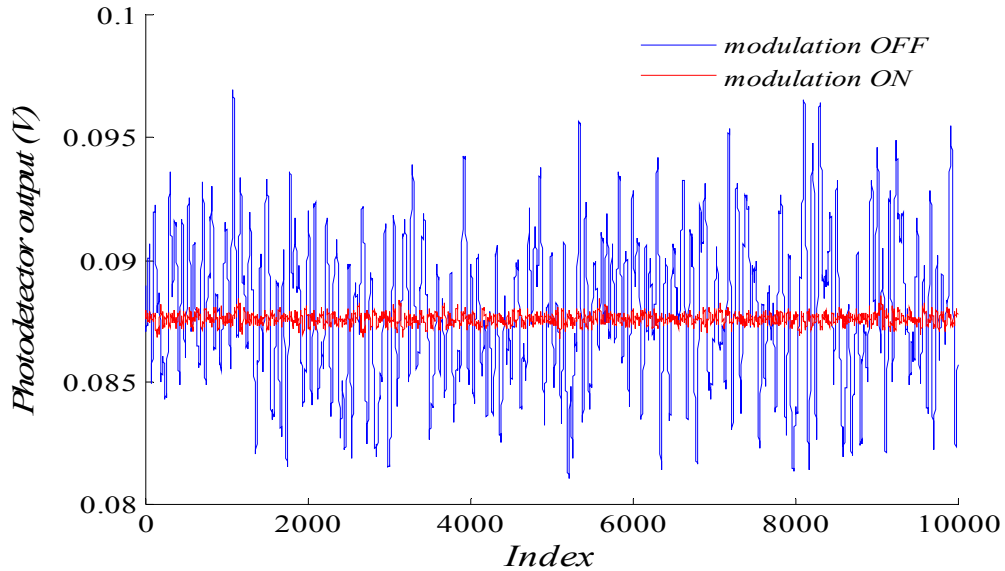


*Fig. 4.7: Effect of the current modulation on the optical interference noise for a constant setting of the polarization controllers demonstrating that the modulation significantly reduces the laser's coherence length and consequently the interference noise*

This is because the modulation of the laser current significantly broadens the frequency spectrum of the laser and therefore greatly reduces the coherence length from its unmodulated value of  $\sim 43\text{m}$  corresponding to a measured line width of 7 MHz. This broadening of the laser spectrum causes an additional reduction of the coherence length of the laser, which further reduces the interference noise.

The results presented in Fig. 4.6 and Fig. 4.7 were obtained with the voltage ramp switched off and therefore correspond to a single value of the laser current and constant optical power. However, it must be ensured that the minimization of the optical noise is

#### Chapter 4: RAM nulling – Principles and Experimental Methods

effective over the entire scan range of the laser current over which the associated power variation is significant. The control over the optical noise over the full scan range is demonstrated in Fig. 4.8 and Fig. 4.9. In Fig. 4.8 the ramp has been applied but the modulation has been switched off. The blue trace is the signal with the delay arm disconnected and therefore corresponds to the case with no optical interference. The red trace corresponds to the output with the delay line connected to the coupler and the two PCs adjusted to give rise to maximum optical interference and therefore this situation represents the worst-case scenario. Clearly the optical noise increases drastically over the scan range.

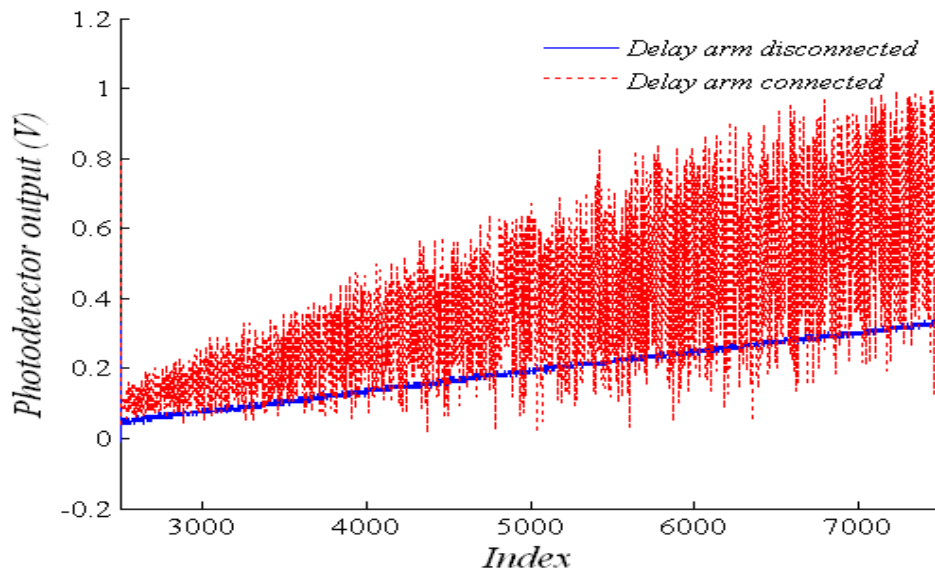


*Fig. 4.8: Photo-detector output with delay arm disconnected (blue), and connected (red) with the modulation off and polarization controllers adjusted for worst-case noise. The voltage ramp has been applied to scan the laser current over a typical range.*

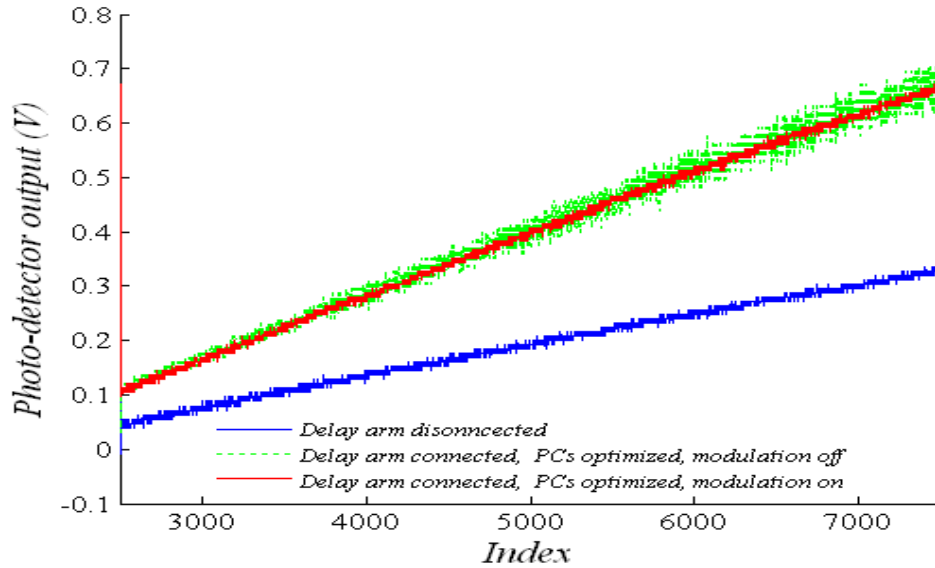


*Fig. 4.9: Robust minimization of optical interference noise over current scan range by the application of the modulation and optimization of the polarization controllers.*

The effect of the two polarization controllers and the modulation is clearly demonstrated in Fig. 4.9. Just as in the previous case, the blue trace is the signal with the delay arm disconnected and therefore corresponds to the case with no optical interference. The green trace represents the output with the modulation switched off and only the PCs adjusted to minimize the optical interference. In comparison to Fig. 4.8 there is a huge reduction of the noise but it is still not at the same level as the signal with the delay arm disconnected. Note that the voltage level has doubled due to the addition of optical signal from the delay fiber that is almost equal in power to the signal on the gas cell arm. The crucial role played by the modulation is shown by the red trace that represents the output with the modulation applied to the laser current. Comparison of the red trace with the green trace shows that there is a significant reduction of the optical noise as a result of the modulation. The noise level in the red trace implies that the optical interference noise has been minimized to that of the blue trace that represents the case when no optical interference noise arises.

It may therefore be asserted that the optical interference of the two signal components is not the fundamental limiting factor. The supporting experimental results

prove that it is indeed possible to minimize the noise of the system to the level of receiver noise by choosing a delay fiber length that is sufficiently long compared to the coherence length of the modulated laser, and then by ensuring that the optical signals are orthogonally polarized by using two polarization controllers in the two signal arms. The arrangement remains stable for very long periods of time without the need for fine tuning.

### **4.3 Basic analytical treatment of RAM nulling**

A brief mathematical analysis of the RAM nulling technique is presented next without which this discussion would remain incomplete. It is necessary to bring out how the absorption signal that appears on a zero background is normalized to recover the relative transmission profile. A detailed treatment of the different possible configurations of the basic system and the wavelength-dependence of various signals and physical components are considered later in chapter 6.

The reduction in transmission due to wavelength-dependent absorption in the vicinity of a gas line is quantified by Beer's Law, and is given by,

$$I_t(\lambda) = I_0(\lambda)e^{-\alpha(\lambda)Cl} \quad (4.7)$$

where all symbols signify the usual quantities as defined earlier in Chapter 2. For weak absorption this may be approximated by  $I_t(\lambda) = I_0(\lambda)[1 - \alpha(\lambda)Cl]$ . In a TDLS-WMS system with such weak absorption the signals at the output of the gas sensing region may be found using a simple Taylor series expansion of  $\alpha(\lambda)$  as shown in Sec 2.4. The expression for the  $1f$  signal with the LIA appropriately phase-tuned for the RAM method of signal recovery, (only strictly applicable at modulation indices,  $m$ , of less than 0.2 [1, 2]) is given by Eq. 2.5 and is reproduced below,

$$I_{1f} = \Delta I(\lambda_c) \cos \omega t - \Delta I(\lambda_c) \alpha(\lambda_c) . Cl \cos \omega t - I(\lambda_c) \left. \frac{d\alpha(\lambda)}{d\lambda} \right|_{\lambda_c} . Cl . \delta\lambda \cos(\omega t - \psi) \quad (4.8)$$

#### Chapter 4: RAM nulling – Principles and Experimental Methods

The first two terms arise from the direct IM and may be referred to respectively as the concentration-independent RAM term, and the concentration-dependent RAM term (collectively simply the RAM signal). The third term is the classic WMS 1<sup>st</sup> harmonic/1<sup>st</sup> derivative signal arising from the interaction of the laser's wavelength/frequency modulation with the gas line. The first term, when recovered by a LIA, gives rise to the high background output signal with the other two terms representing the concentration-dependent changes arising from the presence of the gas that are superimposed on the background signal.

In the RAM technique the LIA signal detection phase is aligned at  $\psi-90^\circ$  to null the 1<sup>st</sup> derivative signal and only the isolated projections of the RAM signals are recovered, with the gas absorption signal (term 2) sitting on a high background signal (term 1). The overall aim of the RAM nulling technique reported here is to eliminate the high background signal through destructive interference at the signal frequency. With reference to Fig. 4.1 and assuming no gas, the signals arriving at the output of the fiber combiner,  $OP_I$ , from the gas cell and the delay line are of nearly equal amplitude (balanced by the VOA) and are anti-phase (due to the delay/modulation frequency choice). Hence, in the absence of gas or off-line, these two components cancel thereby presenting only a high average dc level to the LIA resulting in a zero output. An imbalance results from the presence of gas and a non-zero LIA output arises, essentially from term 2 of Eq. 4.8. However, the elimination of the background leads to a complication in signal normalization because the concentration-dependent absorption signal now appears on a zero background. A simple mathematical formulation of the RAM nulling mechanism shows that it is relatively straightforward to extract a normalization method.

Given the above, the output at  $OP_I$ , in the absence of gas (or off-line) can be written:

$$\begin{aligned} OP_{1no\ gas} &= \Delta I_1(\lambda_c) \cos \omega t + \Delta I_2(\lambda_c) \cos(\omega t + \pi) \\ &= \left[ \Delta I_1(\lambda_c) - \Delta I_2(\lambda_c) \right] \cos \omega t \end{aligned} \tag{4.9}$$

#### Chapter 4: RAM nulling – Principles and Experimental Methods

where,  $\Delta I_1(\lambda_c) \cos \omega t$  and  $\Delta I_2(\lambda_c) \cos \omega t$  denote the individual contributions from the gas arm and the fiber delay line arm respectively and include the wavelength dependencies of the different signal paths through the couplers. Appropriate adjustment of the VOA ensures that these two contributions are equal at a particular wavelength and are approximately equal over the entire wavelength range of a recovered gas line, giving a near-zero background signal.

In the presence of gas in the cell, the signal in that arm is multiplied by  $e^{-\alpha(\lambda_c)Cl}$  due to the absorption. The resulting output,  $OP_{1gas}$ , measured by the LIA is then given by,

$$OP_{1gas} = \Delta I_1(\lambda_c) e^{-\alpha(\lambda_c)Cl} - \Delta I_2(\lambda_c) \quad (4.10)$$

The factor  $\cos \omega t$  has been dropped to depict the effect of phase-sensitive harmonic detection using the LIA, which essentially amounts to multiplying the two sinusoids by  $\cos \omega t$ . It is easy to see that  $OP_{1gas}$  sits on a near-zero background since  $e^{-\alpha(\lambda_c)Cl} = 1$  in the offline regions. Subtracting Eq. 4.9 from Eq. 4.10 and reorganizing we get,

$$\frac{I_1(\lambda_c)}{I_0(\lambda_c)} = e^{-\alpha(\lambda_c)Cl} = 1 + \frac{OP_{1gas} - OP_{1no\ gas}}{\Delta I_1(\lambda_c)} \quad (4.11)$$

The denominator of the last term in Eq. 4.11,  $\Delta I_1(\lambda_c)$ , is simply the output at  $OP_I$  as measured with an LIA with no gas in the cell and with the delay fiber arm disconnected from the coupler. As well as being crucial to recovering the gas absorption line shape, it also serves as a convenient normalization factor that accounts for any changes in background laser intensity and the wavelength dependencies of the laser output and the two couplers as regards the gas cell arm. In practice a fiber-optic switch inserted between the VOA and the coupler can be used to block the signal from the delay fiber line whenever this needs to be measured. Alternatively, it could be obtained using a fiber tap coupler inserted between the gas cell and the system output coupler, provided the relationship between the tap output and  $OP_I$  is known and stable over the required wavelength range. In either case it can be obtained with or without gas in the cell, the former simply requiring a curve fit to the off-line data.

## 4.4 Description of experimental conditions and set-up

This section describes the experimental arrangement including the choice of the near-IR methane line, all optical, electronic and fiber-optic components. The construction of the gas cell is described. Wavelength-referencing of time-indexed data is discussed next, followed by a brief description of how the lock-in amplifier is set up for measurements. The section ends with a discussion of the method to set the modulation index for an experiment.

### 4.4.1 Choice of absorption line

To demonstrate the accurate recovery of absorption lines with the RAM nulling incorporated, a well-isolated near-infrared R-branch absorption line of methane at 1650.956 nm was chosen.

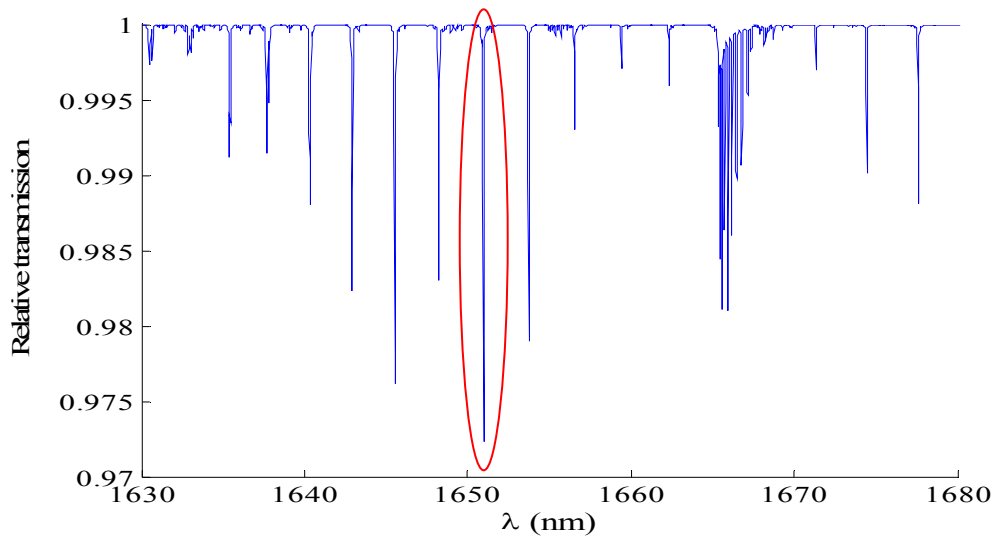


*Fig. 4.10: Simulated near-infrared absorption lines of 1% methane at 1 bar pressure and 22°C temperature.*

This line is actually a combination of two closely spaced lines that are resolvable at low pressures ( $\sim 0.2$  bar). The lines merge into a single symmetric feature at atmospheric pressures at which the calibration-free WMS techniques are intended to operate.

#### Chapter 4: RAM nulling – Principles and Experimental Methods

Therefore, the choice of this line is convenient to demonstrate the newly-proposed RAM nulling technique. The relative transmission is simulated for 1% mixture by volume of methane in nitrogen balance at a pressure of 1 bar and temperature of 22°C. The simulations use values for line strengths based on HITRAN 2004 database [14]. Figure 4.10 shows several near-infrared overtone absorption lines of methane under ambient conditions of temperature and pressure. The absorption feature at 1650.956 nm was selected for measurements because it is well isolated from neighbouring features and is also the strongest in this region.

The strongest of these lines is shown in Fig. 4.11 with the wavelength-scale expanded and a very weak line to the left of the main feature is also seen to be present. This weak feature does not pose serious problems in the signal analysis. In fact this feature serves to test the accuracy of the normalization process. It will be seen in chapter 5 that both the peaks are accurately recovered. It is important to point out that although a well isolated feature has been chosen to demonstrate the results, this is not a necessary requirement for accurate extraction of the absorption lines. As will be demonstrated in due course, the RAM nulling technique and signal normalization strategy are not affected by the presence of this weak feature.

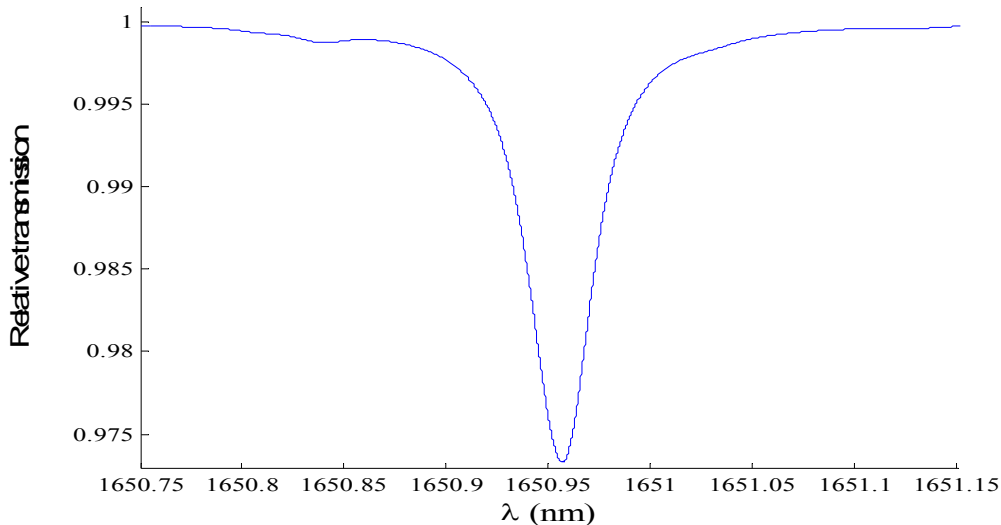


*Fig. 4.11: Near-infrared methane absorption line 1650.956 nm used for all experiments*

#### 4.4.2 Signal Source and Drive Electronics

The experimental system consists of electronic and fiber-optic components which are described in this section.

An OKI 1651nm DFB laser (model no. OL6109L-10B) housed in a 14-pin butterfly package mounted on a 14-pin PCB was used for these experiments. The butterfly package had a built-in isolator, thermistor and Peltier element for cooling and temperature control of the laser head. A Thorlabs LDC 210 current controller and a Thorlabs TEC 210 temperature controller are used to control the current and temperature of the DFB laser. The TEC 210 is used to temperature-tune the emission wavelength of the laser close to the chosen absorption line of methane. Thereafter the temperature is controlled to within 0.2 K, and current tuning is used to sweep the emission wavelength across the absorption line. The resistance of the thermistor on the package is displayed on the front panel of the TEC 210 that provides an indirect reading of the actual laser temperature. The relation between the thermistor's resistance and the actual temperature is given by,

$$T = \frac{3892}{\ln\left(R/2.142 \times 10^{-5}\right)} - 273.15 \quad (4.12)$$

Temperature tuning covers a much wider sweep range but is imprecise and slow. Current tuning is much more accurate and fast and is therefore better suited for wavelength modulation. For all experiments the laser temperature was set to 35°C (6.454 kΩ) and the mean laser current was set to 70mA that set the emission wavelength in the vicinity of the methane line at 1650.956 nm.

Two Agilent 33250A 80MHz arbitrary waveform generators (AWG) are used to apply a slow 5-Hz ramp and a 100 kHz sinusoid to the laser current for wavelength scanning and modulation. A 400mV p-p ramp voltage was applied to the LDC 210, which swept the laser current from 30mA to 110mA. This was found sufficient to cover a wide enough spectral region around the line centre. A very easy way to confirm the

## Chapter 4: RAM nulling – Principles and Experimental Methods

lower and upper limit of the current scan range is to select a square wave output instead of a ramp at a very low frequency (0.1 Hz). The actual laser current displayed on the front panel of the LDC 210 can then be seen to switch from 30mA to 110mA every 10 sec. This direct confirmation was found useful in resolving confusion that can arise regarding the precise current scan range due to the different output impedance settings of signal generators.

### 4.4.3 Design of the gas cell

Gas measurements were performed with a micro-optic gas cell that is basically a short path length of 5.9cm between two graded-index (GRIN) lenses aligned in a ceramic v-groove. The lenses were secured in the v-groove by ultra-violet curing glue. The GRIN lens at the input to the cell collimates the launched light and the lens at the output refocuses the light on to the output fiber and on to the photo-detector. This basic arrangement is placed inside a housing that consists of a 37 cm long tube of 9 cm diameter with two end caps. Rubber gaskets were used between the end caps and the tube to ensure an air tight seal. At one end of the tube the Swagelok valves were used to control the flow of gas in to the gas cell. One valve controls the flow of methane, a second controls the flow of nitrogen used to purge the cell of the methane, and the third valve is connected to an evacuation system consisting of a vacuum pump exhausting in to a fume cupboard. This ensures safe removal of gas from the laboratory.

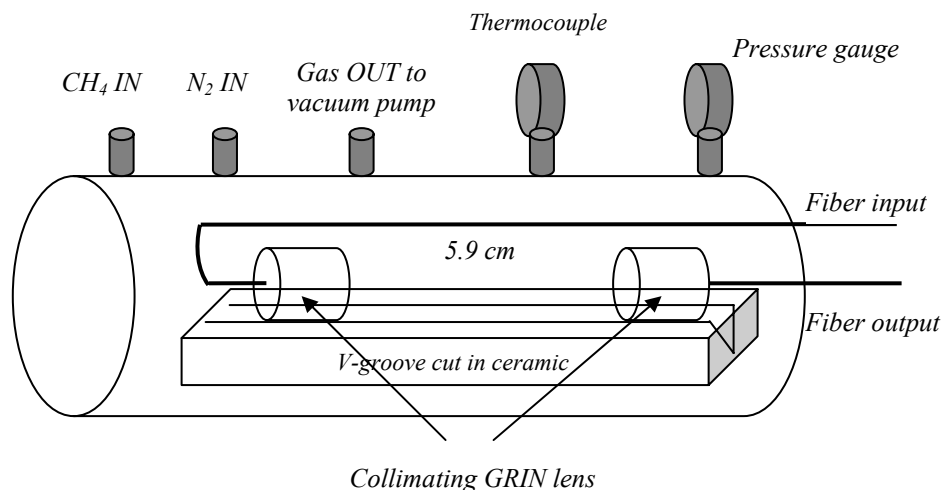


**Fig. 4.12:** Schematic of the arrangement of components within the gas cell.

## Chapter 4: RAM nulling – Principles and Experimental Methods

At the other end cap three holes are provided to insert the input fiber, the output fiber and a digital pressure gauge (LEO-2, Omni instruments) with an absolute pressure range of 0-3 bar. A thermocouple was also inserted in the housing for measurement of the gas temperature with an accuracy of 1°C. The entire housing was tested to ensure leak-proof operation up to 2 bar pressure for a sufficiently long period. Experiments carried out over a period of more than six hours have confirmed the excellent quality of the seals. A second gas cell that was 9.9cm long was also used in later experiments. The new cell had a pair of con-focal C-lenses instead of GRIN lenses.

### 4.4.4 Wavelength referencing of time-indexed signals

All gas signals captured by the digital oscilloscope are by default time-indexed. However, since the emission wavelength of an injection current-tuned DFB laser does not vary linearly with the injection current, the time-indexed abscissa need to be converted to wavelength or equivalently frequency. Figure 4.13 shows the typical variation of the mean laser wavelength as a function of the laser current along with quadratic and cubic polynomial fits.

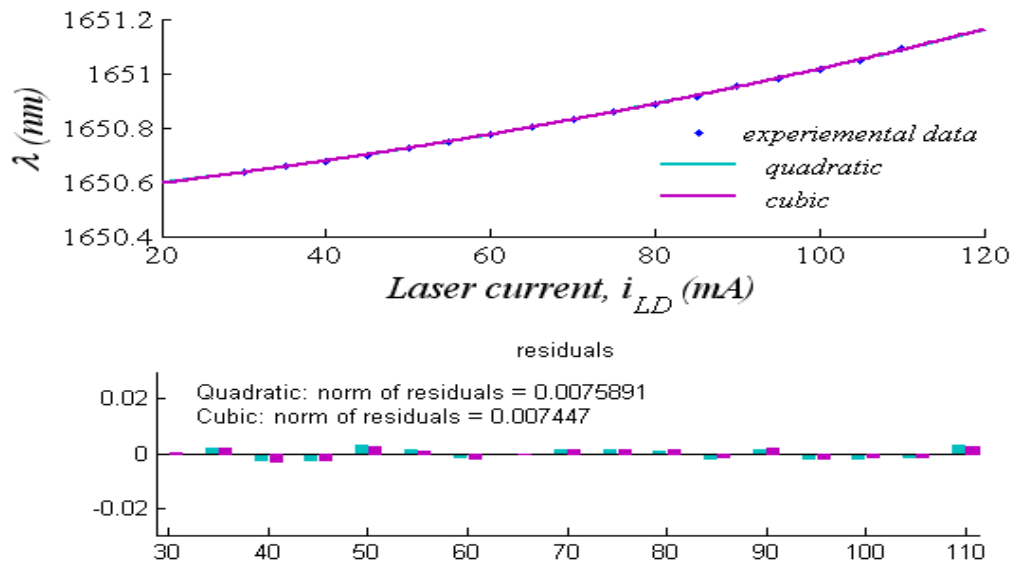


**Fig. 4.13: Nonlinear variation of laser wavelength with injection current.**

#### Chapter 4: RAM nulling – Principles and Experimental Methods

A fiber ring resonator was used to map the time-index to frequency values. This basic technique is implemented using a fiber ring resonator in which two commercial telecom-grade 1550nm 3-dB couplers are configured as shown in Fig. 4.14.

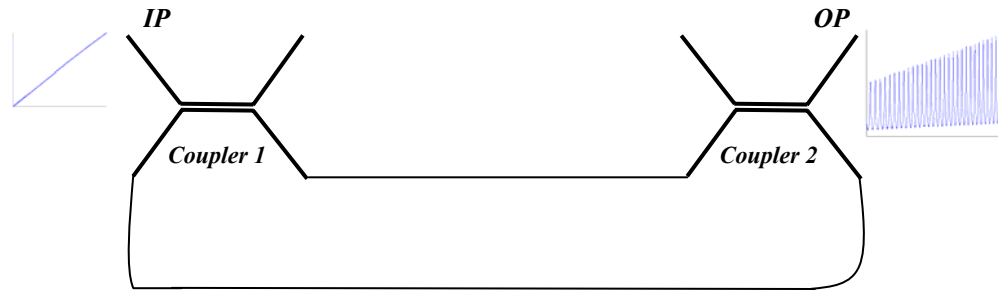


*Fig. 4.14: Fiber ring resonator using two 3-dB couplers.*

It is well-known that the output of such a ring-resonator shows periodic transmission peaks [15-17]. The two factors that mainly decide the frequency response of this resonator are the coupling ratio and ring length. The ring length was 47cm and the corresponding FSR, given by,  $FSR = c/n_{eff}L$ , can be easily calculated. However owing to small uncertainties in the values of  $n_{eff}$  and  $L$  it is best to accurately characterize the resonator using well-known gas absorption lines. This was done using three lines of methane [18, 19] to give an average FSR value of 0.4275 GHz. For accurate frequency referencing the resonator should have high finesse. For further details regarding the modeling of the typical Fabry-Perot-like response of this configuration, and its dependence on the coupling ratio of the couplers, the interested reader is referred to Ref [18] and Ref [19].

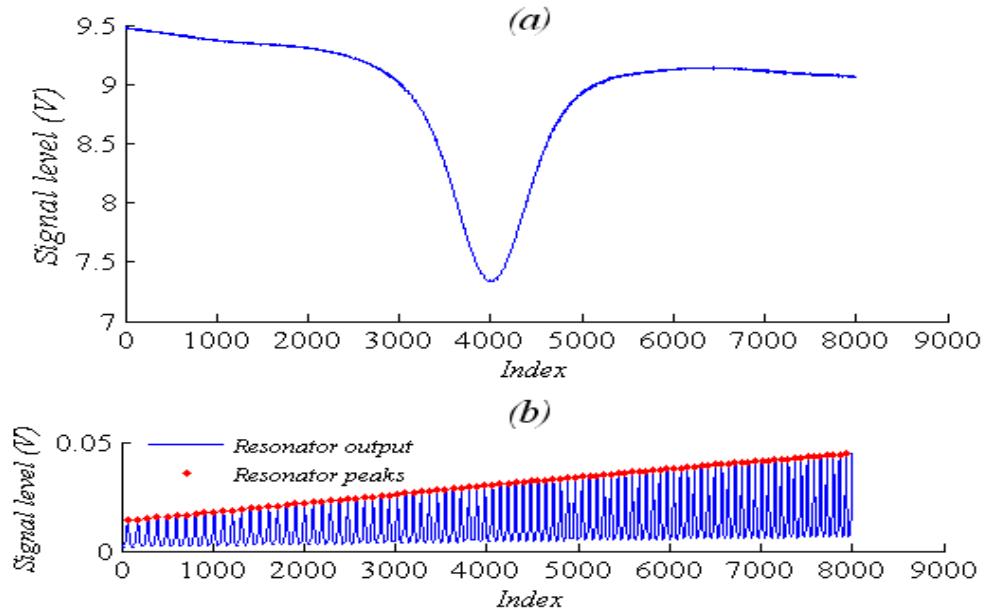


**Fig. 4.15: (a) Time-indexed concentration-dependent RAM signal and (b) fiber-ring resonator peaks captured on the digital oscilloscope.**

It is important to appreciate that the resonator peaks are equally spaced in the *frequency domain* with the separation being equal to the FSR of the resonator (0.4275GHz in this case). However, when the resonator output is captured by the oscilloscope the peak separation is *not* constant in the time domain. This is because the current ramp does not scan the laser frequency linearly. If the frequency scan is linear with current, the successive peaks will also be equally spaced. For the resonator output shown in Fig. 4.15(b), the time-index of resonator peaks and the separation of these time-indices are shown in Fig 4.16. It is seen from Fig 4.16(b) that the spacing of the time indices decreases as the current is ramped up. This is also just about discernible from a close visual inspection of the resonator peaks (red dots) in Fig 4.15(b). This method of inspecting the spacing of the time-indices of resonator peaks is an easy way of detecting nonlinear frequency tuning of a laser. It is important to appreciate this point when constructing the frequency axis from the resonator trace acquired in the time-domain. The program to perform this conversion is detailed in Appendix A.

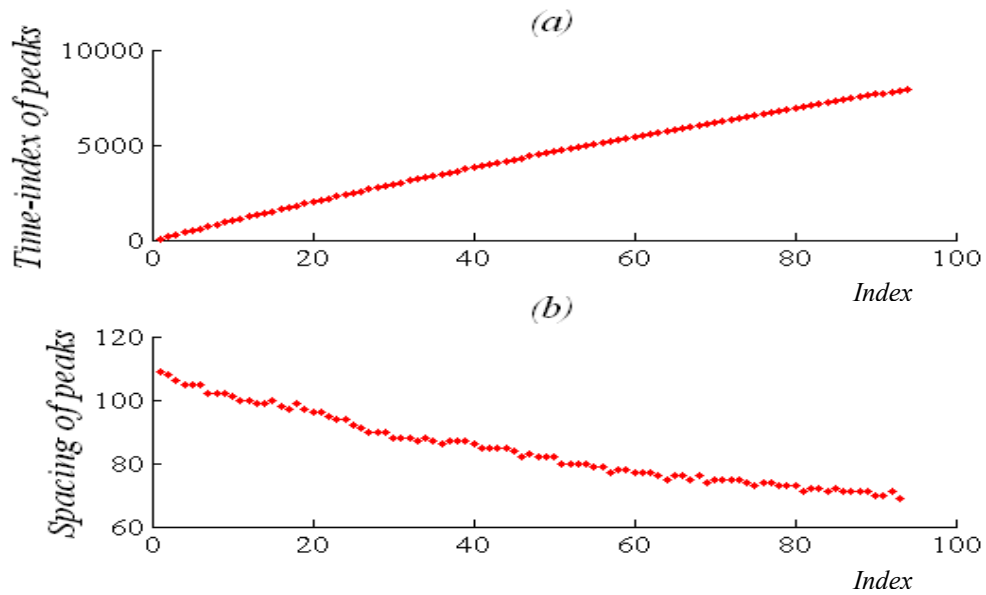


*Fig. 4.16: (a) Time index of resonator peaks, (b) Variation of separation of peaks captured in the time domain by the digital oscilloscope*

#### ***4.4.5 Setting up the lock-in amplifier for signal measurement***

For all measurements the first step is to increase the input gain of the LIA to the maximum extent possible without causing saturation of the input stages. Next, the sensitivity of the LIA is similarly maximized. This ensures that the analog-to-digital converter at the input stage of the LIA is presented with the largest possible analog signal for more accurate digitization. These settings may require adjustment depending on the phase value that is selected to isolate a particular signal.

The LIA phase is set up differently for the RAM method and for the PDM method. For the RAM method the phase of the LIA is at first approximately adjusted to obtain the concentration-dependent RAM signal shown in Fig. 4.15a on channel X. Thereafter a custom LabVIEW VI is used to automatically scan the phase over a small range around this initial value of the phase, and at each point the ratio of the signal minimum to an off-peak value is calculated. The phase at which this ratio is maximized is the phase at which the projection of the RAM on channel X has been maximized. With RAM nulling

## Chapter 4: RAM nulling – Principles and Experimental Methods

in place the signal appears on a zero background, and it is sufficient to find the phase for which the peak of the RAM nulled signal attains its maximum (negative) value.

For the PDM, the LIA phase needs to be adjusted so that a projection of the 1<sup>st</sup> derivative signal is recovered on channel Y in isolation from the RAM signal. The 1<sup>st</sup> derivative of a symmetric absorption line should be symmetric as well. However the actual signal  $-I(\lambda_c) \left. \frac{d\alpha(\lambda)}{d\lambda} \right|_{\lambda_c} . C.I. \delta\lambda \cos(\omega t - \psi)$  that is detected is not symmetric because it is dependent on the intensity that increases significantly over the scan range of the laser current. Therefore the phase of the LIA should be adjusted so that the channel Y signal normalized by the intensity is a symmetric signal that appears on a zero baseline. This ensures that the 1<sup>st</sup> derivative signal is fully isolated from the RAM components. It was observed that no significant error was introduced if the variation of  $\delta\lambda$  is not taken in to consideration.

### 4.4.6 Setting the modulation index

To calculate the amplitude of the modulation current required to obtain a given value of modulation index, the well-characterized resonator is used. With the ramp switched off, a sinusoidal current modulation of  $i_{p-p}$  mA is applied to the laser and the output is passed through the resonator. The resultant frequency tuning of the laser gives rise to several equally-spaced peaks as explained in Sec. 4.4.4. If the number of peaks  $N$ , within one complete period of the sinusoidal current modulation is counted, the net frequency deviation produced by the peak-to-peak value of the current modulation is calculated by simply multiplying  $N$  by the resonator's  $FSR$ . Therefore the current tuning rate is simply the given by  $\frac{\delta\nu}{\delta i} = \frac{N \times FSR}{i_{p-p}}$  in units of GHz/mA. Now, the modulation index is defined as  $m = \frac{\delta\nu}{\gamma}$  where  $\delta\nu$  denotes the amplitude of the frequency deviation due to the current modulation, and  $\gamma$  is the half-width-half-maximum value of the absorption feature of interest. For methane at a pressure of 1 bar this value is approximately 2 GHz. Therefore in order to attain an  $m$ -value of 0.2 for example, the required value of  $\delta\nu$  is

0.4 GHz. Therefore with the knowledge of the laser's tuning rate it is straightforward to calculate and set the appropriate current given by  $\delta v / \left( \frac{\delta v}{\delta i} \right)$  to achieve the required amplitude of current modulation. It should be noted that the tuning rate varies significantly with the frequency of modulation and therefore the laser should be characterized at the frequency at which it is intended to be operated.

## **4.5 Conclusion**

The discussion above introduces a new fiber-optic method to optically eliminate the high, concentration-independent  $1f$  RAM component in TDLS-WMS in real-time. A succinct mathematical treatment was used to show that extraction of the absolute transmission through a gas sample is possible with high accuracy. It is demonstrated that the optical noise of the system can be controlled to within the receiver noise level. This is achieved by selecting an appropriately long delay line and polarization controllers for both signal components. The fiber delay line length is more than 20 times the coherence length of the laser under cw conditions, and even greater with the modulation applied. Hence, even for worst case conditions of beam polarization, the interference noise is minimal. Under conditions of crossed polarization, the interference noise remains stably less than the receiver noise over long periods of time. If required active polarization control can be applied easily to maintain this condition. Polarization-maintaining components and fibers can also be used since these are becoming increasingly affordable.

The problem of a lack of a readily available normalization signal has been addressed. A robust signal normalization method has been devised that avoids the additional step of baseline fitting. It was shown that the output of the system with the delay fiber disconnected (i.e. no nulling) can be used directly to normalize the nulled signal without incurring significant error for low concentrations. This is invaluable for field-deployable, stand-alone instruments that are required to monitor processes in real-time where user-intervention at any step of processing is impractical.

#### **Chapter 4: RAM nulling – Principles and Experimental Methods**

The long-term stability of the RAM nulling condition is excellent, with no need for adjustment over many hours of experimentation. In any case, it is reasonably straightforward to compensate for small drifts with time by periodic adjustment of the VOA. With these features, this new RAM nulling technique can lead to improvements in sensitivity for 1<sup>st</sup> harmonic detection schemes such as the RAM method and the PDM. The technique is fully validated by experimental results presented in the next chapter for different concentrations of methane and varying modulation indices.

## 4.6 References

1. K. Duffin, A. J. McGettrick, W. Johnstone, G. Stewart, D. G. Moodie, “Tunable diode laser spectroscopy with wavelength modulation: a calibration-free approach to the recovery of absolute gas absorption line shapes,” *J. Lightwave Technol.* **25**, 3114-3125 (2007).
2. A. J. McGettrick, K. Duffin, W. Johnstone, G. Stewart, D. G. Moodie, “Tunable diode laser spectroscopy with wavelength modulation: a phasor decomposition method for calibration-free measurements of gas concentration and pressure,” *J. Lightwave Technol.* **26**, 432-440 (2008).
3. J. Reid, J. Shewchun, B. K. Garside, E. A. Ballik, “High sensitivity pollution detection employing tunable diode lasers,” *Appl. Opt.* **17** (2), 300-307 (1978).
4. D. T. Cassidy, J. Reid, “Atmospheric pressure monitoring of trace gases using tunable diode lasers,” *Appl. Opt.* **21** (7), 1185-1190 (1982).
5. X. Zhu, D. T. Cassidy, “Modulation spectroscopy with a semiconductor diode laser by injection-current modulation,” *J. Opt. Soc. Am. B* **14**, 1945-1950 (1997).
6. P. Kluczynski, O. Axner, “Theoretical description based on Fourier analysis of wavelength-modulation spectroscopy in terms of analytical and background signals,” *Appl. Opt.* **38**, 5803-5815 (1999).
7. S. Schilt, L. Thevenaz, P. Robert, “Wavelength modulation spectroscopy: combined frequency and intensity laser modulation,” *Appl. Opt.* **42**, 6728-6738 (2003).
8. L. C. Philippe, R. K. Hanson, “Laser diode wavelength modulation spectroscopy for simultaneous measurement of temperature, pressure, and velocity in shock-heated oxygen flows,” *Appl. Opt.* **32**, 6090-6103 (1993).
9. M. Gehrtz, G. C. Bjorklund, E. A. Whittaker, “Quantum-limited laser frequency-modulated spectroscopy,” *J. Opt. Soc. Am. B*, **2**, 1510-1526 (1985).

#### Chapter 4: RAM nulling – Principles and Experimental Methods

10. C. B. Carlisle, D. E. Cooper, “Tunable-diode-laser frequency-modulation spectroscopy using balanced homodyne detection,” *Opt. Lett.* **14**, 1306-1308 (1989).
11. C. B. Carlisle, D. E. Cooper, “Tunable diode laser frequency modulation spectroscopy through an optical fiber: High sensitivity detection of water vapour,” *Appl. Phys. Lett.* **56**, 805-807 (1990).
12. X. Zhu, D. T. Cassidy, “Electronic subtracter for trace gas detection with InGaAsP diode lasers,” *Appl. Opt.* **34**, 8303-8308 (1995).
13. J. T. C. Liu, J. B. Jeffries, R. K. Hanson, “Large-modulation-depth  $2f$  spectroscopy with diode lasers for rapid temperature and species measurements in gases with blended and broadened spectra,” *Appl. Opt.* **43**, 6500-6509 (2004).
14. L.S. Rothman et al., “The HITRAN 2004 molecular spectroscopic database,” *J. Quant. Spectrosc. Radiat. Transfer*, Vol. 96, pp 139-204, 2005
15. P. Urquhart, “Transversely coupled fiber Fabry-Perot resonator theory,” *Appl. Opt.* **26** (3), 456-463 (1987).
16. P. Urquhart, “Compound optical-fiber-based resonators,” *J. Opt. Soc. Am. A* **3**, 803-812 (1988).
17. L. F. Stokes, M. Chodorow, H. J. Shaw, “All-single-mode fiber resonator,” *Opt. Lett.* **7** (6), 288-290 (1982)
18. K. Duffin, “Wavelength modulation spectroscopy with tunable diode lasers: A calibration-free approach to the recovery of absolute gas absorption line shapes,” Ph.D. Thesis, Dept. of EEE, Univ. Strathclyde, Glasgow, Scotland, 2007.
19. A. J. McGettrick, “Wavelength modulation spectroscopy with tunable diode lasers: A calibration-free approach to the recovery of absolute gas absorption line shapes,” Ph.D. Thesis, Dept. of EEE, Univ. Strathclyde, Glasgow, Scotland, 2007.

#### **Chapter 4: RAM nulling – Principles and Experimental Methods**

20. A. L. Chakraborty, K. Ruxton, W. Johnstone, M. Lengden, K. Duffin, “Elimination of residual amplitude modulation in tunable diode laser wavelength modulation spectroscopy using an optical fiber delay line,” *Opt. Exp.***17** (12), 9602-9607 (2009)
21. W. Demtroder, “Laser Spectroscopy Vol. 1: Basic Principles,” Springer-Verlag Berlin Heidelberg, 2008

# *Chapter 5*

---

## **Calibration-free $1f$ WMS with RAM nulling – Validation of technique**

---

### **5.1 Introduction**

The RAM nulling technique described in the earlier chapter to optically eliminate the concentration-independent  $1f$  RAM component due to the direct IM of the DFB laser represents a significant step towards alleviating the problem of a high background signal in  $1f$  WMS in general. It is also particularly important for the two  $1f$  calibration-free

## Chapter 5: Calibration-free $1f$ WMS with RAM nulling – Validation of technique

techniques namely, the RAM technique [1], and the Phasor Decomposition method (PDM) [2], for the recovery of absolute gas absorption profiles. This chapter first provides a preliminary demonstration of the RAM nulling strategy. RAM-nulled absorption signals for two values of concentration are fully analyzed to demonstrate the recovery of absolute gas absorption line shapes. The issues involved in signal normalization are then discussed followed by a description of a practical and convenient signal normalization method. Results using the RAM method for 10.13% and 1.02% methane and two values of modulation index are presented next. These results show that accurate recovery of absorption lines is possible with RAM nulling in place.

The mathematical formulation necessary for the PDM with RAM nulling incorporated is then introduced along with a description of the signals involved. Detailed experimental demonstrations are presented for the PDM with RAM nulling incorporated for 10.13% and 1.02% methane at varying modulation indices under ambient conditions of pressure and temperature. It is shown that the results with nulling are just as accurate as those without nulling. The validity of a practical normalization strategy introduced in this chapter is also demonstrated. For modulation indices beyond 0.7, however, the accuracy of measurement is degraded because the Taylor series expansion does not account for higher order terms that become significant at high values of modulation index. The chapter ends with a comparison of results for 0.1% methane with and without RAM nulling. It is shown that RAM nulling makes it possible to recover the concentration-dependent absorption profile that is otherwise lost in the high RAM background if RAM nulling is not implemented. The results for 0.1% are fully analyzed at the end of chapter 6.

## 5.2 Preliminary demonstration of RAM nulling

This section presents a preliminary demonstration of the elimination of the  $1f$  RAM background using the experimental arrangement described in the previous chapter. Section 5.2.1 shows the RAM nulled signals for three values of concentration of methane at ambient conditions of temperature and pressure. The elimination of the

background requires the identification of a suitable normalization signal. The normalization technique is described next in Sec. 5.2.2. Finally a practical method of signal normalization is discussed in Sec. 5.2.3 that is better suited for industrial operation of such systems. Detailed experimental results using RAM nulling for various concentrations of methane are presented later in the chapter along with associated issues that complicate signal recovery.

### 5.2.1 Elimination of the 1f background RAM

Figure 5.1 demonstrates the efficacy of RAM nulling process for three concentrations of methane in nitrogen (10%, 1% and 0.1%) at a pressure of approximately 1 bar and a temperature of approximately 20°C.

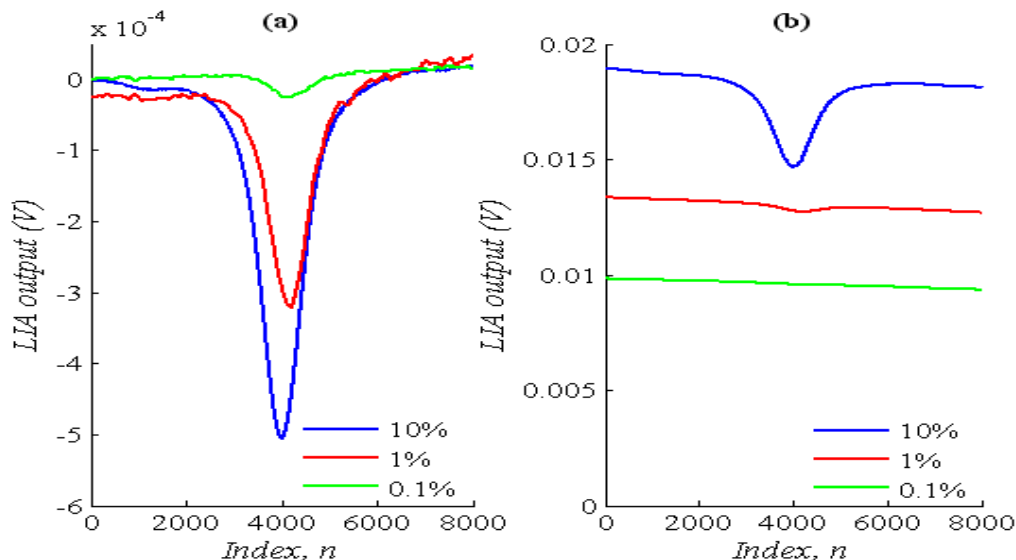


**Fig. 5.1: LIA signals for 10.13%, 1.02% and 0.1017% methane in nitrogen for (a) RAM-nulled case, and (b) Non-nulled case, showing the large background level that obscures the absorption signal.**

In Fig. 5.1b the concentration-independent 1f RAM is clearly evident from the high background. The background level is different because the experiments were performed on different days and the optical throughput of the system was different. The significant reduction in the high, concentration-independent background is clearly seen from a comparison of Fig. 5.1a and Fig. 5.1b. The apparent mismatch in the peak position of the three signals is due to the fact that these data were recorded on different days, and no

## Chapter 5: Calibration-free 1f WMS with RAM nulling – Validation of technique

attempt was made to maintain constant settings for the trigger level and horizontal position setting of the oscilloscope. This apparent anomaly is resolved by wavelength-referencing these signals using the corresponding and simultaneously-recorded resonator output. Clearly, the background level for the nulled case is nominally zero, but with a small sloping non-zero component that arises from the wavelength dependencies of the couplers. This issue is examined more closely in the next chapter. The slope of the non-nulled signal is dictated by the characteristic downward slope of the linear IM term  $\Delta I(\lambda_c)$ , which is in turn governed by the nature of the DFB laser's current-intensity curve. For each case the sensitivity setting of the LIA was different and maximized without causing saturation. For the non-nulled cases it becomes increasingly difficult to selectively and cleanly recover the absorption-dependent signals for low concentrations due to the high background. The significant reduction of the background level allowed the LIA sensitivity/gain to be increased greatly without causing saturation and if required, the recovered absorption signals can be selectively amplified further before being digitized in order to reduce the effects of quantization noise. This clearly demonstrates the recovery of the RAM nulled signals. The recovery of the absorption line by appropriate signal normalization is demonstrated in the following section.

### 5.2.2 Normalization of signals

As explained in Sec. 4.3, the near-perfect cancellation of the baseline with the RAM nulling in place implies that, by default, there is no signal that can be used to normalize the absorption-dependent RAM-nulled signal. Therefore the signal at  $OP_1$  with the delay fiber disconnected must be used for signal normalization. Figure 5.2 shows the nulled and non-nulled outputs at  $OP_1$  along with a baseline fit to the latter for a gas concentration of 10.13%. These are the only signals that are required to extract the gas absorption line.

The  $OP_1$  signal with the delay arm disconnected is shown in green. This signal is the same as that given by Eq. 2.6 and is given by  $\Delta I_1(\lambda_c)[1 - \alpha(\lambda_c)CI] \sin \psi \cos \omega t$ . Note that the relatively strong absorption superimposed on this signal makes it necessary to fit a

## Chapter 5: Calibration-free 1f WMS with RAM nulling – Validation of technique

baseline to it so as to negate the effect of the absorption on the normalization signal. If this is not done the extracted absorption profile will be in significant error. A baseline fit to this signal shown in red, is mathematically given by  $\Delta I_1(\lambda_c) \sin \psi \cos \omega t$ . Using Eq. 4.11 the gas absorption line can now be extracted.

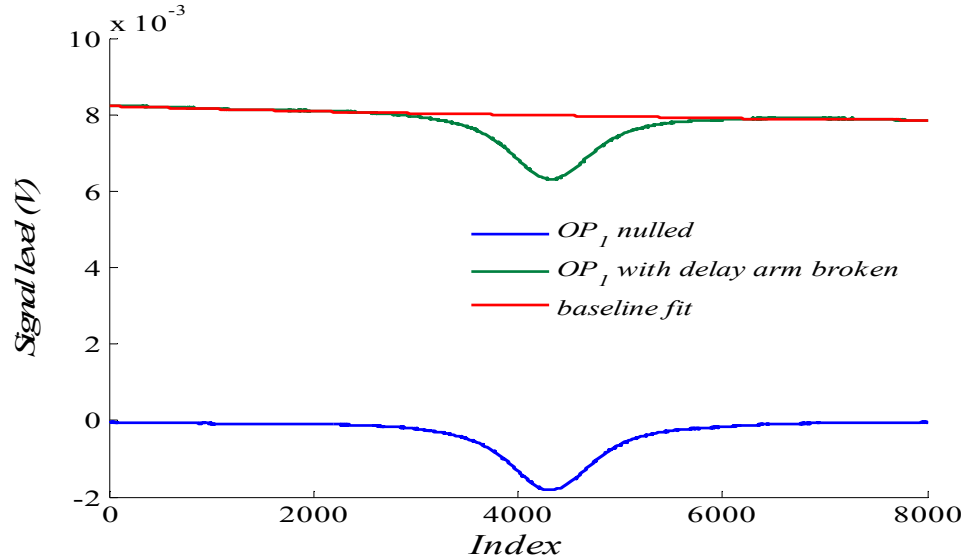
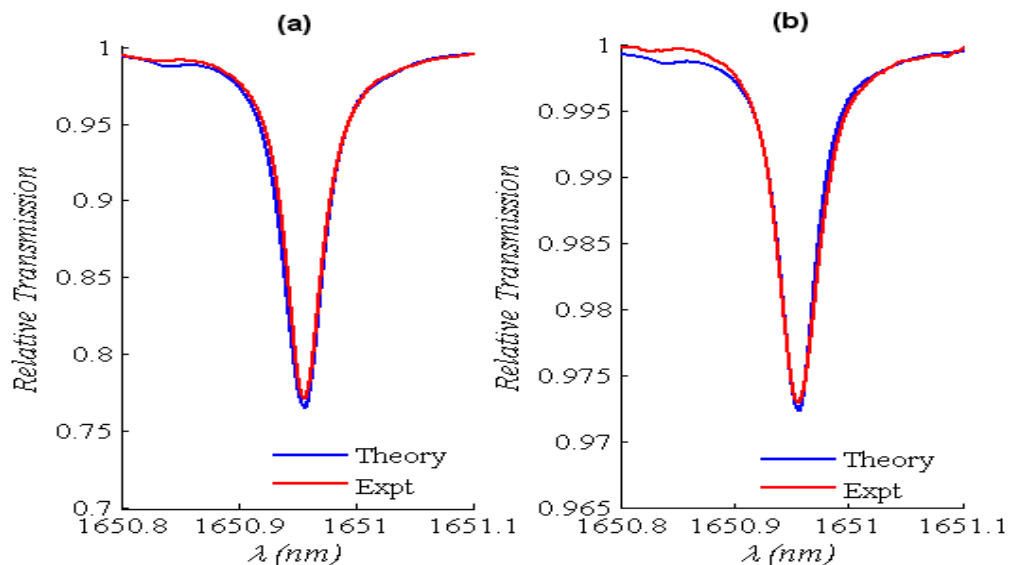


Fig. 5.2 Signal at  $OP_1$  with and without nulling and the baseline fit to the latter.

Finally, the validity of the RAM nulling technique and the normalization strategy are conclusively proved by fully analyzing the results for 10.13% and 1.02% methane under ambient conditions as shown in Fig. 5.3. The time-indexed  $x$ -axis has been converted to wavelength axis by using the fiber ring resonator and the wavelength-referencing strategy described earlier. The signals have been scaled by the corresponding lock-in amplifier sensitivities. Clearly, the absorption line can be recovered with high accuracy with the RAM nulling technique in place. The same method of normalization using baseline fits to the non-nulled signal has been used for both cases.

A subtle practical issue that is apt to be overlooked in a laboratory environment is the process of baseline fitting discussed earlier. This is elaborated in the following section.



*Fig. 5.3: Relative transmission for methane for (a) concentration 10.13%, pressure 1.067 bar temperature 22.6°C, and (b) concentration 1.02% , pressure 1.082 bar and temperature 23.6°C.*

### 5.2.3 Practical method for signal normalization

Although the RAM nulling technique and the normalization process described above work well, the additional requirement of having to fit a baseline to the nulled  $OP_I$  signal in Eq. 4.11 as well as the non-nulled  $OP_I$  signal (with the delay arm disconnected) is inconvenient for stand-alone field-deployment of such instruments. The baseline fitting requires the availability and identification of offline line regions that are spectrally well separated from the target absorption feature. If the baseline for the nulled signal is estimated based on points that are not sufficiently far removed from the line centre, the recovered absorption profile gets artificially narrowed as shown in Fig. 5.4 for a 10.13% mixture of methane under ambient conditions of pressure and temperature.

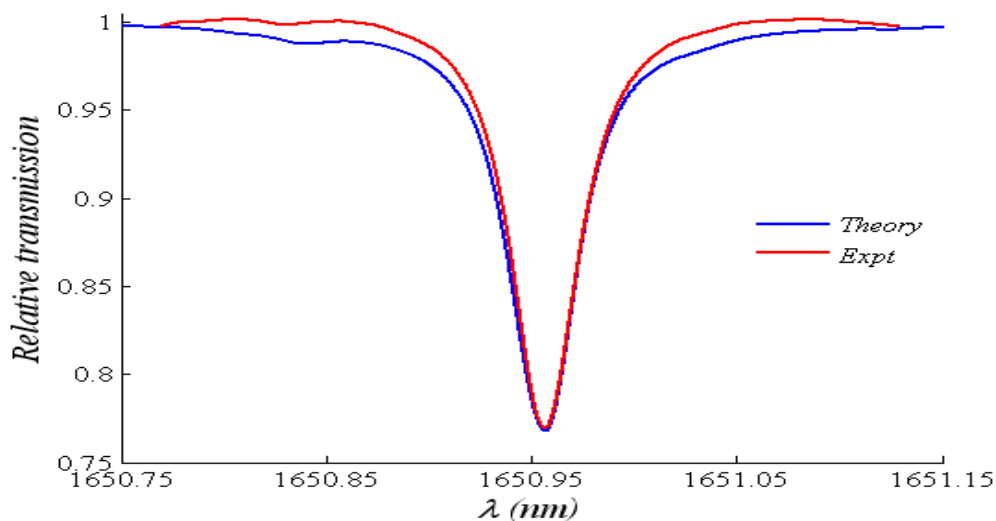


*Fig. 5.4: Systematic measurement error introduced by signal normalization using a baseline fit estimated using off-line regions that are too close to the absorption feature*

The systematic error introduced by the baseline estimation is clearly seen by the narrowing and an apparent upward shift of the line. It is tempting but incorrect to shift the trace down for a better match between the spectral wings of the experimental data and the theoretical plot. The narrowing of the line translates to higher errors in the extraction of pressure which is related to the FWHM of the recovered profile. Any artificial vertical shifting of the experimental plot introduces errors in concentration which is related to the peak depth.

Reduction of this systematic error requires optimization of the baseline fit. This implies a certain degree of user intervention in identifying suitable off-line regions that is crucial for accurate measurements. Although baseline optimization is not difficult in a laboratory environment such operational luxuries are often not afforded by stand-alone instruments in field applications. The requirement of a baseline fit has a two-fold implication for sensitive practical systems. First, a strong and spectrally well-isolated absorption line must be available for interrogation. Second, the laser must be scanned over a spectral range wide enough to enable the identification of suitable off-line regions for baseline fitting. In many industrial applications, it may be difficult to ensure either or both of these conditions. Even for modest pressures a well-isolated line broadens out considerably and its wings may be affected by similar broadening of adjacent spectral

## Chapter 5: Calibration-free 1f WMS with RAM nulling – Validation of technique

features. The range of the wavelength scan is limited by the recommended safe operating range of the laser current which therefore makes it even more difficult to include non-absorbing spectral wings in high pressure applications. Moreover, if multiple gas lines need to be recovered, the need for non-absorbing spectral wings for each feature becomes an even more impractical requirement. For the methane line chosen for these experiments, interference from other spectral features is not a problem but this cannot be expected to be the case in general. Therefore, it is clear that baseline fitting to the nulled signal is a potential limitation and steps need to be taken to deal with this issue.

For the initial results presented here a small residual slope in the nulled signals was unavoidable. As pointed out earlier, this is due to the small wavelength-dependence of the couplers. It is possible, however, to use wavelength-flattened couplers that have much smaller wavelength-dependence and choose the experimental configuration properly to virtually eliminate this slope. By this method the need for baseline fitting to the nulled signal in Eq. 4.11 is removed. This point will be developed further in Chapter 6 where the details of the experimental arrangement and the associated analysis are presented.

The second issue is that of baseline fitting to the non-nulled signal. Ideally the normalization process should require no baseline fitting and therefore no user-intervention. A readily available normalization signal is of great value in a practical system because this enables full automation of the system for maximum robustness and flexibility. It has been shown that for signal normalization, a baseline fit to the non-nulled signal had to be used. It turns out, however, that for low concentrations it may not be necessary to fit a baseline to the non-nulled signal. The signals for a 1.02% methane mixture with and without nulling, as shown in Fig. 5.5, are considered next. It is seen that for this low value of concentration there is very little effect of the gas absorption on the non-nulled signal. This should be contrasted with the case for a concentration of 10.13% shown in Fig. 5.2. Note that amplification of the non-nulled signal is limited by the high offline background level and therefore it is not possible to selectively amplify the absorption signal. However, no such condition exists for the nulled signal. This

## Chapter 5: Calibration-free 1f WMS with RAM nulling – Validation of technique

implies that for such low concentrations the effect of absorption on the non-nulled signal will be negligible, and the acquired signal and its baseline fit will be indistinguishable. This condition can be written mathematically as  $\Delta I_1(\lambda_c)[1 - \alpha(\lambda_c)Cl] \sin \psi \cos \omega t \approx \Delta I_1(\lambda_c) \sin \psi \cos \omega t$ . Therefore, the non-nulled signal itself can be used for normalization.

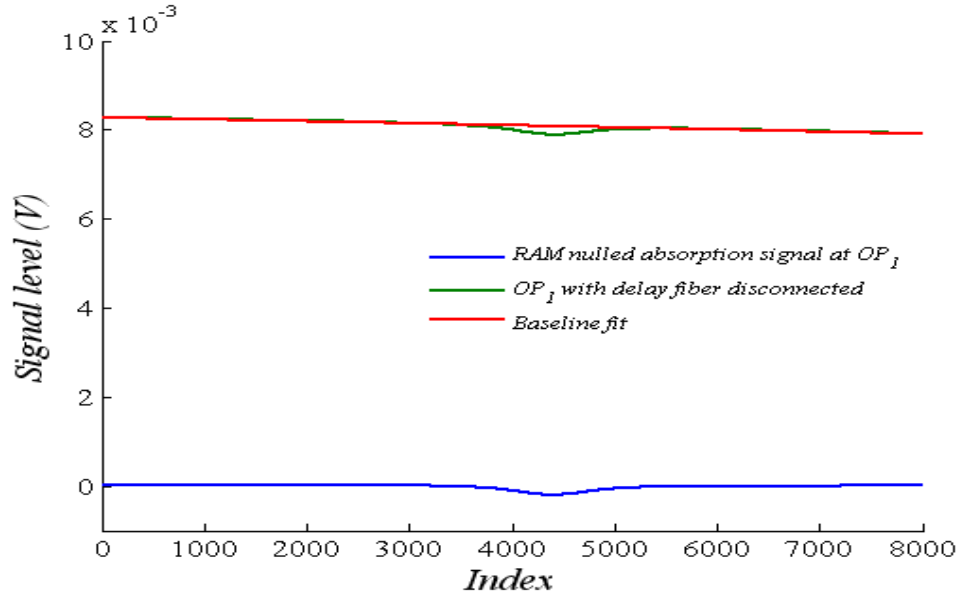


*Fig. 5.5: Raw signals at OP<sub>1</sub> for methane for concentration 1.02%, pressure 1.082 bar and temperature 23.6°C with nulling and without nulling.*

The validity of using the non-nulled signal directly instead of the baseline fit for normalization signal is demonstrated in Fig. 5.6 in which a comparison between the two normalization strategies is made for 1.02% methane. In the first case the absorption signal is normalized by the baseline fit to the non-nulled signal, while in the second the non-nulled signal itself is used for normalization. It is clearly seen that the recovery of the line shape is just as accurate except for a very small difference in the peak value. This difference is in any case very small and will be negligible for lower gas concentrations. The mismatch to left of the traces was verified to be due to electrical noise. The negligible difference between the two cases implies that for the normalization process, it is not necessary to use a baseline fit to the  $OP_1$  signal with the delay arm disconnected.

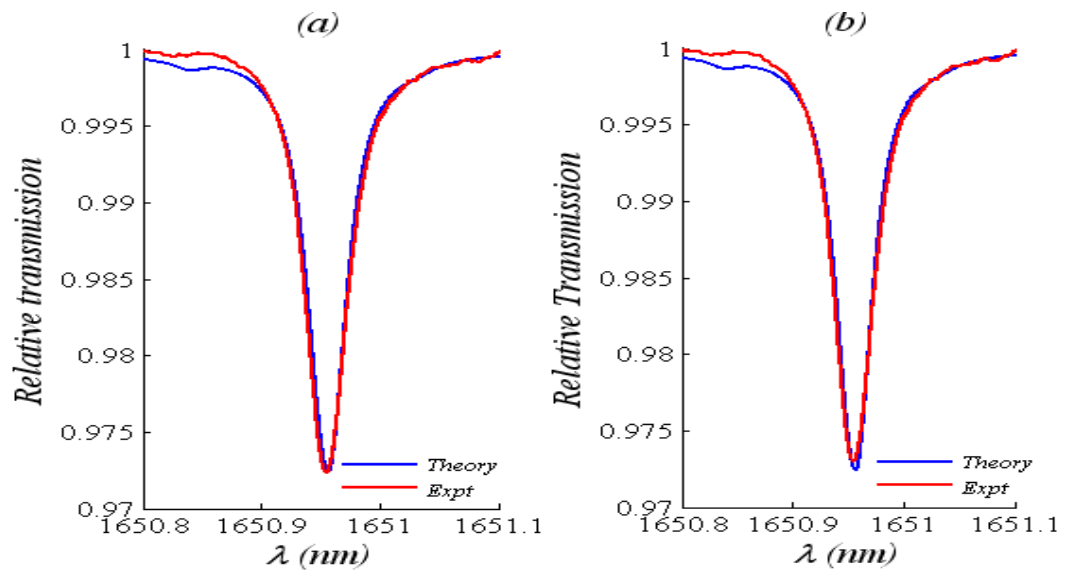


*Fig. 5.6: Relative transmission for methane for concentration 1.02%, pressure 1.082 bar and temperature 23.6°C extracted by, (a) normalization by baseline fit to the signal at  $OP_1$  with the delay arm disconnected, and (b) by the signal at  $OP_1$  with the delay arm disconnected.*

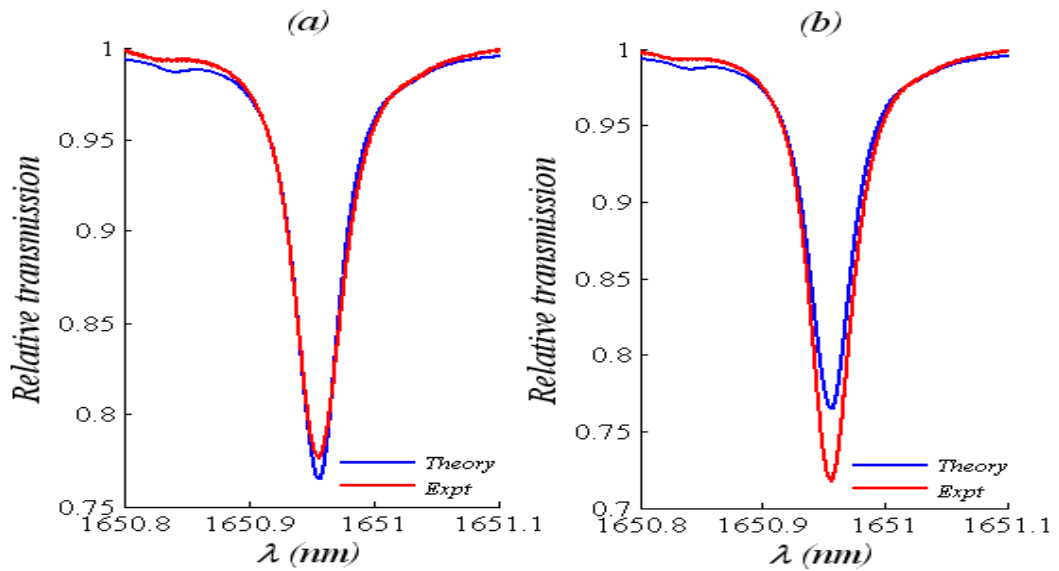


*Fig. 5.7: Relative transmission for methane for concentration 10.13%, pressure 1.082 bar and temperature 23.6°C extracted by, (a) normalization by baseline fit to the signal at  $OP_1$  with the delay arm disconnected, and (b) by the signal at  $OP_1$  with the delay arm disconnected.*

For the case of the 10.13% methane mixture shown in Fig. 5.7 the significant difference between the two cases implies that for higher concentrations the baseline fit to the  $OP_1$  signal with the delay arm disconnected must be used for normalization.

## 5.3 Experimental results using the RAM technique with nulling

To fully validate the method for the recovery of absolute gas absorption line shapes, measurements are presented in the following sections for certified values of 10.13% and 1.02% mixtures of methane in nitrogen balance at atmospheric pressure and temperature. The experimental data are compared with theoretical Voigt profiles simulated using the HITRAN 2004 spectral database. First, the recovered data was processed according to Eq. 4.11 and then the time-indexed horizontal scale was converted to a wavelength scale using the simultaneously recorded output signal from the accurately characterized fiber resonator. The value of the modulation index,  $m$ , was chosen to be approximately 0.2 and 0.7 for the RAM method with nulling. For  $m$ -values greater than 0.2 it is necessary to use appropriate correction factors [1, 2], mentioned in Sec. 2.4.3 to account for additional 1f components that arise due to the cross coupling of the linear IM and higher order terms from the Taylor series expansion of the spectrally-modulated absorption. The excellent agreement between the experiments and the theory proves that the accuracy of measurement has not been compromised by the RAM nulling technique and its data processing algorithm. Results with and without background nulling are compared to prove that the normalization strategy is correct and efficient.

### 5.3.1 RAM method with background nulling for 10.13% $CH_4$

Two sets of results are presented below for each of two  $m$ -values to demonstrate the accurate recovery of the absorption line shape using the RAM method with the 1f background RAM nulling. The small variations in the two sets of data for each  $m$ -value are inevitable under normal experimental conditions. It is seen that the signals for the

Chapter 5: Calibration-free 1f WMS with RAM nulling – Validation of technique

higher  $m$ -value have higher SNR. All signals have been digitally filtered as discussed later in chapter 6.

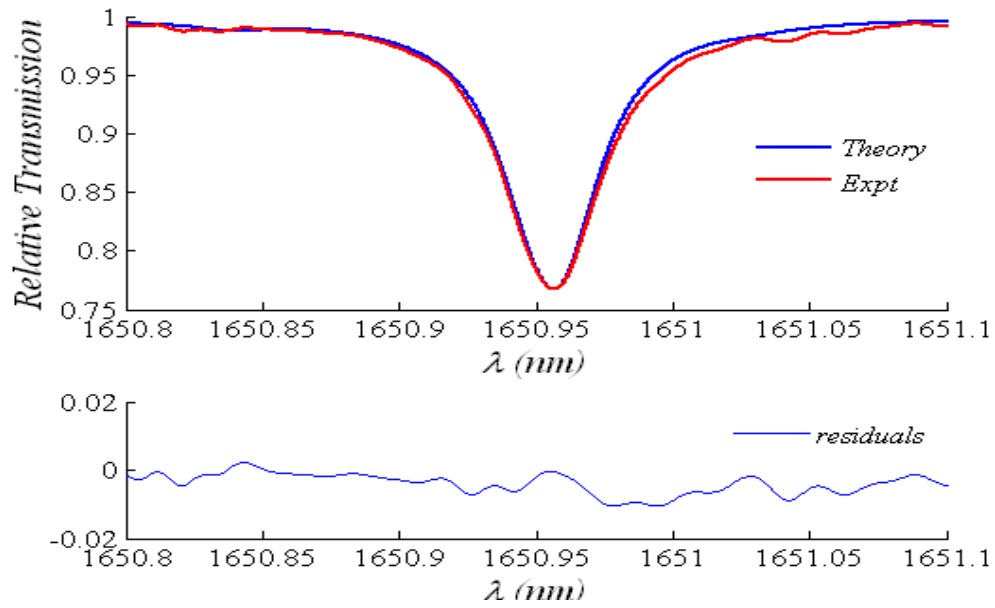


Fig. 5.8: 10.13%  $CH_4$  at 1.014 bar and 20.4°C,  $m = 0.2$ ,  $\Phi = 32^\circ$ , LIA  $t_c = 1ms$ , LIA sens: RAM nulled = 100 $\mu V$ , non-nulled = 500 $\mu V$

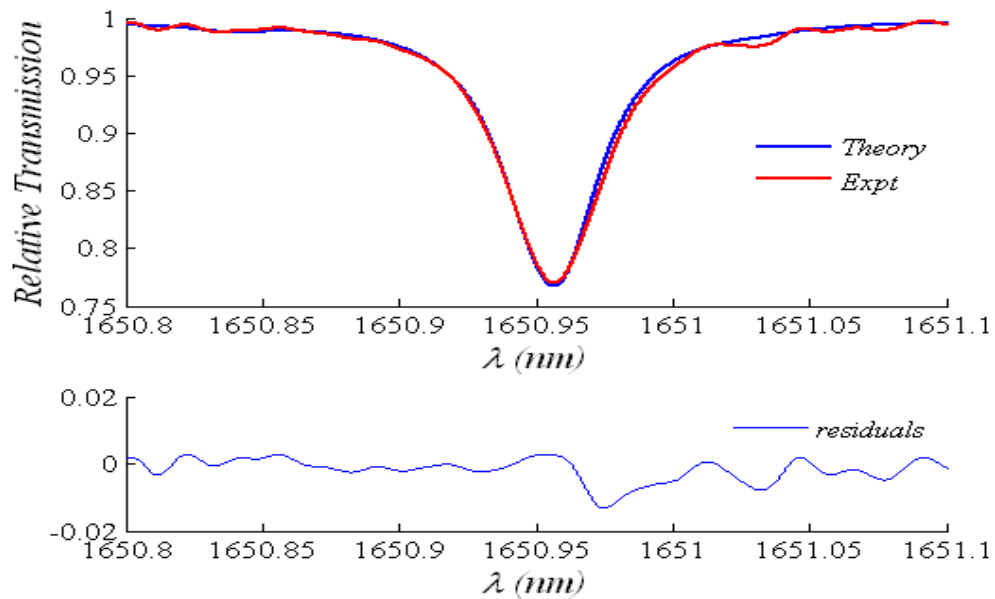


Fig. 5.9: 10.13%  $CH_4$  at 1.026 bar and 20.1°C,  $m = 0.2$ ,  $\Phi = 35^\circ$ , LIA  $t_c = 1ms$ , LIA sens: RAM nulled = 50 $\mu V$ , non-nulled = 100 $\mu V$

Chapter 5: Calibration-free 1f WMS with RAM nulling – Validation of technique

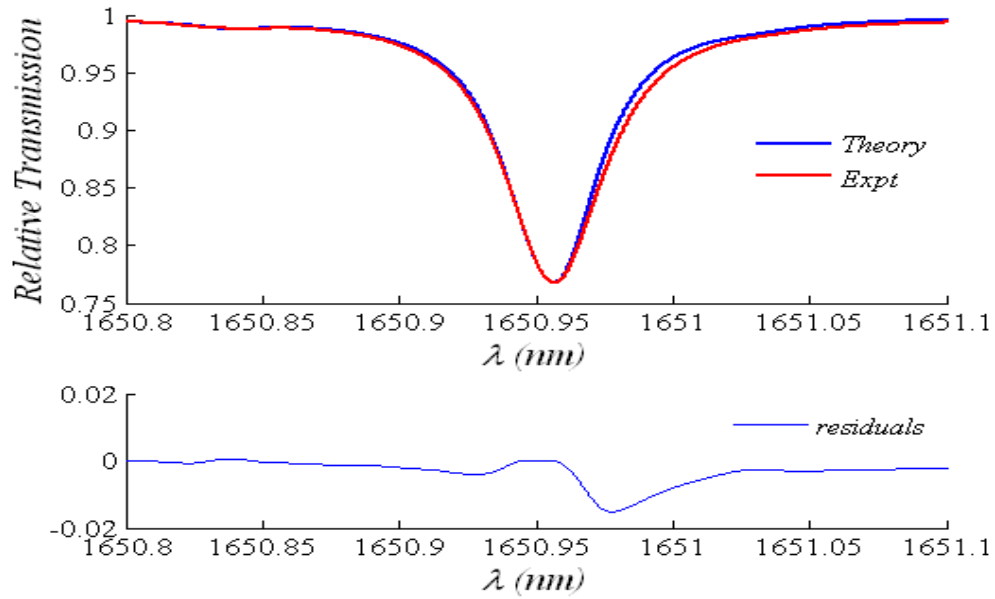


Fig. 5.10: 10.13% CH<sub>4</sub> at 1.010 bar and 20.2°C,  $m = 0.7$ ,  $\Phi = 32^\circ$ , LIA  $t_c = 1\text{ms}$ , LIA sens: RAM nulled = 500 $\mu\text{V}$ , non-nulled = 2mV

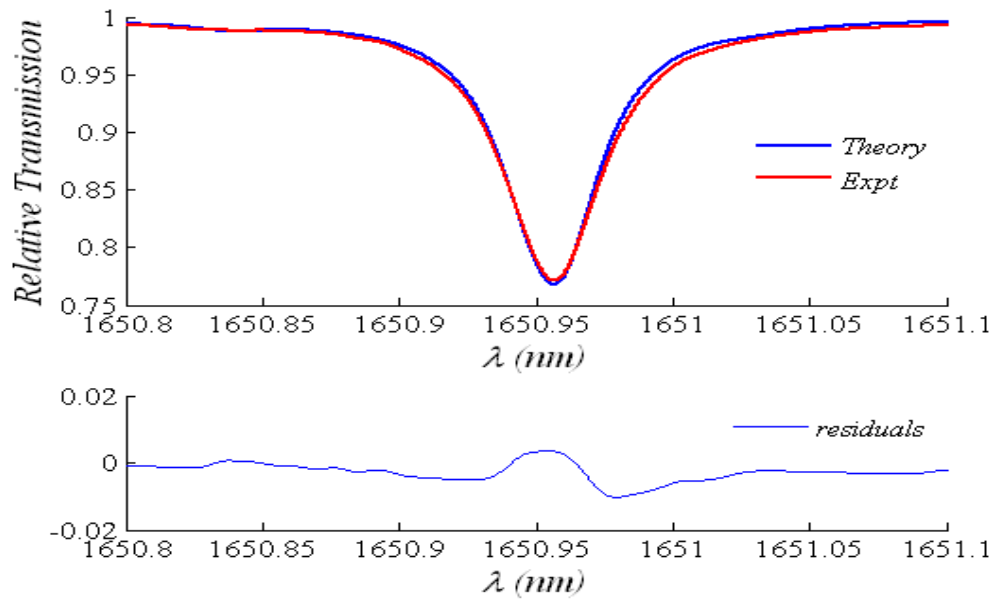


Fig. 5.11: 10.13% CH<sub>4</sub> at 1.014 bar and 19.2°C,  $m = 0.7$ ,  $\Phi = 35^\circ$ , LIA  $t_c = 1\text{ms}$ , LIA sens: RAM nulled = 100 $\mu\text{V}$ , non-nulled = 500 $\mu\text{V}$

## Chapter 5: Calibration-free 1f WMS with RAM nulling – Validation of technique

The variations on the residuals for the data for  $m = 0.2$  reflect the effect of etalon fringes that is also visible on the experimental data. For  $m = 0.7$  the stronger gas signals effectively suppresses this effect and the residuals show much less variations. There is a small but consistent mismatch between the two plots to the right of the line-centre. The reason for this is not yet fully established but could be due to a small error in the selection of the LIA phase or in the correction factor algorithm that assumes a constant value of tuning rate of the laser (GHz/mA) throughout the scan range.

### 5.3.2 Comparison with RAM method without nulling

Results without the background nulling are presented below for  $m = 0.2$  and  $m = 0.7$ , and for almost the same pressure and temperature values to show that accuracy of the recovery of gas absorption lines is not compromised by the RAM nulling arrangement.

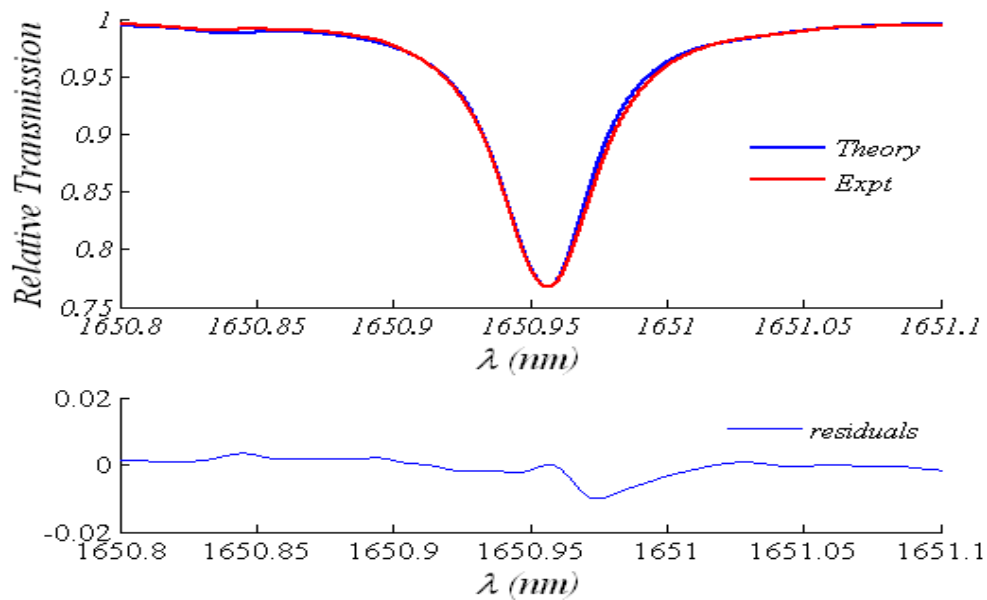


**Fig. 5.12:** 10.13%  $\text{CH}_4$  at 1.014 bar and 20.7°C,  $m = 0.2$ ,  $\Phi = 32^\circ$ , LIA  $t_c = 1\text{ms}$ , LIA sens: RAM signal = 500 $\mu\text{V}$

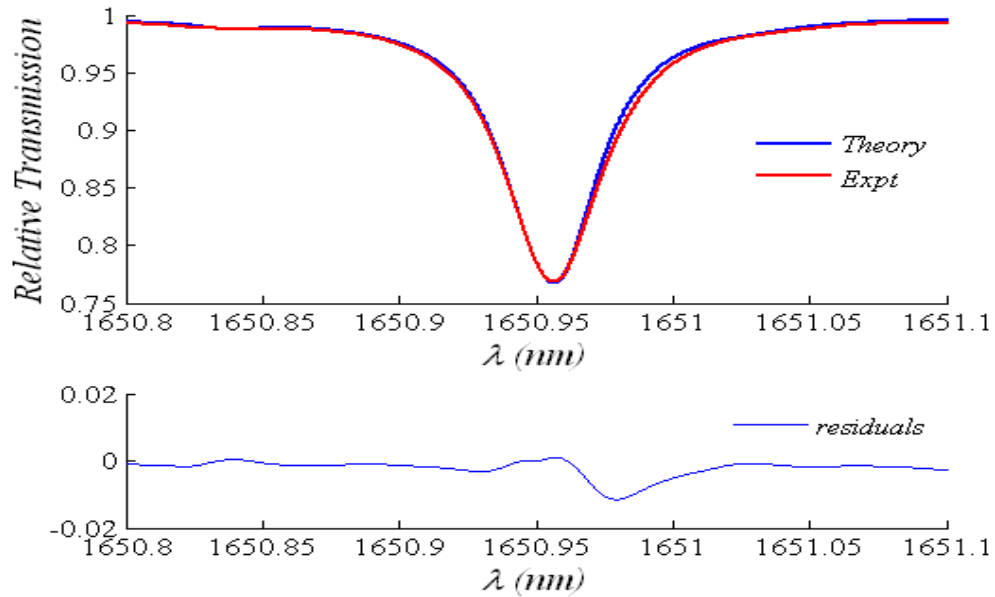


Fig. 5.13: 10.13%  $\text{CH}_4$  at 1.013 bar and 20.5°C,  $m = 0.7$ ,  $\Phi = 32^\circ$ , LIA  $t_c = 1\text{ms}$ , LIA sens: RAM signal = 2mV

### 5.3.3 RAM method with background nulling for 1.02% $\text{CH}_4$

Results for methane concentration of 1.02% in nitrogen balance are shown next to demonstrate the accurate recovery of the absorption line shape for lower concentrations using the RAM method. It is seen that for  $m = 0.2$  the signal-to-noise ratio is poor due to the etalon fringes that arise mainly from the gas cell. However, for  $m = 0.5$  and  $m = 0.7$ , the signal-to-noise ratio improves greatly. Recovery of gas absorption lines with good accuracy is thus possible.

Chapter 5: Calibration-free 1f WMS with RAM nulling – Validation of technique

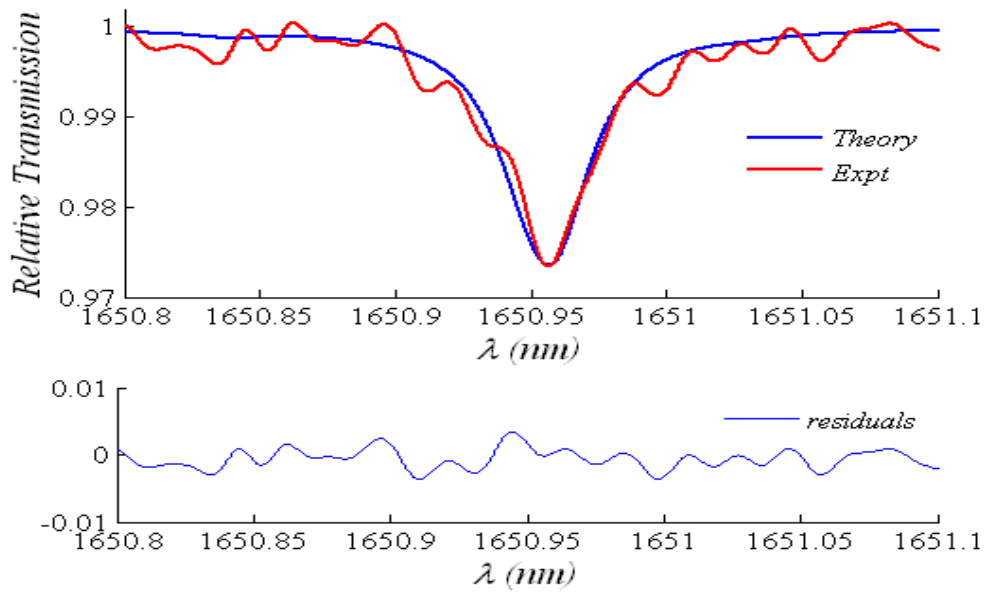


Fig. 5.14: 1.02%  $CH_4$  at 1.013 bar and 17.8°C,  $m = 0.2$ ,  $\Phi = 34^\circ$ , LIA  $tc = 1ms$ , LIA sens: RAM nulled = 10 $\mu V$ , non-nulled = 100 $\mu V$

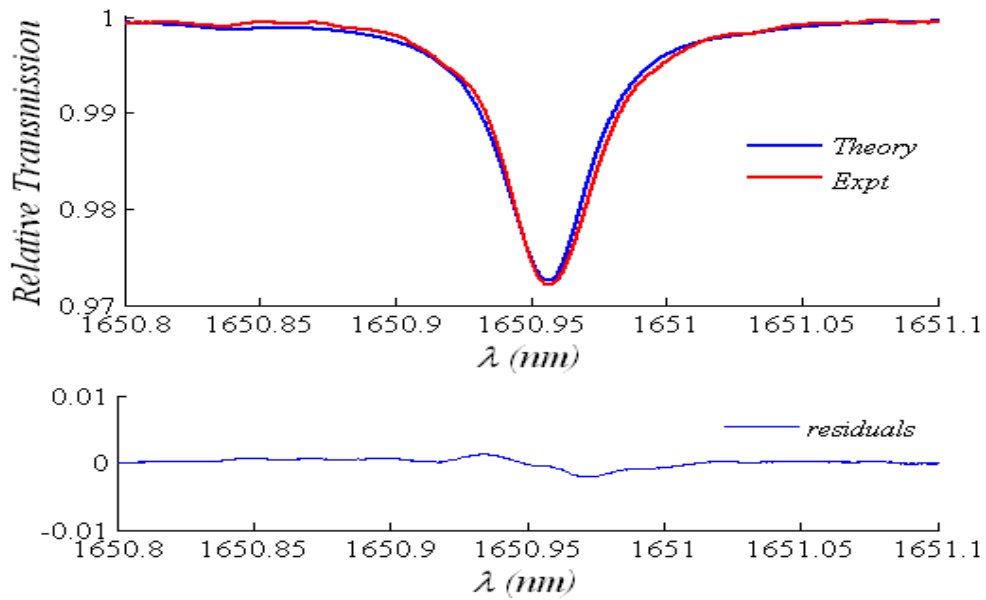


Fig. 5.15: 1.02%  $CH_4$  at 1.051 bar and 23.6°C,  $m = 0.5$ ,  $\Phi = 34^\circ$ , LIA  $tc = 1ms$ , LIA sens: RAM nulled = 100 $\mu V$ , non-nulled = 1mV

Chapter 5: Calibration-free 1f WMS with RAM nulling – Validation of technique

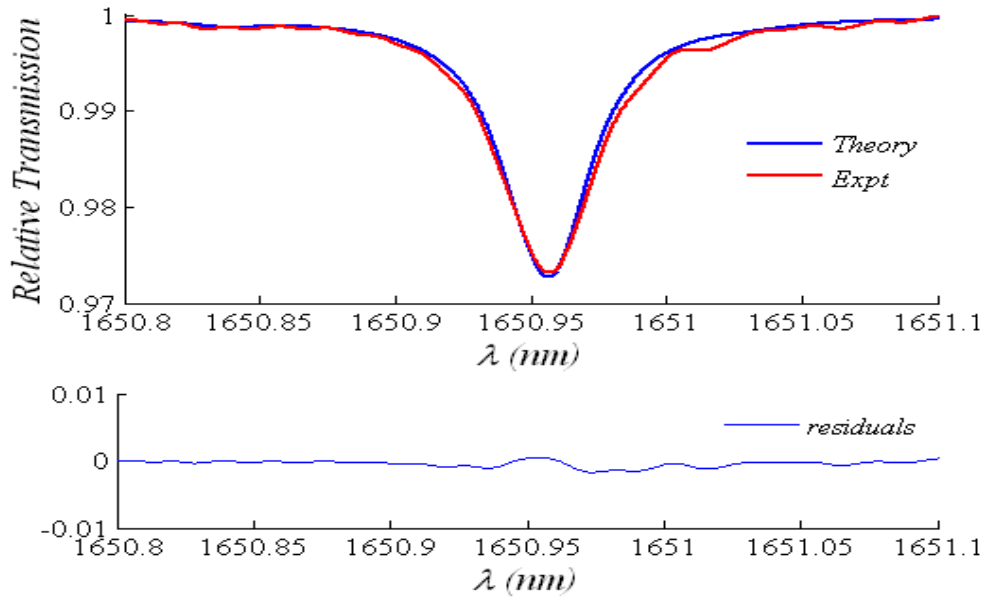


Fig. 5.16: 1.02%  $CH_4$  at 1.052 bar and 20.5°C,  $m = 0.7$ ,  $\Phi = 34^\circ$ , LIA  $tc = 1ms$ , LIA sens: RAM nulled = 50 $\mu V$ , non-nulled = 2mV

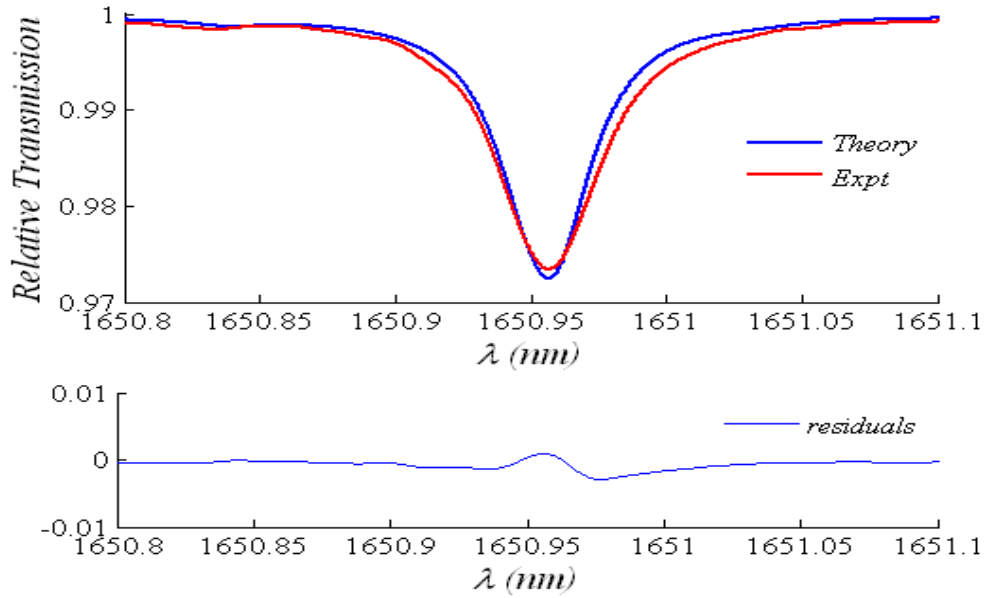


Fig. 5.17: 1.02%  $CH_4$  at 1.054 bar and 23.9°C,  $m = 0.7$ ,  $\Phi = 33^\circ$ , LIA  $tc = 1ms$ , LIA sens: RAM nulled = 50 $\mu V$ , non-nulled = 500 $\mu V$

### 5.3.4 Comparison with RAM method without nulling

Just as in the previous case, the result without nulling is presented for comparison that shows that the nulling does not have any adverse effects on the data.

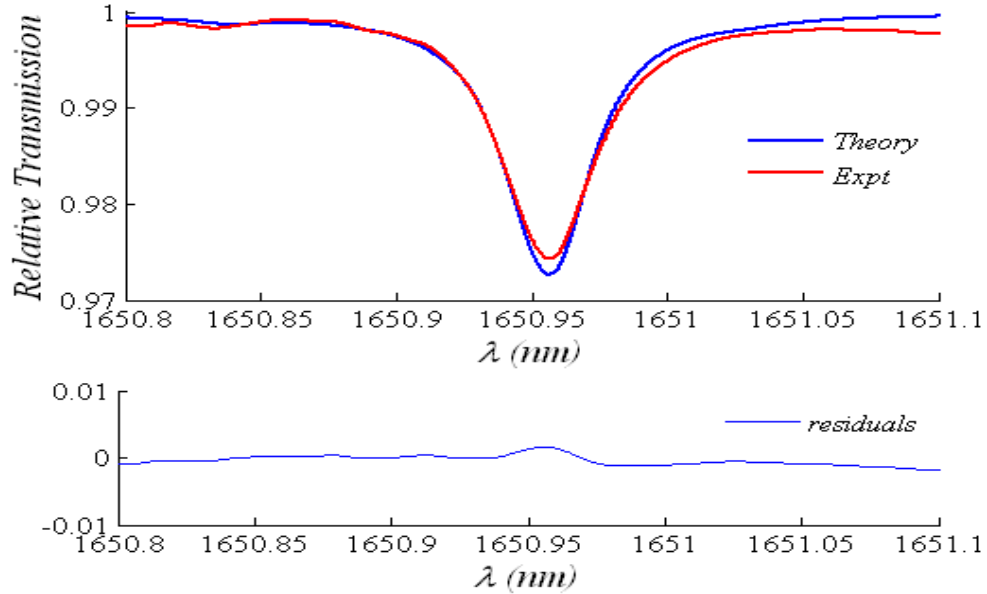


Fig. 5.18: 1.02%  $CH_4$  at 1.013 bar and 20.5°C,  $m = 0.7$ ,  $\Phi = 32^\circ$ , LIA  $t_c = 1ms$ , LIA  $sens$ : RAM signal = 2mV

It is seen from these results that the absorption line can be recovered with high fidelity using the RAM nulling technique. A comparison of results with and without RAM nulling shows that the signal-to-noise ratio of the RAM nulled signals is not compromised. The modulation index for the recovery of these signals was limited to  $m = 0.7$ . This is well below the optimum value of 2.0 for 1f detection. The correction factor algorithm in its present form does not perform adequately for higher  $m$ -values. In the next section results using the PDM are presented for  $m$ -values up to 2.2, where the effect on the recovered line shapes and the inadequacy of the correction factor algorithm are evident. However, as pointed out earlier a new algorithm is being developed that has performed much better. This topic will not however be described here since it does not form the central theme of this thesis.

## 5.4 Experimental results using Phasor Decomposition method with RAM nulling

This section presents detailed results of using the Phasor Decomposition method with RAM nulling. A mathematical treatment of the process and a description of the signals that are involved are presented. Two concentrations of methane are used and the modulation index is varied from low to high values. It is demonstrated that the recovery of line shape is achieved with good accuracy for  $m$ -values up to about 0.75 whereas for higher  $m$ -values the current strategy of correction factors is not adequate. However the validity of using the PDM with RAM nulling is clearly demonstrated.

### 5.4.1 Analytical Description of PDM with RAM nulling

Experimental results are presented in this section with the background RAM nulling incorporated in to the calibration-free Phasor Decomposition Method (PDM). The PDM was extended to detect 10.13% and 1.02% methane under ambient pressure and temperature, and for increasing modulation indices.

To appreciate how the background RAM nulling affects the PDM it is necessary to review the expressions for the signal. The signal on channel Y for non-nulled PDM has been derived earlier in Eq. 2.7 and is reproduced below,

$$I_{1fChY} = \Delta I(\lambda_c) \{1 - \alpha(\lambda_c).CI\} - I(\lambda_c) \left. \frac{d\alpha(\lambda)}{d\lambda} \right|_{\lambda_c} .CI.\delta\lambda \cos\psi \quad (5.1)$$

With the background nulling in place the direct IM term drops out and the channel Y output is given by,

$$I_{1fChY_{nulled}} = -\Delta I(\lambda_c)\alpha(\lambda_c).CI - I(\lambda_c) \left. \frac{d\alpha(\lambda)}{d\lambda} \right|_{\lambda_c} .CI.\delta\lambda \cos\psi \quad (5.2)$$

The signal on the orthogonal channel X is unaffected by the nulling and is given by,

$$I_{1fChX} = -I(\lambda_c) \left. \frac{d\alpha(\lambda)}{d\lambda} \right|_{\lambda_c} . C.I. \delta\lambda \sin \psi \quad (5.3)$$

Therefore, the full absorption-dependent signal is recovered from Eq. 5.2 and Eq. 5.3 and knowledge of  $\psi$  by,

$$I_{RAM} = I_{1fChYnulled} - \frac{I_{1fChX}}{\tan \psi} = -\Delta I(\lambda_c) \alpha(\lambda_c) . C.I \quad (5.4)$$

The signals  $I_{1fChX}$ ,  $I_{1fChY}$  and  $I_{1fChYnulled}$  are shown in Fig. 5.19 and Fig. 5.20, for 10.13% and 1.02% methane respectively, in which the effect of RAM nulling is clear.

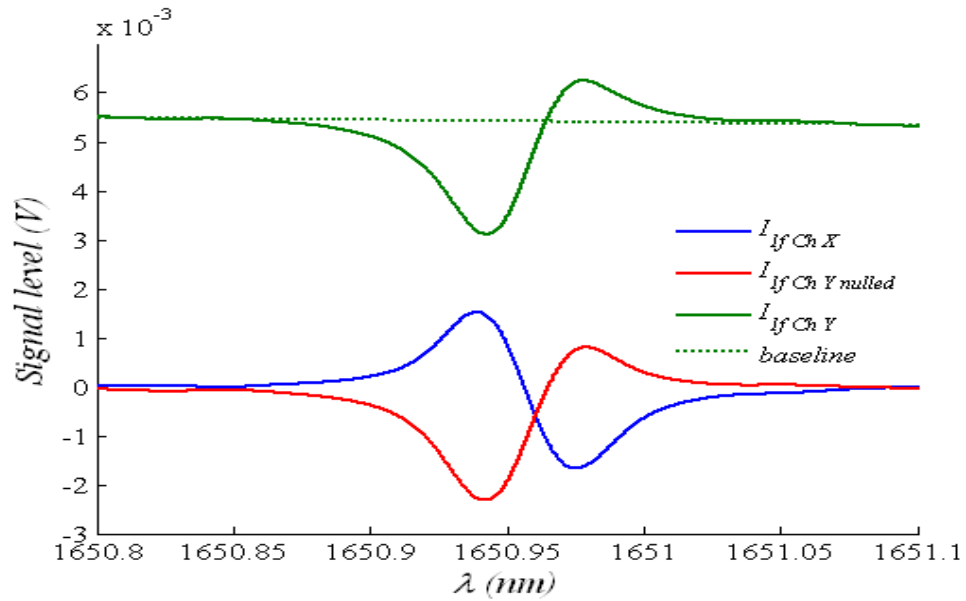


**Fig. 5.19: Signal components used in PDM with RAM nulling for 10.13% methane at 1.095 bar pressure at 21.9°C and for modulation index of 0.75**

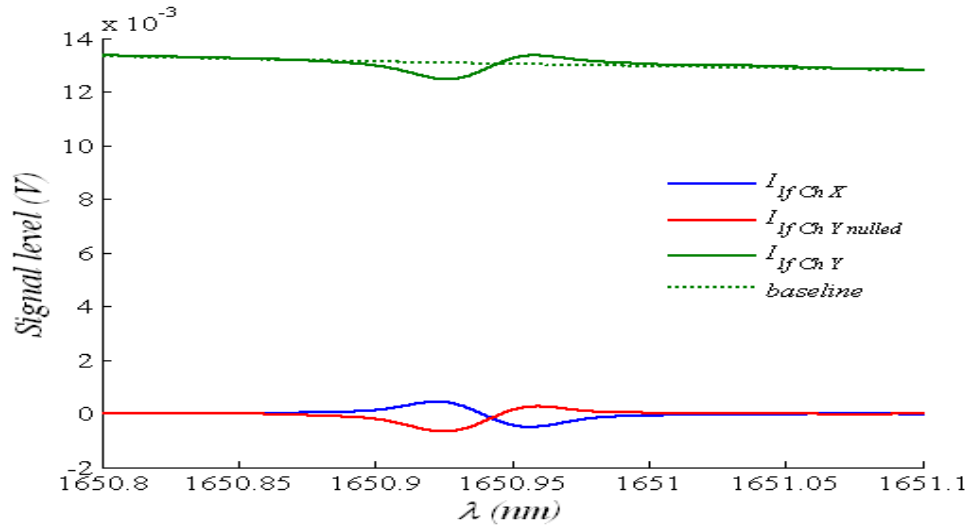


**Fig. 5.20: Signal components used in PDM with RAM nulling for 1.02% methane at 1.082 bar pressure at 22.1°C, and for modulation index of 0.75**

The normalization process is similar to that used in the RAM approach. A baseline fit to off-line points either side of the line centre of the  $I_{1fChY}$  signal is used for normalization. This baseline is essentially the linear IM and is mathematically given by  $I_{baseline} = \Delta I(\lambda_c)$ . For low concentrations it is possible to use the non-nulled signal,  $I_{1fChY}$ , directly for normalization. A comparison of normalization with and without baseline fit for 1.02% methane is shown in Fig. 5.21 that shows that very little error is introduced if the baseline fit is not used. This is not entirely unexpected since the non-nulled signal is heavily dominated by the linear IM term. For low concentrations, the addition of the small 1<sup>st</sup> derivative component to the linear IM background does not change the net value greatly in the vicinity of the line centre because the 1<sup>st</sup> derivative component is nearly zero in this region. Therefore, the  $I_{1fChY}$  signal itself can be used for normalization. However for a concentration of 10.13% using the non-nulled signal directly does not give accurate results as shown in Fig. 5.22. In addition to the error in concentration there is also a shift in the peak position. These are both due to the relatively high value of the 1<sup>st</sup> derivative component that significantly alters the normalization signal and therefore the final value of the relative transmission.

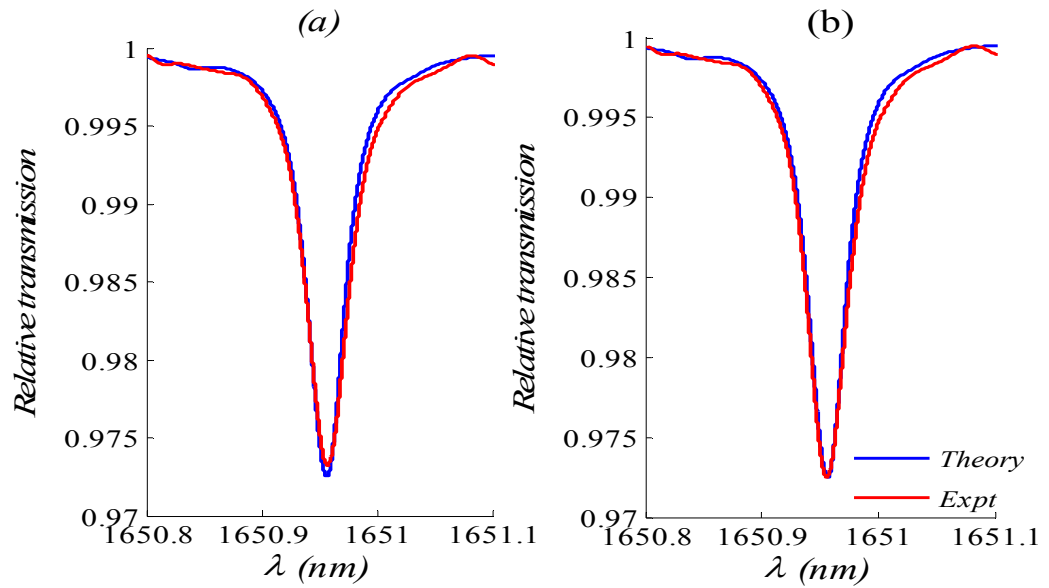


*Fig. 5.21: Relative transmission for 1.02% methane at a pressure of 1.082 bar and temperature of 22.1°C extracted by, (a) normalization by baseline fit to the signal at  $OP_1$  with the delay arm disconnected, and (b) by the signal at  $OP_1$  with the delay arm disconnected.  $m = 0.75$*

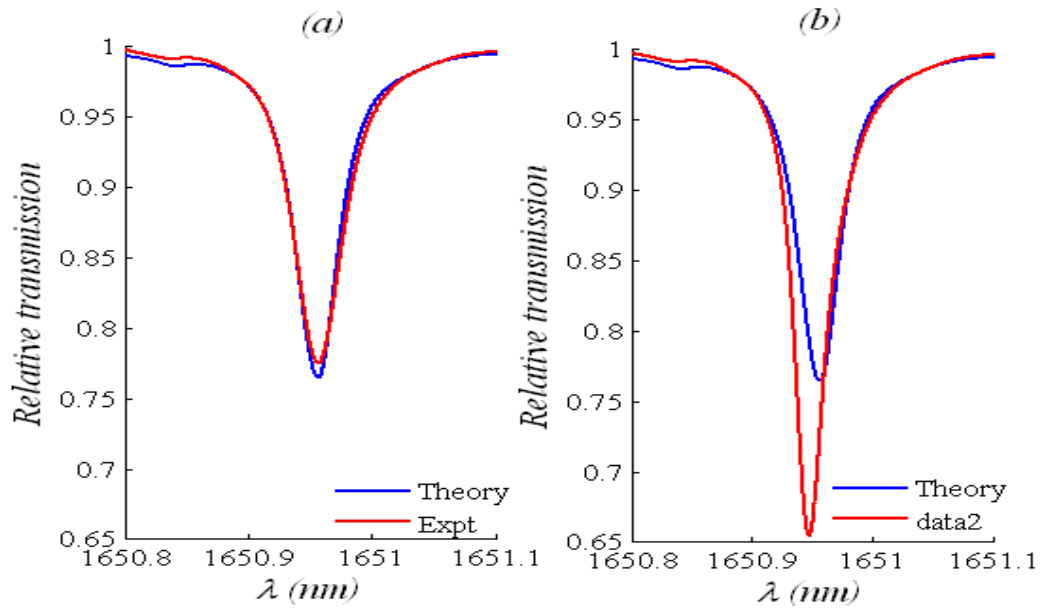


*Fig. 5.22: Relative transmission for methane for concentration 10.13%, pressure 1.095 bar and temperature 21.9°C extracted by, (a) normalization by baseline fit to the non-nulled signal at  $OP_1$ , and (b) normalization by the non-nulled signal at  $OP_1$ , for  $m = 0.75$*

### 5.4.2 PDM with RAM nulling for 10.13%

Detailed results for 10.13% and 1.02% methane under ambient conditions of temperature and pressure are shown next. The  $m$ -value has been varied from 0.2 to 2.2. Accurate recovery of line shapes is possible for  $m$ -values up to about 0.7 with the present correction factors. This limitation is being studied in greater detail by other researchers within the group with promising initial results. Suitable algorithms have been devised that successfully implement the necessary corrections up to the optimum value of  $m = 2$ . However, since the aim of this thesis is to investigate only the RAM nulling technique the imperfect results have been retained since these do not signify shortcomings of the nulling technique itself.

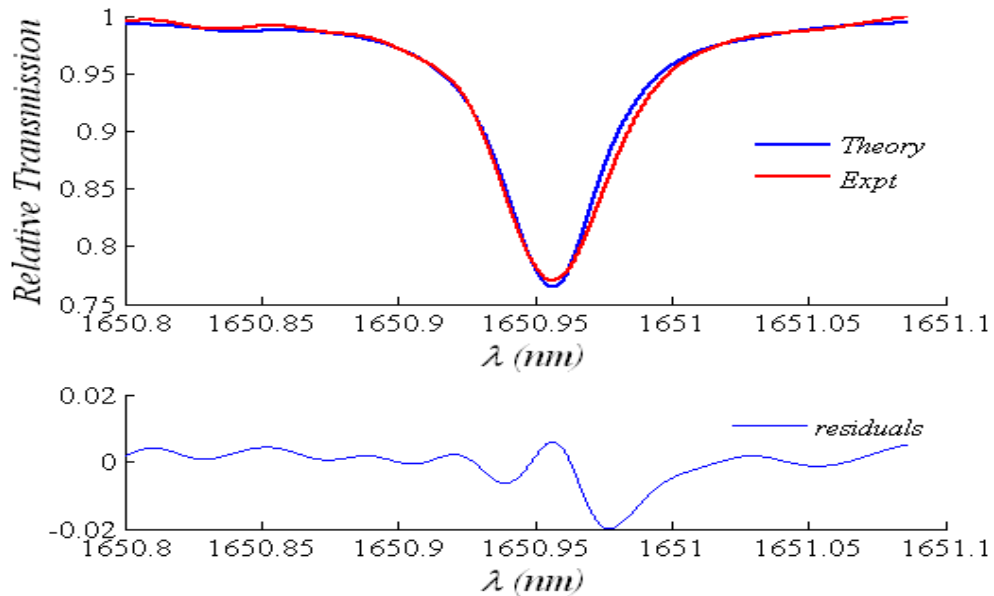


**Fig. 5.23:**  $m = 0.2$ ,  $C = 10.13\%$ ,  $P = 1.099$  bar,  $T = 22^\circ\text{C}$ ,  $f = 101.2$  kHz,  $\Phi = -11.8^\circ$ ,  
 $LIA\ tc = 1\text{ms}$ ,  $Mod\ voltage = 330.6\ mV$ ,  $LIA\ sens: AM\_FM = 200\ \mu V$ ,  $Sep\_FM =$   
 $200\ \mu V$ ,  $Gas\_OP1\_break2 = 200\ \mu V$

Chapter 5: Calibration-free 1f WMS with RAM nulling – Validation of technique

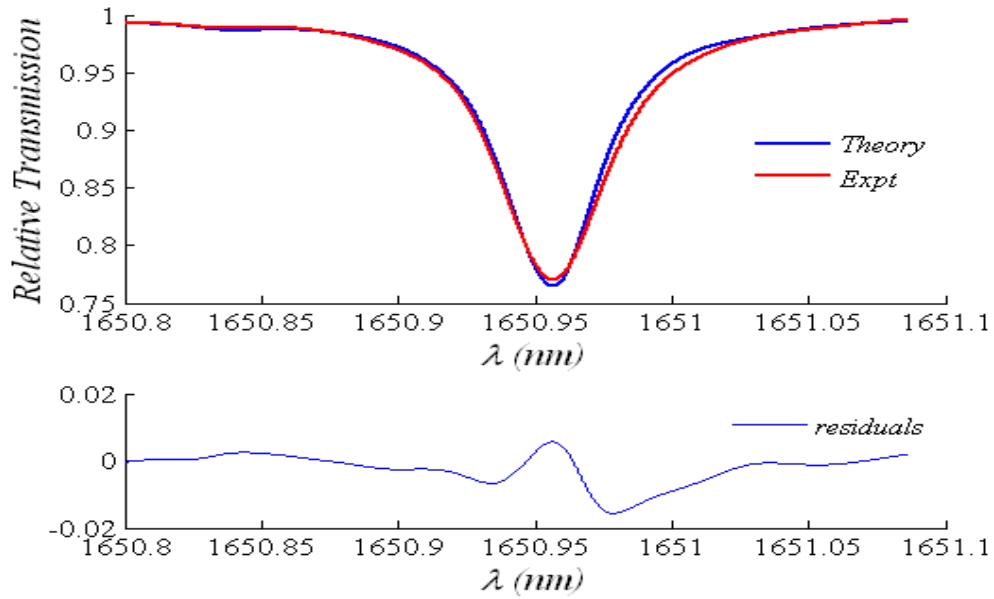


**Fig. 5.24:**  $m = 0.5$ ,  $C = 10.13\%$ ,  $P = 1.095$  bar,  $T = 21.9^\circ\text{C}$ ,  $f = 101.2$  kHz,  $\Phi = -11.8^\circ$ ,  
 $LIA\ tc = 1\text{ms}$ ,  $Mod\ voltage = 826\text{ mV}$ ,  $LIA\ sens: AM\_FM = 200\text{uV}$ ,  $Sep\_FM = 200\text{uV}$ ,  
 $Gas\_OPI\_break2 = 500\text{uV}$

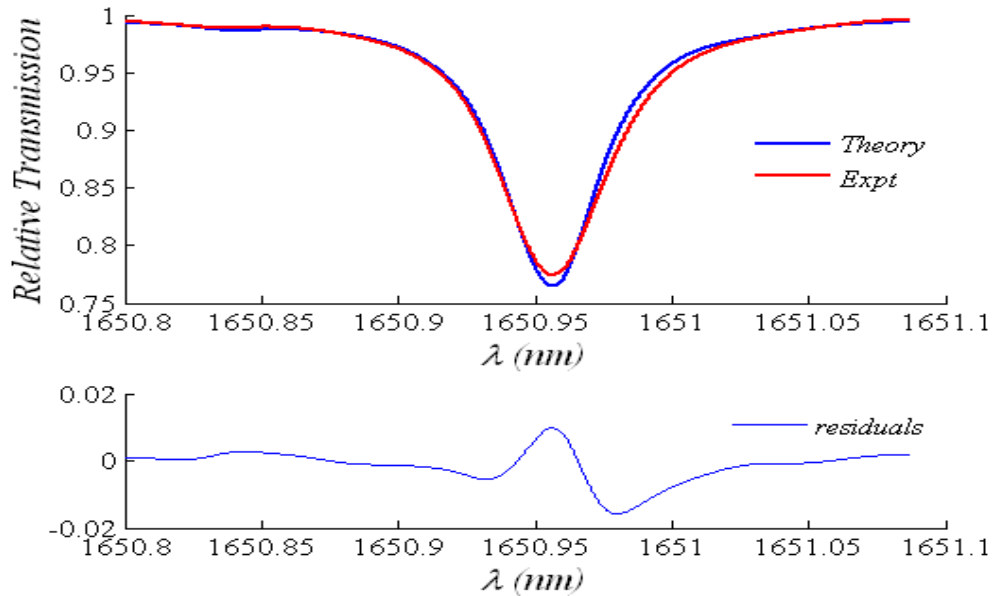


**Fig. 5.25:**  $m = 0.75$ ,  $C = 10.13\%$ ,  $P = 1.095$  bar,  $T = 21.9^\circ\text{C}$ ,  $f = 101.2$  kHz,  $\Phi = -11.8^\circ$ ,  
 $LIA\ tc = 1\text{ms}$ ,  $Mod\ voltage = 1239\text{ mV}$ ,  $LIA\ sens: AM\_FM = 500\text{uV}$ ,  $Sep\_FM =$   
 $500\text{uV}$ ,  $Gas\_OPI\_break2 = 1\text{mV}$

Chapter 5: Calibration-free 1f WMS with RAM nulling – Validation of technique

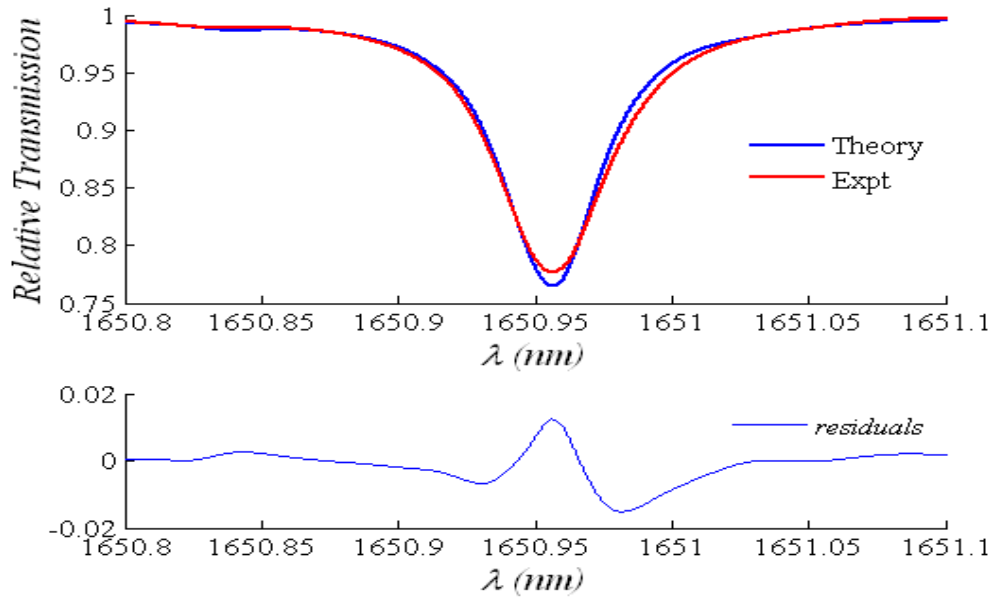


Fig. 5.26:  $m = 1.0$ ,  $C = 10.13\%$ ,  $P = 1.093$  bar,  $T = 21.9^\circ\text{C}$ ,  $f = 101.2$  kHz,  $\Phi = -11.8^\circ$ ,  
 LIA tc = 1ms, Mod voltage = 1653 mV, LIA sens: AM\_FM = 500uV, Sep\_FM =  
 500uV, Gas\_OPI\_break2 = 1mV

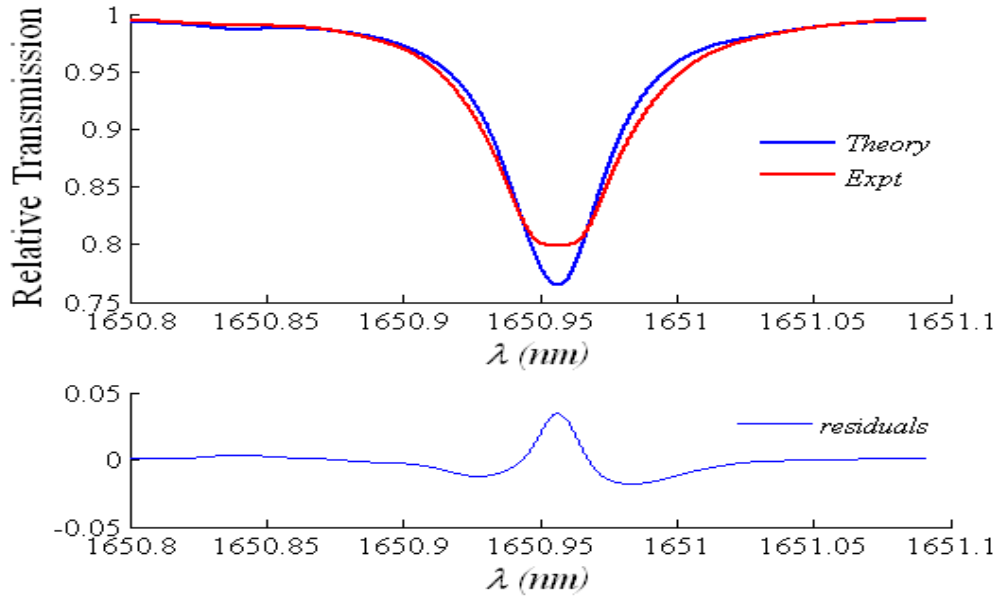
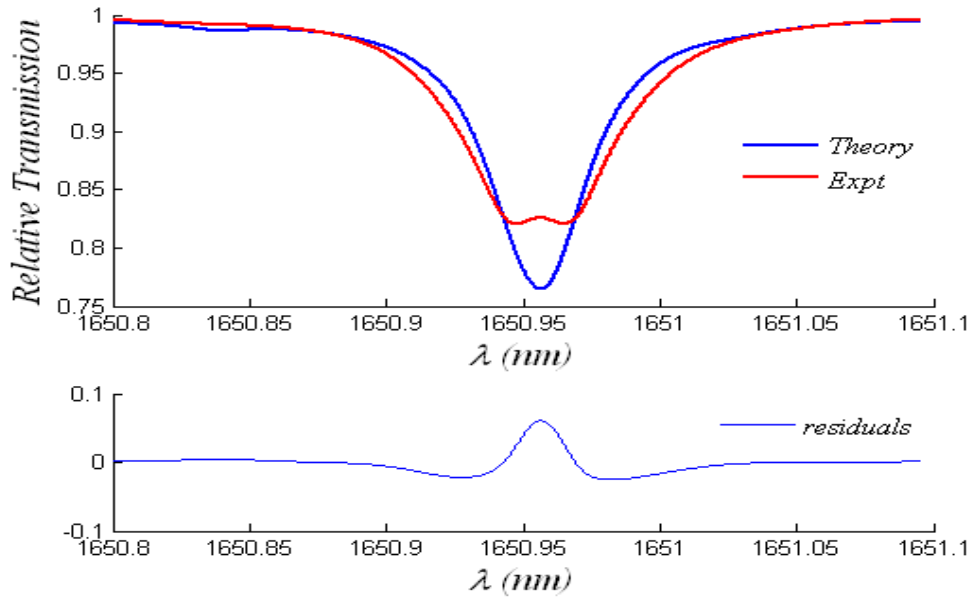


Fig. 5.27:  $m = 1.5$ ,  $C = 10.13\%$ ,  $P = 1.090$  bar,  $T = 21.9^\circ\text{C}$ ,  $f = 101.2$  kHz,  $\Phi = -11.8^\circ$ ,  
 LIA tc = 1ms, Mod voltage = 2479 mV, LIA sens: AM\_FM = 500uV, Sep\_FM =  
 500uV, Gas\_OPI\_break2 = 2mV



**Fig. 5.28:**  $m = 2.2$ ,  $C = 10.13\%$ ,  $P = 1.088$  bar,  $T = 22.0^\circ\text{C}$ ,  $f = 101.2$  kHz,  $\Phi = -11.8^\circ$ ,  
 $LIA\ tc = 1\text{ms}$ ,  $Mod\ voltage = 3306\text{ mV}$ ,  $LIA\ sens: AM\_FM = 500\text{uV}$ ,  $Sep\_FM =$   
 $500\text{uV}$ ,  $Gas\_OPI\_break2 = 2\text{mV}$

These results show that beyond  $m = 0.75$  there is a significant 2<sup>nd</sup> derivative component in the residuals. This implies that for high  $m$ -values the linear IM-induced 2<sup>nd</sup> derivatives of the line shape that are projected on to the RAM axis are not properly accounted for. This results in significant errors in concentration as well as pressure measurements for high  $m$ -values. The nature of the residuals is quite typical of such plots. It is also noted that the fit is very good in regions away from the line centre.

The next section shows results for a similar set of experiments performed on a lower concentration of gas where a consistent behaviour of signals is seen for high  $m$ -values.

### 5.4.3 PDM with RAM nulling for 1.02%

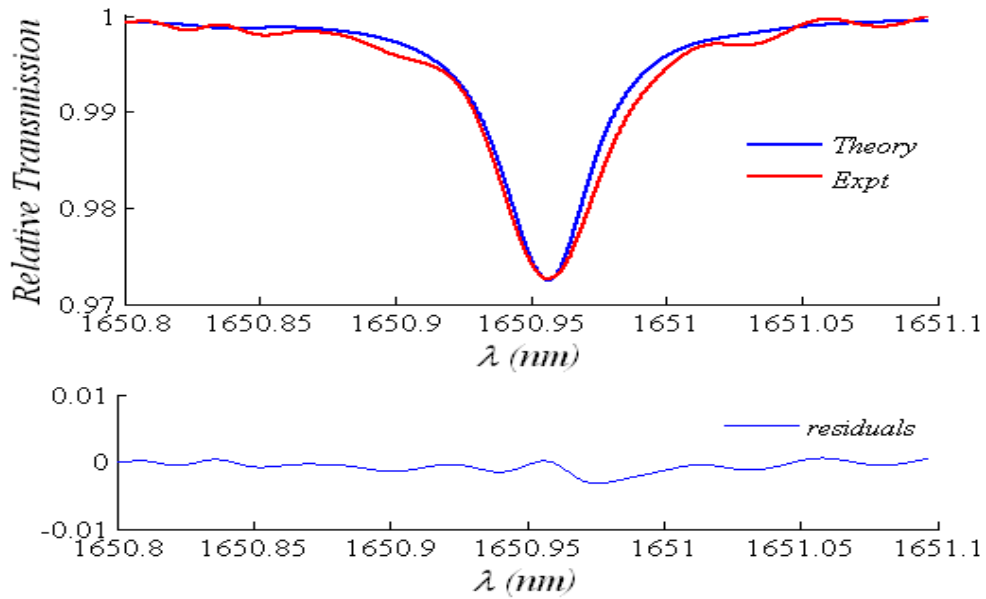


**Fig. 5.29:**  $m = 0.2$ ,  $C = 1.02\%$ ,  $P = 1.085$  bar,  $T = 21.9^\circ\text{C}$ ,  $f = 101.2$  kHz,  $\Phi = -15.98^\circ$ ,  
 LIA tc = 1ms, Mod voltage = 330.6 mV, LIA sens: AM\_FM = 50uV, Sep\_FM = 50uV,  
 Gas\_OP1\_break2 = 500uV

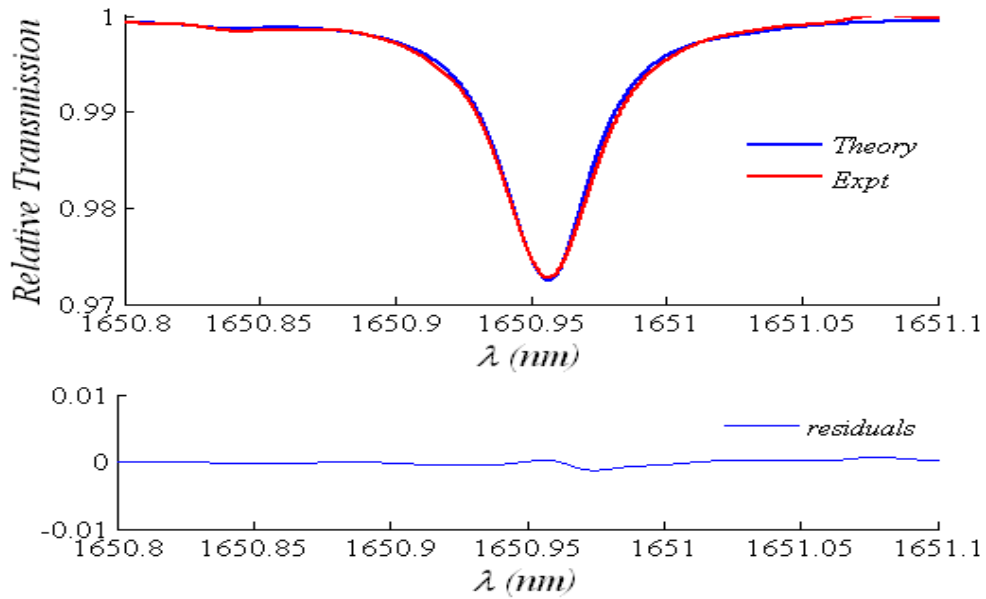


**Fig. 5.30:**  $m = 0.5$ ,  $C = 1.02\%$ ,  $P = 1.083$  bar,  $T = 22.1^\circ\text{C}$ ,  $f = 101.2$  kHz,  $\Phi = -15.98^\circ$ ,  
 LIA tc = 1ms, Mod voltage = 826 mV, LIA sens: AM\_FM = 50uV, Sep\_FM = 50uV,  
 Gas\_OP1\_break2 = 1mV

Chapter 5: Calibration-free 1f WMS with RAM nulling – Validation of technique

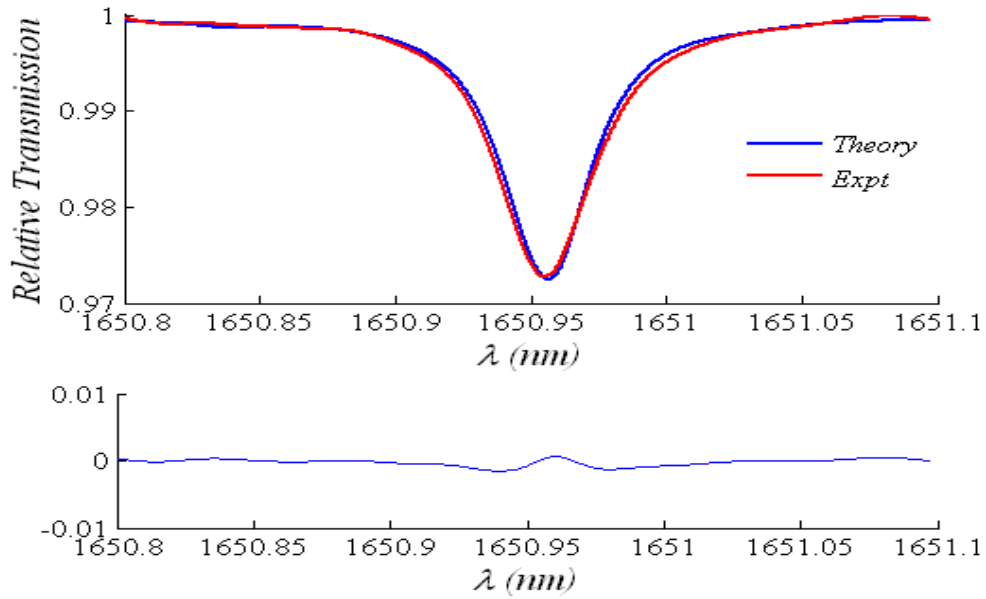


Fig. 5.31:  $m = 0.75$ ,  $C = 1.02\%$ ,  $P = 1.082$  bar,  $T = 22.1^\circ\text{C}$ ,  $f = 101.2$  kHz,  $\Phi = -15.98^\circ$ ,  
LIA tc = 1ms, Mod voltage = 1239 mV, LIA sens: AM\_FM = 100uV, Sep\_FM =  
100uV, Gas\_OPI\_break2 = 2mV

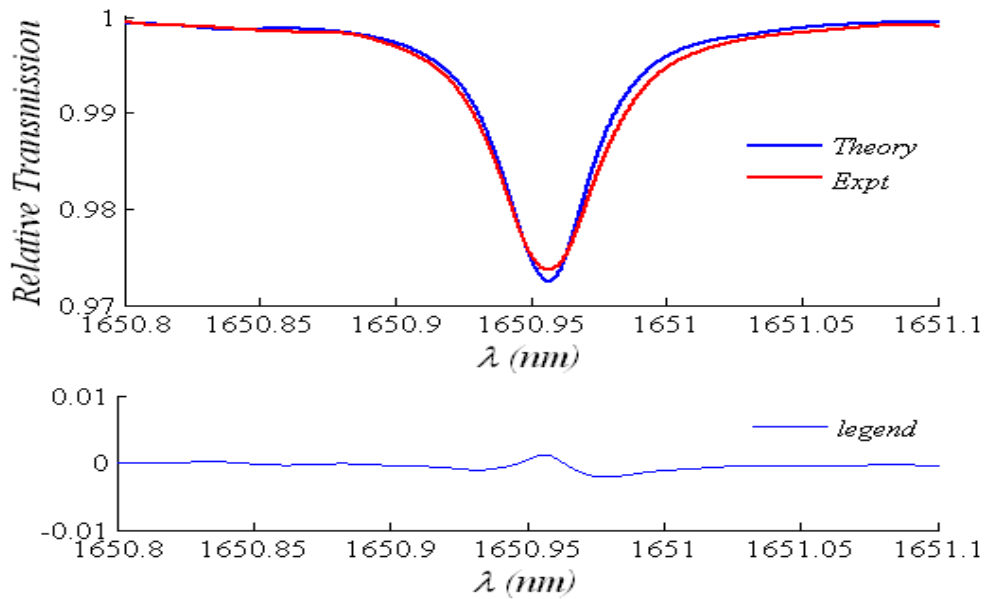
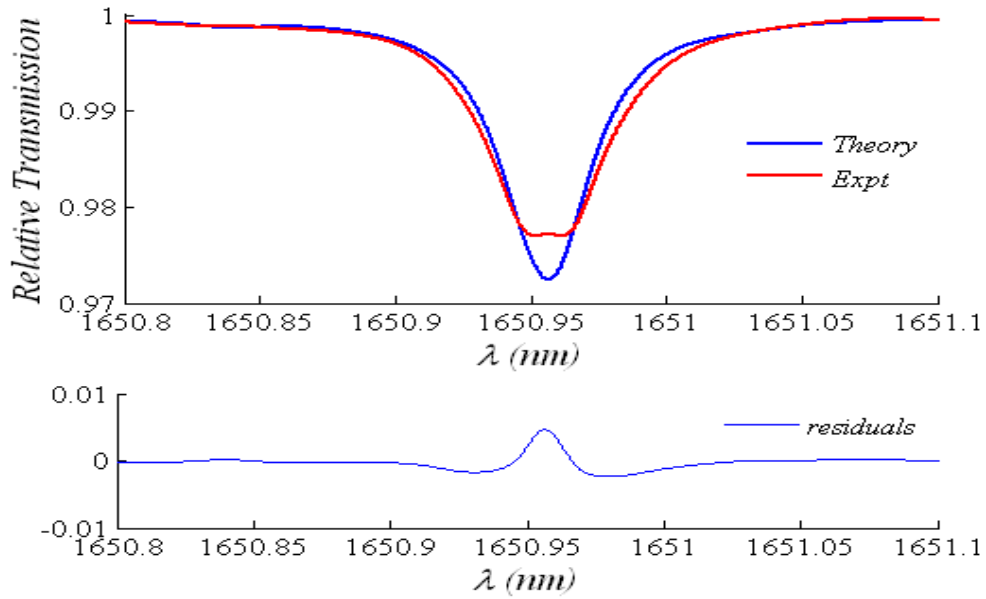
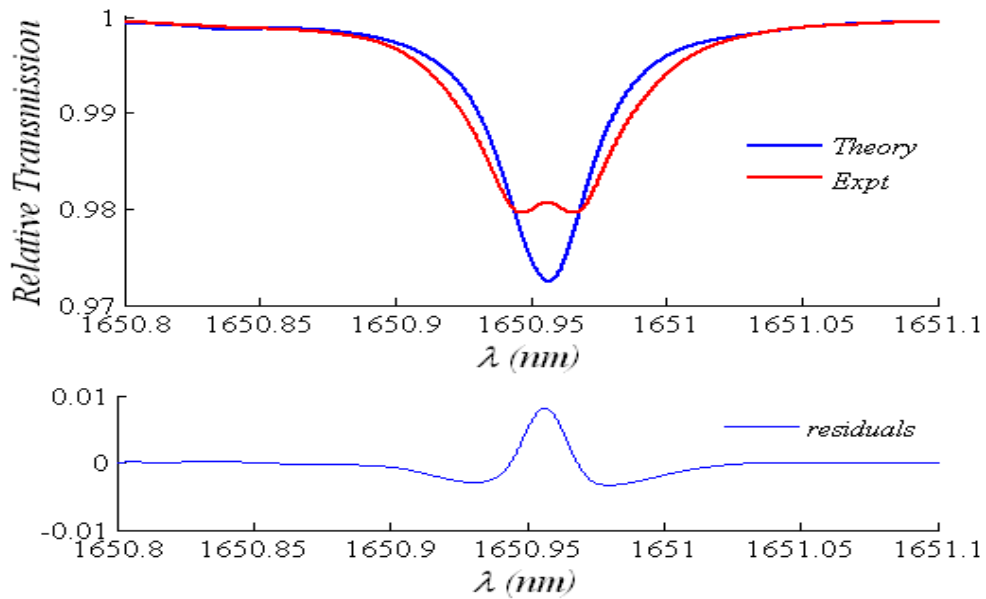


Fig. 5.32:  $m = 1.0$ ,  $C = 1.02\%$ ,  $P = 1.080$  bar,  $T = 22.3^\circ\text{C}$ ,  $f = 101.2$  kHz,  $\Phi = -15.98^\circ$ ,  
LIA tc = 1ms, Mod voltage = 1653 mV, LIA sens: AM\_FM = 100uV, Sep\_FM =  
100uV, Gas\_OPI\_break2 = 2mV

Chapter 5: Calibration-free 1f WMS with RAM nulling – Validation of technique



**Fig. 5.33:**  $m = 1.5$ ,  $C = 1.02\%$ ,  $P = 1.078$  bar,  $T = 22.5^\circ\text{C}$ ,  $f = 101.2$  kHz,  $\Phi = -15.98^\circ$ ,  
 $LIA\ tc = 1\text{ms}$ ,  $Mod\ voltage = 2479\text{ mV}$ ,  $LIA\ sens: AM\_FM = 100\text{uV}$ ,  $Sep\_FM = 100\text{uV}$ ,  $Gas\_OPI\_break2 = 5\text{mV}$



**Fig. 5.34:**  $m = 2.2$ ,  $C = 1.02\%$ ,  $P = 1.077$  bar,  $T = 22.6^\circ\text{C}$ ,  $f = 101.2$  kHz,  $\Phi = -15.98^\circ$ ,  
 $LIA\ tc = 1\text{ms}$ ,  $Mod\ voltage = 3306\text{ mV}$ ,  $LIA\ sens: AM\_FM = 200\text{uV}$ ,  $Sep\_FM = 200\text{uV}$ ,  $Gas\_OPI\_break2 = 5\text{mV}$

#### ***5.4.4 Discussion of results***

These results demonstrate that by incorporating RAM nulling in the system accurate recovery of the absorption line shape is possible using the Phasor Decomposition method. The main limitation of the present system is the presence of etalon fringes that limits measurements of lower concentrations. It should be possible to eliminate these with an optimized design of the gas cell.

At present accurate recovery of the line shape is not possible for high  $m$ -values that actually optimize the signal level. This is slightly disappointing although initial results with a new correction factor strategy that works up to  $m = 2.0$ , have shown a marked improvement. It is expected that further work in this direction will lead to optimization of the correction factor algorithm that in turn will significantly increase the SNR of the RAM technique as well as the PDM and thereby make them competitive with traditional 1f WMS techniques.

### **5.5 Comparison of signals for low concentration with and without RAM nulling**

The effect of RAM nulling is particularly evident for low concentrations as shown in Fig. 5.35 in which the RAM signal is shown with and without background RAM nulling for methane at a concentration of 0.1% . It is clearly seen from Fig. 5.35a that for the measurement made with RAM nulling the low-level absorption-dependent signal (evident from the values on the  $y$ -axis) is distinguishable against the background. As pointed out earlier this signal can be further amplified if necessary. However this is not the case for the measurement made without RAM nulling shown in Fig. 5.35b. It is clear that the absorption dependent signal is almost indistinguishable against the high level of sloping background signal. If this signal were to be used it would be nearly impossible to correctly set up the LIA detection phase since the concentration-dependent signal is obscured by the offline region dominated by the IM of the laser. Another set of results

**Chapter 5: Calibration-free 1f WMS with RAM nulling – Validation of technique**

is shown in Fig. 5.36 and the normalization by the corresponding background is shown in Fig. 5.37.

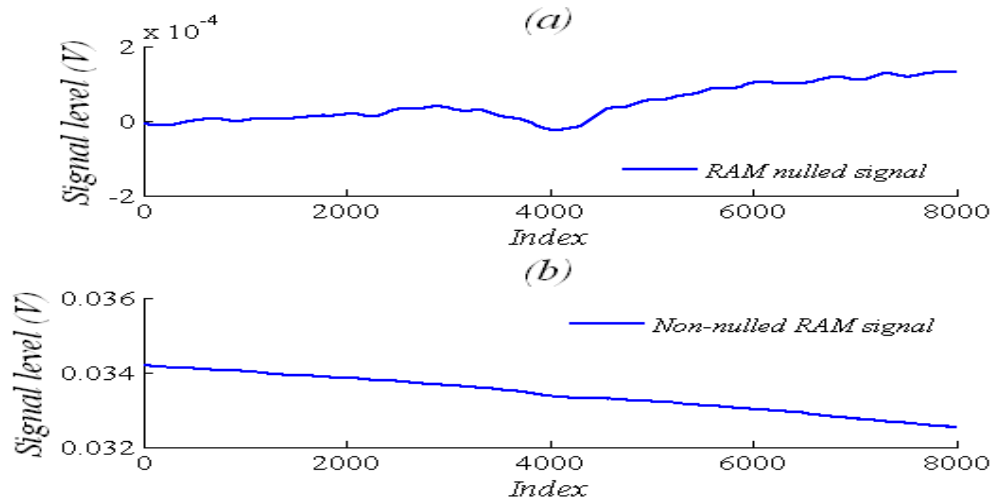


**Fig. 5.35: (a) RAM nulled and (b) non-nulled signals for  $C = 0.1017\%$ ,  $P = 1.116$  bar,  $T = 22.3^\circ\text{C}$ ,  $f = 101$  kHz,  $m = 0.7$ ,  $\Phi = 33^\circ$ , LIA time constant = 1ms, Mod voltage = 1156 mV, LIA sensitivity: RAM with nulling = 100uV, RAM without nulling = 5mV**

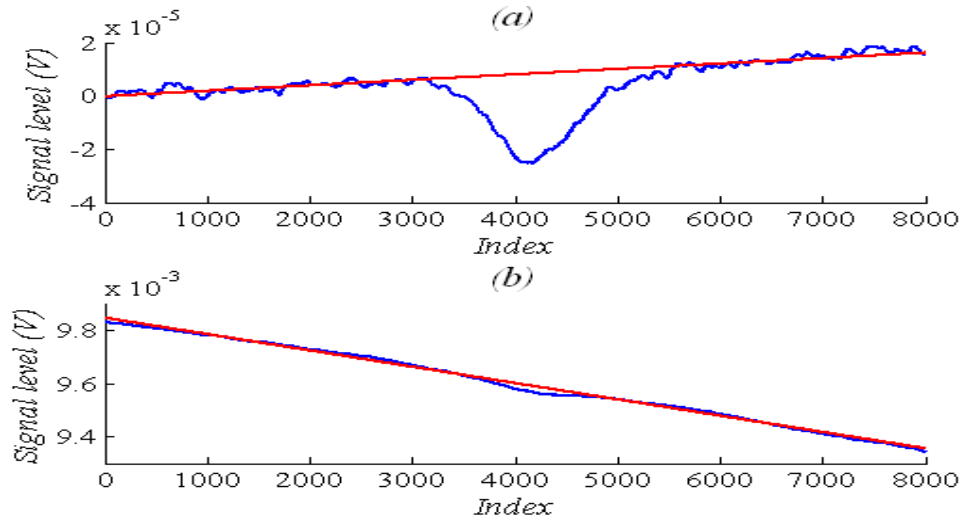


**Fig. 5.36: (a) RAM nulled and (b) non-nulled signals for  $C = 0.1017\%$ ,  $P = 1.116$  bar,  $T = 22.3^\circ\text{C}$ ,  $f = 101$  kHz,  $m = 0.7$ ,  $\Phi = 33^\circ$ , LIA time constant = 1ms, Mod voltage = 1156 mV, LIA sensitivity: RAM with nulling = 20uV, RAM without nulling = 1mV**

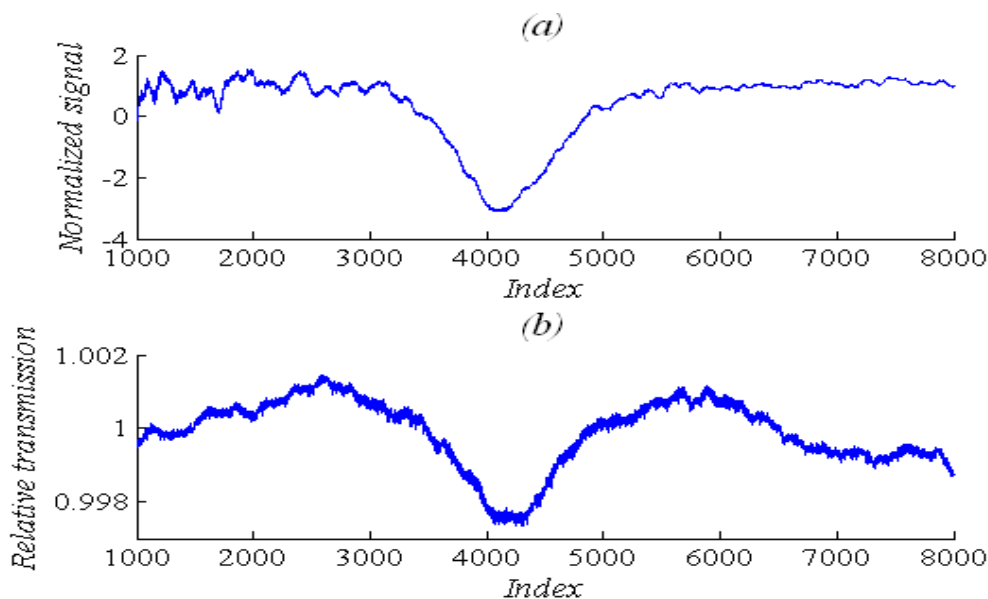


*Fig. 5.37: (a) RAM-nulled absorption signal normalized by a baseline fit, and (b) Non-nulled signal normalized by baseline fit*

The normalization process clearly shows that the baseline fitting to the non-nulled signal is difficult due to the poor contrast between the non-absorbing spectral wings and the actual absorption-dependent signal. The relative transmission recovered in this way cannot be used for the extraction of concentration or pressure. The RAM-nulled signal is much easier to recover and the baseline fitting is indeed easier. It should be noted however that in practice the RAM-nulled case is not normalized by this baseline. This has been done here only to illustrate the relative ease with which a baseline may be fitted to the RAM-nulled signal if that is required. Such a baseline fitting may be useful in removing the residual slope on the RAM-nulled signal.

These results clearly show that for low concentration levels the RAM nulling technique helps to recover low level signal that are otherwise obscured by the concentration-independent signal components due to the laser's IM. However at such signal levels the optical design of the system becomes important because etalon fringes tend to become the dominant source of noise. Although the signal levels encountered with RAM nulling are sufficiently large for digitization it is the preservation of the

## Chapter 5: Calibration-free $1f$ WMS with RAM nulling – Validation of technique

signal shape that is important in these applications. The etalon fringes that are evident in Fig 5.35a and Fig 5.36a tend to mainly distort the shape of the absorption line shape. Therefore careful attention needs to be paid to the optical design in order to fully exploit the RAM nulling technique.

The dominant downward slope of the non-nulled signals in Fig 5.35b and Fig 5.36b is due to the characteristic wavelength-dependent behaviour of the IM of this laser. The upward slope on the RAM-nulled signals is a result of the interplay of the wavelength-dependence of the IM and that of the couplers used in the system. This will be explored in detail in the next chapter along with a strategy to minimize any residual slope on the RAM-nulled signals.

## 5.6 Conclusion

Experimental results have been presented using the two calibration-free  $1f$  WMS techniques namely the RAM method and the PDM with RAM nulling incorporated in them for 10.13% and 1.02% methane in nitrogen balance. Gas measurements for 1.02% methane have been performed with ease at a very modest modulation frequency of 100 kHz. It is seen that for modulation indices above about 0.75 the recovery of the absorption line shape is inaccurate. This is due to the fact that the Taylor series approximation breaks down for high  $m$ -values. However the aim of this thesis was specifically to demonstrate a technique to eliminate the  $1f$  RAM and extract a practical signal normalization strategy. Concurrent research within the group has led to the development of an improved correction-factor algorithm that can handle arbitrarily large modulation indices. Initial results have been promising and it is expected that the implementation of the RAM nulling technique in conjunction with the new algorithm will enable accurate extraction of the absorption line shape for high modulation indices.

A comparison of signals with and without RAM nulling for low concentrations shows that the actual absorption-dependent gas signal that is obscured by the laser's IM in the non-nulled case, can be recovered with RAM nulling in place. This shows the promise that RAM nulling holds for low level gas detection. However, in the current system,

## Chapter 5: Calibration-free 1f WMS with RAM nulling – Validation of technique

etalon fringes arising from the parallel faces of the GRIN lenses in the gas cell are the main limitation to high sensitivity and indeed prevent any meaningful study of sensitivity in relation to detector or optical noise. A new gas cell, based on a con-focal lens arrangement with superior anti-reflection coatings is being designed for more effective suppression of the etalon effects.

In the course of these experiments it was observed that in the RAM method of signal recovery, the background RAM-nulled output at  $OP_I$  with or without gas, does not sit exactly on a zero level but has a small sloping background signal. This is due to the different wavelength dependencies of the signal paths taken by the two signal components through the two couplers. The subtraction of the no-gas signal in the numerator of the last term Eq. 4.11 puts the data on an exactly zero level before normalization and calculation of the gas transmission.  $OP_{I\text{no gas}}$  can be obtained without gas in the cell or from a curve fit to the off-line data in the  $OP_{I\text{gas}}$  signal. However, this observation is contrary to expectations, and is investigated in greater detail in chapter 6 through a mathematical model of the RAM nulling process that takes into account the wavelength-dependencies of the linear IM and the fractional coupling ratios of the two 3dB couplers used in the setup. Three distinct experimental configurations with distinct RAM nulling conditions are shown to exist. The simulated and experimental outputs for these three configurations are shown to agree to a very good extent. The first of these configurations gives an essentially zero baseline for the nulled signal. This makes it very useful for automated systems since baseline fitting to the nulled signal is totally eliminated.

## 5.7 References

1. K. Duffin, A. J. McGettrick, W. Johnstone, G. Stewart, D. G. Moodie, “Tunable diode laser spectroscopy with wavelength modulation: a calibration-free approach to the recovery of absolute gas absorption line shapes,” *IEEE J. Lightwav. Technol.* **25**, 3114-3125 (2007).
2. A. J. McGettrick, K. Duffin, W. Johnstone, G. Stewart, D. G. Moodie, “Tunable diode laser spectroscopy with wavelength modulation: a phasor decomposition method for calibration-free measurements of gas concentration and pressure,” *IEEE J. Lightwav. Technol.* **26**, 432-440 (2008).

# *Chapter 6*

---

## **Mathematical model of RAM nulling**

---

### **6.1 Introduction - unexpected nature of nulled signals**

The experimental results presented earlier adequately demonstrate the RAM nulling technique to optically eliminate the concentration-independent  $1f$  background RAM. As explained in detail earlier, the DFB laser output is symmetrically split in two parts, the relative amplitudes of the two IM components are appropriately adjusted and they are

## Chapter 6: Mathematical model of RAM nulling

recombined through a fiber-optic 3dB coupler so that in the absence of gas they cancel, thereby giving rise to a zero signal in the absence of gas. In the presence of a gas the differential absorption in the gas cell relative to the fiber delay line produces a concentration-dependent imbalance at the output. It had been initially expected that for an optimized nulling arrangement, the RAM nulled absorption signal would appear on a *perfectly* zero baseline. However, repeated experiments have shown that there is a small sloping non-zero baseline signal for all concentrations as borne out by Fig. 6.1 that shows the concentration-dependent RAM component isolated from the IM-WM component.

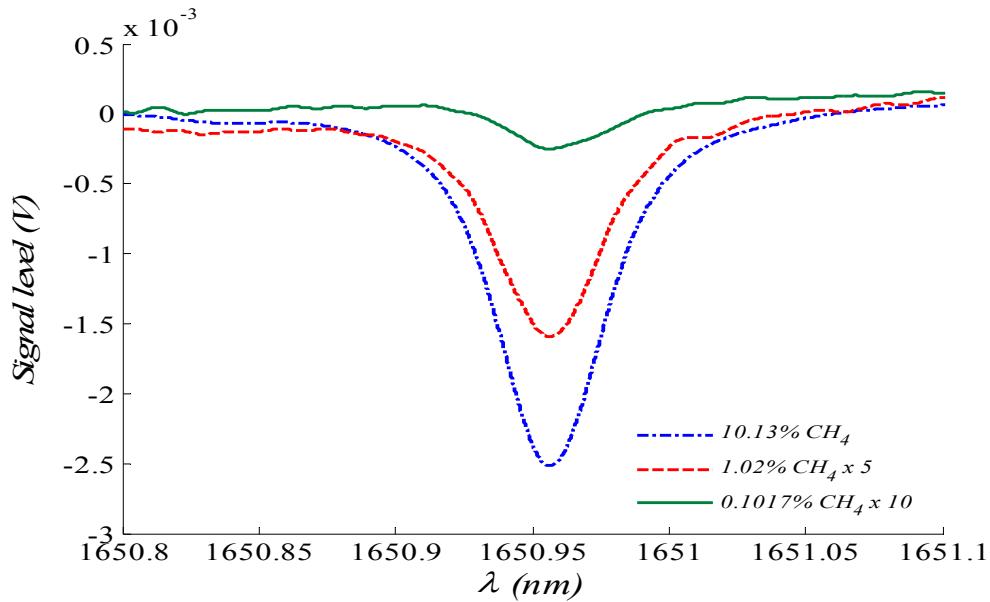


**Fig. 6.1:** RAM nulled gas absorption signals for 10.13%, 1.02% and 0.1017%  $\text{CH}_4$  at ambient pressure and temperature showing the upward slope on signals.

For relatively strong absorption signals the sloping non-zero baseline is not immediately obvious because the low post-detection amplifier gains do not accentuate this feature adequately. It is only when the gain is increased for small absorptions that the baseline becomes prominent. The presence of a non-zero baseline means that contrary to initial expectations, the RAM nulling condition does not hold precisely over the entire wavelength scan. This raises a fundamental question about the basic understanding of the technique. In the preliminary mathematical treatment presented in

## Chapter 6: Mathematical model of RAM nulling

Sec. 4.3, the interplay of the wavelength dependence of the coupling ratios of the 3-dB coupler and that of the IM of the DFB laser were not considered in detail for the sake of brevity and clarity, although it was recognized that they were expected to influence the nature of signals.

Here, a slightly modified experimental setup is considered and a generalized treatment of the RAM nulling technique is presented that explicitly takes into account the wavelength dependence of the various terms. Three different possible experimental configurations are analyzed and it is shown that of the four different input-output configurations only three give rise to distinct expressions for the output, and of those there is one configuration that leads to a precisely zero baseline throughout the wavelength scan range of the laser. This is an important step forward with regard to the RAM nulling technique for the following three reasons. First, although it is straightforward, in principle, to remove the baseline through curve fitting and subtraction, this may not necessarily be practical for systems intended for automated real-time measurement. A second and more subtle but significant issue is that if the nature of the wavelength-intensity (or equivalently, current-intensity) curve for a given laser is significantly nonlinear over the scan range of the laser current, the baseline of the signals shown in Fig. 6.1 that is influenced by the variation of the linear IM with wavelength, will have greater curvature. This will further complicate the baseline fitting. Recently some novel DFB laser structures for carbon monoxide sensing [1, 2], and VCSELs [3, 4], for oxygen and other trace gas sensing have been reported in which the lasers have been shown to have distinctly more nonlinear current-intensity characteristics than a telecom DFB over their typical scan range. The variation of  $\Delta I(\lambda)$  for such lasers can be expected to be significantly more nonlinear than a typical telecom DFB. Finally, for noisy signals it is not easy to define suitable off-line regions of the curve to which a polynomial fit can be made to obtain the trend of the background.

Ideally one would like to avoid the process of baseline fitting and subtraction to eliminate associated errors. A mathematical model of the RAM-nulling process [5], is developed, and the generic nature of background signals due to the wavelength-

dependence of the IM and that of the couplers is explained through simulations for the distinct configurations. Finally experimental results are presented that agree with the simulations to a good extent thereby validating the model.

## 6.2 Modeling of the RAM-nulled output

Figure 6.2 shows a simplified version of the RAM nulling setup in which only the relevant components have been retained. The laser can be connected to either of the input ports of the first coupler (therefore the greyed-out block at  $IP_1$ ), and for each configuration, the output can be measured at either of the two output ports of the second coupler (therefore the greyed-out port  $OP_2$ ).

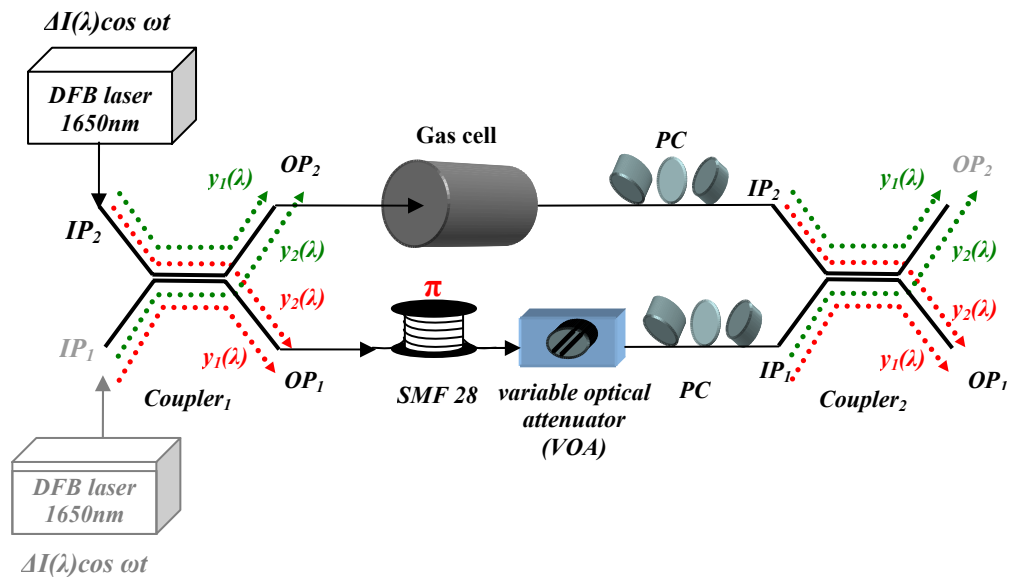


Fig. 6.2: Simplified experimental setup.

For the purpose of the model the two couplers are assumed to be identical. It is also assumed that for each coupler the relative distribution of power from any one input to the two outputs is the same for both input ports that is to say that each coupler is symmetrical with regard to its input and output ports. It is easy to source such pairs of couplers thanks to the highly mature manufacturing technology for various telecoms-grade fiber-optic components. The fractional self-coupling ratio  $y_1(\lambda)$  and cross-

## Chapter 6: Mathematical model of RAM nulling

coupling ratio  $y_2(\lambda)$  for each coupler denote the fraction of launched power retained in the launch fiber, and that transferred to the coupled fiber respectively at the output of the coupler. In accordance with the RAM technique of signal recovery, the lock-in phase was set to isolate the IM-induced component of the signal from the IM-WM. Therefore only the  $\Delta I(\lambda)$  term is considered in the analysis since the intensity-dependent 1<sup>st</sup> derivative term is eliminated by phase-sensitive detection.

### ***6.2.1 Configuration 1: DFB connected to $IP_2$ of coupler<sub>1</sub>; output taken from $OP_1$ of coupler<sub>2</sub>***

The RAM nulling condition is initially established with the gas cell evacuated, the current ramp switched off and only the 100 kHz modulation applied to the laser current. Throughout the analysis  $\Delta I(\lambda_0)$ ,  $y_{20}$  and  $y_{10}$  denote respectively the IM amplitude, the fractional cross-coupling and self-coupling values for the couplers at the starting wavelength  $\lambda_0$ . The losses for the two signal paths along the gas cell arm and the delay fiber arm arise from insertion losses at the connectors, the propagation loss through the cell and the fiber, and the attenuation due to the VOA. Therefore the signals  $y_{20}\Delta I(\lambda_0)$  and  $y_{10}\Delta I(\lambda_0)$  that emerge from  $OP_1$  and  $OP_2$  of coupler<sub>1</sub> arrive at  $IP_1$  and  $IP_2$  of coupler<sub>2</sub> having suffered usually unequal attenuation along their respective paths. For the analysis, the attenuation (loss) factor through the gas cell arm is denoted by  $\alpha_L$ . A variable  $x$  is also defined as the ratio of the loss along the delay line arm to that along the gas cell arm. The factor  $x$  can be varied by adjusting the attenuation factor of the variable optical attenuator (VOA) to achieve perfect balance (and hence cancellation) of the two IM signal components. It will be shown shortly that RAM nulling for each input-output configuration requires a specific value of  $x$  that can be expressed in terms of the fractional coupling ratios of the two couplers. It is also evident from the definition of  $x$  that its value may be equal to, greater than or less than unity.

## Chapter 6: Mathematical model of RAM nulling

The IM signals at the inputs of coupler<sub>2</sub> may therefore be written as,

$$IP_2 = \alpha_L y_{10} \Delta I(\lambda_0) \cos \omega t \quad (6.1)$$

$$IP_1 = x \alpha_L y_{20} \Delta I(\lambda_0) \cos(\omega t + \pi) = -x \alpha_L y_{20} \Delta I(\lambda_0) \cos \omega t \quad (6.2)$$

where, the phase shift of  $\pi$  is due to the appropriate arrangement of the modulation frequency and fiber length given by  $L = c/2nf$ , where  $c$  is the speed of light,  $n$  is the effective index of the fiber and  $L$  is the length of the fiber. The expression for the output at  $OP_1$  of coupler<sub>2</sub> with no gas in the cell and before the ramp is applied can be written as,

$$\begin{aligned} OP_{1no\ gas} &= y_{20} IP_2 + y_{10} IP_1 \\ &= (1 - x) \alpha_L y_{10} y_{20} \Delta I(\lambda_0) \cos \omega t \end{aligned} \quad (6.3)$$

As explained earlier  $x$  will not be unity by default and the output in the absence of gas will be non-zero. However by controlling the attenuation of the VOA the output can be adjusted to be zero by satisfying the RAM nulling condition given by,

$$x = 1 \quad (6.4)$$

In other words, it is necessary and sufficient, in this case, to precisely balance the loss through the two signal paths to ensure a zero output in the absence of gas. The generalized expression for the output including the wavelength-dependence of the terms when the current ramp to sweep the laser wavelength is switched on can be written as,

$$OP_{1no\ gas} = (1 - x) \alpha_L y_1(\lambda_c) y_2(\lambda_c) \Delta I(\lambda_c) \cos \omega t \quad (6.5)$$

Note that if the assumption regarding the two couplers being symmetric is valid, the precisely established RAM nulling condition will hold throughout the scan and the output for this configuration will be zero irrespective of the wavelength-dependence of the other terms. In general, however, the nature of the output is determined by the value

## Chapter 6: Mathematical model of RAM nulling

of  $x$  in conjunction with  $\Delta I(\lambda_c)$ ,  $y_1(\lambda_c)$  and  $y_2(\lambda_c)$ . The cases for which  $x \neq 1$  denotes partial nulling while that for which  $x = 0$  denotes no nulling, with the output being taken with the delay fiber arm disconnected from coupler<sub>2</sub>. These distinct cases for each configuration are discussed in the simulated results presented later. Note that the actual signal  $OP_{1no\ gas}$  is ideally zero in this case and therefore no additional measurement or baseline fitting to the  $OP_{1gas}$  signal is necessary. It will become evident shortly that for the other configurations the  $OP_{1no\ gas}$  will not be zero, and therefore an additional measurement or baseline fitting will be necessary and associated inaccuracies will arise.

For signal normalization it is noted that with gas in the cell, the signal at the input  $IP_2$  of coupler<sub>2</sub> gets multiplied by  $e^{-\alpha(\lambda_c)Cl}$  due to the gas absorption. The resulting generalized output  $OP_{1gas}$  for any value of  $x$  is given by,

$$OP_{1gas} = [e^{-\alpha(\lambda_c)Cl} - x] \alpha_L y_1(\lambda_c) y_2(\lambda_c) \Delta I(\lambda_c) \cos \omega t \quad (6.6)$$

From Eq. 6.5 and Eq. 6.6 the factor  $x$  is eliminated since it is not practical (or necessary) to determine its value experimentally. The relative transmission is given by,

$$e^{-\alpha(\lambda_c)Cl} = 1 + \frac{OP_{1gas} - OP_{1no\ gas}}{\alpha_L y_1(\lambda_c) y_2(\lambda_c) \Delta I(\lambda_c) \cos \omega t} \quad (6.7)$$

Note that for the specific experimental configuration, if the VOA is adjusted so that  $x = 1$ , the  $OP_{1no\ gas}$  signal given by Eq. 6.5 becomes zero irrespective of the other terms in the expression, and the two equations above reduce to,

$$OP_{1gas} = [e^{-\alpha(\lambda_c)Cl} - 1] \alpha_L y_1(\lambda_c) y_2(\lambda_c) \Delta I(\lambda_c) \cos \omega t \quad (6.8)$$

and,

$$e^{-\alpha(\lambda_c)Cl} = 1 + \frac{OP_{1gas}}{\alpha_L y_1(\lambda_c) y_2(\lambda_c) \Delta I(\lambda_c) \cos \omega t} \quad (6.9)$$

## Chapter 6: Mathematical model of RAM nulling

The term  $\alpha_L y_1(\lambda_c) y_2(\lambda_c) \Delta I(\lambda_c)$  is simply the output at  $OP_1$  with the delay fiber arm disconnected from coupler<sub>2</sub> (i.e.  $x=0$ ) and with no gas in the cell. Alternatively, a baseline fit to the signal with the delay arm disconnected can be taken if it is not feasible to take an actual “no-gas” signal. It is noted that this signal is heavily dominated by the  $\Delta I(\lambda_c)$  term which, for the DFB used, produces a monotonically varying, strong and clean signal of high average value and it is very easy to fit a baseline to it making it a convenient normalization signal. It is therefore clear that it is not necessary to separately and accurately determine the values of  $\alpha_L$ ,  $\Delta I(\lambda_c)$ ,  $y_1(\lambda_c)$  and  $y_2(\lambda_c)$ . It is reiterated that a highly useful feature of this configuration is that the RAM nulled output is zero irrespective of the wavelength-dependence of the IM and the couplers. This point will be developed further at a later stage once the other experimental configurations have been analyzed.

### ***6.2.2 Configuration 2: DFB connected to $IP_2$ of coupler<sub>1</sub>; output taken from $OP_2$ of coupler<sub>2</sub>***

In the second distinct configuration the expressions for the signals at  $OP_2$  and  $OP_1$  of coupler<sub>1</sub> and those for the signals at  $IP_2$  and  $IP_1$  of coupler<sub>2</sub> remain unchanged. The output at  $OP_2$  of coupler<sub>2</sub> before the ramp is applied can be written as,

$$\begin{aligned} OP_{2no\ gas} &= y_{10} IP_2 - y_{20} IP_1 \\ &= y_{10}^2 \alpha_L \Delta I(\lambda_0) \cos \omega t - x y_{20}^2 \alpha_L \Delta I(\lambda_0) \cos \omega t \quad (6.10) \\ &= (y_{10}^2 - x y_{20}^2) \alpha_L \Delta I(\lambda_0) \cos \omega t \end{aligned}$$

The RAM nulling condition in this case is different, and is given by,

$$x = \left( \frac{y_{10}}{y_{20}} \right)^2 \quad (6.11)$$

## Chapter 6: Mathematical model of RAM nulling

The generalized expression for the output with the ramp applied and the gas cell empty becomes,

$$OP_{2no\ gas} = [y_1^2(\lambda_c) - x y_2^2(\lambda_c)] \alpha_L \Delta I(\lambda_c) \cos \omega t \quad (6.12)$$

Note that the signal  $OP_{2no\ gas}$  can be obtained from a gas signal given by the next equation by making a baseline fit to it if an actual no-gas signal is inconvenient to record. The signal in the presence of gas in the cell is given by,

$$OP_{2gas} = [y_1^2(\lambda_c) e^{-\alpha(\lambda_c)Cl} - x y_2^2(\lambda_c)] \alpha_L \Delta I(\lambda_c) \cos \omega t \quad (6.13)$$

Using Eq. 6.12 and Eq. 6.13, the relative transmission is given by,

$$e^{-\alpha(\lambda_c)Cl} = 1 + \frac{OP_{2gas} - OP_{2no\ gas}}{\alpha_L y_1^2(\lambda_c) \Delta I(\lambda_c) \cos \omega t} \quad (6.14)$$

Again,  $\alpha_L y_1^2(\lambda_c) \Delta I(\lambda_c)$ , is the output at  $OP_2$  with the delay fiber arm disconnected and the gas cell empty, and the same procedure for normalization can be followed. It is pointed out that even if the RAM nulling condition given by Eq. 6.11 is precisely satisfied, it cannot be assumed that the final output will be zero throughout the scan unless  $y_1(\lambda_c)$  and  $y_2(\lambda_c)$  are totally wavelength-independent. This is where the  $\Delta I(\lambda_c) - \lambda$  curve (or equivalently  $\Delta I(i_{LD}) - i_{LD}$ ) becomes important. If the  $\Delta I(\lambda_c) - \lambda$  curve for a given laser is highly nonlinear [3, 4], the linear IM  $\Delta I(\lambda_c)$ , and therefore the baseline, will have greater curvature and this will further complicate the baseline fitting. However in the case of configuration 1 this would still not matter since the nulling condition forces the baseline to be zero throughout the scan. For applications using such lasers it would certainly be advantageous to have a configuration that will ensure a zero background despite the variation of  $\Delta I(\lambda_c)$ .

**6.2.3 Configuration 3: DFB connected to  $IP_1$  of coupler<sub>1</sub>; output taken from  $OP_1$  of coupler<sub>2</sub>**

In the final distinct configuration the expressions for the signals at  $OP_2$  and  $OP_1$  of coupler<sub>1</sub> and those for the signals at  $IP_2$  and  $IP_1$  of coupler<sub>2</sub> are different. The signals at  $IP_1$  and  $IP_2$  of coupler<sub>2</sub> before the ramp is applied may be written as,

$$IP_2 = y_{20} I(\lambda_0) \cos \omega t \quad (6.15)$$

$$IP_1 = -x \alpha_L y_{10} \Delta I(\lambda_0) \cos \omega t \quad (6.16)$$

The output at  $OP_1$  of coupler<sub>2</sub> before the ramp is applied is given by,

$$\begin{aligned} OP_{1no\ gas} &= y_{20} IP_2 - y_{10} IP_1 \\ &= \alpha_L y_{20}^2 \Delta I(\lambda_0) \cos \omega t - x \alpha_L y_{10}^2 \Delta I(\lambda_0) \cos \omega t \quad (6.17) \\ &= (y_{20}^2 - x y_{10}^2) \alpha_L \Delta I(\lambda_0) \cos \omega t \end{aligned}$$

For this configuration, the RAM nulling condition is slightly different from that for the previous case, and is given by,

$$x = \left( \frac{y_{20}}{y_{10}} \right)^2 \quad (6.18)$$

The generalized expression for the output with the ramp applied and the gas cell empty becomes,

$$OP_{1no\ gas} = [y_2^2(\lambda_c) - x y_1^2(\lambda_c)] \alpha_L \Delta I(\lambda_c) \cos \omega t \quad (6.19)$$

Again, the signal  $OP_{1no\ gas}$  can be obtained from a gas signal given by the next equation by making a baseline fit to it if an actual no-gas signal is inconvenient to record. The signal in the presence of gas in the cell is given by,

## Chapter 6: Mathematical model of RAM nulling

$$OP_{1gas} = [y_2^2(\lambda_c)e^{-\alpha(\lambda_c)Cl} - xy_1^2(\lambda_c)]\alpha_L \Delta I(\lambda_c) \cos \omega t \quad (6.20)$$

Using Eq. 6.19 and Eq. 6.20, the relative transmission is given by,

$$e^{-\alpha(\lambda_c)Cl} = 1 + \frac{OP_{1gas} - OP_{1no gas}}{\alpha_L y_2^2(\lambda_c)\Delta I(\lambda_c) \cos \omega t} \quad (6.21)$$

The term  $\alpha_L y_2^2(\lambda_c)\Delta I(\lambda_c)$  is the output at  $OP_I$  with the delay fiber arm disconnected and the gas cell empty, and the same procedure for normalization can be followed.

It was initially assumed that once the RAM nulling condition (Eq. 6.11 and Eq. 6.18) is established, it would hold over the entire wavelength scan since the wavelength-dependence of  $y_1(\lambda_c)$  and  $y_2(\lambda_c)$  over the very small tuning range of the laser (typically 0.4nm) is weak, and it is well known in modulation spectroscopy that the wavelength-dependence of  $\Delta I(\lambda_c)$  for a given DFB is strong. Therefore it was assumed that  $\Delta I(\lambda_c)$  would be the dominant factor and that nulling it at the starting wavelength would be sufficient to ensure a zero background throughout. However, this assumption was proved to be inaccurate by the distinct slope on the RAM nulled signals. Simulations of the configurations are carried out to reveal the expected trend of signals for the DFB used in the experiments.

### 6.3 Simulation of RAM nulled output

In order to simulate the RAM nulling situation it is necessary to obtain the variation of the laser IM,  $\Delta I(\lambda)$  over the typical range of a wavelength scan, and also the variation of the fractional coupling ratios of the 3-dB coupler. To estimate  $\Delta I(\lambda)$  from the DFB output intensity  $I(\lambda)$ , two approaches may be taken. These are as follows –

1. In the first approach, the mean laser current  $i_{LD}$  is varied in discrete steps over a typical scan range. The current modulation of chosen amplitude is also simultaneously applied. The photodiode voltage displayed on the oscilloscope is recorded for every current step of 5mA. These traces represent

## Chapter 6: Mathematical model of RAM nulling

the simultaneous variation of the mean laser intensity as well as the sinusoidal IM as a function of the mean laser current. From each trace the mean intensity and the IM amplitude are obtained by simply extracting the average and peak-to-peak value of each trace. Although this method of measurement is accurate, it is rather tedious to perform.

2. The alternative method of estimating the variation of the IM is to obtain the variation of the mean intensity over a current scan range and to fit a polynomial to it to establish the functional dependence of the intensity on the laser current. The variation of the IM is estimated programmatically by assuming a constant current dither  $\Delta i$ , and evaluating the polynomial at  $i_{LD} \pm \frac{\Delta i}{2}$  at discrete steps of  $i_{LD}$  to give the intensity excursion about each value of the mean current. This gives an estimate of the nature of variation of the IM as the current is ramped up. This method is more general and less tedious to implement.

In accordance with the first method, Fig. 6.3 shows the output observed on the oscilloscope as the mean laser current is varied over a range of 30-110mA, while the current modulation amplitude is kept constant at 11.56mA, which corresponds to an  $m$ -value of about 0.7 for the DFB laser used and for a pressure of approximately 1 bar. As the mean laser current increases, there is an obvious increase of the mean laser intensity. What is not immediately obvious is the variation of the IM. To clarify these points the mean intensity and the IM amplitude are plotted separately as a function of  $i_{LD}$ .

The variation of the average intensity,  $I$  extracted from the sinusoidal variation of intensity shown in Fig. 6.3 is plotted below in Fig. 6.4. The dependence of  $I$  on laser current  $i_{LD}$  is accurately represented by a cubic function, as borne out by the norm of residues of quadratic and cubic polynomial fits.

It is important to ensure that all measurements are performed within the linear operating range of the photo-detector since detector saturation, particular towards the

**Chapter 6: Mathematical model of RAM nulling**

end of the scan range, introduces artificial nonlinearity in the variation of  $I$  that can significantly change subsequent estimates and results.

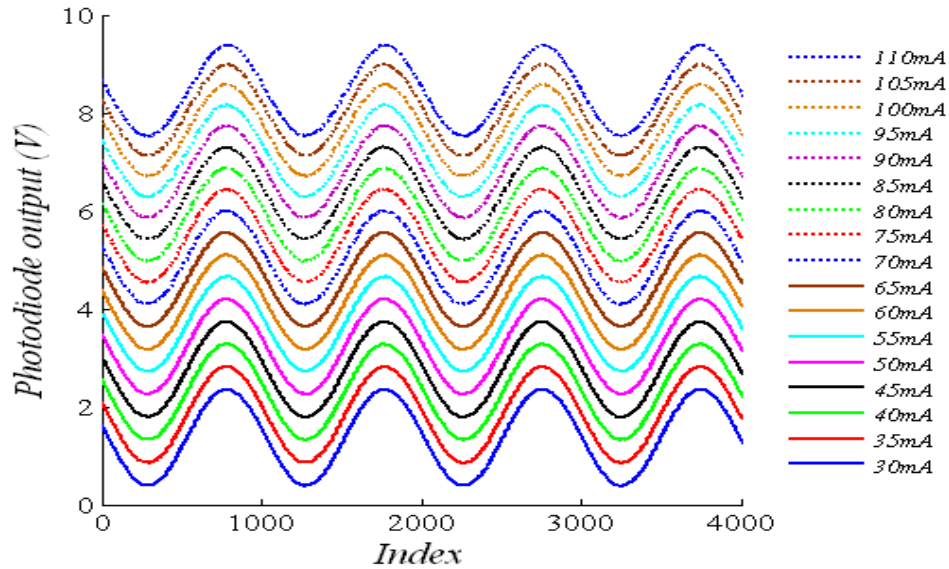


**Fig. 6.3:** Variation of the laser intensity over a typical scan range of the laser current measured at the input of the gas cell for modulation current amplitude of 11.56mA

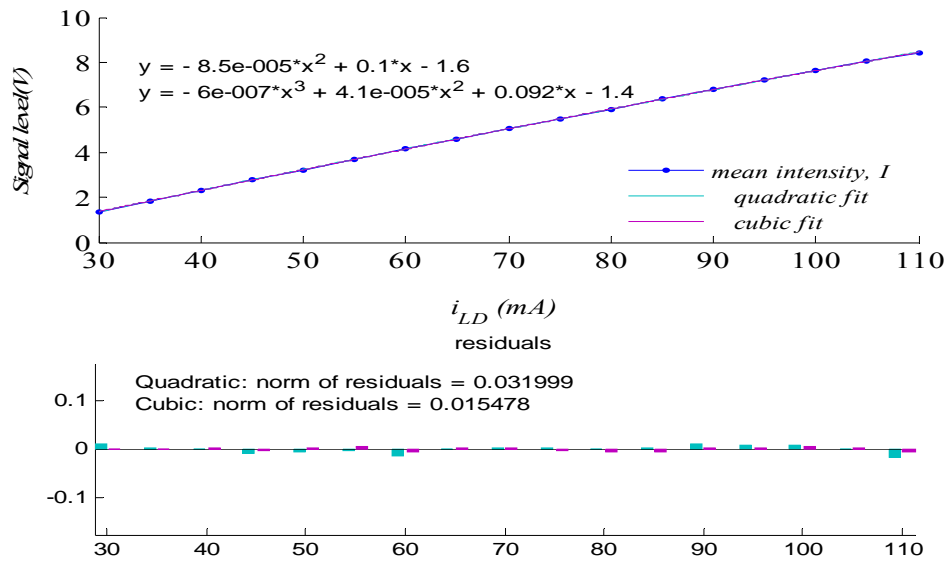


**Fig. 6.4:** Variation of the average intensity  $I$  over the current scan range directly measured at the input of the gas cell, and quadratic and cubic fits.

## Chapter 6: Mathematical model of RAM nulling

The experimentally determined variation of the IM is shown in Fig. 6.5 by extracting the peak-to-peak value of each trace in Fig. 6.3. The variation of the IM is predominantly linear as borne out by the close agreement between the linear and quadratic fits.

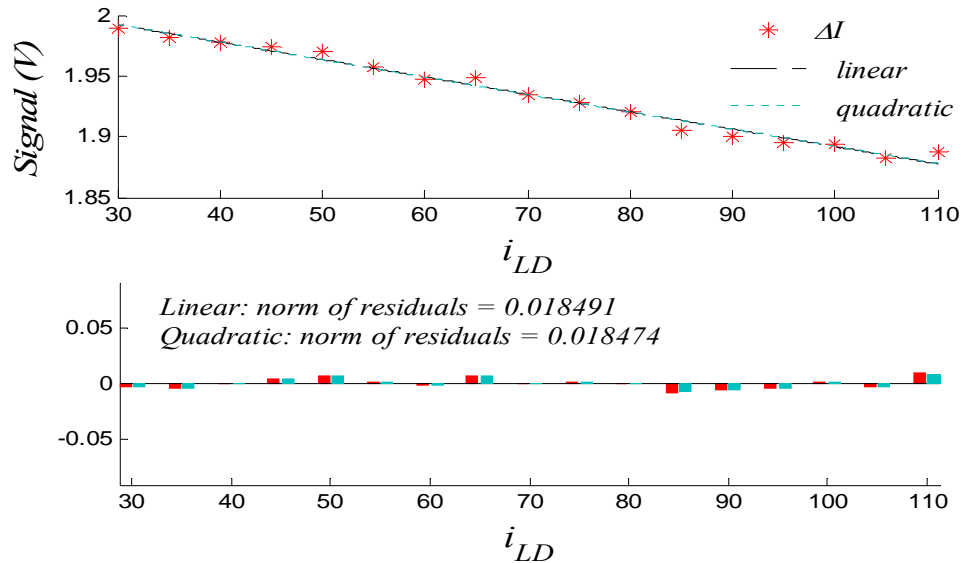


**Fig. 6.5:** The linear variation of  $\Delta I$  over a typical current scan range directly measured at the input of the gas cell for modulation current amplitude of 11.56mA.

From the variation of the mean intensity shown in Fig. 6.4, the variation of the IM amplitude may also be estimated programmatically as explained earlier. The result is shown in Fig. 6.6 below. It is seen that the quadratic fit is only marginally better than the linear fit. The norm of residues is understandably much smaller since this is a simulation where measurement errors are minimized.

The nature of variation depicted in Fig. 6.5 and Fig. 6.6, as well as the actual values are in close agreement. This justifies the use of programmatically estimating the variation of  $\Delta I(\lambda)$  from the nature of the  $I - i_{LD}$  curve that is easier to measure. It is finally worth noting that while  $I$  increases over the scan  $\Delta I(\lambda)$  decreases. This should be apparent from the signs of the coefficients of the cubic equation in Fig. 6.4. This conclusion is also supported by the negative slope of the off-centre regions of the non-nulled, RAM signals (as in Fig.5.1b) that is essentially due to the  $\Delta I(\lambda)$  term.

## Chapter 6: Mathematical model of RAM nulling

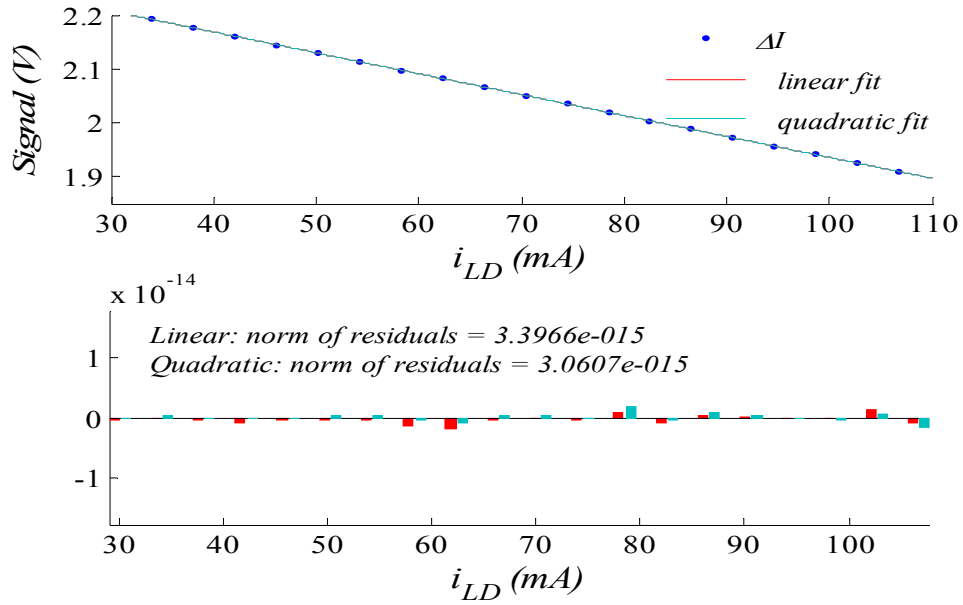


**Fig. 6.6: Programmatically estimated variation of  $\Delta I$  over a typical scan range of the laser current measured at the input of the gas cell for modulation current amplitude of 11.56mA. The variation of  $\Delta I$  is predominantly linear.**

The laser wavelength at each mean current value was also measured using an Agilent optical spectrum analyzer to correlate the laser current with the wavelength. The approach of programmatically extracting the nature of variation of the IM from the  $I(\lambda) - \lambda$  curve has been preferred for the simulations so that a comparison can be made later between the DFB used and recently-reported laser structures with significantly more nonlinear laser characteristics. Although actual experiments were not performed because the group does not have access to such lasers, a reasonable comparison can still be made by this method of simulating the variation of the IM from the nonlinear laser characteristics.

The wavelength-dependent fractional coupling ratios are estimated next. For a phase-matched case of a coupler the fractional coupling ratios  $y_1(\lambda)$  and  $y_2(\lambda)$  are given by [6-12],

$$y_1(\lambda) = \cos^2[\kappa(\lambda)L_c/2] \quad (6.22)$$

## Chapter 6: Mathematical model of RAM nulling

$$y_2(\lambda) = \sin^2[\kappa(\lambda)L_c/2] \quad (6.23)$$

where,  $\kappa(\lambda)$  is the wavelength-dependent coefficient of coupling between the two fibers, and  $L_c$  is the coupling length that denotes the length for complete power transfer from one fiber to the other. It is reasonable to assume a phase-matched case since the wavelength range scanned by the current ramp is a fraction of a nanometer. The expression for the coupling coefficient for the case of coupling between two parallel identical single mode fibers [8, 9] is given by,

$$\kappa(\lambda) = \frac{\pi}{2} \frac{\sqrt{\delta}}{a} e^{-(A+Bd_1+Cd_1^2)} \quad (6.24)$$

where, 
$$\delta = (n_1^2 - n_2^2) / n_1^2 \quad (6.25)$$
and  $d_1 = d/a$ , where  $d$ ,  $a$ ,  $n_1$  and  $n_2$  represent the fiber core separation, core diameter, core index and cladding index respectively. The parameters  $A$ ,  $B$ , and  $C$  are calculated from a set of coefficients and the V-number of the fiber, and are given in Ref. [8, 9].

$$A = 5.2789 - 3.663V + 0.3841V^2 \quad (6.26a)$$

$$B = -0.7769 + 1.2252V - 0.0152V^2 \quad (6.26b)$$

$$C = -0.0175 - 0.0064V - 0.0009V^2 \quad (6.26c)$$

Where, in the above equations,  $V$  represents the V-number of the fiber and is given by,

$$V = \frac{2\pi a}{\lambda} \sqrt{n_1^2 - n_2^2} \quad (6.27)$$

It is reiterated here that if calculated values of  $y_2(\lambda)$  and  $y_1(\lambda)$  are to be used for signal normalization to extract the relative transmission in an actual experiment, it would be necessary to accurately determine the value of  $\kappa(\lambda)$ . However, since the signal normalization method described in the preceding section does not explicitly need these

## Chapter 6: Mathematical model of RAM nulling

values, the exact values of the 3-dB coupler parameters are not required, and calculated values may be used to simulate the nature of signals in order to illustrate the nulling mechanism. For the purpose of the model, typical values of a 3-dB coupler designed to operate at the centre wavelength of 1550nm have been assumed. For a typical telecom-grade 3-dB coupler with  $n_1 = 1.4532$ ,  $n_2 = 1.45$ ,  $a = 5\mu m$ , and  $d = 12\mu m$ , the coupling length,  $L_c$  of the coupler is estimated by assuming that the coupler is a perfect 3-dB coupler at the designed wavelength of 1550nm. By substituting this wavelength value,  $\kappa(\lambda_{design})$  can be calculated. The coupling length  $L_c$  is calculated using the relation  $L_c = \pi/2\kappa_{design}$ . The length of the coupler must be half this value for it to be a 3-dB coupler, and is constant for a given coupler. Assuming this coupler length it is now possible to estimate the coupler's response by re-calculating values of  $y_1(\lambda)$  and  $y_2(\lambda)$  from Eq. 6.22 and Eq. 6.23 for the wavelength range scanned by the laser current. The variation of  $y_1(\lambda)$  and  $y_2(\lambda)$  over the wavelength range actually scanned by the DFB laser used in the experiments is shown in Fig. 6.7a and Fig. 6.7b.

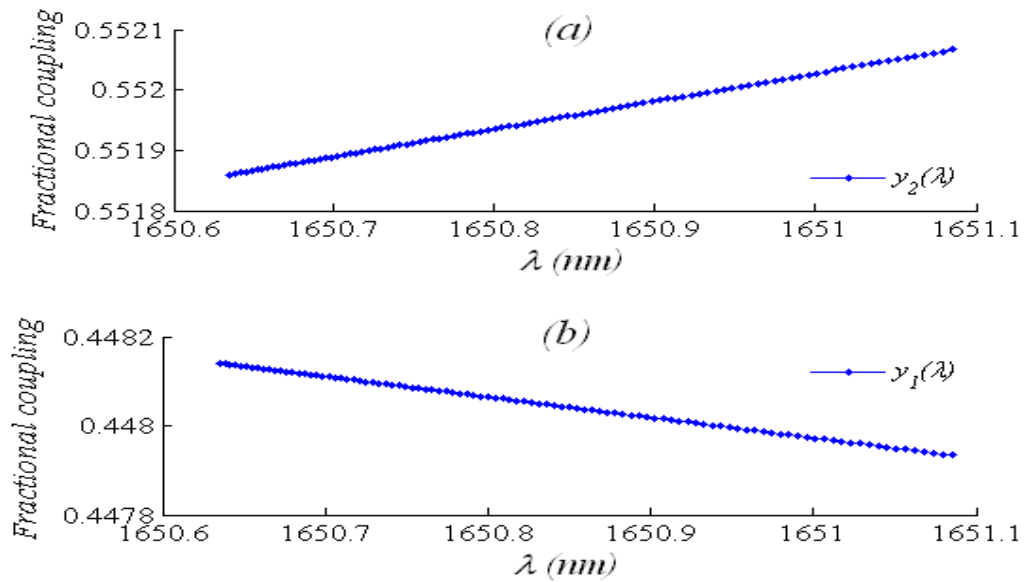


Fig. 6.7: Variation of typical 3-dB coupler's fractional coupling ratios (a)  $y_2(\lambda)$  and (b)  $y_1(\lambda)$

## Chapter 6: Mathematical model of RAM nulling

The figure above shows the variation of fractional coupling ratio of a typical telecom-grade fiber coupler over a typical scan range. The percentage changes in  $y_1(\lambda)$  and  $y_2(\lambda)$  over the wavelength range are only -0.046% and 0.0375% respectively, which shows that the wavelength-dependence of the coupling coefficients is extremely weak in comparison to that of  $\Delta I(\lambda)$  that changes by -14% which justifies the initial assumption that the coupling ratios are constant.

## 6.4 Results of simulation and experiments

The simulated RAM nulled outputs and experimental data for the three experimental configurations analyzed in Sec. 6.2.1 through Sec. 6.2.3 are shown in Fig. 6.8, Fig. 6.9 and Fig. 6.10. In each of these figures the three upper subplots show the simulated outputs for three values of  $x$  for that configuration, while the lower subplots show the corresponding experimental data. A representative absorption profile has been superimposed on the simulated baselines to illustrate the situation better, but it has no bearing on the nature of the baselines.

### *6.4.1 Comparison of simulation and experiments for the three configurations*

In this section the simulated and the experimental outputs for each of the three configurations discussed earlier are compared.

For the first configuration it is seen from Fig. 6.8a and Fig. 6.8d that if the RAM nulling condition is exactly satisfied for the first configuration given by Eq. 5.4, it is indeed possible to achieve a perfectly zero baseline. The absorption signal can then be selectively amplified to a greater desired extent without saturating the electronics. However, any deviation from this condition will produce a non-zero and sloping background as shown in Fig. 6.8e and Fig. 6.8f for two values of  $x$  nearly equal to 1. The extent of the deviation from 1 determines the level of the background.

## Chapter 6: Mathematical model of RAM nulling

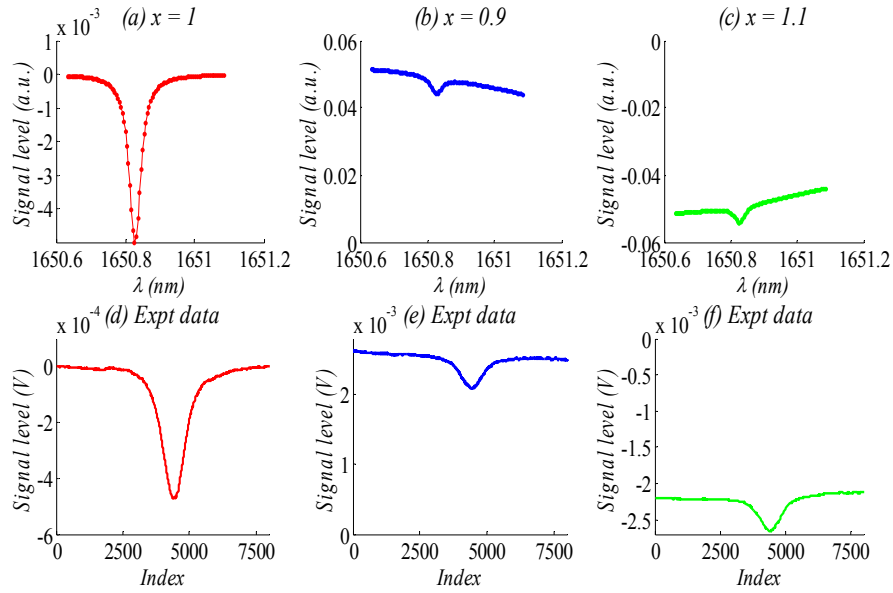


**Fig. 6.8:** Simulation and experiments for configuration 1 - DFB connected to  $IP_2$  of coupler<sub>1</sub>; output from  $OP_1$  of coupler<sub>2</sub>. Concentration 1.02%, pressure 1.038 bar and temperature 19.2°C.

The signal  $\Delta I(\lambda)$  was shown to have a downward slope in Fig. 6.5, and the product  $y_1(\lambda)y_2(\lambda)$  is easily verified to slope downward since  $y_1(\lambda)$  and  $y_2(\lambda)$  have slopes of opposite sign. Therefore for the non-nulled cases the value of  $(1-x)$  determines the sign of the signal, while  $\Delta I(\lambda)$ , being the dominant factor by far, determines the magnitude as well as the nonlinearity of the slope of the output signal. It is noted that the vertical axes of the simulations do not represent actual signal values since certain assumptions have been made regarding the ideal behaviour of the couplers, and the lock-in sensitivity cannot be incorporated in the model. Experimental data is also plotted in the lower subplots of the Fig. 6.8. A 1% mixture of methane in nitrogen was used for Fig. 6.8 and Fig. 6.10, while methane of 0.1% concentration was used for Fig. 6.9. The modulation index was chosen to be  $\sim 0.75$ . The signals recovered by the lock-in amplifier have been scaled by the corresponding sensitivities.

**Chapter 6: Mathematical model of RAM nulling**

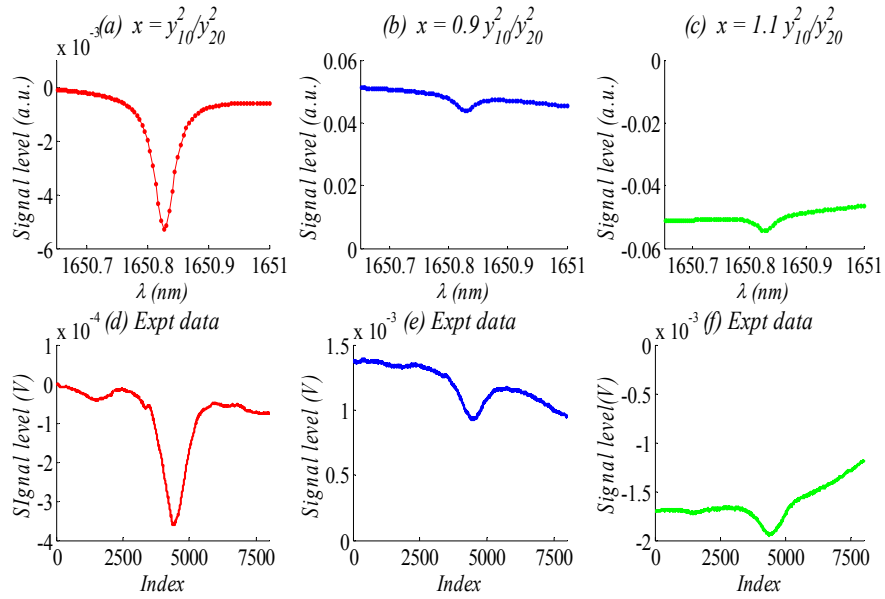


**Fig. 6.9:** Simulation and experiments for configuration 2 - DFB connected to  $IP_2$  of coupler<sub>1</sub>; output from  $OP_2$  of coupler<sub>2</sub>. Concentration 0.1%, pressure 1.038 bar and temperature 19.2°C.

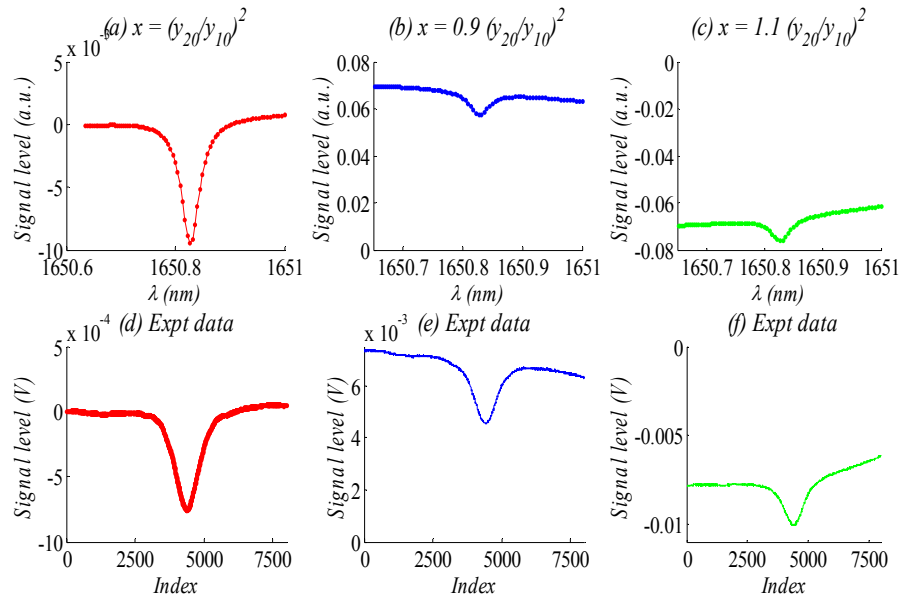


**Fig. 6.10:** Simulation and experiments for configuration 3 - DFB connected to  $IP_1$  of coupler<sub>1</sub>; output from  $OP_1$  of coupler<sub>2</sub>. Concentration 1.02%, pressure 1.038 bar and temperature 19.2°C.

## Chapter 6: Mathematical model of RAM nulling

For the second and third configurations depicted in Fig. 6.9 and Fig. 6.10 respectively, the situation is different in an important respect. As explained earlier, it is not possible, in these cases, to obtain a perfectly zero baseline even with perfect RAM nulling. A residual slope will necessarily remain on the output signal. The variation of  $y_1(\lambda)$  and  $y_2(\lambda)$  is seen to be dominant the closer the system is tuned to the RAM nulling condition given by Eq. 6.11 and Eq. 6.18. As the system moves away from this condition the  $\Delta I(\lambda)$  term again begins to dominate thereby producing the large offset.

The fourth configuration in which the DFB is connected to  $IP_1$  of coupler<sub>1</sub> and the output is measured at  $OP_2$  of coupler<sub>2</sub> is identical to configuration 1 and is therefore not treated separately. These simulations and the corresponding experimental results pertaining to the three configurations clearly bring out the interplay between the wavelength-dependence of the couplers and that of the IM of the laser, and demonstrate that depending on the experimental configuration, a small residual slope may arise in the RAM nulled signals.

### ***6.4.2 Implications of mathematical model of RAM nulling for practical applications***

As a final demonstration of the practical utility of this analysis of the RAM nulling system for future work, the projected behaviour of the system is investigated for a laser source with significantly more nonlinear current-intensity characteristics than the DFB that has been used in these experiments. Figure 6.11 shows a simulated representative current-intensity curve of such a laser and the corresponding variation of  $\Delta I(\lambda)$  extracted in the same way as for the DFB before. As pointed out earlier, VCSELs have already been introduced for some years now and quantum cascade lasers (QCLs) are playing an increasingly prominent role in mid-infrared gas sensing. It is pointed out that the nature of the current-intensity curve is not at all unrealistic, and is in fact a very good representation of actual laser characteristics as borne out by some recent work [1-4]. Clearly the  $\Delta I(\lambda)$  curve is significantly more nonlinear than that for a DFB since the current-intensity curve is highly nonlinear too.

Chapter 6: Mathematical model of RAM nulling

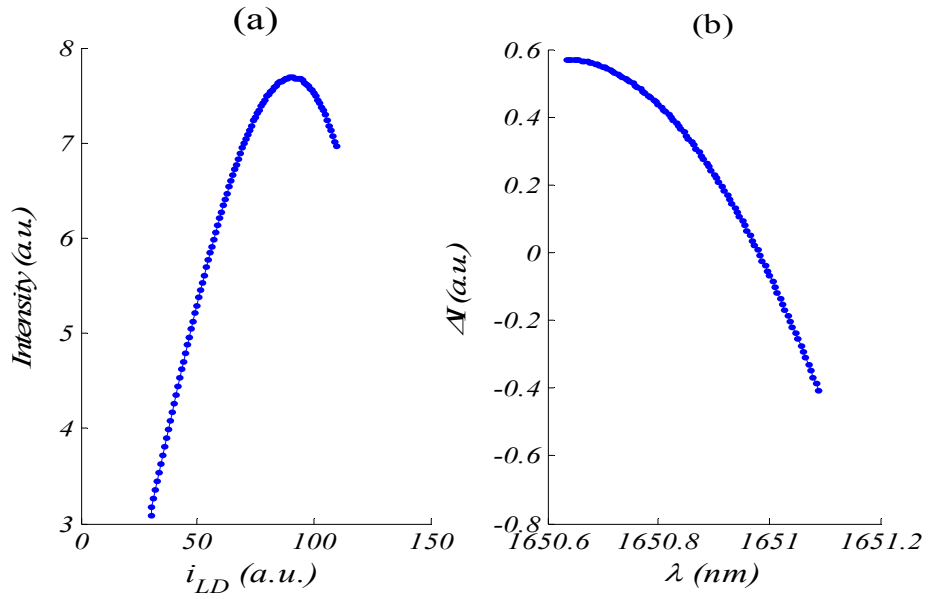


Fig. 6.11: Simulated variation of (a) intensity vs current, (b)  $\Delta I(\lambda)$  vs  $\lambda$  for a laser with highly nonlinear laser characteristics

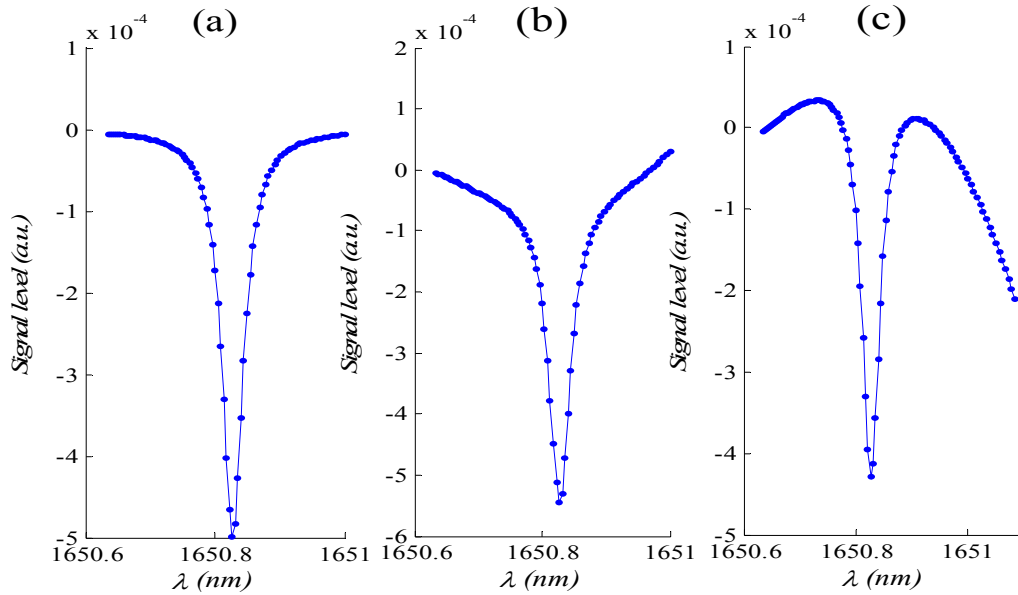


Fig. 6.12: Simulated output for the perfectly nulled case for the three configurations for highly nonlinear laser characteristics

## Chapter 6: Mathematical model of RAM nulling

The output of the precisely nulled case for each of the three configurations is shown in Fig. 6.12, in which the off-centre regions for only the first configuration are flat and zero while for the other two configurations there is a significantly nonlinear baseline due to the nature of the  $\Delta I(\lambda)$  curve. This makes it amply clear that the first configuration can effectively cancel the effect of the significantly nonlinear variation of the  $\Delta I(\lambda)$  curve for a given laser. The important implication of the result of this simulation is that, for future widely tunable  $1f$  gas detection systems based on the new RAM technique (and also PDM) and using long wavelength VCSELs or mid-infrared QCL sources, such an experimental configuration should produce flat, zero-level nulled outputs that will obviate the need for baseline fitting on the nulled signals. This result assumes even greater significance when the normalization strategy discussed in Sec. 5.2.2 is considered in conjunction with this result. It was shown that baseline fitting is not necessary to obtain a normalization signal. The two results together ensure that the RAM method with background nulling is a perfectly robust method for the recovery of absolute gas absorption line shapes in field-deployable, stand-alone applications in process control for the measurement of concentration and pressure.

### 6.5 FIR filtering to eliminate etalon fringes

In its present state the main problem that limits the RAM nulling method is the presence of etalon fringes that corrupt the raw signal for low concentrations as shown by the experimental RAM nulled absorption signal for a sample of methane in nitrogen balance at a concentration of 0.1017% for the first configuration. These results were obtained with the same gas cell (5.9 cm length) used for the previous results using 10% and 1% methane.

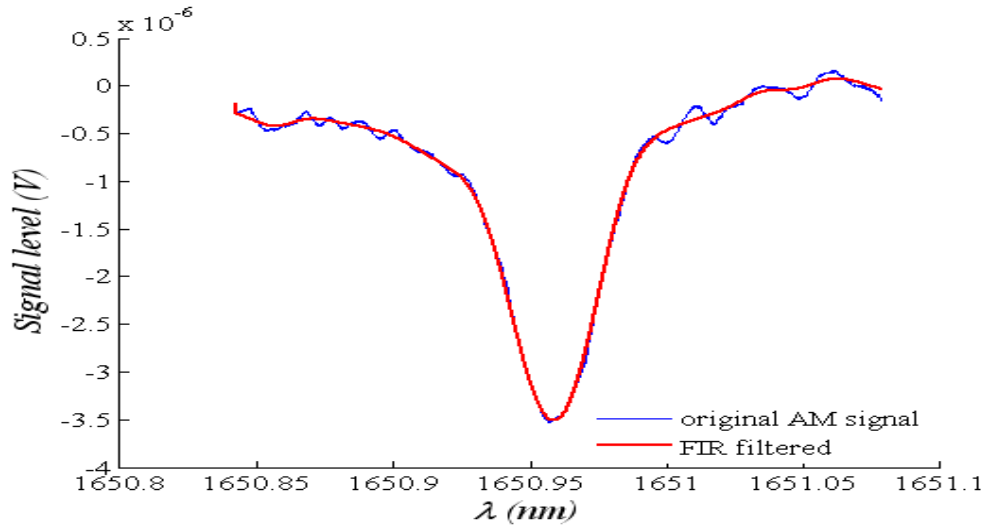


Fig. 6.13: Effect of FIR filtering on 0.1%  $CH_4$  at 1.082 bar and 20.6°C,  $m = 0.75$

The effect of the etalon fringes on the signal is obvious. The etalon fringes arise due to the GRIN lenses within the gas cell. Although the lenses have anti-reflection coatings on them the residual etalon fringes are not sufficiently suppressed and the raw data is corrupted by noise to an appreciable extent. Clearly the recovery of the line shape is very challenging and not as good as in the case for previous results with higher concentrations. The fit is particularly poor towards the far end of the scan. Significant errors will arise in the extraction of concentration and pressure in such cases.

The data was acquired using a digital oscilloscope with the averaging maximized but clearly signal averaging on the oscilloscope alone is not sufficient for the recovery of a clean signal. This is because the etalon fringes and the absorption signal have similar time-domain variations, which causes the respective power spectral densities (PSDs) of the digitized signals to nearly overlap. The etalon fringes can be considered to be a classic case of deterministic frequency-domain noise which cannot be reduced by signal averaging alone since a signal averager has very poor frequency-domain characteristics and therefore poor frequency selectivity. Specialized digital filtering techniques are required to eliminate such type of noise.

The discrete-time Fourier transform of the digitized data is computed using the standard Fast Fourier Transform (FFT) algorithm in MATLAB, and the PSD of the

## Chapter 6: Mathematical model of RAM nulling

acquired signal is shown in Fig. 6.14. The frequency axis is relative to an assumed sampling frequency 5 kHz. The assumed sampling frequency is used only to form the x-axis of the PSD and does not affect the filtering in any way. Therefore this value is completely arbitrary and unimportant for the present application. For high spectral resolution in the transform domain, and more effective filtering, the original data was up-sampled by a factor of 4 to generate more data points.

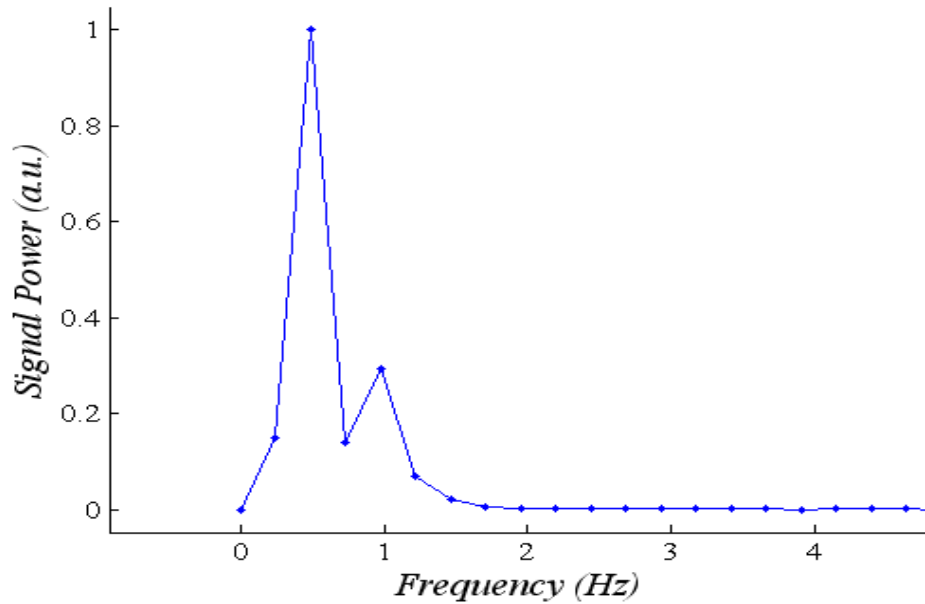


*Fig. 6.14: Power spectral density (PSD) of the raw signal showing the nearly-overlapping PSDs of the gas signal and the etalon fringes*

From the plot of the PSD it is seen that the main signal content is accompanied by a second nearly-overlapping peak. It is now clear why it is not trivial to filter out the noise source. A Finite Impulse Response (FIR) digital filter [13, 14] with a very sharp roll-off was used to filter out the fringes to the best possible extent without compromising the peak depth. The sharpness of the roll-off of such a filter increases with the length of the filter kernel. However, the MATLAB algorithm requires that the data to be filtered be at least three times as long as the filter kernel. This required the original data to be re-sampled to satisfy this requirement.

## Chapter 6: Mathematical model of RAM nulling

The effect of FIR filtering on the raw data is shown in Fig 6.15a. Although the filtering significantly improves the signal quality, the situation is still not ideal.

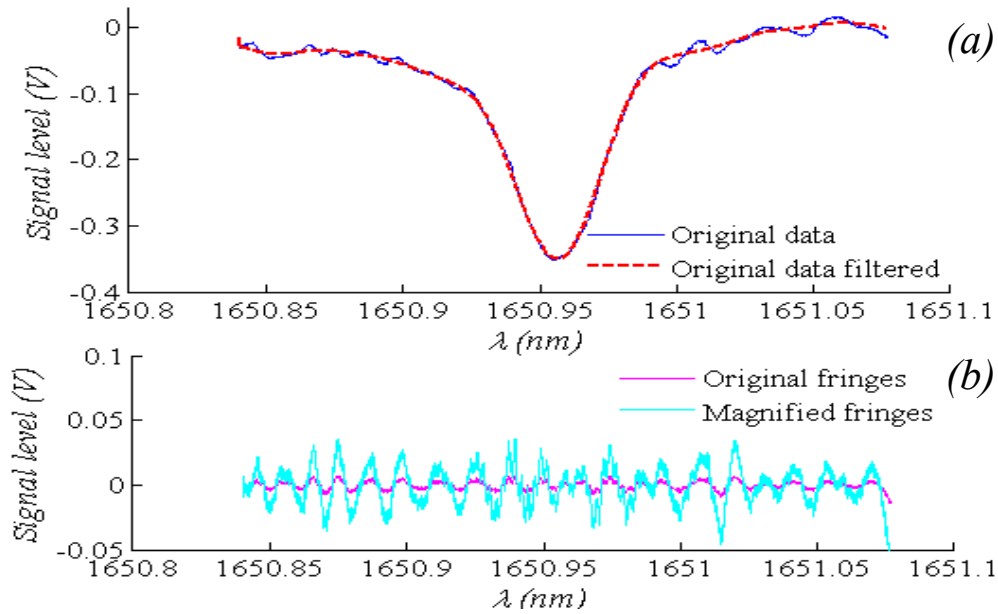


**Fig. 6.15: Effect of FIR filtering on 0.1%  $\text{CH}_4$  at 1.082 bar and 20.6°C,  $m = 0.75$**

In Fig 6.15(b), the etalon fringes have been extracted from the signal using a high-pass filter. The fringes are then magnified three times and added to the original signal. The result is shown in Fig 6.16 in which the signal in green is the original signal with the added corruption. The corrupted signal is filtered with the same filter. The FIR filter is able to recover a relatively clean signal even in the presence of much stronger etalon fringes although it is best to minimize the etalon fringes directly by better design of the optics within the gas cell.

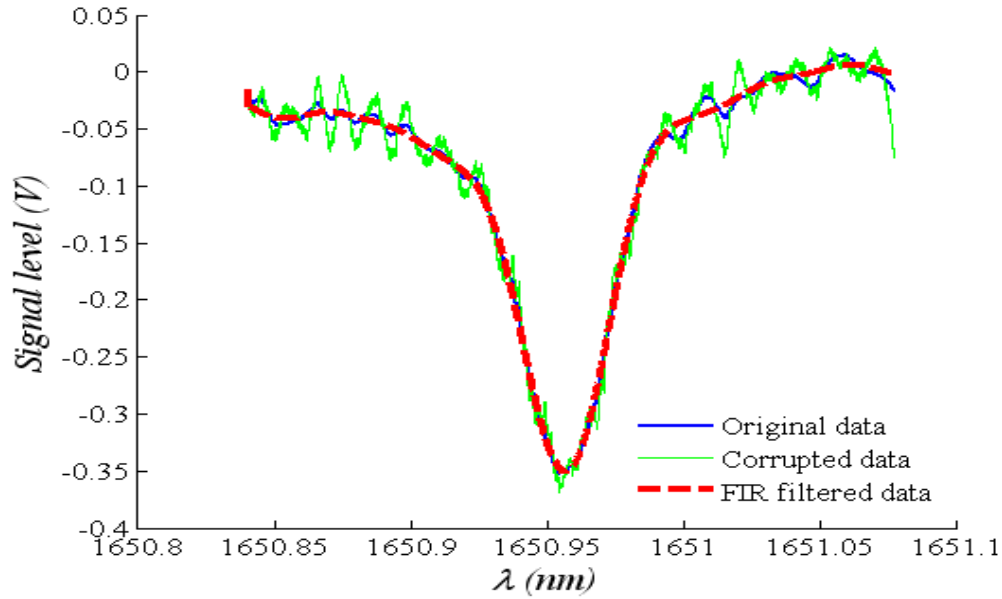


*Fig. 6.16: Effect of FIR filtering on 0.1% CH<sub>4</sub> at 1.082 bar and 20.6°C, m = 0.75*

It is important to note that the wavelength referencing should be performed with the filtered data and not with the raw data. This is because if the digital filter has a nonlinear phase response, this can cause a significant delay in the discrete time domain. This in turn causes a mismatch between minima of the filtered and unfiltered absorption lines. The resultant wavelength mismatch is apt to confound the unsuspecting user. An FIR filter has been preferred over an Infinite Impulse Response (IIR) filter because an FIR filter has inherently linear phase response. It may however be preferable to use an IIR filter in real-time applications because the computation speed of IIR filters is less than that of FIR filters. This is because IIR filters use the method of recursion while FIR filters use convolution to filter the data [13, 14]. The difference in computation time is particularly noticeable if the kernel of the FIR filter is long and the number of data points is large.

The final relative transmission profile is shown in Fig. 6.17 in which it is clear that despite the etalon fringes it is still possible to extract useful information with fairly good accuracy. It is expected that the power spectra can be better separated and the demands on the digital filter relaxed by designing a longer gas cell that would give rise to etalon fringes with a PSD that does not overlap with that of the actual gas absorption signal.

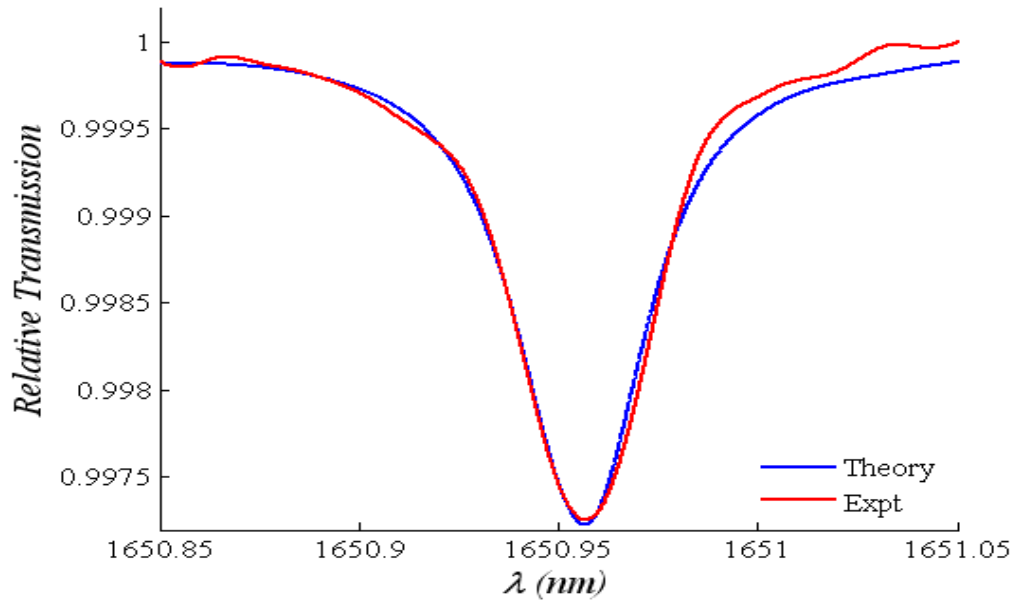


*Fig. 6.17: Recovery of gas absorption line shape for 0.1% CH<sub>4</sub> at 1.082 bar and 20.6°C,  $m = 0.75$*

A set of results using the RAM method with 1f RAM nulling are shown in Fig. 6.18 and Fig. 6.19 for a sample of methane at a concentration of 0.1%. It is clear that the etalon fringes have a pronounced deleterious effect on the shape of the signals. The magnitude of the actual concentration-dependent signal is large enough for it to be digitized accurately. It may be concluded that concentration measurements can still be made with good accuracy but there will be significant errors in the extraction of pressure. The measurements have been restricted to an  $m$ -value of 0.7, although the concentration-dependent amplitude of the RAM signals increases significantly for higher  $m$ -values. This was done because for higher  $m$ -values, the correction factor strategy does not perform well and the gas absorption line shape is not recovered accurately. A new strategy to calculate correction factors for arbitrarily high  $m$ -values is being developed within the group with promising initial results. It is expected that the incorporation of the new algorithm will permit higher  $m$ -values to be used that will, in turn, produce significantly higher signal levels. The effect of the etalon fringes would not be as severe in that case. Moreover, it is reasonable to expect that a better optical design of the micro-

## Chapter 6: Mathematical model of RAM nulling

optic gas cell should lead to greater suppression of the etalon fringes and enable accurate extraction of gas parameters for lower concentrations.

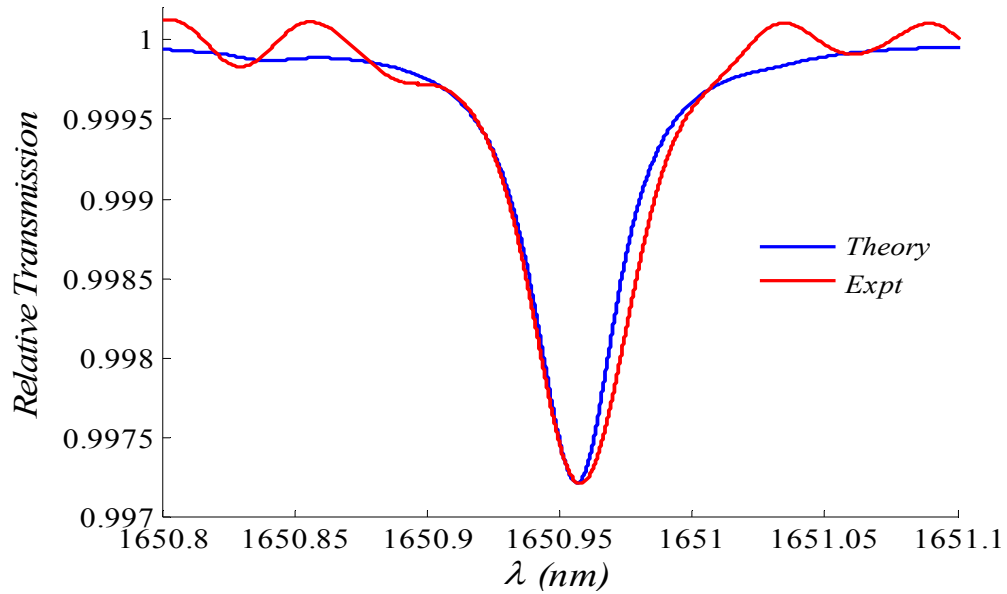


*Fig. 6.18: Recovery of gas absorption line shape for 0.1% CH<sub>4</sub> at 1.043 bar and 23.6°C,  $m = 0.7$*

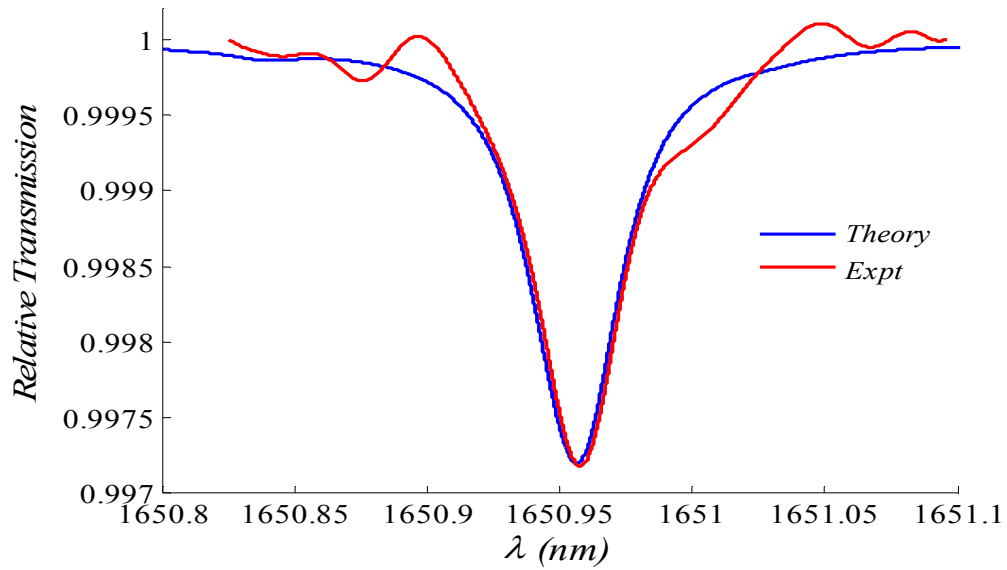


*Fig. 6.19: Recovery of gas absorption line shape for 0.1% CH<sub>4</sub> at 1.116 bar and 22.6°C,  $m = 0.7$*

## 6.6 Conclusion

In the course of this discussion regarding the presence of an unexpected non-zero slope on the RAM-nulled signals a detailed mathematical analysis of the RAM nulling technique has been presented in which the wavelength-dependence of the linear IM and the couplers were considered. It is shown, through simulations and experiments, that the apparently anomalous slope on the output signals arises due to the wavelength-dependence of the fiber-optic couplers and is therefore an inherent attribute of the system. However it turns out that for one experimental configuration the absorption signal appears on an essentially zero baseline. This has a three-fold significance for practical industrial applications.

First, it is not necessary to fit baselines to the nulled signals to obtain the signals  $OP_{2no\ gas}$  and  $OP_{1no\ gas}$  as in Eq. 6.12 and Eq. 6.19. As explained in Sec. 5.2.2, baseline fitting using non-absorbing spectral wings is an inconvenient requirement particularly for stand-alone instruments because this requires the availability of well-isolated absorption features and a sufficiently wide wavelength scan range. A separate problem for practical systems is that, even for relatively strong absorption signals, etalon fringes from the gas cell degrade the offline regions more than they do the actual absorption signal. This makes identifying suitable off-line leading and trailing regions to obtain a proper fit prone to errors which translate to systematic errors in the extraction of pressure and concentration. The fact that for configuration 1, the gas signal appears on a zero background obviates the need for baseline fitting and associated inaccuracies may be avoided.

Second,  $1f$  WMS with RAM-nulling using recently-developed VCSEL sources, that have much more nonlinear characteristics, should also benefit from the same configuration since the IM for these lasers is expected to have greater wavelength-dependence than the DFB laser used here. The RAM nulled signal using such lasers would appear on a flat and zero baseline despite the wavelength-dependence of the laser IM.

## Chapter 6: Mathematical model of RAM nulling

Finally, this is also important for automatic closed-loop feedback control of the nulling process (as opposed to manual tuning of the VOA) to dynamically compensate for departures from an initially established nulled condition due to slow system drifts. Feedback control can be used to re-establish the nulled condition by periodically adjusting the relative signal strengths at the input of the second coupler to bring the offline regions close to zero. To do this accurately, however, the value for the offline region of the nulled output for perfect RAM nulling should be known a priori. For configuration 1 this offline level is flat and zero. Therefore it is sufficient for the feedback algorithm to try and bring the average value of the offline region of the RAM-nulled gas absorption signal as close to zero as possible without having to take into consideration any signal slope. For a sloping nulled signal it is not possible to define a suitable offline region because such a signal will not have a flat region. It is therefore clear that from the point of view of practical signal processing it is very useful to know for which configuration the off-line background will be flat and zero.

Finally gas measurement 0.1017% methane at approximately atmospheric pressure shows that the performance of the system is mainly affected by the etalon fringes due to the gas cell. This makes it significantly more difficult to extract clean signals. For such pressures that are expected for typical applications, the nearly overlapping PSDs of the absorption and the fringes were resolved by a digital filtering technique using an FIR filter. It has been possible to recover the absorption profile for 0.1017% methane with reasonably good accuracy, although the digital filter required significant optimization. A longer and optimized cell under test is expected to lead to smaller etalon fringes whose PSD is spectrally well-separated from that of the absorption signal, thereby leading to higher noise rejection with a digital filter.

In conclusion it may be said that the experimental results and the subsequent mathematical model not only enhance the theoretical understanding of the RAM nulling technique but also provides practical information that enables the selection of a particular configuration of the experimental setup that simplifies signal recovery, post-processing and extraction of information from experimental data.

## 6.7 References

1. T. Sato, M. Mitsuhashi, N. Nunoya, T. Fujisawa, K. Kasaya, F. Kano, Y. Kondo, “2.33 $\mu\text{m}$  wavelength distributed feedback lasers with InAs-In<sub>0.53</sub>Ga<sub>0.47</sub>As multiple quantum wells on InP substrates,” IEEE Photon. Tech. Lett. **20**, 1045-1047 (2008).
2. A. Hangauer, J. Chen, R. Strzoda, M. Orstiefer, M. –C. Amann, “Wavelength modulation spectroscopy with a widely tunable InP-based 2.3  $\mu\text{m}$  vertical-cavity surface-emitting laser”, Opt. Lett., **33**, 1566-1568, (2008).
3. J. M. Ostermann, F. Rinaldi, P. Debernardi, R. Michalzik, “VCSELs with enhanced single-mode power and stabilized polarization for oxygen sensing,” IEEE Photon. Tech. Lett. **17**, 2256-2258 (2005).
4. C. Lauer, M. Orstiefer, R. Shau, J. Roskopf, G. Bohm, E. Ronneberg, F. Kohler, M. C. Amann “80°C continuous-wave operation of 2.01 $\mu\text{m}$  wavelength InGaAlAs-InP vertical-cavity surface-emitting lasers,” IEEE Photon. Tech. Lett. **16**, 2209-2211 (2004).
5. A. L. Chakraborty, K. Ruxton and W. Johnstone, “Influence of the wavelength-dependence of fiber couplers on the background signal in wavelength modulation spectroscopy with RAM-nulling”, Opt. Exp., Vol. **18**, Iss. 1, pp. 267-280 (2010).
6. M. J. F. Digonnet and H. J. Shaw, “Analysis of a tunable single-mode optical fiber coupler,” IEEE J. Quant Elec. **18**, 746-754 (1982).
7. T. Findakly and C. Chen, “Optical directional couplers with variable spacing,” Appl. Opt. **17**(5), 769-773 (1978).
8. R. Tewari and K. Thyagarajan, “Analysis of tunable single-mode fiber directional couplers using simple and accurate relations,” J. Lightwav. Technol. **4**, 386-390 (1986).
9. A. Ghatak and K. Thyagarajan, *Introduction to Fiber Optics* (Cambridge University Press, 1999), Chap. 17.

## Chapter 6: Mathematical model of RAM nulling

10. A. Yariv, *Optical Electronics in Modern Communications* (Oxford University Press, 1997), Chap. 13.
11. A. C. Boucouvalas, "Fiber Optic Components", in *Principles of Modern Optical Systems*, I. Andonovic and D. Uttamchandani, eds (Artech House, 1989).
12. K. Thyagarajan and R. Tewari, "Accurate analysis of single-mode graded-index fiber directional couplers," *IEEE J. Lightwav. Technol.* **3**, 59-62 (1985).
13. A. V. Oppenheim and R. W. Schaffer, *Digital Signal Processing*, (Prentice-Hall India, New Delhi, 1975).
14. S. W. Smith, *The Scientist and Engineer's Guide to Digital Signal Processing*, (California Technical Publishing, San Diego, 1999).

# *Chapter 7*

---

## **Extension of RAM nulling to $2f$ WMS**

---

### **7.1 Introduction**

TDLS with  $2f$  WMS has gained pre-eminence in various applications in industrial processes in which quantitative information must be extracted about the gas [1-4]. Such applications include combustion monitoring [5, 6], ratio thermometry [7-11], and flow

## Chapter 7: Extension of RAM nulling to $2f$ WMS

measurement [12]. In such applications  $2f$  WMS has been widely used to extract information of gas concentration, pressure and temperature under harsh conditions. In  $2f$  WMS the concentration of a gas is proportional to the peak value of the  $2f$  signal at line centre. Temperature measurements are based on the ratio of the peak values of  $2f$  signals from two spectral features.

The most attractive feature of  $2f$  detection in gas sensing applications is that the  $2f$  background RAM is almost zero, although signal interpretation is more involved than, for instance, the previously described  $1f$  RAM technique. A  $2f$  RAM component arises because the power-current characteristics of current-modulated DFB lasers are nonlinear to some extent. This implies that a symmetric sinusoidal current modulation does not translate to a perfectly symmetric sinusoidal intensity modulation, and as a result, higher order Fourier components of the intensity modulation (IM) appear. The nonlinear second harmonic component of the IM produces the  $2f$  residual amplitude modulation (RAM) component and for most lasers, it is the only higher harmonic that has appreciable intensity. The attribute of a nearly zero background seems to have outweighed the inconvenient need for signal calibration. Traditionally,  $2f$  WMS measurements have required calibration of the detected signal. This is to say that before the system can be used for the measurement of unknown gas concentrations it is necessary to establish a unique, well-defined, stable and preferably linear relationship between the detected electrical signal corresponding to known concentrations of the target gas. This relation, which is equivalent to a look-up table, forms what is known as a calibration curve that is specific to the particular instrument. The generation of the calibration curve requires the accurate determination of system parameters by which the detected electrical signal must be scaled in order to obtain a linear relationship between that signal and the gas concentration. System parameters include the IM and WM characteristics of the laser, the modulation index, optical coupling losses within the system and the optical-to-electrical conversion gain and other amplifier gains. While laser characteristics are usually very stable, other system parameters such as optical coupling losses are less predictable and can lead to variable optical throughput and therefore variable output signal levels. Additionally such systems not only require a careful initial characterization

## Chapter 7: Extension of RAM nulling to $2f$ WMS

before field-deployment, but also periodic re-characterization to compensate for calibration-drift. Changes to components such as the laser, the photodiode or the lock-in amplifier will require the system to be re-calibrated because the electrical output signal will also change and the previously established relation to the gas concentration will no longer be valid. The need for calibration is therefore seen to be a distinctly non-trivial problem for the deployment of stand-alone instruments in harsh or varying environments.

Recently calibration-free  $2f$  WMS has been demonstrated and studied in detail for concentration and temperature measurements of gases [10, 13-15], in which the  $2f$  signal is normalized by the  $1f$  RAM signal. For low concentrations the concentration-dependent part of the  $1f$  RAM signal is negligible, and the signal is essentially the  $1f$  background RAM. If the laser is accurately characterized, the very stable relationship between the  $1f$  RAM and the laser intensity can be established. It is then possible to use the  $1f$  RAM to normalize the intensity-dependent  $2f$  signal. Since system parameters that are not related to the laser characteristics affect both harmonic components in the same way, their effect cancels out and one is left with a robust normalization method

This technique does not rely on tuning the laser across an entire absorption feature but over a small spectral region in the vicinity of the line centre [10]. This is essentially because temperature and concentration can be extracted from the line-centre value of the  $2f$  signal. In typical applications the varying pressure is measured by a separate pressure gauge and the modulation current amplitude is adjusted to maintain the modulation index at 2.2 because the variation of the peak  $2f$  signal value exhibits very slow variation around this value. The fact that the  $2f$  signal in the vicinity of the line centre is not significantly affected by the distorting influence of the IM terms is an advantage. This  $1f$  normalization eliminates uncertainties in measurement due to laser power fluctuations and varying optical coupling losses. It has been shown that by incorporating the carefully-characterized IM and WM characteristics of the laser in to the theoretical model for the  $2f$  signal, it is possible to directly compare the simulated theoretical model and the experimental data without additional scaling of the signals. It is important to make the distinction between characterization and calibration. While this approach does

## Chapter 7: Extension of RAM nulling to $2f$ WMS

not require calibration, it does require an accurate laser characterization, which is not difficult to do.

It is also important to note that for linearity of measurement in such applications, the  $2f$  RAM either needs to be simulated and incorporated in the theoretical model, or separately measured and subtracted from the  $2f$  signal before  $1f$  normalization is performed. This is the only issue that needs to be addressed in an otherwise excellent strategy for robust field-deployable measurement systems.

A different field of application is the widely tunable multi-species detection of trace gases using new varieties of widely tunable, current-modulated lasers with significantly more nonlinear current-intensity characteristics [16-18] that have been developed recently. A single widely-tunable laser source such as a vertical-cavity surface-emitting laser (VCSEL) is obviously more advantageous than several multiplexed lasers at different wavelengths for simultaneous detection of several gas species. However, a problem with performing WMS with such lasers is the varying  $2f$  baseline that arises due to the highly nonlinear current-intensity characteristics of these lasers. In gas sensing applications that require calibration any shift of the  $2f$  signals caused by systematic baselines can lead to errors in measurement. Although  $2f$  WMS is expected to show little or no baseline this is not always the case with injection-current-modulated lasers in general, and for high modulation indices in particular.

Figure 7.1 shows representative  $2f$  signals obtained using the 1650nm DFB laser that has been used in previous experiments. The signals for a low and high value of modulation index obtained from a sample of 1.02% methane at ambient temperature and pressure are shown. The precise value of the modulation index is not important at this point. The  $2f$  signal for low modulation index appears on a zero background but for high modulation index a distinct non-zero baseline appears. The  $2f$  peak value in this case is noticeably reduced by the  $2f$  RAM. If the  $2f$  peak height is measured relative to the zero level without taking into account the shift caused by the  $2f$  RAM, subsequent calculations based on the peak value will be in error. Note that the broadening of the signal for high modulation index is due to the linear IM and is not the focus of the present discussion.

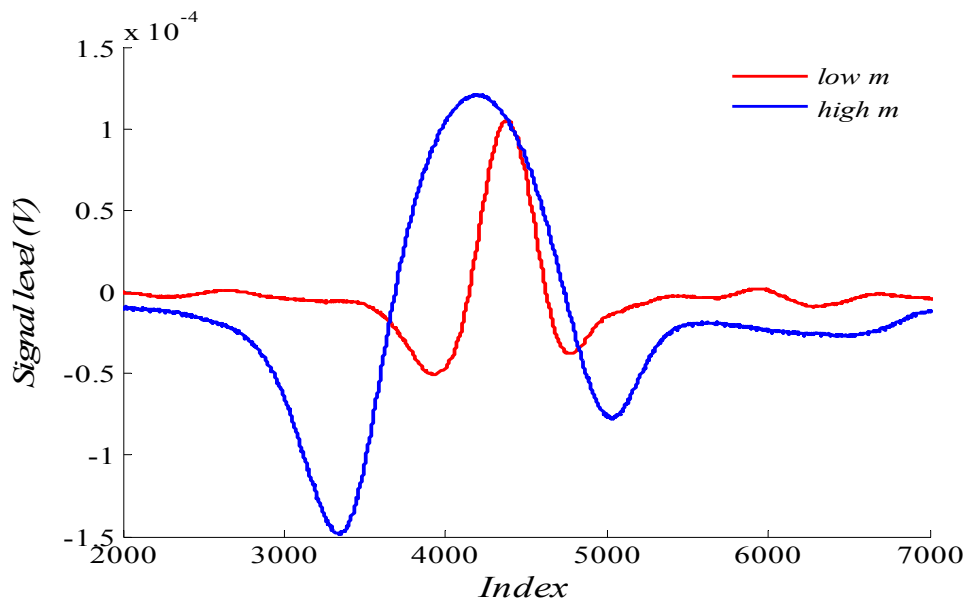


*Fig. 7.1:  $2f$  signals obtained from the 1650.956nm line of a sample of methane at a concentration of 1.02% under ambient conditions of temperature and pressure for low and high modulation index. The appreciable signal offset due to the  $2f$  RAM is evident for the high modulation index*

It is possible to tune the phase of the lock-in amplifier so that the detection axis is at  $90^\circ$  to the  $2f$  RAM. This ensures that the detection axis is free of any projection of this signal. However such an adjustment can move the detection axis significantly away from the angle that maximizes the main  $2^{\text{nd}}$  derivative signal, thereby reducing the net  $2f$  signal peak that is recovered. It is therefore incorrect (besides being impractical for industrial applications) to phase-tune the lock-in amplifier to force the  $2f$  signal to appear on a zero background. The correct approach is to subtract the baseline before making any measurements. This can be achieved either by taking a “no gas” signal by evacuating the test cell, or by using a second and identical reference cell with no gas in it. In a real-life situation obtaining “no gas” signals is not practical. Although reference cells have been widely used for this purpose, there are associated problems of maintaining proper optical alignment and equal power coupling in to the two cells for optimum baseline cancellation.

## Chapter 7: Extension of RAM nulling to $2f$ WMS

Figure 7.2 shows  $2f$  signals obtained from two near-infrared water vapour lines at 1430 nm recorded under ambient conditions. It is seen that for the higher modulation voltage there is a noticeable non-zero baseline arising from the  $2f$  RAM signal that affects the smaller feature more than the larger one. Ratio thermometry applications based on the ratio of the peak values of such a pair of lines is susceptible to errors due to the  $2f$  RAM.

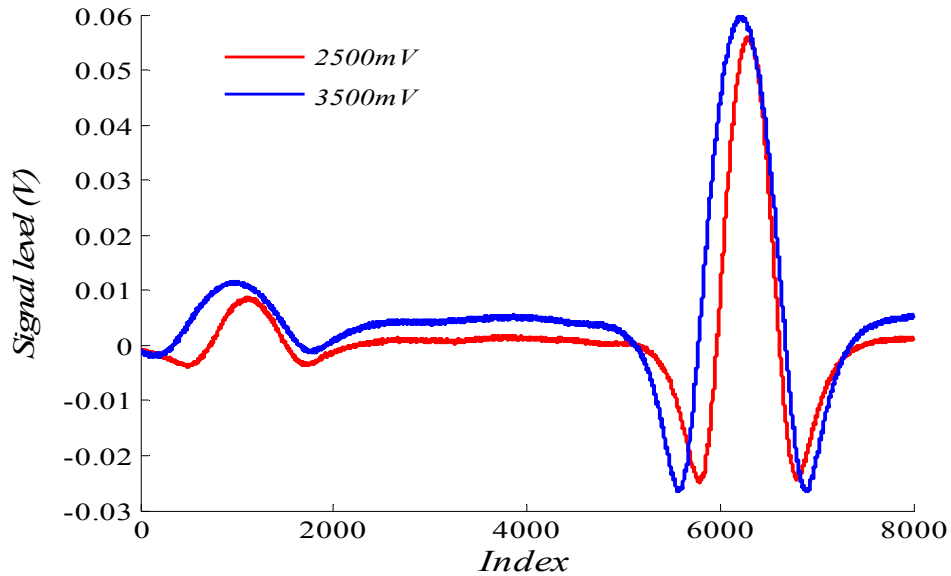


*Fig. 7.2:  $2f$  signals obtained from the 1430nm line of ambient water vapour under ambient conditions of temperature and pressure for two high values of modulation voltages. The effect of the offset due to the  $2f$  RAM is more pronounced for the weaker of the two features*

The issue of significant  $2f$  RAM is very well highlighted in a recent report of WMS with a  $2.3\mu\text{m}$  VCSEL for the detection of carbon monoxide [19]. Figure 7.3 is a reproduction of a figure presented in that study in which the experimental  $2f$  signal and the theoretical signal based on HITRAN database are shown. The noticeable feature is the significantly higher  $2f$  background signal that has a much greater slope compared to that shown in Fig. 7.1 and Fig. 7.2. For an isolated absorption line the authors have incorporated a linear sloping baseline in the theory to compare with experimental data, but for the detection of spectral lines of several gases over a wide scan range, the

## Chapter 7: Extension of RAM nulling to $2f$ WMS

background had to be measured separately and subtracted, since baseline fitting over a wide range was inconvenient.

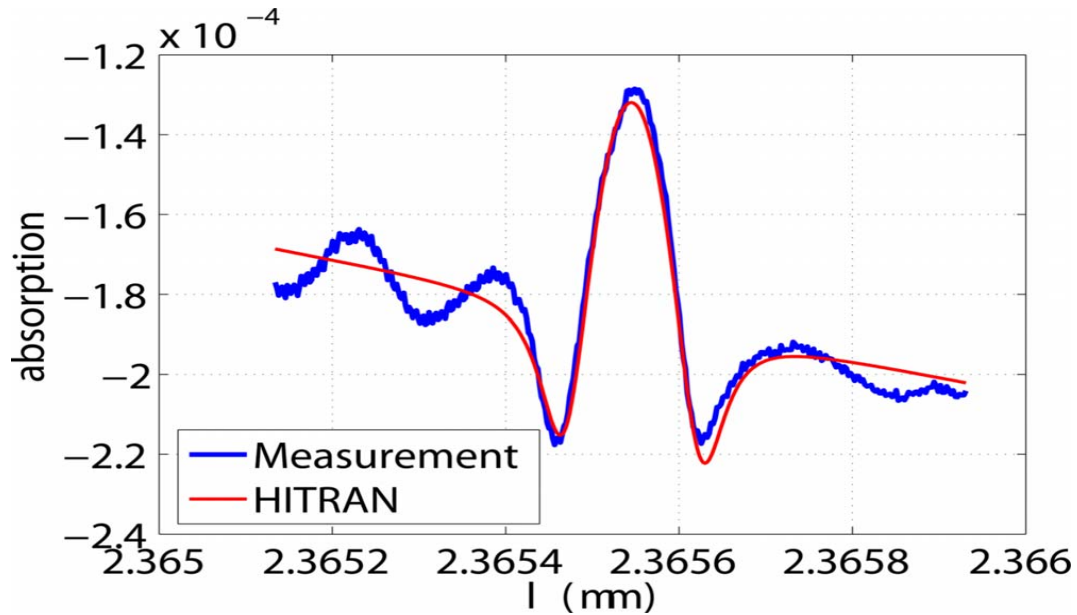


*Fig. 7.3: Significant  $2f$  baseline in a WMS study using a  $2.3\mu\text{m}$  VCSEL. Data courtesy of A. Hangauer et al, *Opt. Lett.*, Vol. 33, No. 14, 2008*

A separate measurement of the background signal requires a reference cell to be used. As mentioned earlier, maintaining alignment of optics in industrial applications can be very challenging and it is not trivial to ensure that equal power levels are directed through the reference cell and the test cell. Periodic realignment of the system to maintain equal power levels and therefore equal background levels may also be impractical in the field.

It appears that in measurements using such lasers the primary advantage of  $2f$  WMS, which is its nearly zero background, is considerably diminished in value. In this context, a method to eliminate the  $2f$  background RAM would clearly be a significant advantage in WMS applications with widely tunable lasers for the detection of multiple gas species, as well as for real-time quantitative  $2f$  WMS for the measurement of gas parameters.

In this chapter the origin of the  $2f$  background is discussed qualitatively and mathematically. A simple and robust method to optically eliminate the  $2f$  background

## Chapter 7: Extension of RAM nulling to $2f$ WMS

RAM is then proposed and demonstrated. This is achieved by extending the fiber-optic  $1f$  RAM nulling technique [20], to the  $2f$  regime. It is demonstrated that the  $2f$  RAM nulling can be performed robustly over a wide range of modulation indices, including the  $m = 2.2$  point that maximizes the  $2f$  signal. Next, the Phasor Decomposition method (PDM) [21], developed by previous researchers and discussed earlier is also extended to  $2f$  WMS to isolate the main  $2^{\text{nd}}$  derivative signal from the distorting influence of the signal due to the predominantly linear IM. Finally a calibration-free  $2f$  WMS technique with  $2f$  background RAM nulling and signal normalization by the  $2f$  RAM is proposed and mathematically analyzed. This strategy is distinct from the  $2f$  calibration-free technique mentioned earlier in that, this method incorporates  $2f$  RAM nulling, normalization by the  $2f$  RAM instead of the  $1f$  RAM and the use of the Phasor Decomposition method to isolate the main  $2^{\text{nd}}$  derivative signal from the main distorting signal arising from the  $1f$ RAM.

## 7.2 Origin of $2f$ Residual Amplitude Modulation

In the discussion of the process of signal generation in WMS in chapter 2, it was explained that for injection-current-modulated semiconductor diode lasers, the predominantly linear IM separated by a phase angle  $\psi_1$  from the synchronous WM, interacts with a gas absorption line to give rise to various concentration-dependent IM-WM terms that become progressively smaller at increasingly higher harmonics of the modulation frequency,  $f_m$  [13, 23]. However since the output intensity of these lasers does not vary linearly with the injection current, a sinusoidal current modulation at a frequency  $f_m$  does not translate to a perfectly sinusoidal IM. Therefore IM components at higher harmonics will also be produced in accordance with the theory of Fourier expansion. Concentration-independent  $1f$  and  $2f$  background signals solely due to the linear and nonlinear IM ( $\Delta I_1(\lambda)$  and  $\Delta I_2(\lambda)$  respectively) also exist, and these are referred to as the  $1f$  and  $2f$  RAM respectively. The nonlinear IM is usually much smaller than the linear IM while higher harmonics are not even discussed because they are

## Chapter 7: Extension of RAM nulling to $2f$ WMS

negligibly small. The relative levels of the linear and nonlinear IM are dependent on the degree of nonlinearity of the intensity-current characteristics of the laser, its WM efficiency (GHz/mA), and the modulation index used for a given application. The variation of the linear and nonlinear IM for a typical telecom-grade laser has been reported in the literature [13], where it has been shown that while the linear IM varies linearly with modulation index, the nonlinear IM increases as a quadratic function. Therefore for high modulation indices the nonlinear IM may not be insignificant. It should be noted however, that such behaviour is highly specific to a particular laser diode. Therefore each laser diode must be characterized individually. The mathematical formulation presented next considers a generalized case of an injection-current modulated laser diode with linear and nonlinear IM. The WM is however assumed to be linear as in all treatments of WMS.

The origin of the  $2f$  RAM becomes clear if a nonlinear IM term  $\Delta I_2(\lambda)$ , at twice the modulation frequency is included in the Taylor series treatment of the signal generation process [21, 22], in a manner analogous to Fourier analysis [7, 10, 13-15]. The phase difference between the linear IM and the WM is denoted by  $\psi_1$  as before, and a phase difference,  $\psi_2$  is assumed between the nonlinear IM and the linear IM. The expression for the total intensity may be written as,

$$I = I(\lambda) + \Delta I_1(\lambda) \cos \omega t + \Delta I_2(\lambda) \cos(2\omega t + \psi_2) \quad (7.1)$$

Using the same Taylor series expansion used in chapter 4 for the RAM technique, the expression for the intensity that results from the interaction of the intensity modulated laser and the spectrally-modulated absorption profile is given by,

**Chapter 7: Extension of RAM nulling to 2f WMS**

$$I_{out} = \left[ I(\lambda) + \Delta I_1(\lambda) \cos \omega t + \Delta I_2(\lambda) \cos(2\omega t + \psi_2) \right] \left[ 1 - \alpha(\lambda).C.I \right. \\ \left. - \frac{d\alpha(\lambda)}{d\lambda}.C.I.\delta\lambda.\cos(\omega t - \psi_1) - \frac{1}{2!} \frac{d^2\alpha(\lambda)}{d\lambda^2}.C.I.(\delta\lambda)^2 \cos^2(\omega t - \psi_1) \right. \\ \left. - \frac{1}{3!} \frac{d^3\alpha(\lambda)}{d\lambda^3}.C.I.(\delta\lambda)^3 \cos^3(\omega t - \psi_1) \right] \quad (7.2)$$

where, the Taylor series expansion of the absorption profile has been limited to the third order term. The expression may be written as,

$$I_{out} = \left[ \overbrace{I(\lambda) + \Delta I_1(\lambda) \cos \omega t + \Delta I_2(\lambda) \cos(2\omega t + \psi_2)}^A \right] \left[ \overbrace{1 - \alpha(\lambda).C.I}^1 \right. \\ \left. - \overbrace{\frac{d\alpha(\lambda)}{d\lambda}.C.I.\delta\lambda.\cos(\omega t - \psi_1)}^2 - \overbrace{\frac{1}{4} \frac{d^2\alpha(\lambda)}{d\lambda^2}.C.I.(\delta\lambda)^2 \{ \underbrace{\cos(2\omega t - 2\psi_1)}_a + \underbrace{\frac{1}{b}} \}}^3 \right. \\ \left. - \overbrace{\frac{1}{24} \frac{d^3\alpha(\lambda)}{d\lambda^3}.C.I.(\delta\lambda)^3 \{ \underbrace{3 \cos(\omega t - \psi_1)}_a + \underbrace{\cos(3\omega t - 3\psi_1)}_b \}}^4 \right] \quad (7.3)$$

The various 2f terms produced by the interactions of the two sets of terms are given by,

$$\text{Term A3a} = -\frac{1}{4} I(\lambda) \frac{d^2\alpha(\lambda)}{d\lambda^2}.C.I.(\delta\lambda)^2 \cos(2\omega t - 2\psi_1) \quad (7.4)$$

$$\text{Term B2} = -\frac{1}{2} \Delta I_1(\lambda) \frac{d\alpha(\lambda)}{d\lambda}.C.I.(\delta\lambda) \cos(2\omega t - \psi_1) \quad (7.5)$$

**Chapter 7: Extension of RAM nulling to  $2f$  WMS**

$$\text{Term B4a} = -\frac{1}{16} \Delta I_1(\lambda) \frac{d^3 \alpha(\lambda)}{d\lambda^3} .C.I.(\delta\lambda)^3 \cos(2\omega t - \psi_1) \quad (7.6)$$

$$\text{Term B4b} = -\frac{1}{48} \Delta I_1(\lambda) \frac{d^3 \alpha(\lambda)}{d\lambda^3} .C.I.(\delta\lambda)^3 \cos(2\omega t - 3\psi_1) \quad (7.7)$$

$$\text{Term C1} = \Delta I_2(\lambda) [1 - \alpha(\lambda) C I] \cos(2\omega t + \psi_2) \quad (7.8)$$

$$\text{Term C3b} = -\frac{1}{4} \Delta I_2(\lambda) \frac{d^2 \alpha(\lambda)}{d\lambda^2} .C.I.(\delta\lambda)^2 \cos(2\omega t + \psi_2) \quad (7.9)$$

The first term is the main  $2f$  term that contains the 2<sup>nd</sup> derivative of the line shape. All other terms comprise the various IM-WM terms arising as a result of the interaction of the linear and nonlinear IM with the various Taylor series components of the spectrally modulated transmission. It is seen that the 1<sup>st</sup> and 3<sup>rd</sup> derivatives of the absorption line appear due to the presence of the linear IM. These comprise the terms B2, B4a and B4b in Eq. 7.5, Eq. 7.6 and Eq. 7.7 respectively. In a typical telecom grade DFB laser the variation of the IM is predominantly linear with current (wavelength). The nonlinear IM term at twice the modulation frequency becomes apparent only for high modulation indices that cause large intensity excursions around the slowly-varying local intensity value set by the ramp voltage. The nonlinear IM is manifest as the  $2f$  background RAM, a concentration-dependent IM-WM term that follows the absorption line shape and a concentration-dependent 2<sup>nd</sup> derivative component that is much smaller than the main intensity-dependent 2<sup>nd</sup> derivative component. The first two components collectively comprise the term C1 Eq. 7.8, while the last component is given by the term C3b in Eq. 7.9 respectively.

It is often convenient to pictorially represent the various signal components. A phasor diagram is shown in Fig. 7.4 that shows the relative orientation of the various signal components. It should be noted that no attempt has been made to scale the lengths of the phasors to accurately represent relative signal strengths. In the phasor diagram the thin black line (dash-dot) acts as an imaginary (but not arbitrary) reference phasor with respect to which all the other phasors are oriented. This line represents the direction

## Chapter 7: Extension of RAM nulling to 2f WMS

along which the phasors representing the main 2<sup>nd</sup> derivative term (term A3a) and the linear IM-induced terms (terms B2, B4a and B4b) would have been oriented if the IM-WM phase difference had been zero. It is essentially the non-zero value of  $\psi_1$  that shifts the linear IM-induced phasors from this reference position. The nonlinear IM-induced terms would also be aligned along this line if  $\psi_2$  is zero.

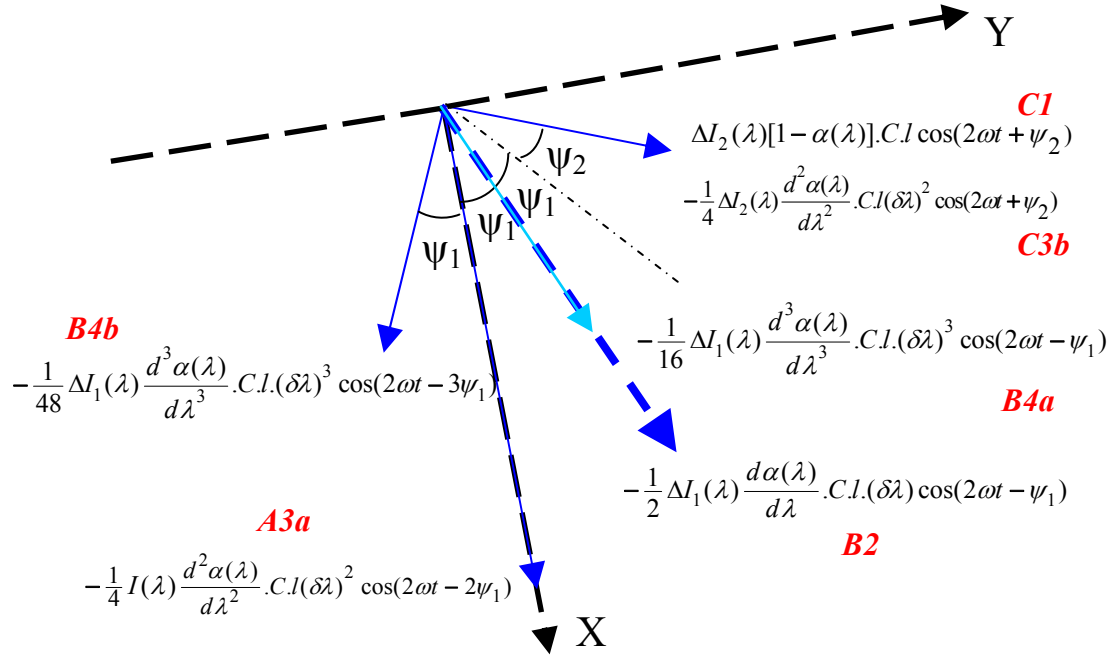


**Fig. 7.4:** Phasor diagram depicting some of the 2<sup>nd</sup> harmonic signal components that arise due to the interaction of the linear and the nonlinear IM with the spectrally-modulated absorption feature. Note that the lengths of the phasors do not represent the relative strengths of the components.

Phase-sensitive detection of the main 2f signal is equivalent to aligning the X-axis of the lock-in amplifier with the main 2<sup>nd</sup> derivative component. It is understandably not possible, in general, to totally isolate the 2<sup>nd</sup> derivative signal from projections of the other IM-WM signal components. When the detection axis of the LIA (X axis in this case) is fully aligned with the 2<sup>nd</sup> derivative signal (term A3a) other signal components are also projected on to it. The dominant projection is that of the 1<sup>st</sup> derivative component given by term B2 scaled by  $\cos\psi_1$ . The effect of this projection is to cause

## Chapter 7: Extension of RAM nulling to $2f$ WMS

significant distortion of the main  $2f$  signal. For high  $m$ -values this distortion can be very significant. Projections of the 3<sup>rd</sup> derivative component are generally negligible in comparison to the other terms. It was pointed out in Sec. 7.1 that in calibration-free  $2f$  WMS applications the emphasis is on line centre measurements for which the effect of the small 3<sup>rd</sup> derivative signal component is usually negligible. The projections of the nonlinear IM-induced terms C1 and C3b need to be considered as well. The  $2f$  background RAM given by term C1 affects the whole signal since it forms a non-zero baseline, the effect of which is to vertically shift the  $2f$  signal. The effect of the concentration-dependent term C3b is most pronounced at line centre since it has the same form as the main 2<sup>nd</sup> derivative signal although its amplitude is much smaller. The point to note is that the extent of these projections is dependent on the values of the two angles  $\psi_1$  and  $\psi_2$ . If the  $\psi_1$  and  $\psi_2$  are small the magnitude of the projected signals will be larger and will significantly affect the recovery of the main  $2f$  signal.

It should now be clear why efforts to adjust the LIA phase to obtain perfectly symmetric  $2f$  signals or to force the  $2f$  signal to appear on a zero level are fundamentally flawed although the method works in particular cases. The first approach involves moving the detection axis (i.e. X-axis) away from the position shown in Fig. 7.4 that maximizes the  $2f$  signal peak, to an angle at which the projection of the 1<sup>st</sup> derivative signal adds to the 2<sup>nd</sup> derivative signal in such a way as to artificially produce symmetric troughs of the 2<sup>nd</sup> derivative signal. Although an appropriately chosen phase does lead to symmetric troughs, it will necessarily reduce the peak value of the signal. Similarly phase-tuning to force the  $2f$  signal to appear on a zero background implies orientating the detection axis at right angles to the  $2f$  RAM phasor. Again, the intentional misalignment of the detection axis leads to a reduction of the  $2f$  peak value since only a projection of the full  $2f$  signal is recovered. This element of uncertainty about the choice of the detection phase is often noticeable in reports on  $2f$  WMS although the effect is not very severe for most applications using telecom-grade DFB lasers and for low  $m$ -values. The ambiguity of the choice of the correct detection phase has a greater effect for experiments with high  $m$ -values and particularly for lasers with either poor WM

## Chapter 7: Extension of RAM nulling to $2f$ WMS

efficiency or highly nonlinear power-current characteristics. This is simply because for such lasers significantly high levels of both linear as well as nonlinear IM are produced. This is also very pronounced for measurements at high pressures at which the gas line broadens out considerably. In order to maximize the  $2f$  signal by maintaining the optimum  $m$ -value, the amplitude of current modulation needs to be increased. As a consequence the levels of the linear and the nonlinear IM also increase significantly and the  $2f$  signal is heavily distorted [10]. This issue of the effect of the detection phase on the  $2f$  signal will be discussed again in the next section after the technique to eliminate the  $2f$  RAM has been demonstrated.

It should be noted that the magnitude of the  $2f$  RAM (and indeed the  $1f$  RAM) is dependent on the WM efficiency (GHz/mA) of the particular laser. A laser with high WM efficiency will require less drive current to achieve a particular  $m$ -value, and the associated IM will also be less. This will in turn cause less signal distortion due to the linear IM and less offset due to the nonlinear IM. The linear and nonlinear IM-WM phase shifts,  $\psi_1$  and  $\psi_2$ , will also influence how the  $2f$  RAM affects the main  $2^{\text{nd}}$  derivative signal. If the  $2f$  RAM component and the  $2^{\text{nd}}$  derivative signal are mutually orthogonal (i.e.  $2\psi_1 + \psi_2 = 90^\circ$ ), it is possible to phase-tune the LIA to simultaneously maximize the  $2^{\text{nd}}$  derivative term and recover it in isolation from the  $2f$  RAM. However, it is impractical to depend on such a special condition to be fulfilled since WMS for gas detection uses off-the-shelf lasers whose IM and WM characteristics are widely variable and are certainly not tailored to suit a particular application. It should be noted, however, that such a special situation can be arranged by adjusting the modulation frequency to vary  $\psi_1$  (and  $\psi_2$  in turn). However for high  $m$ -values it is the linear IM-induced distortion that causes distortion of the  $2^{\text{nd}}$  derivative signal, which may be more pronounced than the  $2f$  RAM. As will be shown shortly, it is desirable and possible to eliminate this distortion by using the PDM approach. However if the  $2^{\text{nd}}$  derivative and the  $2f$  RAM terms are first arranged to be orthogonal (by adjusting the modulation frequency) and then the PDM is applied, the effect is a full projection of the  $2f$  RAM on to the recovered  $2^{\text{nd}}$  derivative signal. The initial orthogonal arrangement of the  $2^{\text{nd}}$

derivative and the  $2f$  RAM therefore presents no advantage if the  $1^{\text{st}}$  derivative distortion needs to be eliminated. In such applications the  $2f$  RAM nulling is particularly useful.

### 7.3 Elimination of the $2f$ background RAM

This section describes the elimination of the  $2f$  RAM background. The experimental arrangement and conditions are discussed first, followed by results that demonstrate the robust cancellation of the  $2f$  RAM.

#### 7.3.1 Experimental arrangement for $2f$ RAM nulling

Figure 7.5 shows the same basic experimental system [20], which was originally used to eliminate the  $1f$  background RAM.

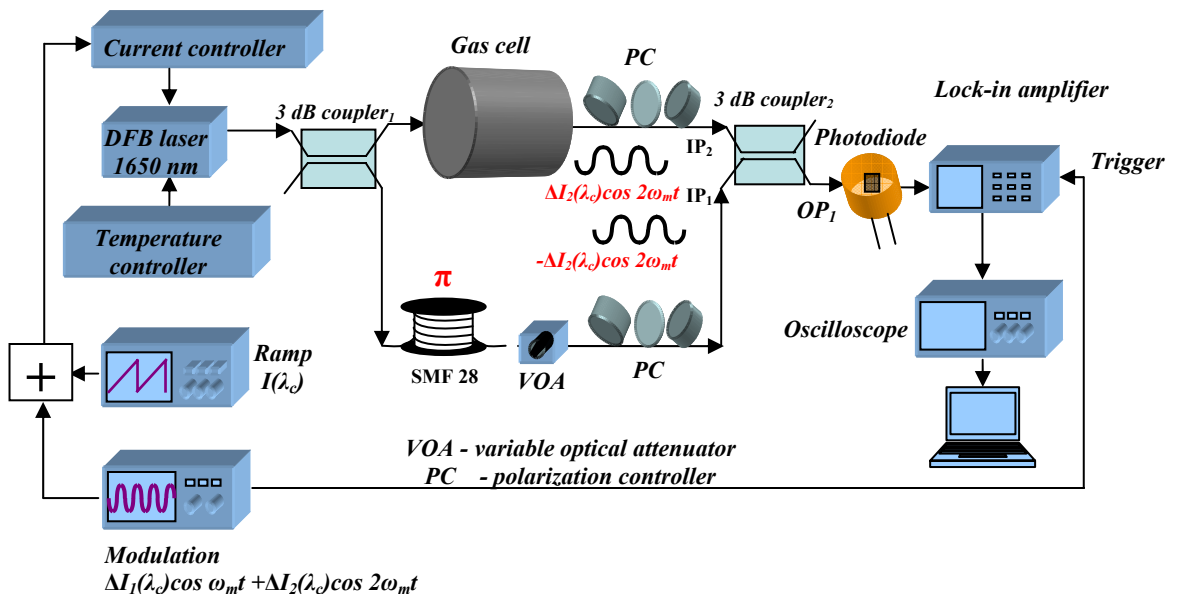


Fig. 7.5: Generic RAM nulling experimental setup used for  $2f$  RAM nulling

It should be noted that the RAM nulling configuration is generic because the choice of the fiber length and modulation frequency is flexible. Therefore the same configuration can be used to eliminate the nonlinear IM-induced background RAM as well. This is achieved by introducing a  $\pi$  phase shift between the two *nonlinear IM*

## Chapter 7: Extension of RAM nulling to $2f$ WMS

components, precisely balancing their relative intensities and recombining them. As explained earlier in Sec. 4.2, the delay line acts as a  $\pi$  phase-shifter for a suitable combination of the modulation frequency and fiber delay length. Therefore, the same fiber length can be used for this purpose if the modulation frequency is chosen to be  $f_m/2$  instead of  $f_m$ , so that the relation,  $L = c/2n(2f_m)$  is satisfied, where  $n$  and  $L$  are the effective index and length of the fiber respectively. Note that unlike the linear IM, it is not straightforward to identify the nonlinear IM on the photo-detector output displayed on the oscilloscope by mere visual inspection. The IM signal detected by the photo-detector is a combination of both the linear and nonlinear IM, with the stronger linear IM masking the weaker nonlinear IM. The two components are not separately detectable from the photo-detector data captured directly in the time-domain unless harmonic detection is used. Therefore it is not possible to show the frequency-tuning of the system to gradually reach the RAM nulling point as depicted in Fig. 4.2 for  $1f$  RAM nulling. However, the presence of a nonlinear IM component can be detected if harmonic detection using an LIA is performed with or without gas in the cell. The presence of any dc offsets on the signals on either lock-in channel proves the existence of the nonlinear IM. Alternatively, if a lock-in amplifier is not available, a discrete Fourier transform (DFT) algorithm may be applied to the time-domain intensity modulated output of the photo-detector in the *absence* of gas to reveal the power spectral density (PSD) of the data. The existence of a signal at  $2f_m$  in the absence of gas in the cell is an indicator of a nonlinear IM component. Note that this approach to identify the  $2f$  RAM requires the gas cell to be evacuated because the presence of gas will produce a  $2f$  component that will be indistinguishable from the  $2f$  RAM on the PSD.

### ***7.3.2 Experimental demonstration of $2f$ RAM nulling***

The  $2f$  RAM nulling technique is demonstrated by experimental results shown in Fig. 7.6 and Fig. 7.7 for methane. The modulation frequency,  $f_m$ , was set to 50.7 kHz for  $L$  of 1km so that  $2f_m$  satisfies the nulling condition. The modulation voltage is varied from 1000mV to 3500mV to cover a wide range of modulation indices.

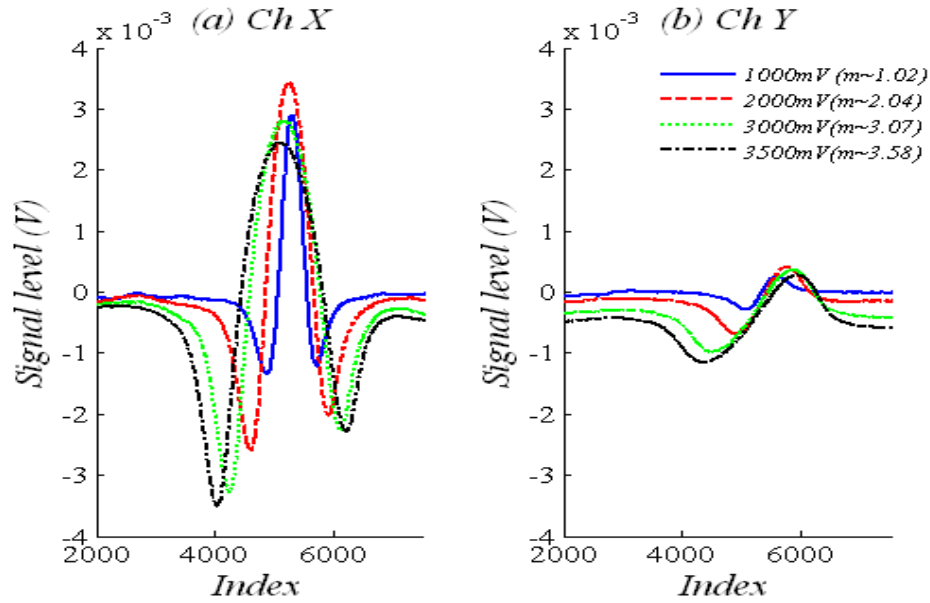


**Fig. 7.6: Variation of  $2f$  signals with the modulation voltage detected on the two lock-in amplifier channels for methane at a concentration of 1.02 %, at a pressure of 0.552 bar and temperature of 17.4 C. The increasing  $2f$  RAM is manifest as a dc offset on both signals, particularly for high modulation voltages**

Figure 7.6 shows the  $2^{\text{nd}}$  derivative and the dominant  $1^{\text{st}}$  derivative IM-WM signal detected on channel X and channel Y of the LIA respectively, for concentration of 1.02% methane in nitrogen balance, at 0.552 bar and 17.4°C. The delay fiber has been disconnected from coupler<sub>2</sub>, and standard  $2f$  detection is performed without any background nulling. The phase of the lock-in amplifier was initially set to maximize the peak value of the  $2f$  signal on channel X for the lowest modulation voltage and no further adjustments were made to it. The signal shown in Fig. 7.6a is predominantly due to the main  $2^{\text{nd}}$  derivative signal given by term A3a along with distorting projections of the  $1^{\text{st}}$  derivative term B2 scaled by  $\cos\psi_1$ . A small projection of the  $2f$  RAM given by terms C1 and C3b are also present. The signal in Fig. 7.6b is predominantly due to the  $1^{\text{st}}$  derivative term B2 scaled by  $\sin\psi_1$  in this case. The projection of the  $2f$  RAM given by terms C1 and C3b is much greater on this signal.

As the modulation voltage (equivalently modulation index,  $m$  from here on) is increased, an increasing dc offset is observed on the signal in Fig. 7.6b. This is the  $2f$

## Chapter 7: Extension of RAM nulling to $2f$ WMS

background RAM arising due to the increasing nonlinear IM component  $\Delta I_2(\lambda)$ . As explained earlier, this is the only way to detect a significantly high nonlinear IM. It should be noted that for high  $m$ -values there is also a noticeable dc shift on the  $2f$  signal due to a projection of the  $2f$  RAM on to channel X (Fig. 7.6a). As pointed out earlier, unless the  $2f$  RAM and the  $2^{\text{nd}}$  derivative terms are exactly orthogonal (i.e.  $2\psi_1 + \psi_2 = 90^\circ$  in Fig. 7.4) the  $2f$  signal cannot be maximized and simultaneously totally isolated from a projection of the  $2f$  RAM. This signal offset will introduce significant error in concentration and temperature measurements that are based on the peak height [13-15], particularly for lower gas concentrations. The concentration-dependent  $1^{\text{st}}$  derivative signal component near the line centre in Fig. 7.6b is predominantly due to the linear IM-induced term B2, and increases monotonically with  $m$ . The  $2f$  signal on channel X in Fig. 7.6a (given by term A3a) initially increases with  $m$  but eventually decreases according to the well-established  $2f$  theory [2]. The  $m$ -value of 2.2 that maximizes the  $2f$  signal was clearly reached and exceeded during this process although no effort was made to identify the corresponding voltage. The asymmetry of the troughs, however, increases monotonically because it is caused by a projection of the  $1^{\text{st}}$  derivative linear IM-induced IM-WM signal on channel Y.

Figure 7.7 demonstrates  $2f$  RAM nulling with the signals obtained for the same gas composition maintained under the same conditions as before. To achieve  $2f$  RAM nulling the delay line is connected to coupler<sub>2</sub>. If the length of the fiber and the modulation frequency are appropriately chosen the two nonlinear IM-induced  $2f$  RAM components arrive at coupler<sub>2</sub> at anti-phase and are cancelled at the output in exactly the same way as the linear IM components are cancelled in  $1f$  RAM nulling. The RAM nulling condition for the  $2f$  signal is given by,

$$L = \frac{c}{2n(2f_m)} \quad (7.10)$$

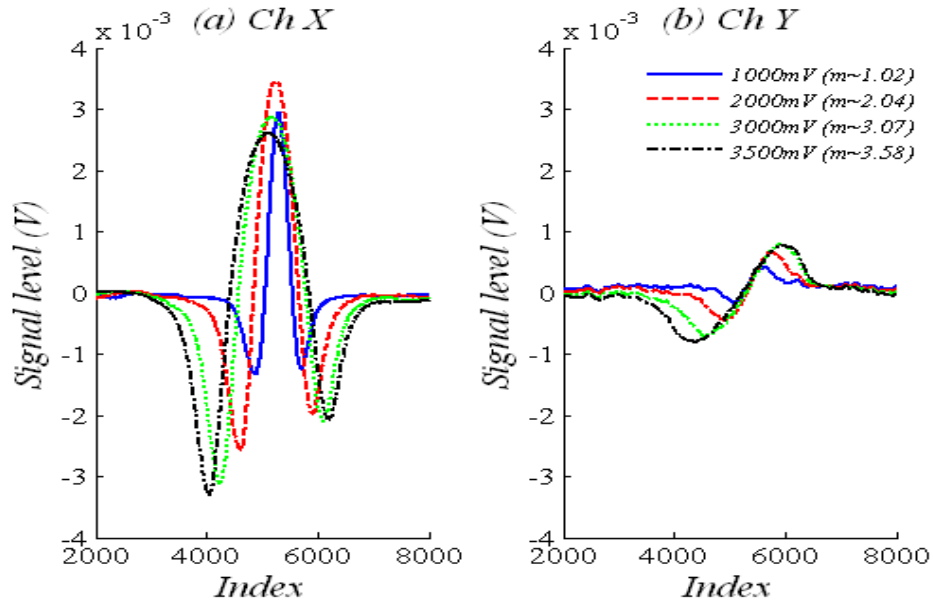


**Fig. 7.7: Demonstration of  $2f$  RAM nulling. The signals are recorded under conditions identical to those in Fig. 7.6. The only modification is that the fiber delay line has been connected to coupler<sub>2</sub> in this case.**

Since a fixed length of fiber (1 km) was used, the modulation frequency was changed to 50.7 kHz. The  $2f$  background is therefore eliminated as seen in the offline regions in Fig. 7.7b. Note that for the sake of clarity, only the regions close to the line centre have been shown although the nulling is rigorously valid and equally effective for the entire scan range. As a direct consequence, the  $2f$  signal in Fig. 7.7a also does not exhibit any spurious dc shift. The  $2f$  signal on channel X and the linear IM-dominated signal on channel Y therefore appear on a perfectly zero baseline. Clearly the nulling is effective over a wide range of  $m$ -values, including those well over the value of 2.2 that maximizes the  $2f$  signal. The signal on channel Y increases monotonically with  $m$  as in the previous case. The behaviour of the  $2f$  signal on channel X is much clearer and the same comments regarding the monotonic behaviour of the trough asymmetry apply.

The fact that the RAM nulling is rigorously valid over a wide range of  $m$ -values and over the entire scan range is important for widely-tunable lasers such as some of the newly developed VCSELs and other DFB lasers [16-19] for which a varying baseline over a wide spectral region can be a problem. Data for the range of  $m$ -values were

## Chapter 7: Extension of RAM nulling to 2f WMS

recorded over a six-hour period during which no adjustment to the system was necessary, which demonstrates the potential for long-term stability of the system.

The effectiveness of the RAM nulling technique is further validated by the results shown in Fig. 7.8 and Fig. 7.9 that show the main 2<sup>nd</sup> derivative signal and the linear IM-induced signal over a wider range of applied modulation indices.

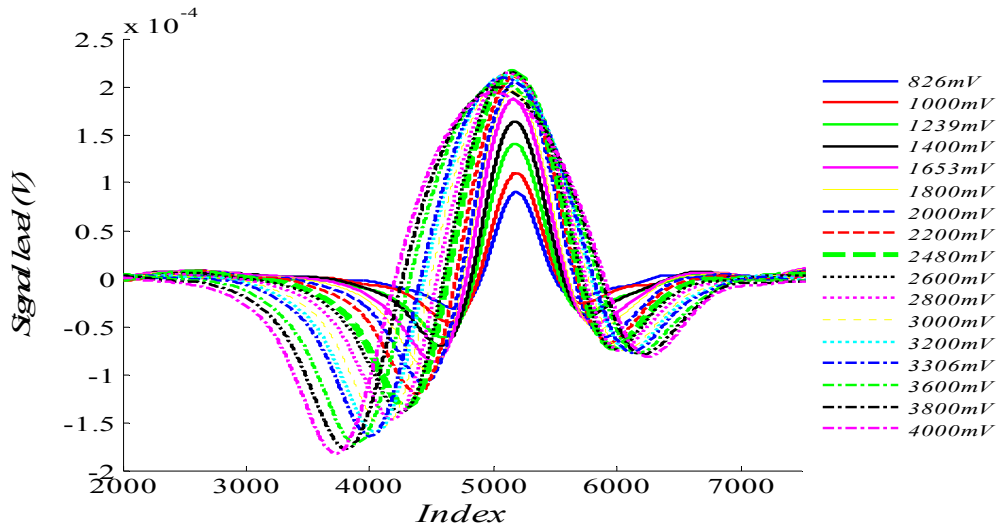


**Fig. 7.8:** RAM nulled 2f signals on Ch X of LIA as a function of modulation voltage –  
Concentration = 1.02%, pressure = 1.004bar, temperature = 20.3°C,

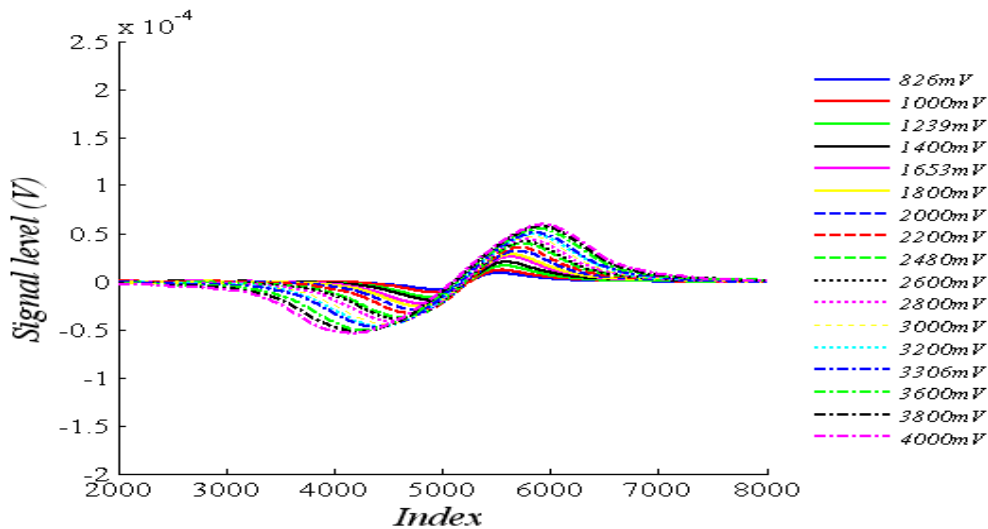


**Fig. 7.9:** RAM nulled 2f signals on Ch Y of LIA as a function of modulation voltage –  
Concentration = 1.02%, pressure = 1.004bar, temperature = 20.3°C,

## Chapter 7: Extension of RAM nulling to $2f$ WMS

The gas composition was 1.02% methane in nitrogen at a pressure of 1.004 bar and temperature of 20.3°C. The modulation voltage was varied over a very wide range. It is observed that the peak value of the  $2f$  signal on channel X continues to increase with the modulation voltage, reaches a peak for about 2480mV and then decreases. This behaviour is typical of the  $2f$  signal in WMS. The very effective RAM nulling ensures that the  $2f$  RAM does not cause any dc offset on the signals on either channel.

The cancellation of the  $2f$  background RAM also simplifies LIA phase-tuning to maximize the  $2f$  signal. As mentioned earlier, there is a temptation in WMS to phase-tune the LIA to obtain symmetric  $2f$  signals without regard for the  $2f$  RAM-induced baseline [19]. This was shown earlier in Fig. 7.3 in which the experimental signal is seen to have symmetric troughs despite the sloping  $2f$  baseline. Such arbitrary adjustment of the phase is not advisable since optimizing the  $2f$  symmetry reduces the  $2f$  peak considerably. This is shown in Fig. 7.10 in which the  $2f$  signals recovered on channel X and channel Y are shown for a sample of 10.13% methane in nitrogen under ambient conditions of temperature and pressure.

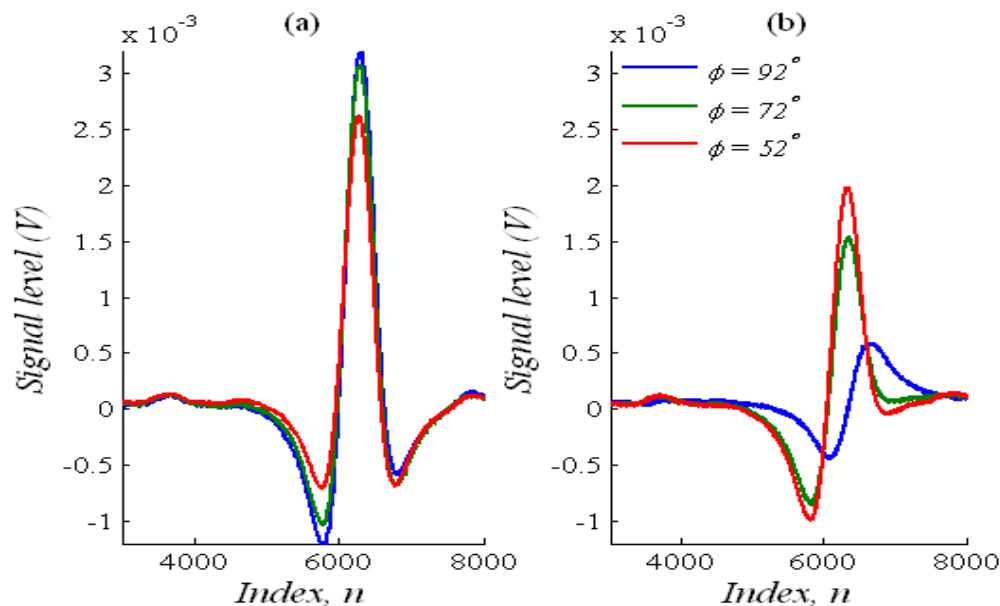


**Fig. 7.10: Effect of phase-tuning the LIA to obtain symmetric  $2f$  signals. (a) Channel X and (b) Channel Y of LIA. Data shown is for a sample of 10.13% methane in nitrogen balance at 1.004 bar and 23.7 C.**

## Chapter 7: Extension of RAM nulling to $2f$ WMS

The signals corresponding to three values of the LIA phase are shown. It is seen that for  $\phi = 92^\circ$  the  $2f$  signal on channel X is maximized. The asymmetry of the troughs is also maximized due to a projection of the linear IM-induced 1<sup>st</sup> derivative signal. The complementary projection of the linear IM-induced 1<sup>st</sup> derivative signal is recovered on channel Y. When the LIA phase is varied to optimize the symmetry of the main  $2f$  signal on channel X, the corresponding  $2f$  peak reduces considerably. This is because phase-tuning the LIA to obtain symmetric  $2f$  signal troughs is equivalent to moving the X axis away from the angle that maximizes the  $2f$  signal. This leads to the recovery of only a projection of the full  $2f$  signal on channel X, while its complementary projection (that is normally not recovered) is superimposed on the signal on channel Y and only serves to distort the linear IM-induced 1<sup>st</sup> derivative signal. Along with the projection of the 2<sup>nd</sup> derivative signal on channel X, projections of the 1<sup>st</sup> derivative signal are also recovered. It is possible for the 1<sup>st</sup> derivative to add to the 2<sup>nd</sup> derivative in such a way that the asymmetry of the troughs of the 2<sup>nd</sup> derivative is removed. Therefore although it may seem natural to adjust the phase to obtain symmetric 2<sup>nd</sup> derivative signals, this is not the correct approach. For high sensitivity applications such a trade-off is not only unnecessary but also fundamentally incorrect.

Figure 7.11 shows the channel X signal from a preliminary experiment on two closely spaced water vapour absorption lines around 1430nm. The LIA phase has intentionally been adjusted to optimize the symmetry of the peaks to underline the problem of using this approach. The  $2f$  RAM is seen to significantly offset the true value of the smaller of the two  $2f$  signal peaks for high values of modulation voltage. The signal on the orthogonal channel Y shown in Fig. 7.12 does not resemble the 1<sup>st</sup> derivative IM signal because the 1<sup>st</sup> derivative signal is distorted by an appreciable complementary projection of the 2<sup>nd</sup> derivative signal to the point that it almost resembles a  $2f$  signal. This clearly implies that a sizable portion of the  $2f$  signal is not recovered on channel X.

Chapter 7: Extension of RAM nulling to  $2f$  WMS

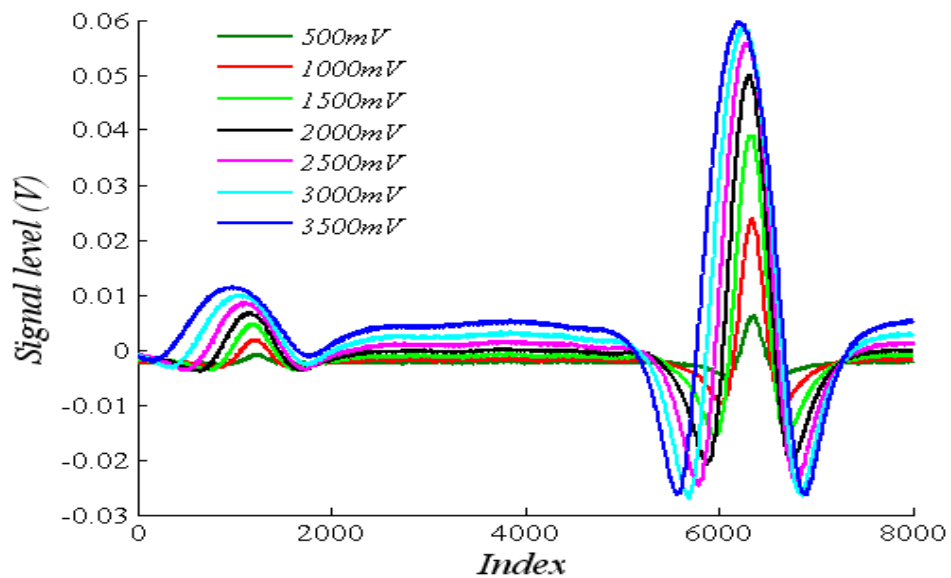


Fig. 7.11: Channel X  $2f$  signals for varying modulation current for two water vapour lines at 1430nm showing the  $2f$  RAM. LIA phase adjusted to optimize symmetry of troughs

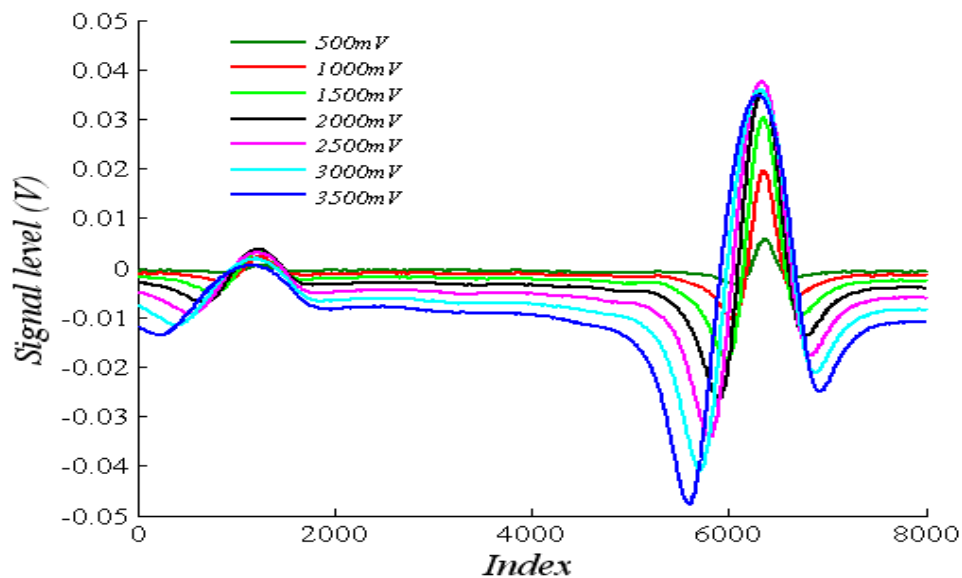


Fig. 7.12: Corresponding  $2f$  signals on channel Y showing the presence of significant  $2^{nd}$  derivative signal

## Chapter 7: Extension of RAM nulling to 2f WMS

The ideal approach in recovering the 2f signal is to implement 2f RAM nulling to totally eliminate the background, maximize the 2f peak by phase-tuning and finally extend the Phasor Decomposition method to the 2f regime to decouple the main 2<sup>nd</sup> derivative signal from the distorting influence of the linear IM-induced 1<sup>st</sup> derivative signal. This is discussed in the next section.

### 7.4 Application of Phasor Decomposition to 2f WMS with 2f RAM nulling

The possibility of applying the PDM to 2f WMS in order to extract the full 2<sup>nd</sup> derivative signal is suggested by the non-zero phase difference between the various 2f terms. In order to use the PDM the LIA is phase-tuned so that channel X recovers the full 2<sup>nd</sup> derivative component along with the distorting projection of the linear IM-induced 1<sup>st</sup> derivative IM-WM component and the nonlinear IM-induced component. Channel Y therefore recovers complementary projections of the various IM-WM terms and the nonlinear IM-induced component, but not the main 2f signal. The relative values of the projections depend on the values of  $\psi_1$  and  $\psi_2$  that are in turn dependent on the operating conditions of the laser.

The signal on channel X of the lock-in amplifier can be written as,

$$\begin{aligned} I_{chX} = & -\frac{1}{4} I(\lambda) \frac{d^2 \alpha(\lambda)}{d\lambda^2} . C.I. (\delta\lambda)^2 - \frac{1}{2} \Delta I_1(\lambda) \frac{d\alpha(\lambda)}{d\lambda} . C.I. \delta\lambda \cos \psi_1 \\ & + \left\{ \Delta I_2(\lambda) - \Delta I_2(\lambda) \alpha(\lambda) . C.I. - \frac{1}{4} \Delta I_2(\lambda) \frac{d^2 \alpha(\lambda)}{d\lambda^2} . C.I. (\delta\lambda)^2 \right\} \cos(2\psi_1 + \psi_2) \quad (7.11) \\ & - \frac{1}{16} \Delta I_1(\lambda) \frac{d^3 \alpha(\lambda)}{d\lambda^3} . C.I. (\delta\lambda)^3 \cos \psi_1 - \frac{1}{48} \Delta I_1(\lambda) \frac{d^3 \alpha(\lambda)}{d\lambda^3} . C.I. (\delta\lambda)^3 \cos \psi_1 \end{aligned}$$

while, the signal on channel Y can be written as,

**Chapter 7: Extension of RAM nulling to 2f WMS**

$$\begin{aligned}
 I_{chY} &= \frac{1}{2} \Delta I_1(\lambda) \frac{d\alpha(\lambda)}{d\lambda} .CI.\delta\lambda .\sin \psi_1 + \frac{1}{16} \Delta I_1(\lambda) \frac{d^3\alpha(\lambda)}{d\lambda^3} .CI.(\delta\lambda)^3 \sin \psi_1 \\
 &- \left\{ \Delta I_2(\lambda) - \Delta I_2(\lambda)\alpha(\lambda).CI - \frac{1}{4} \Delta I_2(\lambda) \frac{d^2\alpha(\lambda)}{d\lambda^2} .CI.(\delta\lambda)^2 \right\} \sin(2\psi_1 + \psi_2) \quad (7.12) \\
 &- \frac{1}{48} \Delta I_1(\lambda) \frac{d^3\alpha(\lambda)}{d\lambda^3} .CI.(\delta\lambda)^3 \sin \psi_1
 \end{aligned}$$

The orientation of the various signal components is similar to that for the 1f PDM. The predominant 2<sup>nd</sup> derivative term can be isolated from the main linear IM-induced 1<sup>st</sup> derivative component by applying the relation,

$$I_{2f} = I_{chX} + \frac{I_{chY}}{\tan \psi_1} \quad (7.13)$$

After some simple trigonometric manipulation the generalized expression for the 2f signal recovered after applying the PDM is given by,

$$\begin{aligned}
 I_{2f} &= -\frac{1}{4} I(\lambda) \frac{d^2\alpha(\lambda)}{d\lambda^2} .CI.(\delta\lambda)^2 - \frac{1}{24} \Delta I_1(\lambda) \frac{d^3\alpha(\lambda)}{d\lambda^3} .CI.(\delta\lambda)^3 \cos \psi_1 \\
 &- \Delta I_2(\lambda) \left[ 1 - \alpha(\lambda).CI - \frac{1}{4} \frac{d^2\alpha(\lambda)}{d\lambda^2} .CI.(\delta\lambda)^2 \right] \frac{\sin(\psi_1 + \psi_2)}{\sin \psi_1} \quad (7.14)
 \end{aligned}$$

It is noted that the application of Eq. 7.13 does not eliminate all other terms. As is evident from Eq. 7.14 there are some terms that are inevitably recovered along with the main 2<sup>nd</sup> derivative term. However the main distortion caused by the 1<sup>st</sup> derivative signal is eliminated.

Under specific operating conditions it may be possible to simplify this expression further. The linear IM-induced 3<sup>rd</sup> derivative signal component is much weaker than the intensity-dependent 2<sup>nd</sup> derivative term. In any case for 2f measurements at line-centre,

## Chapter 7: Extension of RAM nulling to 2f WMS

the contribution of the 3<sup>rd</sup> derivative term is negligible because it is weak and zero-valued at line-centre. Therefore this term can in general be neglected. If 2f RAM nulling is also implemented the nonlinear IM term  $\Delta I_2(\lambda)$  in Eq. 7.14 drops out, and the expression can be simplified to,

$$I_{2f} = -\frac{1}{4}I(\lambda)\frac{d^2\alpha(\lambda)}{d\lambda^2}.C.I.(\delta\lambda)^2 + \Delta I_2(\lambda)\left[\alpha(\lambda).C.I. + \frac{1}{4}\frac{d^2\alpha(\lambda)}{d\lambda^2}.C.I.(\delta\lambda)^2\right]\frac{\sin(\psi_1 + \psi_2)}{\sin\psi_1} \quad (7.15)$$

Not all 2f WMS applications require operation at very high modulation indices. If low  $m$ -values are used then the nonlinear IM is also negligible. In such a case the result of the PDM analysis leads to the extraction of the full 2<sup>nd</sup> derivative signal, and the expression is given by,

$$I_{2f} = -\frac{1}{4}I(\lambda)\frac{d^2\alpha(\lambda)}{d\lambda^2}.C.I.(\delta\lambda)^2 \quad (7.16)$$

Note that in this form the signal still requires calibration to get around the dependence on the laser intensity term. This can be achieved either in the traditional way of using a reference gas cell if that is convenient, or the 1f-normalization method [13-15] may be used.

The decoupling of the 2<sup>nd</sup> derivative signal for high modulation indices is shown in Fig. 7.13. The signals appear on a zero background because 2f RAM nulling has been performed. Therefore this situation corresponds to that depicted by Eq. 7.15. The data shown is for methane at a concentration of 1.02% in nitrogen balance, at a pressure of 1.002 bar and temperature of 20.3°C, and for high  $m$ -values corresponding to modulation voltages of 2480mV and 3306mV. The LIA is appropriately phase-tuned to fully align channel X with the second derivative signal. This is achieved by simply maximizing the signal obtained on channel X. The two signals on channel X and channel Y correspond to the expressions given by Eq. 7.11 and Eq. 7.12 respectively.

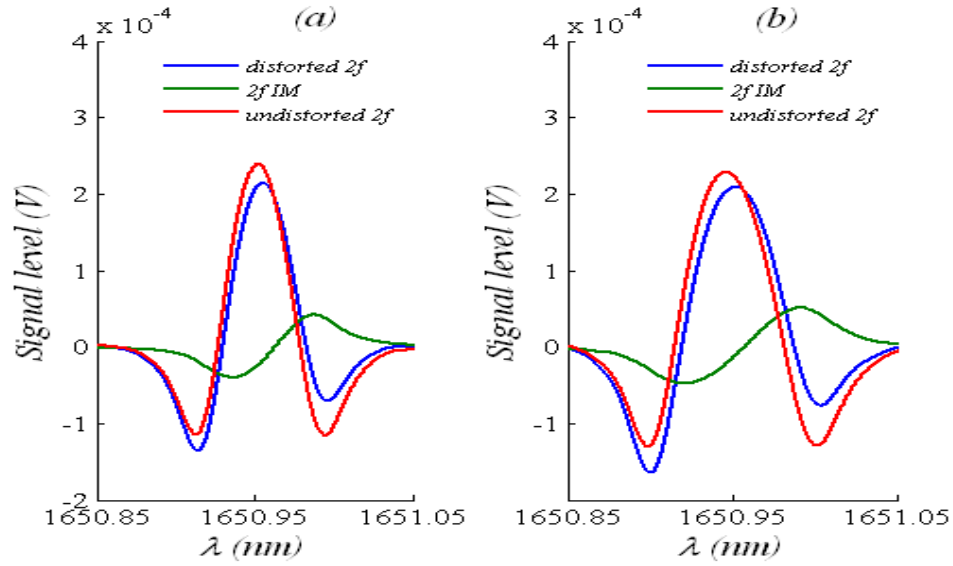


**Fig 7.13: Phasor Decomposition of RAM-nulled  $2f$  signals for the 1650.956nm line of methane ( $C = 1.02\%$ ,  $P = 1.002$  bar,  $T = 20.3^\circ\text{C}$ ) for modulation voltage of (a) 2480 mV and (b) 3306mV**

The  $2^{\text{nd}}$  derivative signal is extracted next by applying the PDM formula given by Eq. 7.13 as explained earlier. The  $2f$  signal recovered on channel X, the distorting IM-WM signal recovered on channel Y and the decoupled  $2f$  signal are shown, clearly demonstrating that the effect of the predominant linear IM-induced distortion has been eliminated. The signal for the modulation voltages of 3306 mV is slightly less than that for 2480mV because for 3306 mV at the modulation frequency of 50.7 kHz the  $m$ -value is greater than 2.2.

The small discrepancy in the peak is mainly due to the concentration-dependent  $2f$  RAM term given by  $\Delta I_2(\lambda)\alpha(\lambda).C.l$  in Eq. 7.15 that is not negligible for such high modulation indices. It should be noted that the effect of these terms are specific to the laser used. The IM and WM characteristics of DFB lasers are known to vary significantly. They also depend on the specific operating conditions such as modulation frequency.

## 7.5 Calibration-free $2f$ WMS with RAM nulling

## Chapter 7: Extension of RAM nulling to $2f$ WMS

The expression for the  $2f$  signal after applying the PDM given by Eq. 7.15 may be simplified further by making certain assumptions that are valid under typical operating conditions of a particular application. For typical DFB lasers the magnitude of  $\Delta I_2(\lambda)$  is much smaller than the intensity  $I(\lambda)$  as shown earlier. Therefore, the nonlinear IM-induced  $2^{\text{nd}}$  derivative term may be neglected in comparison to the intensity-dependent  $2^{\text{nd}}$  derivative term. The  $2f$  signal is then heavily dominated by the conventional  $2^{\text{nd}}$  derivative along with a small nonlinear IM-induced RAM signal that follows the absorption line shape.

Under these assumptions, the  $2f$  signal may be written as,

$$I_{2f} = -\frac{1}{4} I(\lambda) \frac{d^2 \alpha(\lambda)}{d\lambda^2} \cdot C.I.(\delta\lambda)^2 + \Delta I_2(\lambda) \alpha(\lambda) C.I. \frac{\sin(\psi_1 + \psi_2)}{\sin \psi_1} \quad (7.17)$$

However it is important to note that even in this present form, the signal requires calibration because of three reasons. First and most important, the net intensity impinging on the photo-detector is liable to vary due to variations in optical coupling through the system. Second, different lasers will have different output powers and the  $2f$  signal from a given concentration of gas will therefore change if the laser is changed. Finally, the LIA gain applied to the electrical signal is also liable to vary depending on the optical-to-electrical conversion efficiency. Therefore for calibration-free operation a suitable normalization signal must be obtained.

Such a signal can be extracted from the channel Y signal given by Eq. 7.12 if it is noted that the only difference that the  $2f$  RAM nulling makes to this expression is the elimination of the direct nonlinear IM term  $\Delta I_2(\lambda)$ . Therefore if the non-nulled signal on channel Y given by Eq. 7.12 is subtracted from that *with*  $2f$  RAM nulling in place, the background signal due to  $\Delta I_2(\lambda)$  can be recovered. The  $2f$  RAM is therefore given by,

$$I_{chY2f \text{ nulled}} - I_{chY} = \Delta I_2(\lambda) \sin(2\psi_1 + \psi_2) \quad (7.18)$$

For an isolated line this signal can also be obtained by making a baseline fit to the signal on channel Y, but as pointed out in earlier chapters also, this may be inconvenient in

## Chapter 7: Extension of RAM nulling to 2f WMS

congested spectral regions. Note that in a practical instrument the signal through the delay line can be connected to coupler<sub>2</sub> through a fiber-optic switch that can be electrically controlled to make or break the connection. This presents a very easy and repeatable way to obtain the nulled and non-nulled channel Y signal without having to physically disconnect fiber-optic connections that can lead to variations in the coupled power and degrade performance. It should be noted that although such switches have issues regarding their repeatability, it is not necessary to perform the switching frequently. This is because a fully fiber-coupled system is very stable in terms of coupled power, which implies that once the system has been nulled and the normalization signal has been initially obtained, subsequent measurements of the normalization signal need only be made after long intervals.

The 2<sup>nd</sup> derivative signal normalized by the 2f RAM is therefore given by,

$$I_{2f} = \frac{1}{\sin(2\psi_1 + \psi_2)} \left[ -\frac{1}{4} \frac{I(\lambda)}{\Delta I_2(\lambda)} \frac{d^2 \alpha(\lambda)}{d\lambda^2} \cdot C.I.(\delta\lambda)^2 + \alpha(\lambda) C.I. \frac{\sin(\psi_1 + \psi_2)}{\sin \psi_1} \right] \quad (7.19)$$

Note that for a constant  $m$ -value (and therefore  $\Delta I_2(\lambda)$ ), the normalized 2f signal varies linearly with concentration as well as the value of the 2<sup>nd</sup> derivative of the line shape. The cell length, which is essentially the distance between the laser and the photo-detector, is known in a given application while all the other factors that appear in Eq. 7.19 are parameters of the laser that can be carefully characterized and are constant. The phase value,  $\psi_1$ , can easily be determined from a PDM analysis of the 1f signals, which was found to be about 39° at a modulation frequency of 50.7 kHz. The value of  $\psi_2$  will have to be determined separately for the given laser. This is done by least squares fitting of the experimentally obtained IM to a sum of appropriately weighted contributions of sinusoids at the frequencies  $f$  and  $2f$  with appropriate phase values. The value of  $\psi_2$  can be estimated in this way as has been demonstrated in other reports [13].

The normalization of the 2f signal by the 2f RAM is shown in Fig. 7.14 and Fig. 7.15.

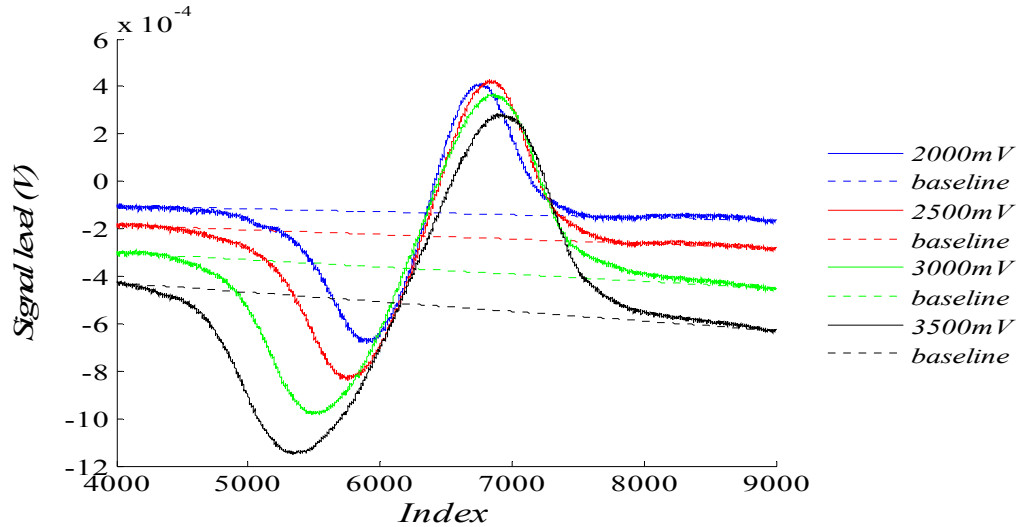


**Fig. 7.14: Ch Y  $2f$  signal without  $2f$  RAM nulling for increasing values of modulation indices**

Figure 7.14 shows the IM-WM signal component recovered on channel Y of the LIA for increasing values of modulation index. The baseline fit to the signal is shown that represents the  $2f$  RAM component. The main  $2f$  signal on channel X is shown in Fig. 7.15a. The  $2f$  signal with the  $2f$  RAM eliminated and then normalized by the  $2f$  RAM (baseline fits in Fig. 7.14) is shown in Fig 7.15b. The normalized signal decreases as the modulation index increases because the  $2f$  RAM background increases. However in typical  $2f$  calibration-free applications [13-15] an  $m$ -value of 2.2 is maintained to maximize the signal. The variation of the  $2f$  signal in the vicinity of the  $m = 2.2$  point is very small and therefore this is not a problem.

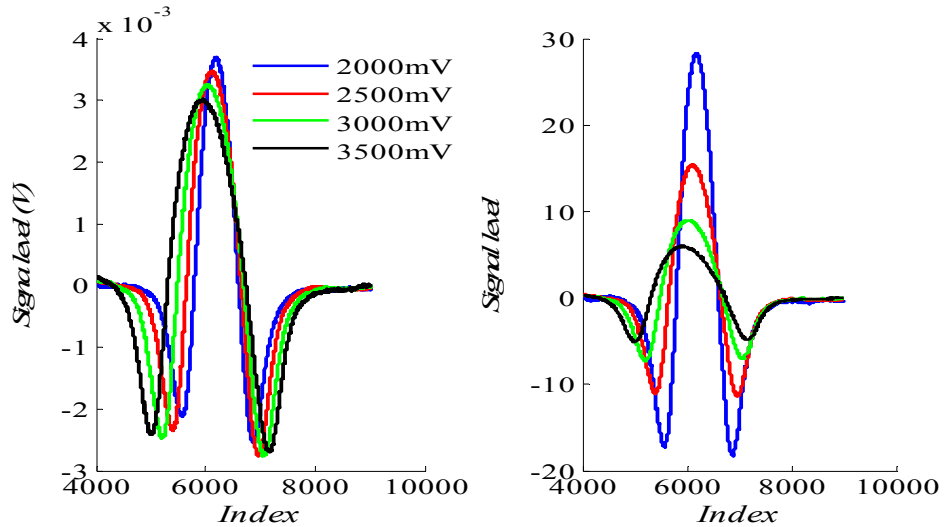


*Fig. 7.15: (a) Ch X  $2f$  signal and (b)  $2f$  signal normalized by  $2f$  RAM for increasing values of modulation indices*

## 7.6 Estimating linear and nonlinear IM

It is useful to estimate the relative variation of the intensity, linear IM and nonlinear IM with modulation voltage for the 1650nm DFB laser that has been used for these experiments. To extract these parameters the polynomial fit to the current-intensity curve obtained in Sec. 6.3 and shown in Fig. 6.4 is used and the programmatic approach is taken. In a manner similar to that for estimating the linear IM, a sinusoidal variation of the current amplitude is first considered. The corresponding modulation of the intensity around a local value of current is obtained by evaluating the polynomial at every value of the modulated current. One period of the sinusoidal variation of the IM is thus obtained and is shown in Fig. 7.16 for increasing values of the sinusoidal modulation current amplitude.

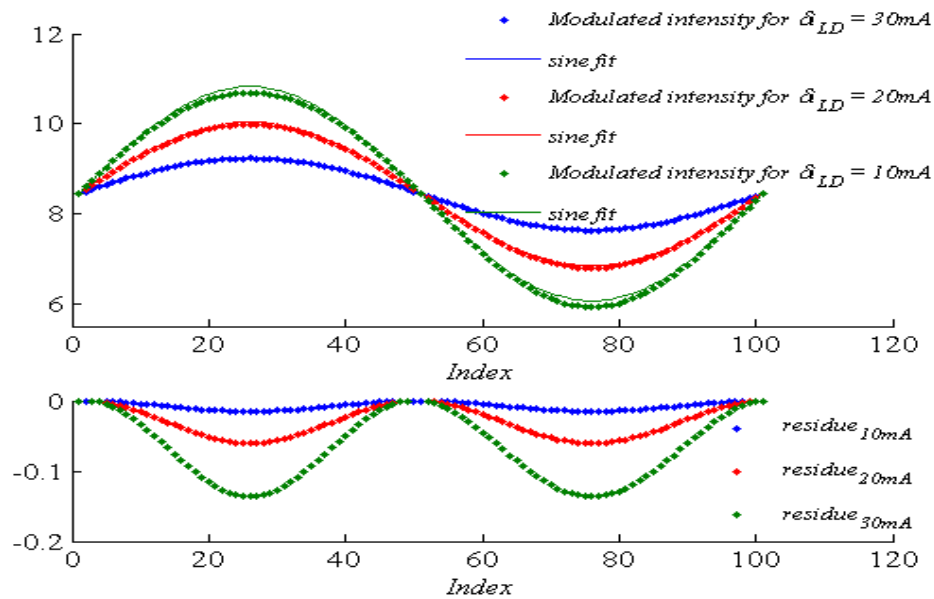


**Fig. 7.16: Modulated intensity corresponding to sinusoidal current modulation of increasing amplitude obtained programmatically. (a) The excellent sinusoidal fit shows that the IM is predominantly linear (b) Residue shows a much smaller  $2f$  IM component whose amplitude increases with the amplitude of the modulation current**

A sinusoidal fit to the IM is obtained and is plotted (solid line) along with the corresponding curve for the IM (dotted line). The residue after the sinusoidal fit is shown in the lower plot which clearly shows a sinusoidal component at twice the applied frequency. The amplitude of this residual signal represents the nonlinear IM that is seen to increase with the amplitude of the modulation current.

The programmatically extracted variation of the linear IM, nonlinear IM, linear IM index ( $M_1 = \Delta I_1/I$ ) and the nonlinear IM index ( $M_2 = \Delta I_2/I$ ) as a function of the modulation current amplitude are shown in Fig. 7.17 for a typical scan range of the laser current. As the modulation current amplitude is increased the overall level of the linear as well as the nonlinear IM at any given value of mean laser current increases in magnitude. This is understandable since larger current modulation about the mean value causes larger intensity excursions. However, as the current is ramped up the amplitude of the linear IM decreases due to the nature of the power-current characteristics of the laser as discussed earlier in chapter 5 as well.

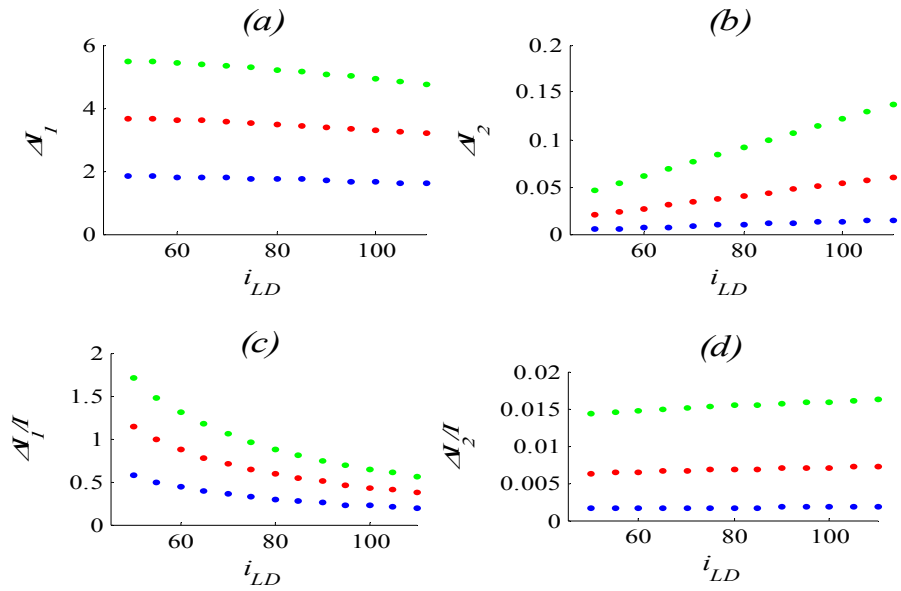


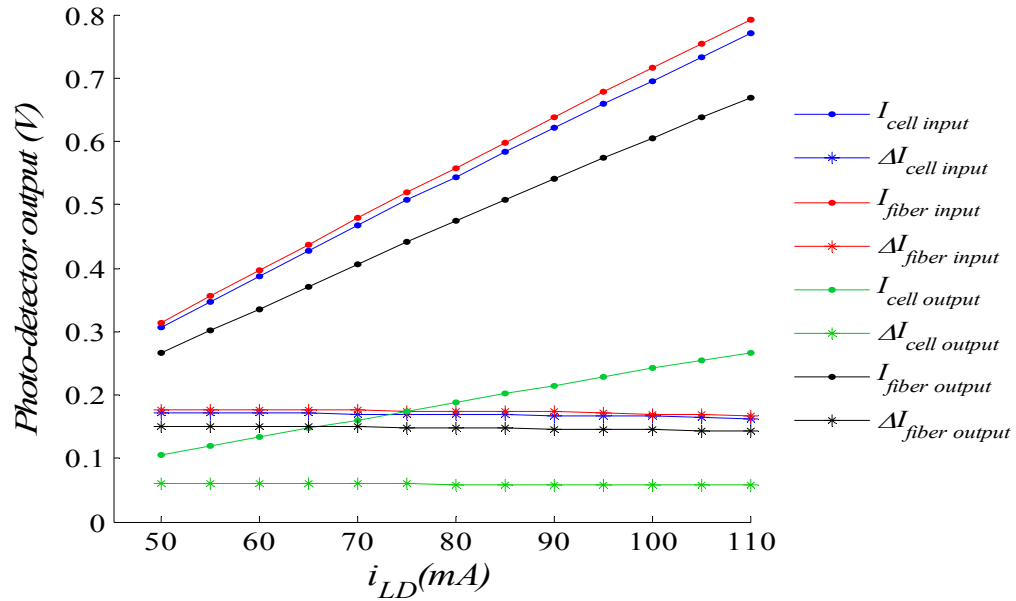
**Fig. 7.17: Programmatically estimated variation of (a) linear IM, (b) nonlinear IM, (c) linear IM index, and (d) nonlinear IM index as a function of amplitude of current modulation**

The linear IM index decreases across the scan. The slope is steep towards the left because of the greater nonlinearity of the power-current characteristics near the threshold current of the DFB laser. In comparison the nonlinear IM index does not vary significantly over the scan range of the current. Ideally the laser should be temperature-tuned so that it can be operated in the linear region of the characteristic curve.

It is instructive to examine the consistency of the variation of the IM index of the laser obtained experimentally. To do this the same experiment described in Sec. 6.3 for the simulation of RAM nulling is performed. The current ramp is switched off. The laser current is sinusoidally modulated with constant amplitude of modulation current and the photo-detector output captured by the oscilloscope is recorded at increasing values of the mean laser current that is manually varied in discrete steps. The values of the mean intensity and the IM are extracted by simply determining the mean and the peak-to-peak value of the modulated intensity captured on the oscilloscope. This process is repeated at various points within the system.

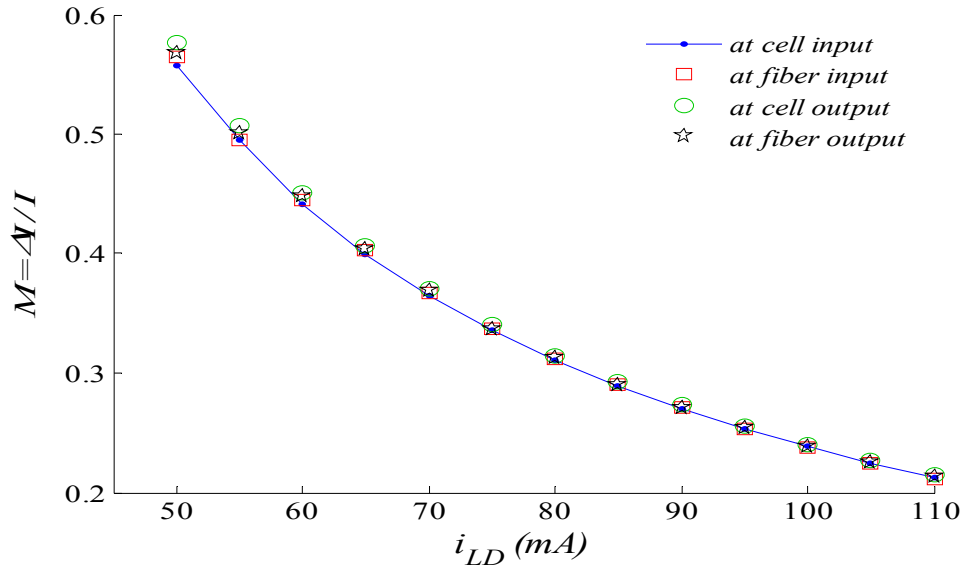
**Chapter 7: Extension of RAM nulling to  $2f$  WMS**

Figure 7.18 shows the variation of intensity and the linear IM at various locations within the system as the laser current is varied in steps of 5mA over a typical scan range.



**Fig. 7.18: Variation of intensity and linear IM of the 1650nm DFB at various locations within the system for modulation current of 11.56 mA**

The variation of the intensity is understandably far more dominant than that of the IM. The values of  $I$  and  $\Delta I$  at the input of the gas cell are almost equal to the values of the corresponding quantities at the input of the delay fiber. This is because the laser output is symmetrically split by the first 3dB coupler. However these values at the output of the gas cell and the delay fiber are lower by the different attenuation factors through the gas cell and the fiber. Note that the actual measured values are liable to vary depending on the physical connections of the fiber connectors, and therefore these measurements have poor repeatability.



**Fig. 7.19: Variation of the intensity modulation index,  $M_I = \Delta I/I$ , with laser current at various locations within the system showing a consistent variation across the current scan range for modulation current of 11.56 mA**

However, it is observed that although the values of  $I$  and  $\Delta I$  vary considerably at different locations in the system, the linear IM index  $M_I$  remains constant as shown in Fig. 7.19. The consistency of these measurements implies that the nonlinear IM index must also be at least as consistent since it is very intimately linked to the linear IM index. Therefore if these parameters are accurately determined by careful laser characterization, they can be treated as constants for that laser operating under conditions that are specific and optimized for a given application. This is further demonstrated by Fig. 7.20 and Fig. 7.21. These results were obtained by performing the same experiment under the same operating conditions but on a different day with the only difference being the significantly different levels of coupled power evident from the much larger values of  $I$  and  $\Delta I$  at all locations.

Chapter 7: Extension of RAM nulling to  $2f$  WMS

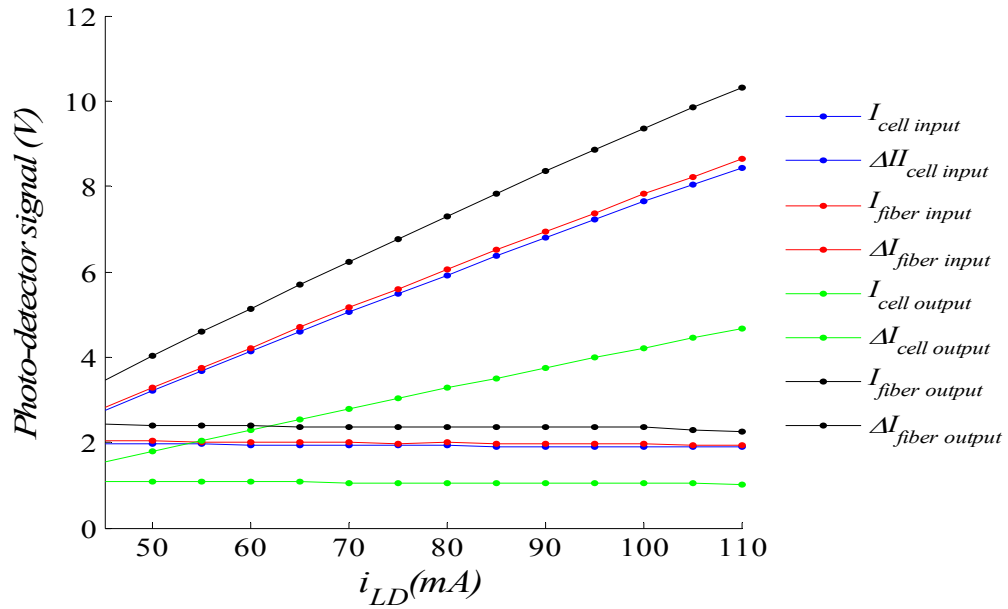


Fig. 7.20: Variation of intensity and linear IM of the 1650nm DFB laser at various points in the system for modulation current of 11.56 mA

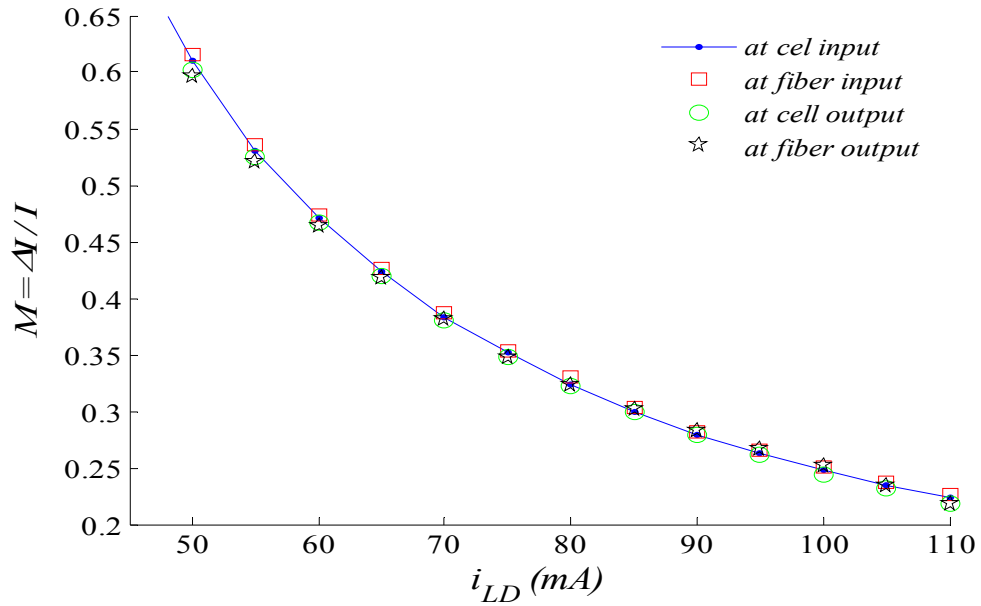


Fig. 7.21: Variation of the amplitude modulation index,  $M = \Delta I/I$ , at various points within the system showing a consistent variation across the current scan range for modulation current of 11.56 mA

## Chapter 7: Extension of RAM nulling to $2f$ WMS

The influence of variable fiber connections is seen in Fig. 7.20 in which the values of  $I$  and  $\Delta I$  at the output of the fiber are greater than those at its input. This is physically impossible and is due to the variation in power coupled to the photo-detector. However, when the linear IM index is plotted the same consistent behaviour at various locations is observed as shown in Fig. 7.21. Comparison with Fig. 7.19 shows remarkable consistency between the measurements performed with significantly different conditions of power coupling on two days.

This discussion and the results help to show that if the laser is accurately characterized then the laser's linear and nonlinear IM parameters may be treated as systematic constants that do not vary significantly for a given laser under known conditions of modulation. Therefore either the linear or the nonlinear IM may be used for the purpose of normalizing the  $2f$  signal.

## 7.7 Conclusion

In this chapter a conceptually simple and operationally robust method is demonstrated to eliminate the  $2f$  RAM. This is achieved by extending the  $1f$  RAM nulling technique to the  $2f$  regime. This only requires the modulation frequency to be changed to half the value for a given length of delay line. The Phasor Decomposition method is used next to decouple the  $2^{\text{nd}}$  derivative signal from the predominant distorting component due to the linear IM-induced. Recent evidence of significant  $2f$  RAM in VCSEL-based WMS [19], strongly suggest that this technique will prove useful for existing widely tunable multi-component gas analysis using lasers with highly nonlinear characteristics. The inconvenient step of separately fitting a baseline can then be dispensed with. The robust nulling at high  $m$ -values is also directly applicable to recently-proposed calibration-free quantitative  $2f$  WMS [13-15], for ratio thermometry applications. In such applications, the  $2f$  background RAM needs to be measured separately and subtracted, and therefore the RAM nulling is expected to be useful for such applications. Finally an alternative normalization technique that uses the  $2f$  RAM background is discussed that can be used for quantitative calibration-free  $2f$  WMS.

## 7.8 References

1. J. Reid, J. Shewchun, B. K. Garside, E. A. Ballik, "High sensitivity pollution detection employing tunable diode lasers," *Appl. Opt.* **17**, 300-307 (1978).
2. J. Reid, D. Labrie, "Second harmonic detection with tunable diode lasers – comparisons of experiment and theory", *Appl. Phys. B*, **26**, pp 203-210, 1981
3. D. T. Cassidy, J. Reid, "Atmospheric pressure monitoring of trace gases using tunable diode lasers," *Appl. Opt.* **21**, 1185-1190 (1982).
4. M. Gabrysch, C. Coris, F. S. Pavone, M. Ignuscio, "Simultaneous detection of CO and CO<sub>2</sub> using a semiconductor DFB diode laser at 1.578 $\mu$ m", *Appl. Phys. B*, **65**, pp 75-79, 1997
5. T. Aizawa, T. Kamimoto, T. Tamaru, "Measurements of OH radical concentration in combustion environments by wavelength-modulation spectroscopy with a 1.55 $\mu$ m distributed-feedback diode laser," *Appl. Opt.* **38** (9), 1733-1741 (1999).
6. V. Nagali, R. K. Hanson, "Design of a diode laser sensor to monitor water vapour in high-pressure combustion gases," *Appl. Opt.* **36** (36), 9518-9527 (1997).
7. L. C. Philippe, R. K. Hanson, "Laser diode wavelength modulation spectroscopy for simultaneous measurement of temperature, pressure, and velocity in shock-heated oxygen flows," *Appl. Opt.* **32** (30), 6090-6103 (1993).
8. T. Aizawa, "Diode-laser wavelength-modulation absorption spectroscopy for quantitative in situ measurements of temperature and OH radical concentration in combustion gases," *Appl. Opt.* **40** (27), 4894-4903 (2001).
9. J. T. C. Liu, J. B. Jeffries, R. K. Hanson, "Wavelength modulation spectroscopy with  $2f$  detection using multiplexed diode lasers for rapid temperature measurements in gaseous flows," *Appl. Phys. B* **78**, 503-511 (2005).

## Chapter 7: Extension of RAM nulling to $2f$ WMS

10. J. T. C. Liu, J. B. Jeffries, R. K. Hanson, "Large-modulation-depth  $2f$  spectroscopy with diode lasers for rapid temperature and species measurements in gases with blended and broadened spectra," *Appl. Opt.* **43** (35), 6500-6509 (2004).
11. Y. Gerard, R. J. Holdsworth, P. A. Martin "Multispecies *in situ* monitoring of a static internal combustion engine by near-infrared diode laser sensors," *Appl. Opt.* **46** (19), 3937-3945 (2007).
12. M. F. Miller, W. J. Kessler, M. G. Allen, "Diode laser-based air mass flux sensor for subsonic aero-propulsion inlets," *Appl. Opt.* **35** (24), 4905-4912 (1996).
13. H. Li, G. B. Rieker, X. Liu, J. B. Jeffries, R. K. Hanson, "Extension of wavelength-modulation spectroscopy to large modulation depth for diode laser absorption measurements in high-pressure gases," *Appl. Opt.* **45**, 1052-1061 (2006).
14. G. B. Rieker, J. B. Jeffries, R. K. Hanson, "Calibration-free wavelength-modulation spectroscopy for measurements of gas temperature and concentration in harsh environments," *Appl. Opt.* **48** (29), 5546-5559 (2009).
15. A. Farooq, J. B. Jeffries, R. K. Hanson, "Measurements of CO<sub>2</sub> concentration and temperature at high pressures using  $1f$ -normalized wavelength-modulation spectroscopy with second harmonic detection near  $2.7\mu\text{m}$ ," *Appl. Opt.* **48** (35), 6740-6753 (2009).
16. T. Sato, M. Mitsuhashi, N. Nunoya, T. Fujisawa, K. Kasaya, F. Kano, Y. Kondo, " $2.33\mu\text{m}$  wavelength distributed feedback lasers with InAs-In<sub>0.53</sub>Ga<sub>0.47</sub>As multiple quantum wells on InP substrates," *IEEE Photon. Tech. Lett.* **20**, 1045-1047 (2008).
17. J. M. Ostermann, F. Rinaldi, P. Debernardi, R. Michalzik, "VCSELs with enhanced single-mode power and stabilized polarization for oxygen sensing," *IEEE Photon. Tech. Lett.* **17**, 2256-2258 (2005).
18. C. Lauer, M. Orstiefer, R. Shau, J. Roskopf, G. Bohm, E. Ronneberg, F. Kohler, M. C. Amann "80°C continuous-wave operation of  $2.01\mu\text{m}$  wavelength

## Chapter 7: Extension of RAM nulling to $2f$ WMS

- InGaAlAs-InP vertical-cavity surface-emitting lasers,” IEEE Photon. Tech. Lett. **16**, 2209-2211 (2004).
19. A. Hangauer, J. Chen, R. Strzoda, M. Orstiefer, M. –C. Amann, “Wavelength modulation spectroscopy with a widely tunable InP-based 2.3  $\mu\text{m}$  vertical-cavity surface-emitting laser”, Opt. Lett., **33**, 1566-1568, (2008).
  20. A. L. Chakraborty, K. Ruxton, W. Johnstone, M. Lengden, K. Duffin, “Elimination of residual amplitude modulation in tunable diode laser wavelength modulation spectroscopy using an optical fiber delay line,” Opt. Exp. **17** (12) , 9602 (2009).
  21. A. J. McGettrick, K. Duffin, W. Johnstone, G. Stewart, D. G. Moodie, “Tunable diode laser spectroscopy with wavelength modulation: a phasor decomposition method for calibration-free measurements of gas concentration and pressure,” IEEE J. Lightwav. Technol. **26**, 432-440 (2008).
  22. K. Duffin, A. J. McGettrick, W. Johnstone, G. Stewart, D. G. Moodie, “Tunable diode laser spectroscopy with wavelength modulation: a calibration-free approach to the recovery of absolute gas absorption line shapes,” IEEE J. Lightwav. Technol. **25**, 3114-3125 (2007).
  23. S. Schilt, L. Thevenaz, P. Robert, “Wavelength modulation spectroscopy: combined frequency and intensity laser modulation,” Appl. Opt. **42**, 6728-6738 (2003).
  24. X. Zhu, D. T. Cassidy, “Modulation spectroscopy with a semiconductor diode laser by injection-current modulation,” J. Opt. Soc. Am. B **14**, 1945-1950 (1997).
  25. P. Kluczynski, O. Axner, “Theoretical description based on Fourier analysis of wavelength-modulation spectroscopy in terms of analytical and background signals,” Appl. Opt. **38**, 5803-5815 (1999).

# *Chapter 8*

---

## **Conclusion and Future work**

---

### **8.1 Conclusion**

The work presented in this thesis was specifically focussed on the development of a fiber-optic technique to eliminate the background residual amplitude modulation (RAM) in 1<sup>st</sup> harmonic wavelength modulation spectroscopy. This is a significant step in alleviating the problem of saturation of the detection electronics by the high concentration-independent background signal.

## Chapter 8: Conclusion and Future Work

It had been shown by previous research within this group that accurate recovery of gas absorption lines using the new  $1f$  calibration-free RAM technique [1, 2] and Phasor Decomposition Method [3, 4] are viable alternatives to conventional  $1f$ WMS techniques that require calibration. These techniques have been used to measure concentration, pressure and temperature of methane under various operational conditions [5, 6]. The most attractive feature of these techniques is that the absorption line shapes can be directly recovered and gas parameters can be extracted from them using appropriate least-squares fitting algorithms. The next logical step therefore was to optimize the  $1f$  calibration-free RAM and PDM techniques and make them competitive with the conventional  $1f$  and  $2f$ WMS strategies.

The first step in this direction is to eliminate the background RAM due to the linear IM of the laser. In chapter 4 a fiber-optic RAM nulling technique to optically eliminate the background  $1f$  RAM has been successfully implemented [7] and explored in detail [8]. It has been shown that the  $1f$  RAM that severely limits the sensitivity of both the  $1f$  calibration techniques can be optically eliminated. This is achieved by splitting the output of the DFB laser into two symmetric parts, directing one part through the gas cell and the other through a fiber delay line of appropriate length that introduces a phase shift of  $\pi$  between the linear IM components on the two arms. When the two components are recombined the two anti-phase IM components cancel, thereby eliminating the background RAM. However, the superposition of two optical signals leads to the problem of significant interference noise. The optical interference noise was robustly minimized by a two-fold approach as explained in Sec. 4.2. First it was ensured that the delay line of 1km was much longer than the coherence length of the DFB laser that is known to be about 47m. Since the mutual coherence function reduces sharply as the path difference between the two optical fields increases, no stable interference was observed but there was significantly high interference noise. This was then drastically reduced by using two polarization controllers to obtain orthogonal polarization states of the two optical fields. The small residual interference noise was totally eliminated when the laser modulation was applied that resulted in a further reduction of the coherence length of the laser. This conclusively demonstrated that the optical interference noise does not limit

## Chapter 8: Conclusion and Future Work

detection sensitivity. The main source of noise is the etalon fringes that arise from the arrangement of GRIN lenses (and later con-focal C lenses) within the gas cell.

The incorporation of RAM nulling in both  $1f$  calibration-free techniques was then demonstrated in chapter 5 with methane at a concentration of 10.13% and 1.02% in nitrogen balance at ambient temperature and pressure. It was shown that the absorption line can be recovered with high accuracy for modulation indices up to about 0.75. For higher  $m$ -values the higher order cross modulation terms become significant and the correction factor algorithm does not work adequately. A general approach for implementing correction factors for high  $m$ -values is being investigated and is briefly outlined later.

The practical issue of devising a robust and convenient signal normalization method was also addressed. It was shown that a baseline fit to the output signal with the delay arm disconnected can be used to normalize the nulled signal. In a practical system a fiber-optic switch can be used to disrupt the nulling process and thereby allow the normalization signal to be obtained without having to physically disconnect the delay arm. Alternatively, the normalization signal can be obtained by using a fiber tap coupler inserted between the gas cell and the system output coupler, provided the relationship between the tap output and main output of the system at  $OP_I$  in Fig. 4.1 is known and stable over the required wavelength range. It was also shown that for low concentrations the non-nulled signal itself can be used to normalize the nulled signal without introducing significant error in measurement. This is much more convenient than having to fit a baseline before normalization since any baseline fitting requires user-intervention that may not be practical in industrial deployment of these sensors. The issue of cancellation of optical interference noise by maintaining orthogonal polarization states of the two signals is also a requirement that can be realistically fulfilled. Polarization maintaining fibers are becoming increasingly affordable and can be used in a real system instead of the manual polarization controllers that have been used for the laboratory demonstrations. Electronically controlled variable optical attenuators are also readily available that can be operated by appropriate hardware interfaces controlled by software.

## Chapter 8: Conclusion and Future Work

These practical aspects are highlighted to convey the message that the RAM nulling setup can be engineered into a compact, robust and remotely operated stand-alone instrument for field applications.

The RAM nulling technique was also incorporated in the PDM which is another very useful  $1f$  calibration-free technique for the recovery of gas absorption lines. The PDM is particularly useful when the IM-WM phase shift  $\psi$ , is small. In such a case the RAM method suffers from the drawback of being able to directly recover only a very small projection of the RAM signal (factor of  $\sin\psi$  down) on to one of the lock-in amplifier axes. The PDM on the other hand can recover the full RAM signal. The elimination of the high background RAM signal is therefore of great importance for the PDM as well.

In the initial work the RAM signals with background nulling showed an unexpected non-zero sloping baseline that required an additional baseline fitting and subtraction that was clearly inconvenient besides being impractical for automated measurements. This artefact was thoroughly investigated and it was found to be caused by the weak wavelength-dependence of the fiber couplers. It was shown that for a particular configuration of the RAM nulling setup the wavelength-dependence of one coupler can be made to cancel that of the other. This result together with the earlier conclusion that the normalization process does not require any baseline fitting makes it easier to automate the whole process of line shape recovery using the RAM method with background nulling.

Finally, the RAM nulling technique was extended to the  $2f$  detection regime in chapter 6. The background signal in  $2f$  WMS signal is usually negligible, which is the reason why it is not discussed in most treatments of WMS. However even with the 1650nm DFB laser a significant baseline was observed for the modulation index value of 2.2 that is known to maximize the  $2f$  signal. The same RAM nulling setup was used to cancel the nonlinear IM that essentially causes the  $2f$  RAM. This merely involved changing the modulation frequency to 50 kHz instead of 100 kHz for the same length of fiber. The  $2f$  RAM nulling was precise and performed robustly for a wide range of high modulation index values. This should be useful to widely tunable  $2f$  WMS for the

## Chapter 8: Conclusion and Future Work

detection of multiple gas species. Over the last few years novel lasers with significantly more nonlinear power-current characteristics have been developed and used in gas sensing [9-11]. In a recent report of  $2f$  WMS [12] the  $2f$  signal has been shown to have a high baseline that complicates the process of extraction of information. Such applications should benefit from the  $2f$  RAM nulling technique. A different application is the recently-proposed calibration-free  $2f$  WMS [13, 14]. These experiments involve making line-centre measurements of  $2f$  signals and normalizing them by the  $1f$  signal for the extraction of gas concentration and temperature. A separate measurement of the  $2f$  RAM followed by its subtraction from the concentration-dependent  $2f$  signal is necessary to maintain linearity of measurement. It is envisaged that the real-time nature of  $2f$  RAM nulling scheme will facilitate real-time measurements in such applications. An alternative to  $1f$  normalization is also proposed in which the  $2f$  RAM itself can be used to normalize the  $2f$  signal. This would obviate the need to switch back and forth between detection harmonics to recover the main signal and the normalization signal, and the cancellation of the respective gain factors of the whole detection process would then be exact.

The main limitation of the system in its present form is the presence of etalon fringes arising from within the micro-optic gas cell. It is possible to design the system better to suppress the fringes to a greater degree, although it is acknowledged that this can be very challenging. However, the absolute absorption line shape can be recovered with good accuracy for gas concentration levels that are sufficiently low for the system to be useful in many applications. The main idea of RAM nulling can however be implemented using the scheme of balanced-detection proposed by Hobbs [15] and Zhu [16].

In summary it may be said that a robust fiber-optic  $1f$  RAM nulling scheme has been devised and demonstrated that can optically eliminate the high background RAM signal that places severe limits on the detection sensitivity for  $1f$  detection. This technique significantly enhances the two  $1f$  calibration-free techniques namely the RAM method [1], and the Phasor Decomposition method [4], devised by previous researchers. These

## Chapter 8: Conclusion and Future Work

$1f$  calibration-free techniques in conjunction with RAM nulling allow for the direct recovery of absolute gas absorption line shapes with high sensitivity from which concentration and pressure can be directly recovered by a straightforward least squares fitting approach. Through a wavelength-dependent analysis of the whole system it was shown that small residual signal slopes can be eliminated through proper choice of fiber-optic components and the experimental configuration. This is important if this technique is used with the new types of lasers (such as VCSELs and other structures [9-12]) that have significantly nonlinear power-current characteristics. The generic RAM nulling technique was also applied to  $2f$  WMS for the elimination of the  $2f$  RAM that complicates signal recovery in conventional  $2f$  WMS [12] and in particular for the newly proposed calibration-free  $2f$  WMS strategy [13, 14].

The demonstration of the RAM nulling technique and the combination of all of these elements represents a significant advancement of the field of quantitative calibration-free  $1f$  WMS for the recovery of gas absorption line shapes for industrial process control applications. The next logical steps would be to optimize the performance of every aspect of the design of the sensor by studying the IM and WM characteristics of the DFB lasers under different conditions of modulation to select the most suitable operating conditions. Several aspects of instrumentation also need to be addressed after a thorough survey of the recent advances in electronics and fiber-optics.

## 8.2 Future work

The  $1f$  calibration-free WMS technique with RAM nulling that has been demonstrated has the potential to be optimized further. An important aspect of the RAM nulling technique is that it is a generic technique. It should therefore be possible to use it in various modulation spectroscopy applications with different types of current-modulated lasers. Some of the aspects that can potentially lead to better performance of the sensor are discussed in this section.

### 8.2.1 Variation of the RAM and the 1<sup>st</sup> derivative signals with modulation frequency

All the experimental results presented in this thesis are for an operating frequency of 100 kHz. It has been observed that the raw voltage signal values obtained at the output of the lock-in amplifier with the RAM method are smaller than the 1<sup>st</sup> derivative component that is used in conventional  $1f$  WMS measurements. This is shown in Fig 8.1 in which the RAM signal and the 1<sup>st</sup> derivative signal are shown for a modulation frequency of 100 kHz and for varying modulation indices. A close inspection of Fig 8.1 reveals that the concentration-dependent RAM signal is much smaller than the positive or negative peak of the 1<sup>st</sup> derivative signal. For the accurate extraction of concentration and pressure using the calibration-free RAM technique in particular, it is critical that this raw signal is recovered with high signal-to-noise ratio. The relative magnitude of signals is therefore the first and most obvious issue that needs to be addressed.

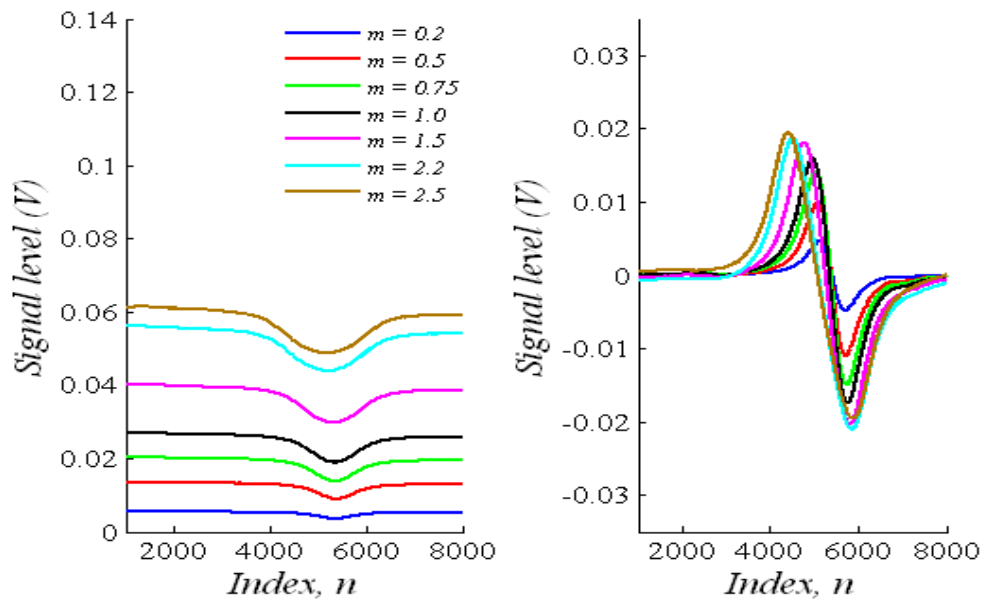


**Fig. 8.1:**  $1f$  RAM and 1<sup>st</sup> derivative terms for a modulation frequency of 100 kHz and for increasing modulation index

The WM efficiency (GHz/mA) of a typical telecom-grade DFB laser decreases as the modulation frequency is increased while the IM-WM phase shift  $\psi$  approaches the 90°

## Chapter 8: Conclusion and Future Work

separation point. This implies that a particular amplitude of current modulation will produce less FM at higher frequencies but the level of IM that is dictated by the power-current characteristics should remain constant. Additionally as  $\psi$  approaches  $90^\circ$  the full RAM signal is projected on the channel X of the lock-in amplifier. For a sufficiently high frequency the recovered RAM signal should therefore become comparable with the 1<sup>st</sup> derivative signal. If this is achieved the attribute of calibration-free direct recovery of absorption lines would make the RAM technique highly competitive with conventional  $1f$ WMS techniques that require calibration.

The effect of increasing the modulation frequency on the RAM signal and the 1<sup>st</sup> derivative signal is shown in Fig. 8.1 through Fig. 8.5. It is seen that the RAM signal (background and concentration-dependent RAM) increases as a whole, and for high values of modulation frequency the concentration-dependent RAM signal becomes comparable to the amplitude of the 1<sup>st</sup> derivative signal.

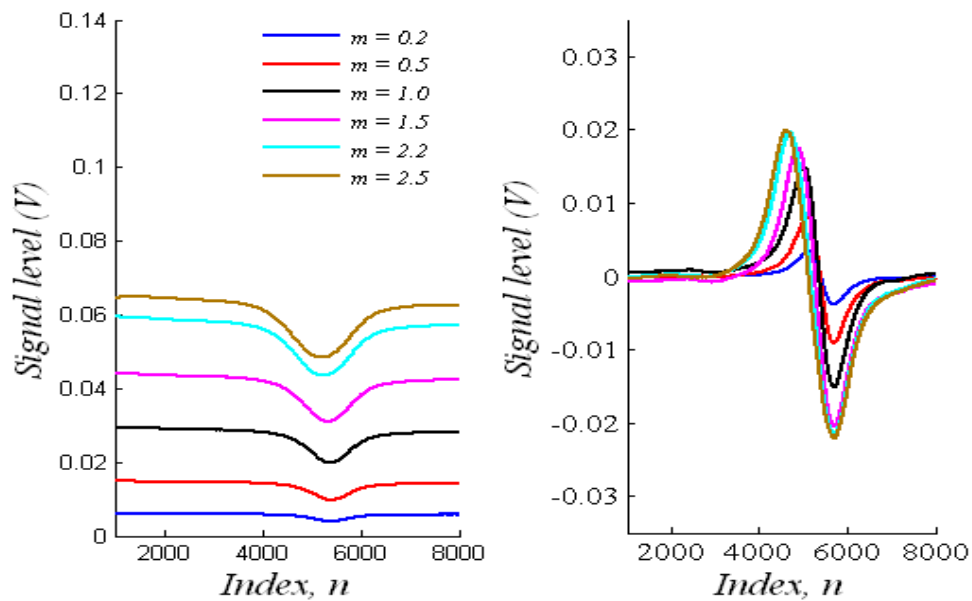


**Fig. 8.2:**  $1f$  RAM and 1<sup>st</sup> derivative terms for a modulation frequency of 200 kHz and for increasing modulation index

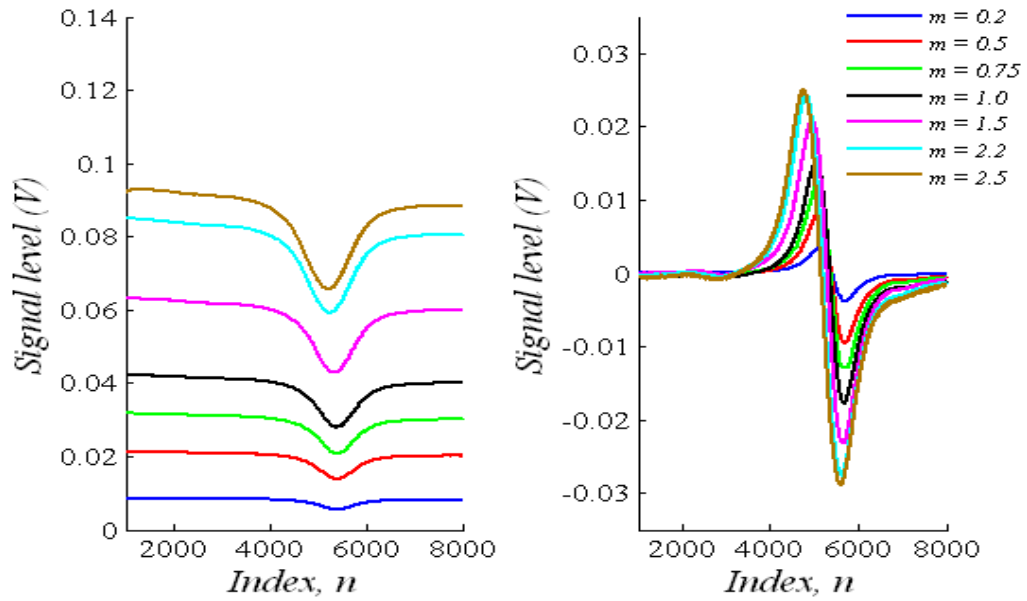


**Fig. 8.3:**  $1f$  RAM and  $1^{\text{st}}$  derivative terms for a modulation frequency of 500 kHz and for increasing modulation index

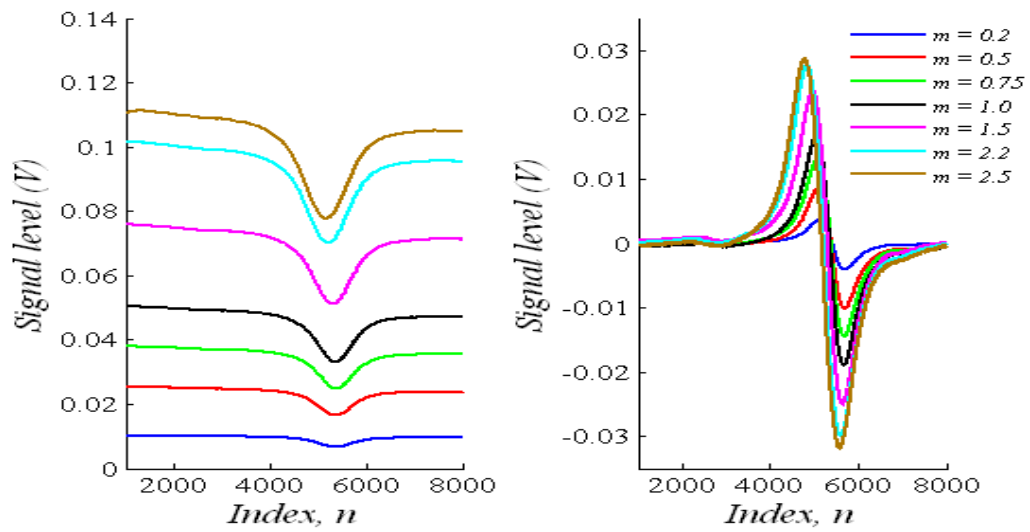


**Fig. 8.4:** RAM  $1f$  RAM and  $1^{\text{st}}$  derivative terms for a modulation frequency of 750 kHz and for increasing modulation index

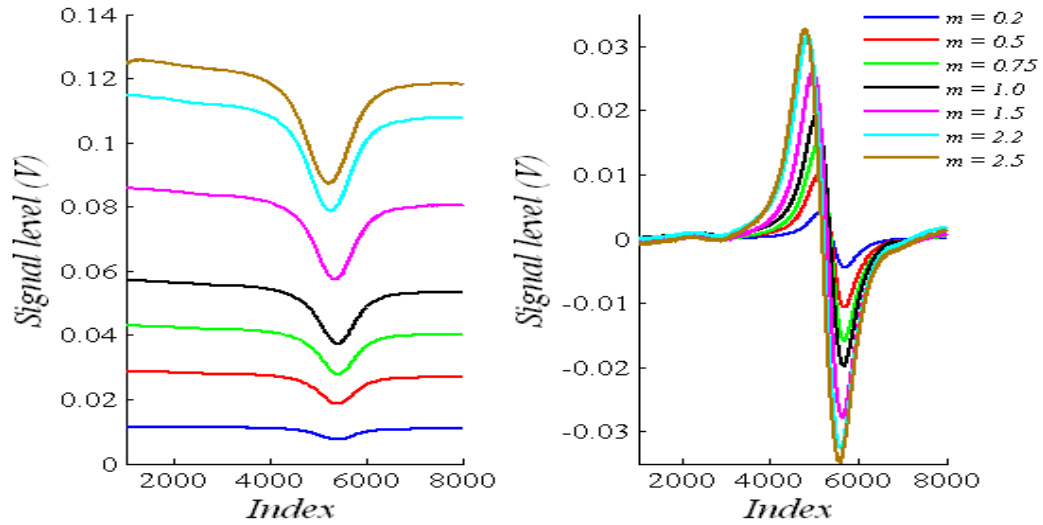


*Fig. 8.5: 1f RAM and 1<sup>st</sup> derivative terms for a modulation frequency of 1 MHz and for increasing modulation index*

A systematic study needs to be carried out to identify an optimum frequency and modulation index to fully exploit this behaviour of the RAM signals and make this approach competitive. The dependence of the tuning rate (GHz/mA) on the modulation frequency needs to be considered to ensure that signals for the same modulation index are compared at different frequencies. The variation of the IM-WM phase shift with frequency must also be considered when phase-tuning the lock-in amplifier. A thorough study of these aspects is being carried out by other researchers within the group and the encouraging results await publication.

### **8.2.2 Scope for RAM nulling at high modulation frequencies**

The preliminary results in the previous section show that although the concentration-dependent RAM signal increases as the frequency increases, the background RAM increases significantly as well. The RAM nulling technique should be useful in eliminating this background and thereby help to negate criticism of the RAM method with respect to this drawback. Once an optimum value of the modulation frequency is identified, the RAM nulling technique may be tailored to eliminate the background to increase the sensitivity further. However, an important practical issue that needs to be

## Chapter 8: Conclusion and Future Work

considered is that the fiber delay length varies inversely as the modulation frequency. For high frequencies the required delay length may approach the coherence length of the laser and optical interference noise may become a severe problem if this issue is not addressed. However the suppression of the optical interference noise by the combination of the laser modulation and the polarization controllers has been demonstrated to be very robust. Fig. 4.9 suggests that the mutual coherence function should rapidly decay to small values if the delay length is only about five times the coherence length of the laser. In these experiments the 1km length of fiber that has been used is much longer than the coherence length of the laser which is about 47m. This suggests that even if the fiber length is reduced by a factor of 5 the optical interference noise should not be catastrophic and it should be possible to minimize it. If this found to be the case, RAM nulling can be realized at high frequencies without significantly compromising the signal-to-noise of the system.

### ***8.2.3 Implementation of RAM nulling at mid-infrared wavelengths***

Mid-infrared gas sensing has the significant advantage of offering much higher sensitivity since the fundamental absorption lines that lie in this region are stronger than the near-IR overtone lines by an order of magnitude. Lasers and photo-detectors in this operating region are now widely available. However the optical fiber technology is not yet as advanced as it is in the near-IR region. The best mid-IR fibers have typical attenuation of 0.1dB/m [17]. This precludes the use of long lengths of these fibers in any application. The RAM nulling technique requires a long length of fiber and does not appear to be well suited for extension in to the mid-IR. However operation at high modulation frequencies significantly reduces the length of fiber required. If shorter lengths of fiber that are still larger than the coherence length of the source can be used it may be possible to implement RAM nulling at mid-IR wavelengths as well. A fiber length of 100m would have a loss of 10dB. It is worth pointing out that in many experiments with the 1650nm laser the gas signal required to be attenuated by as much as 10dB to maintain linearity of detection. Despite this, sufficiently clean signals were detectable. The mid-IR absorption lines that are stronger by an order of magnitude may

## **Chapter 8: Conclusion and Future Work**

offset this loss so that RAM nulling may be viable. With the current mid-IR fiber technology such a scheme may seem to be mere speculation. However this short discussion goes to show that RAM nulling in the mid-IR is limited only by material issues that are likely to be addressed in future with realistic hope of breakthroughs being made in mid-IR fiber technology.

### ***8.2.4 Correction factors for accurate recovery of line shape for high modulation indices***

As shown in chapter 5 the results using the calibration-free RAM technique and PDM for modulation indices beyond about 0.75 have large errors in them. This is due to the fact that the algorithm used to obtain the correction factors for these results is not optimized to handle high values of modulation index. However it is well known that a modulation index of 2 is optimum for  $1f$  detection. A generalized algorithm that can handle arbitrarily large values of modulation indices is expected to be a significant addition to these techniques. Investigation of this aspect is also being carried out by other researchers within the group and the initial results have been very promising.

### ***8.2.5 WMS with gas cell placed outside the RAM nulling setup***

An interesting effect is observed if the gas cell is placed at the output of the RAM nulling setup as shown in Fig. 8.6. It can be rigorously proved that if the RAM nulling condition is satisfied for a particular harmonic of the modulation frequency, all signal components at that harmonic and its odd multiples are precisely cancelled at the output of the gas cell. To be specific, if the  $1f$  RAM nulling is arranged then signal components at all odd harmonics ( $1f$ ,  $3f$ ,  $5f$  etc) are found to be absent at the output of the gas cell.

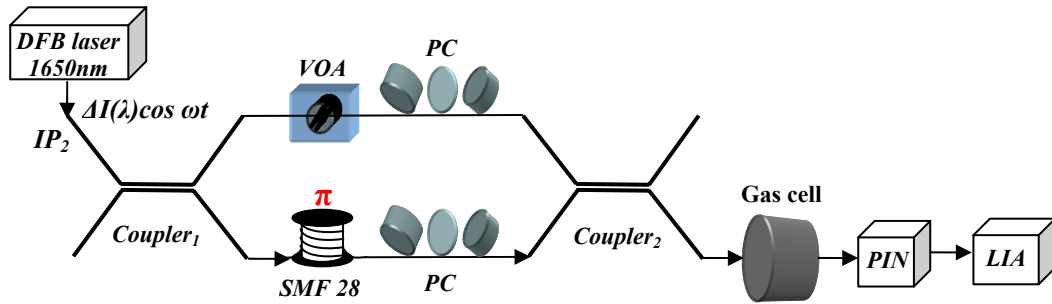


Fig. 8.6: Experimental for WMS with the cell placed outside the RAM nulling setup

This is shown in Fig. 8.7 where RAM nulling is satisfied for the 1<sup>st</sup> harmonic. The predominant signal component is the 2 $f$  component while the odd harmonic components are almost zero. A small 1 $f$  component is due to the intentional imprecise adjustment of the RAM nulling condition.

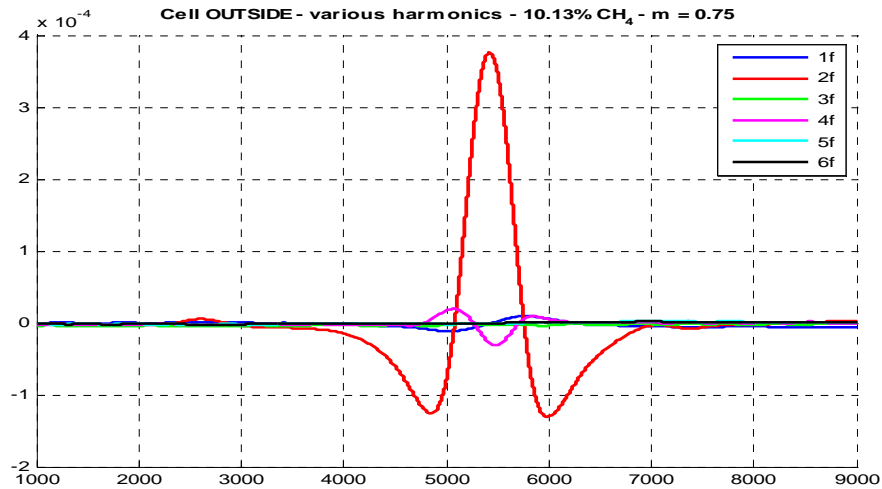


Fig. 8.7: Cancellation of odd harmonic signal components with the gas cell placed outside the nulling setup and with the 1 $f$  RAM nulling condition satisfied

This configuration has not yet been fully explored but it might be useful in a difference frequency generation system [18] in which the RAM technique has recently been applied.

## 8.3 Conclusion

In conclusion it may be said that the successful demonstration of the RAM nulling technique and its incorporation in to the two  $1f$  calibration-free WMS techniques is a significant advancement of the field of industrial gas sensing. There is much scope for improvement and optimization of this technique in terms of detection sensitivity and noise reduction. However, despite the many complex issues and potential pitfalls, there is reason to be optimistic about the prospect of realizing  $1f$  calibration-free direct recovery of absorption line shapes with detection sensitivity that rivals (and possibly exceeds) that of conventional  $1f$  and  $2f$  WMS techniques that suffer from the drawback of requiring calibration.

## 8.4 References

1. K. Duffin, A. J. McGettrick, W. Johnstone, G. Stewart, D. G. Moodie, “Tunable diode laser spectroscopy with wavelength modulation: a calibration-free approach to the recovery of absolute gas absorption line shapes”, *IEEE J. of Lightwav. Technol.*, Vol. 25, No.10, pp 3114-3125, October 2007
2. K. Duffin, “Wavelength modulation spectroscopy with tunable diode lasers: A calibration-free approach to the recovery of absolute gas absorption line shapes,” Ph.D. Thesis, Dept. of EEE, Univ. Strathclyde, Glasgow, Scotland, 2007.
3. A. J. McGettrick, “Wavelength modulation spectroscopy with tunable diode lasers: A calibration-free approach to the recovery of absolute gas absorption line shapes,” Ph.D. Thesis, Dept. of EEE, Univ. Strathclyde, Glasgow, Scotland, 2007.
4. A. J. McGettrick, K. Duffin, W. Johnstone, G. Stewart, D. G. Moodie, “Tunable diode laser spectroscopy with wavelength modulation: a phasor decomposition method for calibration-free measurements gas concentration and pressure”, *IEEE J. Lightwav. Technol.*, Vol. 26, No. 4, pp 432-440, 15 February 2008
5. W. Johnstone, A. J. McGettrick, K. Duffin, A. Cheung, G. Stewart, “Tunable diode laser spectroscopy for industrial process applications: system characterization in conventional and new approaches,” *IEEE Sensors J.* **8** (7), 1079-1088 (2008).
6. A. J. McGettrick, W. Johnstone, R. Cunningham, J. D. Black, “Tunable diode laser spectroscopy with wavelength modulation: calibration-free measurements of gas compositions at elevated temperatures and varying pressure,” *IEEE J. Lightwav. Technol.*, **27** (15), 3150-3161 (2009).
7. A. L. Chakraborty, K. Ruxton, W. Johnstone, M. Lengden, K. Duffin, “Elimination of residual amplitude modulation in tunable diode laser wavelength

## Chapter 8: Conclusion and Future Work

modulation spectroscopy using an optical fiber delay line,” *Opt. Exp.* **17** (12) , 9602 (2009).

8. A. L. Chakraborty, K. Ruxton and W. Johnstone, “Influence of the wavelength-dependence of fiber couplers on the background signal in wavelength modulation spectroscopy with RAM-nulling”, *Opt. Exp. Vol.* **18**, Issue 1, pp. 267-280 (2010).
9. C. Lauer, M. Orstiefer, R. Shau, J. Roskopf, G. Bohm, E. Ronneberg, F. Kohler, M. C. Amann “80°C continuous-wave operation of 2.01 $\mu$ m wavelength InGaAlAs-InP vertical-cavity surface-emitting lasers,” *IEEE Photon. Tech. Lett.* **16**, 2209-2211 (2004).
10. J. M. Ostermann, F. Rinaldi, P. Debernardi, R. Michalzik, “VCSELs with enhanced single-mode power and stabilized polarization for oxygen sensing,” *IEEE Photon. Tech. Lett.* **17**, 2256-2258 (2005).
11. T. Sato, M. Mitsuhashi, N. Nunoya, T. Fujisawa, K. Kasaya, F. Kano, Y. Kondo, “2.33 $\mu$ m wavelength distributed feedback lasers with InAs-In<sub>0.53</sub>Ga<sub>0.47</sub>As multiple quantum wells on InP substrates,” *IEEE Photon. Tech. Lett.* **20**, 1045-1047 (2008).
12. A. Hangauer, J. Chen, R. Strzoda, M. Orstiefer, M. –C. Amann, “Wavelength modulation spectroscopy with a widely tunable InP-based 2.3  $\mu$ m vertical-cavity surface-emitting laser”, *Opt. Lett.*, **33**, 1566-1568, (2008).
13. H. Li, G. B. Rieker, X. Liu, J. B. Jeffries, R. K. Hanson, “Extension of wavelength-modulation spectroscopy to large modulation depth for diode laser absorption measurements in high-pressure gases,” *Appl. Opt.* **45**, 1052-1061 (2006)
14. G. B. Rieker, J. B. Jeffries, R. K. Hanson, “Calibration-free wavelength-modulation spectroscopy for measurements of gas temperature and concentration in harsh environments,” *Appl. Opt.* **48** (29), 5546-5559 (2009)

## Chapter 8: Conclusion and Future Work

15. P. C. Hobbs, "Ultra-sensitive laser measurements without tears," *Appl. Opt.* **36** (4), 903-920 (1997)
16. X. Zhu, D. T. Cassidy, "Electronic subtractor for trace gas detection with InGaAsP diode lasers," *Appl. Opt.* **34** (36), 5546-5559 (1995)
17. <http://www.iguide-irphotonics.com/>
18. I. Armstrong, W. Johnstone, K. Duffin, M. Lengden, A. L. Chakraborty, K. Ruxton "Detection of CH<sub>4</sub> in the Mid-IR using Difference Frequency Generation with Tunable Diode Laser Spectroscopy", in press *IEEE J. Lightwav. Technol.*

## Chapter 9: Extras

# Appendix A: MATLAB program for RAM-nulling

```
% RAM Nulling program
% developed by Arup Lal Chakraborty, 2007-2010
% Steps -
% 1. Input Theory file
% 2. Input resonator file for wavelength referencing
% 3. Input OP1_gas signal
% 4. Input OP1_nogas signal which is a baseline fit to OP1_gas using...
%   program developed by Dr Michael Lengden
% 5. Input OP1_nogas_break2 signal which is the baseline fit to the...
%   OP1_gas signal with the delay arm disconnected
%   For low gas concentrations a baseline fit is not necessary.
% 6. Calculate wavelength-referenced absorption profile
% 7. Finally, apply 2nd and 4th order corrections for high modulation
indices

clc;close all;clear;format long;

% Digital filter design
N = 6; Rp = 0.01; Rs = 90; Wn = 0.005;
[b1 a1] = ellip(N,Rp,Rs,Wn);

% Set limits for data truncation
l1 = 1000;
l2 = 9000;

% *****
%           PART 1 - Read in experimental signals
% *****

% Theory file
[filename, pathname, filterindex] = uigetfile('*..*', 'Step 1: Input
theory data file');
if ~(isequal(filename,0) && isequal(pathname,0))
    theoryfile = xlsread(strcat(pathname, filename));
    waves      = theoryfile(:,1); waves = waves(3:end);
    waves      = waves(:);
    amps       = theoryfile(:,2); amps  = amps(3:end);
    amps       = amps(:);
    cd(pathname);
end

% Resonator data file
[filename, pathname, filterindex] = uigetfile('*..*', 'Step 2: Input
Resonator file');
if ~(isequal(filename,0) && isequal(pathname,0))
    res      = dlmread(strcat(pathname,filename));
    N1 = 3; Rp1 = 0.01; Rs1 = 90; Wn1 = 0.01 ; % use a 'softer' filter
           for resonator trace
    [b_res a_res] = ellip(N1,Rp1,Rs1,Wn1);
```

## Chapter 9: Extras

```
res = res(11:12);
res = filtfilt(b_res,a_res,res);
res = res(:);
% Peak identification
diff_res = diff(res);
peak = []; % vector of peaks of res
for n = 1:length(diff_res)-1
    if ( ne(sign(diff_res(n)),sign(diff_res(n+1))) &&
(diff_res(n)>diff_res(n+1)) )
        peak = [peak n+1];
    end
end
peak = peak(:);
% Peak identification end
cd(pathname);
end
% Plot resonator output and its peaks
f1 = figure;
index = 1:length(res);
subplot(211);
plot(index,res,index(peak),res(peak),'ro');
title('Resonator output and the peaks');

% Input O/P1 Gas
[filename, pathname, filterindex] = uigetfile('*..*', 'Step 3: Input OP1
gas file');
if ~(isequal(filename,0) && isequal(pathname,0))
    OP1_gas = dlmread(strcat(pathname,filename));
    OP1_gas = OP1_gas(11:12);
    LIA_sens_gas = str2num(char(inputdlg('Input O/P1 gas sensitivity in
volts: ')));
    cd(pathname);
end

% Input O/P1 NO Gas - baseline fit
[filename, pathname, filterindex] = uigetfile('*..*', 'Step 4: Input
baseline fit for OP1 gas');
if ~(isequal(filename,0) && isequal(pathname,0))
    OP1_nogas = dlmread(strcat(pathname,filename));
    OP1_nogas = OP1_nogas(11:12);
    cd(pathname)
end

% Input O/P1 No Gas Break Arm 2
[filename, pathname, filterindex] = uigetfile('*..*', 'Step 5: Input
O/P1 no gas break arm2 file');
if ~(isequal(filename,0) && isequal(pathname,0))
    OP1_nogas_break2 = dlmread(strcat(pathname,filename));
    OP1_nogas_break2 = filtfilt(b1,a1,OP1_nogas_break2(:));
    OP1_nogas_break2 = OP1_nogas_break2(11:12);
    LIA_sens_nogas_break2 = str2num(char(inputdlg('Input O/P1 no gas
sensitivity in volts: ')));
    cd(pathname);
end
```

## Chapter 9: Extras

```
% Actual Wavelength Referencing
%-----

clear K_Index Line_Cent_Wave Q_Index Line_Cent_Index error1
      closest_peak Res_Peak_Wave
clear leftside rightside Res_Peak_Wave x P_res YYY Theory_Cent_freq
      wavelength frequencies Line_Cent_frequency

% Find the line centre wavelength of the THEORY plot
Line_Cent_freq      = (3e8/waves(find(amps == min(amps))));
                    % Freq of line centre

% Find the line centre index from the experimental plot
Line_Cent_Index     = find(OP1_gas == min(OP1_gas));
                    % Index of gas minimum
Line_Cent_Index     = Line_Cent_Index(1); % ignore double values
[error1, closest_peak] = min(abs(peak - Line_Cent_Index));
                    % peak closest to Line_Cent_Index
delta_f             = 0.4275; % FSR of fiber ring resonator

% Convert zero-crossing indices to frequencies
Res_Peak_freq      = [];
Res_Peak_freq(closest_peak) = 150000;
leftside           = Line_Cent_freq + ((closest_peak) -
                                       (1:closest_peak))*delta_f;
rightside          = Line_Cent_freq -
                    (([:(closest_peak+1):length(peak)] -
                      closest_peak)*delta_f);
Res_Peak_freq      = [leftside rightside];
Res_Peak_freq      = Res_Peak_freq(:);

% 2nd order poly fit to interpolate between the resonator frequencies
x_res              = (1:length(OP1_gas));
P_res              = polyfit(peak(:),Res_Peak_freq(:),2);
frequencies        = polyval(P_res, x_res);

% Extract values of polynomial fit at each increment x
% Shift polyfit to match the expt file at line centre
Theory_Cent_freq   = 3e8./waves(find(amps == min(amps)));
shift              = Theory_Cent_freq -
                    frequencies(Line_Cent_Index);
frequencies        = frequencies + shift;
wavelength         = 3e8./frequencies;
%-----

% *****
%           PART 2 - Calculation of Absorption
% *****

nulled_output = (OP1_gas(:) -
                 OP1_nogas(:))*(LIA_sens_gas/LIA_sens_nogas_break2);
absorption     = -nulled_output(:)./OP1_nogas_break2(:);
transmission   = 1 - absorption;
```

## Chapter 9: Extras

```
figure;
plot(waves,amps,'b'); hold on;
plot(wavelength,transmission,'r');
xlabel('\bf\lambda (nm)');ylabel('Relative Transmission');
title('\bfExperimental Results');
legend('Theory','Expt');

% *****
%           PART 3 - 2ND AND 4TH ORDER CORRECTIONS
% *****

% Enter current dither size (mA)
current_dither_size = str2double(char(inputdlg('Enter current dither
amplitude (mA peak)')));
% Enter delta_nu/delta_i (Ghz/mA)
del_nu_del_i       = str2double(char(inputdlg('Input delta_nu/delta_I
in GHz/mA: ')));
del_nu              = del_nu_del_i * current_dither_size * 1e9;

corrected_transmission(:,1) = transmission;

for c = 1:4
    % Calculate HWHM of the original distorted AM trace
    L(c) = (1 + min(corrected_transmission(:,c)))/2; %
    % Calculates the FWHM amplitude
    [M(c),N(c)] = min(abs(corrected_transmission(:,c) - L(c))); %
    % Find nearest value to calculated FWHM
    FWHM_freq(c) = frequencies(N(c)); % frequency at
    % the point of inflection of the absorption profile
    % Calculate HWHM magnitude as frequency difference between
    % FWHM_freq and line centre
    line_cent_index(c)=
    find(corrected_transmission(:,c)==min(corrected_transmission(:,c)));
    line_cent_freq(c) = frequencies(line_cent_index(c));
    line_cent_freq(c) = line_cent_freq(1);
    HWHM(c) = abs(FWHM_freq(c) - line_cent_freq(c));
    % Calculate 2nd and 4th order correction factor
    delta(:,c) = (frequencies-line_cent_freq(c))./HWHM(c);
    B(:,c) = (3.*(delta(:,c).^2)-
    1)./((1+(delta(:,c).^2)).^2);
    D(:,c) = (5.*(delta(:,c).^4)-
    (10.*(delta(:,c).^2)+1)./((1+(delta(:,c).^2)).^4);
    m(c) = (del_nu/HWHM(c));
    correction_factor(:,c) =
    (1./(1+(0.25*(m(c)^2).*B(:,c))+((0.125*(m(c)^4)).*D(:,c))));
    corrected_transmission(:,c+1) = (1 -
    corrected_transmission(:,1)).*correction_factor(:,c);
    corrected_transmission(:,c+1)=1-corrected_transmission(:,c+1);
    % convert back to relative transmission
end

% Comparison of nth order corrections
fig2 = figure;
plot(waves,amps,'b');hold on;grid on;
```

## Chapter 9: Extras

```
plot(wavelength,corrected_transmission(:,1), 'c');
plot(wavelength,corrected_transmission(:,2), 'g');
plot(wavelength,corrected_transmission(:,3), 'k');
plot(wavelength,corrected_transmission(:,4), 'y');
plot(wavelength,corrected_transmission(:,5), 'r');
xlabel('\lambda (nm)');ylabel('Transmission');
legend('theory', '0th', '1st', '2nd', '3rd', '4th');
title('Comparison of nth order corrections');

min_corrected_signals      = min(corrected_transmission,[],1);
error                     = (min(amps) -
(min_corrected_signals))/min(amps) * 100;
[min_error min_error_index] = min(abs(error));
best_iteration_index      = min_error_index - 1
error_for_best_iteration  = error(min_error_index)

% Saving best iteration result
[filename, pathname, filterindex] = uiputfile('*.dat', 'Save best
iteration result as...');
if ~(isequal(filename,0) && isequal(pathname,0))
    dlmwrite(strcat(pathname,filename),[wavelength'
corrected_transmission(:,min_error_index)], 'delimiter', '\n', 'precisi
on', '%.6f');
end

fig2 = figure;
plot(waves,amps,'b');hold on;grid on;
plot(wavelength,corrected_transmission(:,5), 'r');
legend('Theory', 'Expt');

% ***** E N D   O F   P R O G R A M   *****
```

## Chapter 9: Extras

# Appendix B: MATLAB program for PDM with RAM-nulling

```
% PDM with RAM Nulling program
% developed by Arup Lal Chakraborty, 2007-2010
% Steps -
% 1. Input Theory file
% 2. Input resonator file for wavelength referencing
% 3. Input sep_FM signal
% 4. Input AM_FM signal
% 5. Input OP1_nogas_break2 signal which is the baseline fit to the...
%     OP1_gas signal with the delay arm disconnected
%     For low gas concentrations a baseline fit is not necessary.
% 6. Calculate wavelength-referenced absorption profile
% 7. Finally, apply 2nd and 4th order corrections for high modulation
indices

close all;clc;clear all;format long;
N = 6; Rp = 0.01; Rs = 90; Wn = 0.005 ;
[b1 a1] = ellip(N,Rp,Rs,Wn);

l1 = 1000;
l2 = 9000;

% *****
%           PART 1 - Read in experimental OP1 signals
% *****

% Theory file
[filename,pathname,filterindex] = uigetfile('*.','Step 2:Input theory
file');
if ~(isequal(filename,0) && isequal(pathname,0))
    g = xlsread(strcat(pathname,filename));
    waves = g(:,1);waves = waves(3:end);
    amps = g(:,2);amps = amps(3:end);
    clear g
    cd(pathname)
end

% Resonator file
[filename,pathname,filterindex] = uigetfile('*.','Step 1:Input
resonator file');
if ~(isequal(filename,0) && isequal(pathname,0))
    res = dlmread(strcat(pathname,filename));
    N1 = 3; Rp1 = 0.01; Rs1 = 90; Wn1 = 0.1 ;
    [b_res a_res] = ellip(N1,Rp1,Rs1,Wn1);
    res = res(l1:l2);
    res = filtfilt(b_res,a_res,res);
    res = res(:);
    f1 = figure;
    index = 1:length(res);
    plot(index,res,'b');hold on;
    xlim([1 8001]);
```

## Chapter 9: Extras

```
% Peak identification
diff_res = diff(res);
peak     = [];
for n = 1:length(diff_res)-1
    if ( ne(sign(diff_res(n)),sign(diff_res(n+1))) && (diff_res(n)
> diff_res(n+1)) )
        peak = [peak n+1];
    end
end
peak = peak(:);
% Eliminate spurious peaks at the bottom
newpeak = [];
threshold = res(peak(1))/2;
for n = 1:length(peak)
    if (res(peak(n)) > threshold)
        newpeak = [newpeak peak(n)];
        plot(index(newpeak),res(newpeak), 'r. ');pause(0.005);
    end
end
legend('Resonator output', 'Peaks');
cd(pathname);
end

% Sep_FM - Channel Y
[filename,pathname,filterindex] = uigetfile('*.wav','Step 4:Input sep_FM
(chY/ch2) file:');
if ~(isequal(filename,0) && isequal(pathname,0))
    sep_FM = dlmread(strcat(pathname,filename));
    sep_FM = sep_FM(11:12);
    x = sep_FM;
    P = 4;
    Q = 1;
    x = resample(x,P,Q);           % upsample by factor P/Q
    fs = 1000;                    % assumed sampling
frequency
    fft_points = 4096; % no of points in computing the DFT - higher
value gives better resolution
    % Actual DFT calculation
    X = fft(x,fft_points);
    Pxx = (X.*conj(X))/fft_points;
    Pxx(1) = 0;                   % first term is just sum of
all terms - dc term
    Pxx = Pxx/max(Pxx);
    f = fs/fft_points*(0:fft_points/2 - 1)'; % frequency axis
    % Plot PSD of input sequence
    figure;
    plot(f,Pxx(1:fft_points/2),'.-');grid on;hold on;
    title('\bfPower spectral density');xlabel('Frequency (Hz)')
    N = 8000;                     % length of FIR filter -
the longer the better
    fc = 0.4;                     % cut off frequency (Hz) -
inspect PSD and choose value
    wn = fc/(fs/2);              % normalized cutoff
```

## Chapter 9: Extras

```
b_fir = fir1(N,wn); % actual filter
coefficients
% Filter frequency response
[H_fir w_fir] = freqz(b_fir,1,4096);
H_fir_mag = abs(H_fir);
H_fir_phase = unwrap(angle(H_fir)*180/pi);
f_fir = w_fir/(2*pi)*fs;
plot(f_fir,H_fir_mag,'g.-');
xlim([-1 5]);
% Filter input sequence
filtered_x = filtfilt(b_fir,1,x);
% Plot result
figure;hold on;
plot(x,'b');plot(filtered_x,'m');
legend('Original','Filtered');
title('\bfFIR filtering - original and filtered');
cd(pathname)
end
% Downsample to original sequence length
sep_FM = resample(filtered_x,Q,P);

% AM_FM - channel X
[filename,pathname,filterindex] = uigetfile('*.','Step 5:Input AM_FM
(chX/ch1) file:');
if ~(isequal(filename,0) && isequal(pathname,0)) % check
for Cancel
AM_FM = dlmread(strcat(pathname,filename));
AM_FM = AM_FM(11:12);
x = AM_FM;
P = 4;
Q = 1;
x = resample(x,P,Q); % upsample by factor P/Q
fs = 1000; % assumed sampling
frequency
fft_points = 4096; % no of points in computing
the DFT - higher value gives better resolution
% Actual DFT calculation
X = fft(x,fft_points);
Pxx = (X.*conj(X))/fft_points;
Pxx(1) = 0; % first term is just sum of
all terms - dc term
Pxx = Pxx/max(Pxx);
f = fs/fft_points*(0:fft_points/2 - 1)'; % frequency axis
% Plot PSD of input sequence
figure;
plot(f,Pxx(1:fft_points/2),'.-');grid on;hold on;
title('\bfPower spectral density');xlabel('Frequency (Hz)')
N = 8000; % length of FIR filter -
the longer the better
fc = 0.4; % cut off frequency (Hz) -
inspect PSD and choose value
wn = fc/(fs/2); % normalized cutoff
b_fir = fir1(N,wn); % actual filter
coefficients
```

## Chapter 9: Extras

```
% Filter frequency response
[H_fir w_fir] = freqz(b_fir,1,4096);
H_fir_mag     = abs(H_fir);
H_fir_phase   = unwrap(angle(H_fir)*180/pi);
f_fir        = w_fir/(2*pi)*fs;
plot(f_fir,H_fir_mag,'g.-');
xlim([-1 5]);
% Filter input sequence
filtered_x = filtfilt(b_fir,1,x);
% Plot result
figure;hold on;
plot(x,'b');plot(filtered_x,'m');
legend('Original','Filtered');
title('\bfFIR filtering - original and filtered');
cd(pathname);
end
AM_FM = resample(filtered_x,Q,P);

% NoGas_OP1_ch1 to normalise
[filename,pathname,filterindex] = uigetfile('*.','Step 7:Input no gas
OP1 ch1 file:');
if ~(isequal(filename,0) && isequal(pathname,0)) % check
for Cancel
    OP1_nogas = dlmread(strcat(pathname,filename));
%     OP1_nogas = OP1_nogas(11:12);
    OP1_nogas = filtfilt(b1,a1,OP1_nogas);
    cd(pathname)
end

% Get sensitivities
sep_FM_sens = str2num(char(inputdlg('Input sep_FM sensitivity in
volts')));
AM_FM_sens = sep_FM_sens; %
Sensitivities will necessarily be equal
OP1_nogas_sens = str2num(char(inputdlg('Input O/P1 no gas sensitivity
in volts')));

f2 = figure;
plot(sep_FM*sep_FM_sens,'b');hold on;
plot(AM_FM*AM_FM_sens,'r');
plot(OP1_nogas*OP1_nogas_sens,'g');

% ***** CALCULATION OF PHI - AM/WM PHASE SHIFT *****
%
% Locate +ive & -ive peaks on ch Y to calculate AM/WM phase shift
y1 = min(sep_FM); % amplitude of negative peak of
sep_FM = y1
y1_index = find(sep_FM == y1); % index of neg peak

y2 = max(sep_FM); % amplitude of positive peak of
sep_FM = y2
y2_index = find(sep_FM == y2); % index of pos peak
```

## Chapter 9: Extras

```
% Calculate x1, x2 corresponding to indices for y2 and y2 - note
"corresponding"
min_AM_FM = AM_FM(y2_index);           % not necessarily min (or
max)of AM_FM_amps...
max_AM_FM = AM_FM(y1_index);           % ...min (or max) of sep_FM

% Therefore, x1 and x2...
x1      = max_AM_FM(1);
x2      = min_AM_FM(1);

% FINALLY...Calculate phi = AM_WM_phase_shift
phi      = atand((abs(y2)+abs(y1))/abs((x1-x2)))
% -----
% -----

% Calculate direct absorption signal using phasor decomposition method
AM_whole = AM_FM + sep_FM./tand(phi);
figure;plot(AM_whole);

% Quick Baseline for AM_whole
figure;
plot(AM_whole);
hold on;
index = 1:length(AM_whole);
index = index(:);
fitx = [index(1:10);index(end-10:end)];
fity = [AM_whole(1:10);AM_whole(end-10:end)];
pol = polyfit(fitx,fity,1);
AM_whole_fit = polyval(pol,index);
hold on;
plot(AM_whole_fit,'r');
baseline_AM_whole = AM_whole_fit;

% Saving AM_whole to get baseline
[filename, pathname, filterindex] = uiputfile('AM_whole.dat', 'Save
AM_whole as...');
if ~(isequal(filename,0) && isequal(pathname,0))

dlmwrite(strcat(pathname,filename),AM_whole,'delimiter','\n','precision
', '%.6f');
end

% -----
% -----

% New Wavelength Referencing
clear Line_Cent_freq Line_Cent_Index error1 closest_peak Res_Peak_freq
clear x_res P_res Theory_Cent_freq wavelength frequencies shift
% Convert zero-crossing indices to frequencies
Res_Peak_freq = zeros(size(peak));           % initialize for for-end
loop
Res_Peak_freq(1) = 1;           % ANY arbitrary initial frequency
value
```

## Chapter 9: Extras

```
% Construct frequency scale with actual frequency SPACING (not VALUES)
for n = 1:length(peak)-1
    Res_Peak_freq(n+1) = Res_Peak_freq(n) - 0.4275;
end
% Fit polynomial to get functional dependence
x_res = (1:length(AM_whole));
P_res = polyfit(peak(:),Res_Peak_freq(:),2);
frequencies = polyval(P_res, x_res); % Extract values of polynomial
fit at each increment x
% Shift frequency values to theoretical line centre
nu_zero = 3e8/waves(find(amps == min(amps)));
% Find the line centre index from the experimental plot
Line_Cent_Index = find(AM_whole == min(AM_whole)); % gas minimum
index
Line_Cent_Index = Line_Cent_Index(1); % check for double
value
shift = nu_zero - frequencies(Line_Cent_Index);
frequencies = frequencies + shift; % actual
frequencies
wavelength = 3e8./frequencies; % actual
wavelength
wavelength = wavelength(:);
frequencies = 3e8./(wavelength*1e-9);
%-----
----

f2 = figure;
plot(wavelength,sep_FM*sep_FM_sens,'b');hold on;
plot(wavelength,AM_FM*AM_FM_sens,'r');
plot(wavelength,OP1_nogas*OP1_nogas_sens,'g:');

% Baseline to AM_whole
[filename, pathname, filterindex] = uigetfile('*..*', 'Input baseline
fit for AM_whole...');
if ~(isequal(filename,0) && isequal(pathname,0))
    baseline_AM_whole = dlmread(strcat(pathname,filename));
    cd(pathname)
end
figure;plot(wavelength,AM_whole,wavelength,baseline_AM_whole);

% *****
% PART 2 - Calculation of Absorption
% *****
nulled_output = (AM_whole-baseline_AM_whole)*AM_FM_sens;;
absorption = -nulled_output./(OP1_nogas*OP1_nogas_sens);
transmission = 1 - absorption;

% Interpolate theory plot
amps = interp1(waves,amps,wavelength);

figure;
```

## Chapter 9: Extras

```
subplot(3,1,[1 2]);hold on;
plot(wavelength,amps,'b');
plot(wavelength,transmission,'r');
xlabel('\bf\lambda (nm)');ylabel('Relative Transmission');
title('\bfExperimental Results');
legend('Theory','Expt');
xlim([1650.8 1651.1]);

subplot(313);
plot(wavelength,transmission - amps);
xlim([1650.8 1651.1]);
% -----
% -----

% *****
% PART 3 - 2ND AND 4TH ORDER CORRECTIONS
% *****
clear corrected_transmission correction_factor L M N line_cent_index
line_cent_freq HWHM
clear delta B D m correction_factor

% Enter current dither size (mA)
current_dither_size = str2double(char(inputdlg('Enter current
dither amplitude (mA peak)')));
% Enter delta_nu/delta_i (Ghz/mA)
del_nu_del_i = str2double(char(inputdlg('Input
delta_nu/delta_I in GHz/mA: ')));
del_nu = del_nu_del_i * current_dither_size * 1e9;
corrected_transmission(:,1) = transmission;

for c = 1:4
    % Calculate HWHM of the original distorted AM trace
    L(c) = (1 +
min(corrected_transmission(:,c)))/2; % Calculates the FWHM amplitude
[M(c),N(c)] =
min(abs(corrected_transmission(:,c) - L(c))); % Find nearest value to
calculated FWHM
FWHM_freq(c) = frequencies(N(c)); % frequency at
the point of inflection of the absorption profile
% Calculate HWHM magnitude as frequency difference between
FWHM_freq and line centre
line_cent_index(c) =
find(corrected_transmission(:,c)==min(corrected_transmission(:,c)));
line_cent_freq(c) = frequencies(line_cent_index(c));
line_cent_freq(c) = line_cent_freq(1);
HWHM(c) = abs(FWHM_freq(c) -
line_cent_freq(c));
% Calculate 2nd and 4th order correction factor
delta(:,c) = (frequencies-
line_cent_freq(c))./HWHM(c);
B(:,c) = (3.*(delta(:,c).^2)-
1)./(1+(delta(:,c).^2).^2);
D(:,c) = (5.*(delta(:,c).^4)-
(10.*(delta(:,c).^2)+1))./(1+(delta(:,c).^2).^4);
```

## Chapter 9: Extras

```
m(c) = (del_nu/HWHM(c));
correction_factor(:,c) =
(1./(1+(0.25*(m(c)^2).*B(:,c))+((0.125*(m(c)^4)).*D(:,c)))));
corrected_transmission(:,(c+1)) = (1 -
corrected_transmission(:,1)).*correction_factor(:,c);
corrected_transmission(:,(c+1)) = 1 -
corrected_transmission(:,(c+1)); % convert back to relative
transmission
end
% Comparison of nth order corrections
fig2 = figure;
plot(wavelength,amps,'b');hold on;
plot(wavelength,corrected_transmission(:,1), 'c');
plot(wavelength,corrected_transmission(:,2), 'g');
plot(wavelength,corrected_transmission(:,3), 'k');
plot(wavelength,corrected_transmission(:,4), 'y');
plot(wavelength,corrected_transmission(:,5), 'r');
xlabel('\bf\lambda (nm)');ylabel('\bf Relative Transmission');
legend('theory', '0th', '1st', '2nd', '3rd', '4th');
title('\bfExperimental results for 10.13% CH_4 - PDM RAM-nulled - m =
0.2');

min_corrected_signals = min(corrected_transmission,[],1);
error = (min(amps) -
(min_corrected_signals))/min(amps) * 100;
[min_error min_error_index] = min(abs(error));
best_iteration_index = min_error_index - 1
error_for_best_iteration = error(min_error_index)

% Saving uncorrected result
[filename, pathname, filterindex] = uiputfile('uncorrected_result.dat',
'Save uncorrected result as...');
if ~(isequal(filename,0) && isequal(pathname,0))
    dlmwrite(strcat(pathname,filename),[wavelength
corrected_transmission(:,1)], 'delimiter', '\n', 'precision', '%.6f');
end

% Saving best iteration result
[filename, pathname, filterindex] =
uiputfile('corrected_best_iteration.dat', 'Save best iteration result
as...');
if ~(isequal(filename,0) && isequal(pathname,0))
    dlmwrite(strcat(pathname,filename),[wavelength
corrected_transmission(:,min_error_index)], 'delimiter', '\n', 'precision',
'%.6f');
end

figure;
subplot(3,1,[1 2]);hold on;
plot(wavelength,amps,'b');
plot(wavelength,corrected_transmission(:,4), 'r');
xlabel('\bf\lambda (nm)');ylabel('Relative Transmission');
title('\bfExperimental Results');
legend('Theory', 'Expt');
```

## Chapter 9: Extras

```
xlim([1650.8 1651.1]);
```

```
subplot(313);
```

```
plot(wavelength,corrected_transmission(:,4)- amps);
```

```
xlim([1650.8 1651.1]);
```

```
% % END OF PROGRAM
```

```
% %-----
```